Analysis by Meshless Local Petrov-Galerkin Method of Material Discontinuities, Pull-in Instability in MEMS, Vibrations of Cracked Beams, and Finite Deformations of Rubberlike Materials

Maurizio Porfiri

Dissertation submitted to the Faculty of the
Virginia Polytechnic Institute and State University
in partial fulfillment of the requirements for the degree of

Doctor of Philosophy
in
Engineering Mechanics

Prof. Romesh C. Batra, Chair
Prof. Edmund G. Henneke
Prof. Michael W. Hyer
Prof. Liviu Librescu
Prof. Douglas K. Lindner

April 27, 2006
Blacksburg, Virginia

Keywords: MLPG method, MEMS, Vibrations,
Rubberlike Materials, Discontinuities

Analysis by Meshless Local Petrov-Galerkin Method of Material Discontinuities, Pull-in Instability in MEMS, Vibrations of Cracked Beams, and Finite Deformations of Rubberlike Materials

Maurizio Porfiri

(Abstract)

The Meshless Local Petrov-Galerkin (MLPG) method has been employed to analyze the following linear and nonlinear solid mechanics problems: free and forced vibrations of a segmented bar and a cracked beam, pull-in instability of an electrostatically actuated microbeam, and plane strain deformations of incompressible hyperelastic materials. The Moving Least Squares (MLS) approximation is used to generate basis functions for the trial solution, and for the test functions. Local symmetric weak formulations are derived, and the displacement boundary conditions are enforced by the method of Lagrange multipliers. Three different techniques are employed to enforce continuity conditions at the material interfaces: Lagrange multipliers, jump functions, and MLS basis functions with discontinuous derivatives. For the electromechanical problem, the pull-in voltage and the corresponding deflection are extracted by combining the MLPG method with the displacement iteration pull-in extraction algorithm. The analysis of large deformations of incompressible hyperelastic materials is performed by using a mixed pressure-displacement formulation. For every problem studied, computed results are found to compare well with those obtained either analytically or by the Finite Element Method (FEM). For the same accuracy, the MLPG method requires fewer nodes but more CPU time than the FEM.

Acknowledgments

I wish to first and foremost acknowledge my advisor Dr. Romesh C. Batra. Without his guidance, advice and encouragement this work would not have come to existence. I would like to express my deep gratitude to my parents, my sister and all my late grandparents who have always supported me, believed in me and covered me with love during all my studies. Next, I would like to thank Dr. Edmund G. Henneke, my other committee members, Dr. Michael W. Hyer, Dr. Liviu Librescu and Dr. Douglas K. Lindner, and the entire Department of Engineering Science and Mechanics that gave me the chance to complete my studies in this wonderful country, where I will hopefully find my way as a researcher. This dissertation would not be complete without the unique collaboration over the past years with my friend and colleague Davide Spinello. I also would like to express my gratitude to Dr. Daniel J. Stilwell and the entire Autonomous Systems and Control Laboratory for hosting me as a Post-Doctoral Fellow in the last year. I want to thank all my international friends, Alis, Bin, Courtney, Farid, Gray, Hanif, Jan, Javier, Najm, Nawazish, Omid, Sibel and Umut for the great friendship they always demonstrated with me. And finally, I would like to thank my wife Maria for her endless support and help during these sometimes difficult years.

This work was partially supported by the Office of Naval Research grant N-00014-98-1-0300 to Virginia Polytechnic Institute and State University (VPI&SU), and the AFoSR MURI grant to Georgia Tech that awarded a subcontract to VPI&SU. Views expressed in this dissertation are those of the author and not of the funding agency.

Contents

List of Figures

List of Tables

Chapter 1

Introduction

Recently, considerable research in computational mechanics has been devoted to the development of meshless methods, that lessen the difficulty of meshing and remeshing the entire structure, by only adding or deleting nodes at suitable locations (see, e.g., Liu (2003) for a thorough review of meshless methods). Meshless methods may also alleviate some other problems associated with the Finite Element Method (FEM), such as locking and element distortion. In many applications, they provide smooth, and accurate approximate solutions with a reduced number of nodes.

During the last two decades, several meshless methods for seeking approximate solutions of partial differential equations have been proposed; these include the element-free Galerkin (Belytschko, Lu and Gu (1994)), hp-clouds (Duarte and Oden (1996)), the reproducing kernel particle (Liu, Jun, Adee and Belytschko (1995), Liu, Jun and Zhang (1995), Chen, Pan and Wu (1997)), the smoothed particles hydrodynamics (SPH) (Lucy (1977)), the diffuse element (Nayroles, Touzot and Villon (1992)), the partition of unity finite element (Melenk and Babuska (1996)), the natural element (Sukumar, Moran and Belytschko (1998)), meshless Galerkin using radial basis functions (Wendland (1995)), the meshless local Petrov-Galerkin (MLPG) (Atluri and Zhu (1998)), the modified smoothed particle hydrodynamics (MSPH) (Zhang and Batra (2004)), and the collocation method with radial basis functions (Ferreira, Batra, Roque, Qian and Martins (2005)). All of these methods, except for the MLPG, the SPH, the MSPH, and the collocation method are not truly meshless since the use of shadow elements is required for evaluating integrals appearing in the governing weak formulations (see, e.g., Atluri and Shen (2002)). The MLPG method has been successfully applied to several structural problems: static linear plane elasticity (Atluri and Zhu (1998)); vibrations of elastic planar bodies (Gu and Liu (2001a)); static analysis of thin plates (Gu and Liu (2001b)); static analysis of beams (Atluri, Cho and Kim (1999), Raju and Phillips (2003)); vibrations of cracked beams (Andreaus, Batra and Porfiri (2005)); static and dynamic problems for functionally graded materials (Qian, Batra and Chen (2004a,b)) and (Qian and

Batra (2004)); static and dynamic problems for thick rectangular plates (Qian, Batra and Chen (2003a,b); analysis of transient problems with material discontinuities (Batra, Porfiri and Spinello (2006a)); heat conduction problems in multimaterial bodies (Batra, Porfiri and Spinello (2004)) and analysis of microelectromechanical problems (Batra, Porfiri and Spinello (2006b,c)). The MLPG method is based on local weak forms of governing equations and employs meshless interpolations for both the trial and the test functions. The trial functions are constructed by using the Moving Least Squares (MLS) (Lancaster and Salkauskas (1981)) approximation and its enhanced versions proposed by Atluri, Chom and Kim (1999), and Kim and Atulri (2000), or the radial basis functions (see, e.g., Kansa (1990)). These approximations simply rely on the location of points or nodes in the body, rather than complex meshes. In the Petrov-Galerkin formulation, test functions may be chosen from a space different from the space of trial functions; in this way, depending upon the choice of the test function, and the employment of a local symmetric or local asymmetric weak form, Atluri and Shen (2002) proposed six variants, namely MLPG1, MLPG2,..., MLPG6, of the MLPG method. In MLPG6, the local symmetric Bubnov-Galerkin formulation, the test function for each subdomain is chosen to be the MLS basis function associated with a node. Another relevant feature of the MLPG method is that, the domains of integration may either overlap or their union may not equal the domain occupied by the body.

Thus the key ingredients of the MLPG method may be summarized as: local weak formulation, MLS interpolation, Petrov-Galerkin projection, evaluation of domain integrals appearing in the weak formulation, imposition of essential boundary conditions, and for transient problems time-integration of the resulting ordinary differential equations.

Chapter 2

Free and Forced Vibrations of a Segmented Bar

2.1 Introduction

For a body made of two or more materials, the derivative of displacements in the direction normal to the interface between two materials must be discontinuous in order for surface tractions there to be continuous. For the analysis of linear elastostatic problems by the EFG method, Cordes and Moran (1996) used the method of Lagrange multipliers, Krongauz and Belytschko (1998) employed a special jump function at the line or the surface of discontinuity, and Noguchi and Sachiko (2006) modified the Moving Least Square (MLS) basis functions so that their derivative jumps at desired locations. Whereas a two-dimensional (2-D) static problem was analyzed by Krongauz and Belytschko (1998), a 1-D static problem was scrutinized by Cordes and Moran (1996). Batra, Porfiri and Spinello (2004) have compared the performance of two MLPG formulations in the analysis of a parabolic 1-D problem, i.e., the axisymmetric transient heat conduction in a bimetallic disk with the material discontinuity treated either by the method of Lagrange multipliers or the jump function. Note that no waves propagate in a parabolic problem. However, waves propagate in a hyperbolic problem, and may be reflected and refracted at the interface between the two materials.

In this chapter, we use the MLPG6 formulation, that is trial and test functions are chosen from the same space generated by the Moving Least Squares (MLS) approximation. We compare the performance of the three aforementioned techniques to account for material discontinuities in the analysis of free, and forced vibrations of a segmented bar. As a sample problem we consider a clamped-free bimaterial bar, although the approach is also suitable for other boundary conditions. The essential (i.e. displacement) boundary condition is imposed

Material in this Chapter is part of the paper "Free and Forced Vibrations of a Segmented Bar by a Meshless Local Petrov-Galerkin (MLPG) Formulation," accepted for publication in *Computational Mechanics*.

in all cases by introducing a Lagrange multiplier; this technique was used by Warlock, Ching, Kapila and Batra (2002) and Batra and Wright (1986) to satisfy contact conditions at a rough surface. Following the idea developed by Andreaus, Batra and Porfiri (2005) for a beam, it is shown that the MLPG6 numerical solution is stable and optimal by showing that the related mixed formulations satisfy the ellipticity and the inf-sup conditions (see Bathe (1996)). Numerical results are compared with analytical and FE solutions. In particular, the convergence with an increase in the number of nodes of the first two eigenfrequencies, first three mode shapes, and a static solution are shown, revealing a monotonically decreasing trend at a rate faster than that obtained with the FE method. The transient response to an axial traction of finite duration applied at one end of the bar is shown to match very well with the analytical solution of the problem.

The rest of the Chapter is organized as follows. In Section 2.2 we introduce the MLS basis functions with discontinuous derivatives (Noguchi and Sachiko (2006)). Section 2.3 gives differential equations, and initial and boundary conditions for wave propagation in a segmented elastic bar with one end clamped and the other free. Section 2.4 presents the MLPG6 formulations for the method of Lagrange multipliers, the method of jump function, and the method of MLS basis functions with discontinuous derivatives. In Section 2.4, we also very briefly discuss the numerical evaluation of domain integrals, and the method used to numerically integrate, with respect to time, the semidiscrete system of ordinary differential equations. Numerical results computed with the three methods of treating material discontinuities are discussed in Section 2.5 where the convergence of the MLPG6 solution for static deformations, and mode shapes is compared with that of the FE solution, and the transient response to a time dependent axial traction is compared with the analytical solution of the corresponding problem. Section 2.6 summarizes conclusions. The ordinary MLS approximation may be found in Appendix A.1. Analytical solutions of the problem for free, and forced vibrations of the segmented bar are given in the Appendices B.1 and B.2 respectively.

2.2 Modified MLS basis functions with discontinuous derivatives

Let a material interface be located at the point $a \in (0, L)$ in the global domain $\Omega = [0, L]$. Consider N scattered points $x_1, \ldots, x_N$ and let a node be located at $x = a$. Herein, we derive a modified MLS approximation that allows for the reconstruction of a function w in Ω whose derivative jumps at $x = a$. We refer to Appendix A.1 for a detailed explanation of the ordinary MLS approximation. We denote by N_1 and N_2 the number of nodes whose location x_j satisfies the condition $x_j \leq a$, and $x_j > a$ respectively. Let W_j be the weight function of the j-th node and r_j be the radius of its support. Also, let n_1 and n_2 be the number of nodes

whose location x_j satisfies the condition $a - r_{N_1} < x_j \leq a$, and $a < x_j < a + r_{N_1}$ respectively. In other words, n_1 and n_2 equal the number of nodes in the domain of influence of the weight function W_{N_1} associated with the interface node at $x_{N_1} = a$, placed, respectively, to the left and to the right of the interface. In order to modify the ordinary MLS basis functions in the domain of influence of the weight function W_{N_1} in such a way that all basis functions which are nonzero at the interface are continuous but have discontinuous derivative, we consider the following global approximation of the function w in the region $(a - r_{N_1}, a + r_{N_1})$:

$$w^h(x) = \begin{cases} \mathbf{p}_1^{\mathrm{T}}(x)\,\mathbf{b}(x), & x \in (a - r_{N_1}, a] \\ \mathbf{p}_2^{\mathrm{T}}(x)\,\mathbf{b}(x), & x \in (a, a + r_{N_1}) \end{cases}, \tag{2.1}$$

with

$$\begin{aligned} \mathbf{p}_1^{\mathrm{T}}(x) &= \begin{bmatrix} 1 & x-a & 0 & (x-a)^2 & 0 & \cdots & (x-a)^{m-1} & 0 \end{bmatrix}, \\ \mathbf{p}_2^{\mathrm{T}}(x) &= \begin{bmatrix} 1 & 0 & x-a & 0 & (x-a)^2 & \cdots & 0 & (x-a)^{m-1} \end{bmatrix}, \end{aligned} \tag{2.2}$$

and

$$\mathbf{b}(x) = \begin{bmatrix} b_0(x) & b_{1,1}(x) & b_{2,1}(x) & \cdots & b_{1,m-1}(x) & b_{2,m-1}(x) \end{bmatrix}. \tag{2.3}$$

For example, for $m = 2$ one gets

$$w^h(x) = \begin{cases} b_0(x) + (x-a)\,b_{1,1}(x), & x \leq a \\ b_0(x) + (x-a)\,b_{2,1}(x), & x > a \end{cases}. \tag{2.4}$$

The weighted discrete L^2 error norm to be minimized is (see (A.5))

$$J_{\overline{x}}(\mathbf{b}) = \sum_{i=1}^{n_1} W_i(\overline{x}) \left[\mathbf{p}_1^{\mathrm{T}}(x_i)\,\mathbf{b}(\overline{x}) - \widehat{w}_i\right]^2 + \sum_{i=n_1+1}^{n_1+n_2} W_i(\overline{x}) \left[\mathbf{p}_2^{\mathrm{T}}(x_i)\,\mathbf{b}(\overline{x}) - \widehat{w}_i\right]^2, \tag{2.5}$$

for $\overline{x} \in (a - r_{N_1}, a + r_{N_1})$. By extremizing the functional J in (2.5) one obtains

$$\mathbf{A}(\bar{\mathbf{x}}) = \mathbf{P}^{\mathrm{T}}\mathbf{W}(\bar{\mathbf{x}})\,\mathbf{P}, \quad \mathbf{B}(\bar{\mathbf{x}}) = \mathbf{P}^{\mathrm{T}}\mathbf{W}(\bar{\mathbf{x}}). \tag{2.6}$$

where

$$\begin{aligned} \mathbf{A}(\overline{x}) &= \sum_{i=1}^{n_1} W_i(\overline{x})\,\mathbf{p}_1(x_i)\,\mathbf{p}_1^{\mathrm{T}}(x_i) + \sum_{i=n_1+1}^{n_1+n_2} W_i(\overline{x})\,\mathbf{p}_2(x_i)\,\mathbf{p}_2^{\mathrm{T}}(x_i), \\ \mathbf{B}(\overline{x}) &= [W_1(\overline{x})\,\mathbf{p}_1(x_1), \ldots, W_{n_1}(\overline{x})\,\mathbf{p}_1(x_{n_1}), \\ &\qquad W_{n_1+1}(\overline{x})\,\mathbf{p}_2(x_{n_1+1}), \ldots, W_{n_1+n_2}(\overline{x})\,\mathbf{p}_2(x_{n_1+n_2})]. \end{aligned} \tag{2.7}$$

Solving (2.6) for $\mathbf{b}$ we obtain

$$\mathbf{b}(x) = \mathbf{A}^*(x)\,\mathbf{B}(x), \tag{2.8}$$

where $\mathbf{A}^*$ is the pseudoinverse of matrix $\mathbf{A}$. Indeed, assuming that at every evaluation point x there are at least m nonvanishing weight functions, for the null space of the $(2m-1 \times 2m-1)$ matrix $\mathbf{A}$ the following holds:

$$0 \leq \dim \ker \mathbf{A} \leq m - 1. \tag{2.9}$$

When $\dim\ker \mathbf{A} = 0$, $\mathbf{A}$ is invertible, and its inverse and pseudoinverse coincide. However, when $\dim\ker \mathbf{A} > 0$, there are as many zero rows and columns in $\mathbf{A}$ as the number of vanishing weight functions at x; in this case the nonzero entries of the pseudoinverse are equal to the entries of the matrix obtained from $\mathbf{A}$ by deleting its zero rows and columns. Note that the corresponding rows of the matrix $\mathbf{B}$ are also zero; therefore (2.8) states that the related entries in the vector $\mathbf{b}$ are zero.

For 11 uniformly distributed nodes in the domain $[0, L]$ with the interface between two materials located at $a = L/2$ or at node 6, the modified MLS basis functions for nodes 1 through 6 are plotted in Figure 2.1, where we have set $m = 2$, $r_i = 3L/10$, and two nodes in the radius of support of each weight function. We emphasize that, in this approach, the weight functions are not modified, while all basis functions in the domain of influence of the weight function W_{N_1} are modified due to the introduction of the discontinuous monomial basis (2.2) in the region $(a - r_{N_1}, a + r_{N_1})$, which affects matrices $\mathbf{A}$ and $\mathbf{B}$ in the same region, and therefore the MLS basis functions. Even though the weight functions in (2.5) are non-negative, the basis functions may assume negative values. Also, a basis function is non-zero at more than one node. It is clear that basis functions for nodes in the domain of influence of the weight function W_6 (i.e., for nodes 4, 5, and 6), have discontinuous derivative at node 6.

2.3 Governing equations

We study wave propagation in a segmented bar of length L with the left segment of length a made of one material, and the right one of length $L - a$ made of a different material (Figure 2.2); E_i and ϱ_i, $i = 1, 2$, are, respectively, Young's modulus, and the volumetric mass density of the material constituting the left, and the right parts. As an example problem, the right end of the bar is clamped, and a time dependent axial traction $p(t)$ is applied at the left end. By assuming a uniform cross section, governing equations are

$$\varrho_1 \ddot{w}_1(x,t) - E_1 w_1''(x,t) = 0, \quad x \in (0,a),\ t > 0, \tag{2.10}$$

$$\varrho_2 \ddot{w}_2(x,t) - E_2 w_2''(x,t) = 0, \quad x \in (a,L),\ t > 0, \tag{2.11}$$

with boundary conditions

$$E_1 w_1'(0,t) = p(t), \tag{2.12}$$

$$w_1(a,t) = w_2(a,t), \tag{2.13}$$

$$E_1 w_1'(a,t) = E_2 w_2'(a,t), \tag{2.14}$$

$$w_2(L,t) = 0. \tag{2.15}$$

We assume homogeneous initial conditions

$$w_1(x,0) = w_2(x,0) = 0,$$
$$\dot{w}_1(x,0) = \dot{w}_2(x,0) = 0. \tag{2.16}$$

Here, $w_i(x,t)$ is the longitudinal displacement of point x in the $i-th$ segment of the bar; a superimposed dot means partial differentiation with respect to time t, while a prime means partial differentiation with respect to x. The global axial displacement field, w, is given by

$$w(x,t) = \begin{cases} w_1(x,t), & x \in (0,a) \\ w_2(x,t), & x \in (a,L) \end{cases}, \tag{2.17}$$

and a similar notation will be adopted for the global volumetric mass density, and Young's modulus.

Equations (2.13) and (2.14) state the continuity of the displacement, and of the axial stress at the interface. We note that the derivative w' must be discontinuous at the interface to guarantee the continuity of the axial stress.

In the forced vibration analysis, we will consider an axial traction applied at $x = 0$, shown in Figure 2.3, and given by

$$p(t) = P \sin\left(\frac{\pi t}{T}\right) [\mathcal{H}(t) - \mathcal{H}(t-T)], \tag{2.18}$$

where $\mathcal{H}$ is the Heaviside function, the dimension of P is force/area, and T measures the finite duration of the applied traction.

2.4 MLPG6 weak and semidiscrete formulations

In this Section, the MLPG6 formulation of the boundary-value problem (2.10)-(2.15) is derived. A Local Symmetric Augmented Weak Formulation (LSAWF) is stated for each one of the three methods of treating material discontinuities. The projection of trial and test functions on finite-dimensional basis functions leads to semidiscrete formulations of the problem, or equivalently a system of ordinary differential equations in time. It is shown that these mixed semidiscrete formulations are optimal, and stable in the sense that they satisfy both the ellipticity, and the inf-sup (Babuška-Brezzi) conditions.

2.4.1 Discontinuity modeled by a jump function

Semidiscrete formulation

Let $\Omega_S^i \subseteq [0,L]$, $i = 1,2,\ldots,N$ be a family of subdomains of the global domain such that $\cup_{i=1}^N \Omega_S^i = [0,L]$. We introduce the following LSAWF of the problem on the i-th subdomain

Ω_{S}^i:

$$0 = \int_{\Omega_{\mathrm{S}}^i} \varrho \ddot{w} \widetilde{w}_i \mathrm{d}x + \int_{\Omega_{\mathrm{S}}^i} E w' \widetilde{w}_i' \mathrm{d}x \\ - \left[(1-\delta_L) E w' \widetilde{w}_i + \delta_L \left(\lambda_L \widetilde{w}_i + \widetilde{\lambda}_L w \right) \right] \Big|_{\Gamma_{\mathrm{S}}^{i+}} + \left[(1-\delta_0) E w' \widetilde{w}_i + \delta_0 p \widetilde{w}_i \right] |_{\Gamma_{\mathrm{S}}^{i-}} . \tag{2.19}$$

Here, $\widetilde{w}_i \in H^1(0, L)$ is a test function for w,

$$\delta_y(x) := \begin{cases} 1, & x = y \\ 0, & x \neq y \end{cases} , \tag{2.20}$$

and Γ_{S}^{i-}, Γ_{S}^{i+} are the left, and the right boundary points of the subdomain Ω_{S}^i. In order to enforce the essential boundary condition (2.15), the Lagrange multiplier λ_L has been introduced, and the scalar $\widetilde{\lambda}_L$ is the corresponding test function. We emphasize that the natural boundary condition (2.12) has also been considered. The variational statement (2.19) can be derived by extremizing the Action related to an augmented Lagrangian on the set of isochronous motions following classical arguments, see, e.g., Mura and Koya (1992).

In order to capture the discontinuity in w' at the interface we enrich the set of smooth MLS basis functions $\psi(x)$ with a special jump function $\varkappa(x)$. Therefore, we approximate the axial displacement field by

$$w^h(x,t) = \psi^{\mathrm{T}}(x) \widehat{\mathbf{w}}(t) + q(t) \varkappa(x) , \tag{2.21}$$

where the additional unknown $q(t)$ represents the jump in the axial strain at time t and $\widehat{\mathbf{w}}$ is comprised of nodal unknowns. The jump function $\varkappa(x)$ and its first derivative are continuous in both segments of the bar, and its first derivative jumps at $x = a$ in order to ensure the continuity of the axial stress without affecting the continuity of the displacement field. Following Krongauz and Belytschko (1998), we take

$$\varkappa(x) = \begin{cases} \dfrac{1}{6} - \dfrac{1}{2}\left(\dfrac{|x-a|}{r_{\mathrm{J}}}\right) + \dfrac{1}{2}\left(\dfrac{|x-a|}{r_{\mathrm{J}}}\right)^2 - \dfrac{1}{6}\left(\dfrac{|x-a|}{r_{\mathrm{J}}}\right)^3, & \dfrac{|x-a|}{r_{\mathrm{J}}} \leq 1 \\ 0, & \dfrac{|x-a|}{r_{\mathrm{J}}} > 1 \end{cases} . \tag{2.22}$$

The size of the support of $\varkappa(x)$ equals $2r_{\mathrm{J}}$ and, as shown in Figure 2.4, the jump function and its derivative go to zero smoothly as $|x-a|/r_{\mathrm{J}} \to 0$, while the derivative of $\varkappa\left(\frac{|x-a|}{r_{\mathrm{J}}}\right)$ jumps from $1/2$ at $x = a^-$ to $-1/2$ at $x = a^+$.

In order to generate $N+2$ equations for the $N+1$ nodal unknowns

$$\widehat{\mathbf{u}}(t) = \begin{bmatrix} \widehat{\mathbf{w}}(t) & q(t) \end{bmatrix}^{\mathrm{T}} , \tag{2.23}$$

and the Lagrange multiplier λ_L, we consider the set of $N+2$ independent test functions

$$\mathbf{\Psi}(x) = \begin{bmatrix} \psi_1(x) & \cdots & \psi_N(x) & \varkappa(x) \end{bmatrix}^{\mathrm{T}} , \tag{2.24}$$

and $\widetilde{\lambda}_L$. Thus an additional node is introduced at $x = a$. Setting the subdomain of integration to be the support of the i-th test function, and substituting into (2.19), the following semidiscrete local Bubnov-Galerkin (MLPG6) formulation arises:

$$\begin{cases} \mathbf{M}\ddot{\widehat{\mathbf{u}}}(t) + \mathbf{K}\widehat{\mathbf{u}}(t) + \mathbf{G}\lambda_L(t) = \mathbf{F}(t) \\ \mathbf{G}^{\mathrm{T}}\widehat{\mathbf{u}}(t) = 0 \end{cases} . \tag{2.25}$$

Here,

$$[\mathbf{M}]_{ij} = \int_{\Omega_{\mathrm{S}}^i} \varrho \Psi_i \Psi_j \mathrm{d}x, \quad [\mathbf{K}]_{ij} = \int_{\Omega_{\mathrm{S}}^i} E\Psi_i' \Psi_j' \mathrm{d}x, \quad [\mathbf{F}(t)]_i = -\delta_0 p(t) \Psi_i|_{\Gamma_{\mathrm{S}}^{i-}}, \tag{2.26}$$
$$i, j = 1, 2, \ldots, N+1,$$

are the $(N+1)\times(N+1)$ mass, the stiffness, and the $(N+1)\times 1$ load matrices respectively, while the $(N+1)\times 1$ matrix $\mathbf{G}$ appearing both in the equation of motion, and in the constraint equation is given by

$$[\mathbf{G}]_i = -\delta_L \Psi_i|_{\Gamma_{\mathrm{S}}^{i+}}. \tag{2.27}$$

Inf-Sup test

In order to achieve a stable, and optimal procedure for the MLPG6 method employing a Lagrange multiplier, the mixed formulation in static regimes should satisfy the ellipticity condition and the inf-sup condition (see, e.g., Bathe (1996)).The ellipticity condition is satisfied because of Poincaré's inequality. However, some effort is needed in proving that the present formulation satisfies the inf-sup condition, which reads

$$\inf_{\lambda_L \in \mathbb{R}/\{0\}} \sup_{w^h \in W^h/\{0\}} \frac{\lambda_L w^h(L)}{\|\lambda_L\| \, \|w^h\|_{H^1}} \geq \bar{\beta} > 0, \tag{2.28}$$

where $\|\lambda_L\| = |\lambda_L|$,

$$\|w\|_{W^h}^2 := \int_0^L \left[w^2 + L^2 (w')^2 \right] \mathrm{d}x, \tag{2.29}$$

$\bar{\beta}$ is a constant independent of the nodal spacing, and W^h is the MLS solution space which is a subspace of $H^1(0, L)$. For $m = 1$, i.e., for complete monomial basis of order 0, the MLS basis functions reproduce exactly a constant function (see (A.4)), i.e., a rigid translation of the bar. Following Andreaus, Batra and Porfiri (2005) we choose, for any λ_L

$$w^h(x) = \lambda_L, \tag{2.30}$$

from which it follows that the inf-sup condition (2.28) is satisfied.

Reduced semidiscrete system of equations

The second equation in (2.25) provides a constraint for the unknown vector $\widehat{\mathbf{u}}$. By properly manipulating the system (2.25) we obtain a simpler formulation where the constraint is automatically satisfied.

Let $\ker \mathbf{G}^{\mathrm{T}}$ be the null space of $\mathbf{G}^{\mathrm{T}}$; since the inf-sup condition holds, $\dim \ker \mathbf{G}^{\mathrm{T}} = N$ (see, e.g., Bathe, 1996). Next, we introduce the $N \times (N+1)$ matrix $\mathbf{X}$ whose rows constitute a basis for $\ker \mathbf{G}^{\mathrm{T}}$, and the reduced N-vector of unknowns $\mathbf{u}$:

$$\widehat{\mathbf{u}} = \mathbf{X}^{\mathrm{T}}\mathbf{u}. \tag{2.31}$$

It is clear that the constraint equation is automatically satisfied for every $\mathbf{u} \in \mathbb{R}^N$. Substituting (2.31) into $(2.25)_1$, and premultiplying by $\mathbf{X}$ one obtains the following reduced semidiscrete system of equations for $\mathbf{u}$:

$$\mathbf{m}\,\ddot{\mathbf{u}}\,(t) + \mathbf{k}\,\mathbf{u}\,(t) = \mathbf{f}\,(t)\,, \tag{2.32}$$

where

$$\mathbf{m} = \mathbf{X}\mathbf{M}\mathbf{X}^{\mathrm{T}}, \quad \mathbf{k} = \mathbf{X}\mathbf{K}\mathbf{X}^{\mathrm{T}}, \quad \mathbf{f} = \mathbf{X}\mathbf{F}. \tag{2.33}$$

After solving for $\mathbf{u}$, we obtain the complete vector of unknowns $\widehat{\mathbf{u}}$ by using (2.31).

2.4.2 Discontinuity modeled by modified MLS basis functions with discontinuous derivative

Let N nodes be located in the global domain $[0, L]$ with a node placed at the interface $x = a$, and let $\varphi\,(x)$ be the set of MLS basis functions modified as in Section 2.2. The MLPG6 semidiscrete formulation is obtained in a similar way as for the method of jump function, i.e. by substituting in the LSAWF (2.19) the approximation $w^h\,(x,t) = \varphi^{\mathrm{T}}\,(x)\,\widehat{\mathbf{w}}\,(t)$ for the trial solution, by considering the basis function φ_i as test function for the i-th subdomain, and by setting Ω_{S}^i equal to the support of φ_i. Therefore, the following $N+1$ equations for the N nodal unknowns $\widehat{\mathbf{w}}$, and the Lagrange multiplier λ_L are obtained:

$$\begin{cases} \mathbf{M}\ddot{\widehat{\mathbf{w}}}\,(t) + \mathbf{K}\widehat{\mathbf{w}}\,(t) + \mathbf{G}\lambda_L\,(t) = \mathbf{F}\,(t)\,, \\ \mathbf{G}^{\mathrm{T}}\widehat{\mathbf{w}}\,(t) = 0. \end{cases} \tag{2.34}$$

The entries of the $(N \times N)$ mass and stiffness matrices, of the N load vector, and of the $(N \times 1)$ matrix $\mathbf{G}$ are given by

$$[\mathbf{M}]_{ij} = \int_{\Omega_{\mathrm{S}}^i} \varrho\varphi_i\varphi_j \mathrm{d}x, \quad [\mathbf{K}]_{ij} = \int_{\Omega_{\mathrm{S}}^i} E\varphi_i'\varphi_j' \mathrm{d}x, \quad [\mathbf{F}\,(t)]_i = -\,\delta_0 p\,(t)\,\varphi_i|_{\Gamma_{\mathrm{S}}^{i-}}\,, \tag{2.35}$$

$$[\mathbf{G}]_i = -\,\delta_L\varphi_i|_{\Gamma_{\mathrm{S}}^{i+}}\,, \qquad i,j = 1,2,\ldots,N. \tag{2.36}$$

It is easy to check (see Section 2.4.1) that the static form of the semidiscrete formulation (2.34) is elliptic, and that it satisfies the inf-sup condition. Therefore, we can introduce the reduced $(N-1)$-vector of unknowns $\mathbf{w}$:

$$\widehat{\mathbf{w}} = \mathbf{X}^{\mathrm{T}}\mathbf{w}, \tag{2.37}$$

where $\mathbf{X}$ is the $(N-1)\times N$ matrix whose rows constitute a basis for $\ker \mathbf{G}^{\mathrm{T}}$. The constraint represented by the second equation in (2.34) is then automatically satisfied; upon substitution from (2.37) into the first equation in (2.34), and premultiplication by $\mathbf{X}$ one obtains a reduced system of $N-1$ equations for the $N-1$ unknowns $\mathbf{w}$ formally analogous to (2.32).

2.4.3 Continuity of the displacement at the interface modeled by a Lagrange multiplier

Semidiscrete formulation

Let $\{x_i \in [0,a]\,,\ i=1,\dots,N_1\}$, and $\{x_i \in [a,L]\,,\ i=N_1+1,\dots,N_1+N_2\}$ be two sets of nodes such that $x_{N_1} \equiv x_{N_1+1} = a$, and

$$\Omega^i_{\mathrm{S}1} \subset [0,a]\,,\ i=1,\dots,N_1; \qquad \Omega^k_{\mathrm{S}2} \subset [a,L]\,,\ k=N_1{+}1, N_1{+}2,\dots,N_1{+}N_2{-}1, N_1{+}N_2 =: N, \tag{2.38}$$

be the corresponding disjoint families of subdomains covering $[0,a]$, and $[a,L]$ respectively. Following Cordes and Moran (1996), we consider the augmented variational statement

$$\begin{aligned} 0 = &\int_{\Omega^i_{\mathrm{S}1}} \varrho_1 \ddot{w}_1 \widetilde{w}_{1i}\mathrm{d}x + \int_{\Omega^i_{\mathrm{S}1}} E_1 w_1' \widetilde{w}_{1i}'\mathrm{d}x + \int_{\Omega^k_{\mathrm{S}2}} \varrho_2 \ddot{w}_2 \widetilde{w}_{2k}\mathrm{d}x + \int_{\Omega^k_{\mathrm{S}2}} E_2 w_2' \widetilde{w}_{2k}'\mathrm{d}x \\ &- \left[(1-\delta_a)\, E_1 w_1' \widetilde{w}_{1i} - \delta_a \left(\lambda_a\, \widetilde{w}_{1i} + \widetilde{\lambda}_a\, w_1\right)\right]\Big|_{\Gamma^{i+}_{\mathrm{S}1}} + \left[(1-\delta_0)\, E_1 w_1' \widetilde{w}_{1i} + \delta_0 p \widetilde{w}_{1i}\right]|_{\Gamma^{i-}_{\mathrm{S}1}} \\ &- \left[(1-\delta_L)\, E_2 w_2' \widetilde{w}_{2k} + \delta_L \left(\lambda_L\, \widetilde{w}_{2k} + \widetilde{\lambda}_L\, w_2\right)\right]\Big|_{\Gamma^{k+}_{\mathrm{S}2}} \\ &+ \left[(1-\delta_a)\, E_2 w_2' \widetilde{w}_{2k} - \delta_a \left(\lambda_a\, \widetilde{w}_{2k} + \widetilde{\lambda}_a\, w_2\right)\right]\Big|_{\Gamma^{k-}_{\mathrm{S}2}}. \end{aligned} \tag{2.39}$$

Here, $\widetilde{w}_{1i}$, $\widetilde{w}_{2k}$, $\widetilde{\lambda}_a$, and $\widetilde{\lambda}_L$ are test functions for the displacement fields, and the Lagrange multipliers λ_a and λ_L introduced to enforce the continuity of the displacement at the interface (2.13), and the essential boundary condition (2.15). In this approach, two problems are separately formulated in the two homogenous parts of the bar; two overlapping nodes are placed at the interface, and the two problems are connected by the Lagrange multiplier λ_a. Note that the natural boundary condition (2.14) is taken into account only in the weak sense.

The MLPG6 semidiscrete formulation is derived by substituting into the LSAWF (2.39) the global approximations for the trial solutions:

$$w_1^h(x,t) = \psi_1(x)^{\mathrm{T}}\, \widehat{\mathbf{w}}_1(t)\,, \quad w_2^h(x,t) = \psi_2(x)^{\mathrm{T}}\, \widehat{\mathbf{w}}_2(t)\,, \tag{2.40}$$

where $\psi_1(x)$ and $\psi_2(x)$ are the MLS basis functions defined separately in domains $[0,a]$ and $[a,L]$, and $\widehat{\mathbf{w}}_1$ and $\widehat{\mathbf{w}}_2$ are the nodal unknowns in the two regions. Furthermore, the MLS basis function $\psi_{\alpha i}$ $(\alpha=1,2)$ is taken as the test function in the subdomain $\Omega^i_{\mathrm{S}\alpha}$ $(\alpha=1,2)$ with support equal to that of the corresponding MLS basis function. Therefore, the system of $(N+2)$ ODEs

$$\left\{\begin{array}{r} \mathbf{M}\,\ddot{\widehat{\mathbf{w}}}(t)+\mathbf{K}\,\widehat{\mathbf{w}}(t)+\mathbf{G}\,\boldsymbol{\Lambda}(t)=\mathbf{F}(t) \\ \mathbf{G}^{\mathrm{T}}\,\widehat{\mathbf{w}}(t)=\mathbf{0} \end{array}\right. , \quad N=N_1+N_2, \tag{2.41}$$

for the $(N+2)$ unknowns

$$\widehat{\mathbf{w}}=\begin{bmatrix}\widehat{\mathbf{w}}_1 & \widehat{\mathbf{w}}_2\end{bmatrix}^{\mathrm{T}}, \quad \boldsymbol{\Lambda}=\begin{bmatrix}\lambda_a & \lambda_L\end{bmatrix}^{\mathrm{T}}, \tag{2.42}$$

is obtained. In (2.41), $\mathbf{M}$, $\mathbf{K}$, and $\mathbf{F}$ are, respectively, the $(N\times N)$ mass, the $(N\times N)$ stiffness, and the $N\times 1$ load matrices:

$$\mathbf{M}=\begin{bmatrix}\mathbf{M}_1 & \mathbf{0}\\ \mathbf{0} & \mathbf{M}_2\end{bmatrix}, \quad \mathbf{K}=\begin{bmatrix}\mathbf{K}_1 & \mathbf{0}\\ \mathbf{0} & \mathbf{K}_2\end{bmatrix}, \quad \mathbf{F}=\begin{bmatrix}\mathbf{F}_1\\ \mathbf{0}\end{bmatrix}, \tag{2.43}$$

with

$$\begin{aligned}[\mathbf{M}_\alpha]_{ij}=\int_{\Omega^i_{\mathrm{S}\alpha}}\varrho_\alpha\psi_{\alpha i}\psi_{\alpha j}\mathrm{d}x, \quad [\mathbf{K}_\alpha]_{ij}=\int_{\Omega^i_{\mathrm{S}\alpha}}E_\alpha\psi'_{\alpha i}\psi'_{\alpha j}\,\mathrm{d}x, \quad [\mathbf{F}_1]_i=-p\delta_0\left(\Gamma^{i-}_{\mathrm{S}1}\right)\,\psi_{1i}\left(\Gamma^{i-}_{\mathrm{S}1}\right),\\ \alpha=1,2, \quad i,j=1,2,\ldots,N_\alpha.\end{aligned} \tag{2.44}$$

The $(N\times 2)$ matrix

$$\mathbf{G}=\begin{bmatrix}\mathbf{G}_{1\lambda_a} & \mathbf{0}\\ \mathbf{G}_{2\lambda_a} & \mathbf{G}_{2\lambda_L}\end{bmatrix}, \tag{2.45}$$

is defined by

$$\begin{aligned}[\mathbf{G}_{1\lambda_a}]_i=\delta_a\left(\Gamma^{i+}_{\mathrm{S}1}\right)\,\psi_{1i}\left(\Gamma^{i+}_{\mathrm{S}1}\right), \quad [\mathbf{G}_{2\lambda_a}]_k=-\delta_a\left(\Gamma^{i-}_{\mathrm{S}2}\right)\,\psi_{2i}\left(\Gamma^{i-}_{\mathrm{S}2}\right),\\ [\mathbf{G}_{2\lambda_L}]_k=-\delta_L\left(\Gamma^{i+}_{\mathrm{S}2}\right)\,\psi_{2i}\left(\Gamma^{i+}_{\mathrm{S}2}\right), i=1,\ldots,N_1, \quad k=1,\ldots,N_2.\end{aligned} \tag{2.46}$$

Inf-sup test

For the static version of this linear problem, the ellipticity condition is readily satisfied. More effort is needed to show that the mixed formulation in static regimes satisfies the inf- sup condition as well, that is

$$\inf_{\boldsymbol{\Lambda}\in\mathbb{R}^2/\{0\}}\sup_{w^h\in W^h/\{0\}}\frac{\lambda_a\left(w^h_2(a)-w^h_1(a)\right)+\lambda_L w^h_2(L)}{\|\boldsymbol{\Lambda}\|\,\|w^h\|_{W^h}}\geq\tilde{\beta}>0, \tag{2.47}$$

where $\tilde{\beta}$ is a constant independent of the nodal spacing, $W^h \subset H^1(0,a) \times H^1(a,L)$ is the N -dimensional MLS solution space, $\|\mathbf{\Lambda}\|^2 = \mathbf{\Lambda}^{\mathrm{T}}\mathbf{\Lambda}$, and

$$\left\|w^h\right\|_{W^h}^2 := \int_0^a \left[\left(w_1^h\right)^2 + L^2\left(w_1^{h'}\right)^2\right] \mathrm{d}x + \int_a^L \left[\left(w_2^h\right)^2 + L^2\left(w_2^{h'}\right)^2\right] \mathrm{d}x, \tag{2.48}$$

is the W^h norm. From (A.4) it is clear that the MLS basis functions with $m = 1$ exactly reproduce a constant function. Therefore, for any given $\mathbf{\Lambda}$ we choose

$$w_1^h(x) = \lambda_L - \lambda_a, \quad w_2^h(x) = \lambda_L. \tag{2.49}$$

Hence

$$\lambda_a\left(w_2^h(a) - w_1^h(a)\right) + \lambda_L w_2^h(L) = \|\mathbf{\Lambda}\|^2, \quad \left\|w^h\right\|_{W^h}^2 = \mathbf{\Lambda}^{\mathrm{T}}\mathbf{S}\mathbf{\Lambda}, \tag{2.50}$$

where $\mathbf{S}$ is the following symmetric positive-definite matrix:

$$\mathbf{S} = \begin{bmatrix} a & -a \\ -a & L \end{bmatrix}. \tag{2.51}$$

From (2.50) we can establish that

$$\mu_1 \|\mathbf{\Lambda}\|^2 \leq \left\|w^h\right\|_{W^h}^2 \leq \mu_2 \|\mathbf{\Lambda}\|^2, \tag{2.52}$$

where

$$\mu_1 = \frac{1}{2}\left(a + L - \sqrt{(L-a)^2 + 4a^2}\right), \quad \mu_2 = \frac{1}{2}\left(a + L + \sqrt{(L-a)^2 + 4a^2}\right), \tag{2.53}$$

are eigenvalues of $\mathbf{S}$. Since

$$\frac{\lambda_a\left(w_2^h(a) - w_1^h(a)\right) + \lambda_L w_2^h(L)}{\|\mathbf{\Lambda}\| \left\|w^h\right\|_{W^h}} = \sqrt{\frac{\mathbf{\Lambda}^{\mathrm{T}}\mathbf{\Lambda}}{\mathbf{\Lambda}^{\mathrm{T}}\mathbf{S}\mathbf{\Lambda}}}, \tag{2.54}$$

we have

$$\sup_{w^h \in W^h/\{0\}} \frac{\lambda_a\left(w_2^h(a) - w_1^h(a)\right) + \lambda_L w_2^h(L)}{\|\mathbf{\Lambda}\| \left\|w^h\right\|_{W^h}} \geq \sqrt{\frac{\mathbf{\Lambda}^{\mathrm{T}}\mathbf{\Lambda}}{\mathbf{\Lambda}^{\mathrm{T}}\mathbf{S}\mathbf{\Lambda}}}, \tag{2.55}$$

which implies that

$$\inf_{\mathbf{\Lambda} \in \mathbb{R}^2/\{0\}} \sup_{w^h \in W^h/\{0\}} \frac{\lambda_a\left(w_2^h(a) - w_1^h(a)\right) + \lambda_L w_2^h(L)}{\|\mathbf{\Lambda}\| \left\|w^h\right\|_{W^h}} \geq \inf_{\mathbf{\Lambda} \in \mathbb{R}^2} \sqrt{\frac{\mathbf{\Lambda}^{\mathrm{T}}\mathbf{\Lambda}}{\mathbf{\Lambda}^{\mathrm{T}}\mathbf{S}\mathbf{\Lambda}}} = \frac{1}{\sqrt{\mu_2}}. \tag{2.56}$$

Thus the inf-sup condition is satisfied since μ_2 depends only on a and L, and is independent of the nodal spacing.

Reduced semidiscrete system of equations

Let $\ker \mathbf{G}^{\mathrm{T}}$ be the null space of $\mathbf{G}^{\mathrm{T}}$; since the inf-sup condition holds, we have $\dim \ker \mathbf{G}^{\mathrm{T}} = N-2$. Next, let rows of the $(N-2 \times N)$ matrix $\mathbf{X}$ be comprised of $(N-2)$ linearly independent vectors in $\ker \mathbf{G}^{\mathrm{T}}$, and let us introduce the $(N-2)$ reduced vector of unknowns $\mathbf{w}$:

$$\widehat{\mathbf{w}} = \mathbf{X}^{\mathrm{T}}\mathbf{w}. \tag{2.57}$$

In this way, the constraint represented by the second equation in (2.41) is automatically satisfied for every $\mathbf{w} \in \mathbb{R}^{(N-2)}$. Upon substitution into the first equation of (2.41), and premultiplication by $\mathbf{X}$ one obtains the reduced semidiscrete system of $N-2$ equations:

$$\mathbf{m}\,\ddot{\mathbf{w}} + \mathbf{k}\,\mathbf{w} = \mathbf{f}, \tag{2.58}$$

where the $(N-2 \times N-2)$ reduced mass and stiffness matrices, and the reduced $(N-2)$ load vector are defined as in (2.33).

2.4.4 Time integration scheme

We integrate the reduced semidiscrete system of equations with initial conditions

$$\begin{aligned} \mathbf{w}(0) &= \mathbf{0}, \\ \dot{\mathbf{w}}(0) &= \mathbf{0}, \end{aligned} \tag{2.59}$$

with the Newmark family of methods (Hughes (2001)), and get

$$\begin{aligned} \mathbf{m}\,\mathbf{a}_{n+1} + \mathbf{k}\,\mathbf{w}_{n+1} &= \mathbf{f}_{n+1}, \\ \mathbf{w}_{n+1} &= \mathbf{w}_n + \Delta t \mathbf{v}_n + \frac{\Delta t^2}{2}\left[(1-2\beta)\,\mathbf{a}_n + 2\beta \mathbf{a}_{n+1}\right], \\ \mathbf{v}_{n+1} &= \mathbf{v}_n + \Delta t\left[(1-\gamma)\,\mathbf{a}_n + \gamma \mathbf{a}_{n+1}\right], \end{aligned} \tag{2.60}$$

where $\mathbf{a}_n$, $\mathbf{v}_n$, and $\mathbf{w}_n$ are approximations of $\ddot{\mathbf{w}}(t_n)$, $\dot{\mathbf{w}}(t_n)$, and $\mathbf{w}(t_n)$ respectively, $\mathbf{f}_{n+1} = \mathbf{f}(t_{n+1})$, Δt is the time step, and β and γ are parameters.

Depending upon the choice of β and γ, different members of the Newmark family arise. Gu and Liu (2001), in the analysis of forced vibrations of homogeneous bodies, compared the performances of the explicit and conditionally stable central difference method ($\beta = 0$, $\gamma = 1/2$), and the implicit and unconditionally stable average acceleration ($\beta = 1/4, \gamma = 1/2$) method. They showed that the average acceleration method gives very good results with larger time steps than those allowed by the central difference method. Qian and Batra (2004a) employed the central-difference method to integrate the coupled ordinary differential

equations derived by the MLPG approximation of the transient thermoelastic problem for a functionally graded material.

Here we also use these two methods, and both the consistent, and the lumped mass matrices. For the average acceleration method we set

$$\begin{aligned} \Delta t = 10^{-2}T, \quad T = \frac{2}{5}\tau, \\ \tau := \frac{a}{c_1} + \frac{L-a}{c_2}, \\ c_1 = \sqrt{\frac{E_1}{\rho_1}}, \quad c_2 = \sqrt{\frac{E_2}{\rho_2}}, \end{aligned} \tag{2.61}$$

where τ is the time when the wave is reflected at the clamped end, and c_1 and c_2 are wave speeds in the two materials. For values assigned to material parameters the first reflection of the wave occurs at the clamped end.

2.4.5 Numerical evaluation of domain integrals

Since the MLS basis functions are not polynomials, it is difficult to integrate accurately the discrete local weak forms associated with the MLPG6 formulation, and obtain the mass, and the stiffness matrices.

We adopt the integration procedure proposed by Atluri, Cho and Kim (1999). The idea is sketched in Figure 2.5, where a possible arrangement of nodes is shown. The integration on Ω_{S}^i is performed by carrying out the integration on each subregion, obtained by dividing Ω_{S}^i by boundaries of subdomains of other nodes in the neighborhood of node i. With this method, integrals are evaluated with five quadrature points in each intersected region.

2.5 Numerical results and comparisons

2.5.1 Values of parameters

Results have been computed for following values of the material parameters

$$\begin{aligned} \varrho_1 = 7860 kg/m^3, \quad E_1 = 200 GPa, \\ \varrho_2 = 2710 kg/m^3, \quad E_2 = 70 GPa, \end{aligned} \tag{2.62}$$

corresponding to steel (material "1") and aluminum (material "2"). The geometry is defined by

$$L = 50mm, \quad a = L/2 = 25mm. \tag{2.63}$$

For these values we have

$$\tau = 9.87\mu s, \quad T = 3.95\mu s. \tag{2.64}$$

The numerical value of P has been chosen as

$$P = 100MPa. \tag{2.65}$$

The MLS basis functions are generated by complete monomials of degree 1. Except when we discuss convergence of the solution with an increase in the number of uniformly spaced nodes, results presented below have been computed with 81 uniformly spaced nodes. When we model the discontinuity with either the jump function or the modified MLS basis functions the domain $[0, L]$ is discretized with equally spaced nodes with one node placed at the interface. In both cases the semi-support r_i of the weight function W_i is

$$r_i = \begin{cases} 2\dfrac{L}{N-1}, & i = 2, 3, ..., N-1 \\ \\ 4\dfrac{L}{N-1}, & i = 1, N \end{cases}; \tag{2.66}$$

and for the modified MLS basis functions the semi-support of the weight function for the node at the interface is set equal to $4L/(N-1)$.

When using a Lagrange multiplier to enforce the continuity of displacements at $x = a$, an equal number of uniformly spaced nodes is used in the domains $[0, a]$ and $[a, L]$, and (2.66) holds in each homogeneous part of the bar with L equal to the segment length and N equal to the total number of nodes in the segment.

From numerical experiments it has been found that the choice of the radius r_{J} of the jump function support strongly affects the accuracy of computed results. Here we take

$$r_{\text{J}} = \frac{N}{2}\frac{L}{N-1}; \tag{2.67}$$

thus one-half of nodes used in the discretization are included in the jump function semisupport.

2.5.2 Convergence analysis

For each of the three methods of accounting for the material discontinuity at $x = a$, convergence tests are performed for both the solution of a static problem, and mode shapes of the bimaterial clamped bar. Two relative error norms are used for this purpose:

- Relative L^2 error norm

$$\sqrt{\frac{\int_0^L \left(w^h - w^e\right)^2 \mathrm{d}x}{\int_0^L \left(w^e\right)^2 \mathrm{d}x}}; \tag{2.68}$$

- Relative H^1 error norm

$$\sqrt{\frac{\int_0^L \left((w^h - w^e)^2 + L^2 \left((w^h)' - (w^e)' \right)^2 \right) \mathrm{d}x}{\int_0^L \left((w^e)^2 + L^2 \left((w^e)' \right)^2 \right) \mathrm{d}x}}; \tag{2.69}$$

where superscripts h and e refer to the MLPG6 numerical solution, and the analytical solution respectively. For the static deformation with constant uniformly distributed load P/L, Figure 2.6 shows variations of the relative L^2 and H^1 error norms with an increase in the number of nodes obtained with, and without employing one of the three techniques to account for the material discontinuity at $x = a$. Results have also been computed with the FEM with piecewise linear basis functions, and a node placed at the interface. In this and other Figures, notations J, L and MMLS signify, respectively, results obtained with the methods of jump function, the Lagrange multipliers, and the modified MLS basis functions. The plots reveal the monotonic convergence of the MLPG solution; the error without treatment of the material discontinuity, denoted by the curve marked MLS, is higher than that with the FEM, with convergence rates of 1 (0.5) and 2 (1), respectively, in the L^2 (H^1) norm. When a special technique is used to treat the material discontinuity, the error in the MLPG solution is always lower than that with the FEM, and the MLPG solution converges faster to the analytical one at approximate rates of 2.5 and 1.5 respectively in the L^2 and H^1 norms. The need for treating the material discontinuity is evident from examining Figure 2.7, where the axial displacement derivative near the interface computed with and without the use of these special methods is depicted. A treatment of discontinuity is necessary in order to accurately model the jump in the displacement gradient at the interface $x = a$; however, the displacement gradient computed away from $x = a$ without employing any one of the three methods is close to the analytical one. We have plotted the percentage error in the four numerical solutions in Figure 2.7. It is evident that without using a method to account for the discontinuity in the displacement gradient at $x = a$, the error in the computed solution exceeds 50%. However, when any one of the three methods is used to consider the material discontinuity, then the maximum error in the displacement gradient is less than 0.5%.

The numerical eigenfrequencies, and mode shapes are obtained by searching for solutions of the type

$$\mathbf{w}(t) = \underline{\mathbf{w}} \exp(i\omega t), \tag{2.70}$$

of the reduced semidiscrete system of equations, and discarding the applied loads. Therefore, the following eigenvalue problem arises:

$$\left(\mathbf{k} - \omega^2 \mathbf{m} \right) \underline{\mathbf{w}} = \mathbf{0}. \tag{2.71}$$

In Figure 2.8, we report the relative L^2 and H^1 error norms of the first three mode shapes; the mode shapes are shown in Figure 2.9. As before, the MLPG6 solution without treatment

of the material discontinuity gives higher errors than the MLPG6 solutions obtained by modeling the material discontinuity with any one of the three techniques. In both the L^2 and the H^1 norms, whereas the rate of convergence of the numerical solution without treatment of material discontinuity is lower than that of the FE solution, the MLPG6 solutions with the material discontinuity treatment converge faster. For the first three modes, the convergence rates in the L^2 norm with and without treatment of discontinuity are 2.5 and 1.5 respectively, against a convergence rate of 2 for the FEM. In the H^1 norm, the corresponding convergence rates are 1.5, 0.5 and 1 respectively.

In Figure 2.10 the relative errors in the first two eigenfrequencies are reported; the analytically computed first two eigenfrequencies are $0.108MHz$, and $0.528MHz$. In both cases, the convergence rates are 3 and 1 for the MLPG6 solutions with, and without the treatment of material discontinuity respectively, and 2 for the FE solution. Furthermore, frequencies converge monotonically from above to their analytical values. For the MLPG1 formulation of plate-theory equations, Qian, Batra and Chen (2003b) found that the first four flexural frequencies did not converge from above with an increase in the number of nodes.

2.5.3 Forced vibrations

The MLPG solutions have been computed by using uniformly spaced 81 nodes on the global domain.

In Figure 2.11 we report two snapshots of the traveling stress wave computed with the average acceleration method at

$$t_1 = \frac{a}{c_1} + \frac{3T}{4} \simeq 7.9\mu s, \quad t_2 = \tau + 2T \simeq 17.7\mu s, \tag{2.72}$$

and in Figure 2.12 we show the axial displacement at the same instants. Times t_1 and t_2 are, respectively, the instants when $3/4^{th}$ of the wave has crossed the interface $x = a$ between the two materials, and when the two waves reflected from the free, and the clamped edges overlap at $x = a$. Comparisons have been made with analytical solutions obtained by setting $j = 3$ in summations (B.16), and (B.17), since for this value of j

$$\max_{t\in\{t_1,t_2\}} \left(\int_0^L \left(w^e\left(x,t\right)\big|_{j+1} - w^e\left(x,t\right)\big|_j \right)^2 \mathrm{d}x \right) \leq 10^{-15} L^3, \tag{2.73}$$

where $w^e\left(x,t\right)\big|_j$ is the analytical solution in (B.16) and (B.17) computed for a given value of j. The good agreement with the analytical results shows that all three methods for the treatment of material discontinuity are able to capture well both the reflection of, and the interaction among propagating waves; the numerical solutions virtually overlap the analytic solution.

In Figure 2.13 we depict the time history of the axial displacement at the left end computed with the central difference method by using both the consistent, and the lumped mass matrices, with $\Delta t = 0.9\Delta t_{\text{cr}}$ and $1.01\Delta t_{\text{cr}}$ respectively. The critical time step is given by

$$\Delta t_{\text{cr}} = \frac{2}{\max\left(\omega_i^h\right)}. \tag{2.74}$$

	Mass matrix	
	Consistent	Lumped
Jump function	0.0393	0.204
Lagrange multiplier	0.0671	0.203
Modified MLS	0.0671	0.203

Table 2.1: Critical time step, Δt_{cr} $[\mu s]$, for different methods of accounting for material discontinuity.

Here ω_i^h is i-th natural eigenfrequency of the system. Values of Δt_{cr} for the consistent, and the lumped mass matrices, and the three methods of accounting for the material discontinuity are listed in Table 2.1. Comparisons are made with analytical solutions obtained by summing up to $j = 7$ in (B.16) and (B.17), since for this value of j

$$\int_0^{\bar{t}} \left(w^e\left(0,t\right)\big|_{j+1} - w^e\left(0,t\right)\big|_j \right)^2 \mathrm{d}t \leq 10^{-15} L^2 \bar{t}, \tag{2.75}$$

where $w^e\left(x,t\right)\big|_j$ is the analytical solution computed for a given value of j, and $\bar{t} = 8\left(a/c_1 + (L-a)/c_2\right)$ is the maximum time considered in the computations.

Whereas for the lumped mass matrix obtained by the row sum technique Δt_{cr} has the same value for the three methods of accounting for the material discontinuity, it is not so for the consistent mass matrix; Δt_{cr} for the method of jump function is nearly one-half of that for the other two methods. A possible explanation is that the jump function technique with the consistent mass matrix modifies the basis functions unfavorably for the maximum eigenfrequency of the system. However, when the lumped mass matrix is obtained by the row sum technique, the effect of the modification of basis functions is eliminated, and the maximum natural frequency is the same for the three methods.

Solutions obtained with the three methods of accounting for the material discontinuity essentially coincide with the analytical solution of the problem. Results plotted in Figure 2.13 signify the well known fact that the solution computed with $\Delta t < \Delta t_{\text{cr}}$ is stable, and that with $\Delta t > \Delta t_{\text{cr}}$ is unstable. A comparison of plots of Figures 2.13a and 2.13c reveals that the consistent mass matrix gives lower errors than the lumped mass matrix.

For the average acceleration method, only the consistent mass matrix is considered. Figure 2.13 exhibits the well known fact that the average acceleration algorithm is unconditionally

stable, as evidenced by the stability of the solution even when the time step size equals $1.5\Delta t_{\rm cr}^{\rm consistent}$, and $1.5\Delta t_{\rm cr}^{\rm lumped} \sim 0.3\mu s$.

In Figure 2.14 we report the time history of the jump

$$\left|\sigma^h\left(a^+,t\right)-\sigma^h\left(a^-,t\right)\right|, \tag{2.76}$$

in the axial stress at the interface computed by using the method of (a) the jump function, (b) the Lagrange multiplier, and (c) the modified MLS basis functions. Ideally it should be zero for all times. As we can see, the method (a) is the most accurate; this is because it models both the displacement continuity, and the axial stress continuity at $x = a$, while with the other two techniques the essential boundary condition (2.13) is directly enforced but the axial stress continuity (2.14) is weakly satisfied.

For the average acceleration method and the consistent mass matrix, Figure 2.15 exhibits the effect of decreasing the time step size on the L^2 error norm of the axial stress at times $7.91\mu s$ and $17.8\mu s$. The MLPG method with one of the three methods of considering the material discontinuity gives lower errors than the FEM.

Batra, Porfiri and Spinello (2004), and Qian and Batra (2004a) have compared the MLPG and the FE formulations for transient problems.

2.6 Conclusions

We have used the meshless local Bubnov-Galerkin (MLPG6) method to study free, and forced vibrations of a segmented bar comprised of two materials. Because of the higher-order differentiability of the MLS basis functions, special techniques are needed to accurately model jumps in displacement gradients at the material interfaces. Here, we have employed methods of (a) the jump function, (b) the Lagrange multiplier, and (c) the modified MLS basis functions with discontinuous derivative. In all cases the essential boundary condition has been enforced by introducing a Lagrange multiplier.

The stability of methods has been assessed by analytically proving the inf-sup condition. Reduced semidiscrete systems are derived, where constraints are automatically satisfied. The direct analysis of forced vibrations is performed by using the β-Newmark family of methods, and the spatial integration in the MLPG formulation uses Gauss quadrature rules. Both the lumped, and the consistent mass matrices with the central-difference method are used, while only consistent mass matrix with the average acceleration method is considered.

Numerical results for a bimaterial bar, clamped at one end, and free at the other end, computed with the MLPG6 formulations have been compared with those obtained with the FEM, and analytically. Both for static, and dynamic problems studied, convergence rates

of the MLPG6 solution without any treatment of material discontinuities are lower than those of the FE solution. However, when any one of the three techniques to account for the material discontinuity is used, the MLPG6 solution converges faster than the FE solution. For a fixed number of nodes, errors in the MLPG6 solution are lower than those in the FE solution. This is a very favorable feature of the MLPG6 method with respect to the FEM; the higher computational time required to evaluate domain integrals is balanced somewhat by a gain in accuracy.

The analysis of the transient response due to an axial traction of finite time duration applied at one end of the bar reveals a very good agreement between the MLPG6 and the analytical solutions. Each technique for the treatment of the material discontinuity is able to capture the wave reflection, and interaction between waves at the interface between two materials. Whereas the method of the special jump function is the most accurate in modeling the continuity of the axial stress at the interface because of the introduction of a dedicated degree of freedom, the size of the support of the jump function significantly affects the accuracy of computed results. Numerical experiments suggest that, for this problem, about one half of the nodes employed in the discretization of the global domain need to be included in the radius of the support of the jump function in order to ensure good results. For the consistent mass matrix, the critical time step size for the method of jump function is nearly one-half of that for the other two methods. Both the method of Lagrange multipliers, and the MLS discontinuous basis functions can be generalized to more complex geometries involving material discontinuities.

For the lumped mass matrix, the three methods of accounting for the material discontinuity give the same maximum frequency of the segmented bar. However, when the consistent mass matrix is employed, the maximum natural frequency computed with the method of jump function is nearly twice of that for the other two methods. The largest frequency computed with the lumped mass matrix is nearly one-third of that obtained with the consistent mass matrix. Thus for the explicit time-integration method, it is more efficient to use the lumped mass matrix.

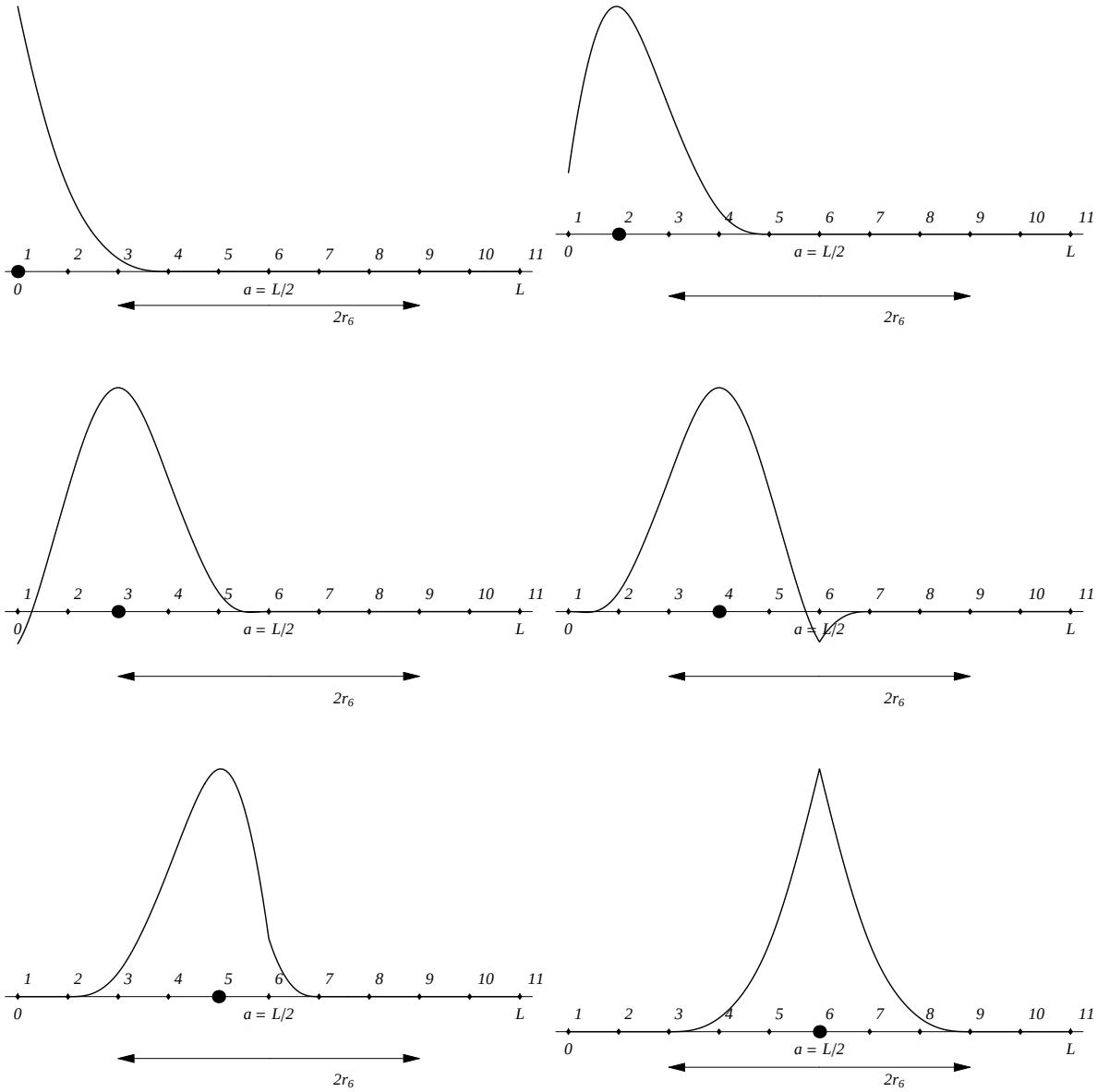

Figure 2.1: Modified MLS basis functions for nodes 1 through 6 obtained with $m = 2$ and $r_i = 3L/(N-1)$.

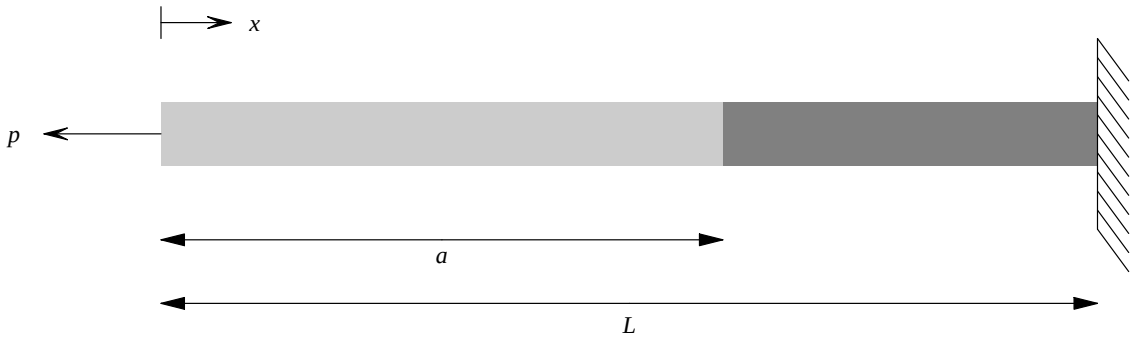

Figure 2.2: Schematic sketch of the problem studied.

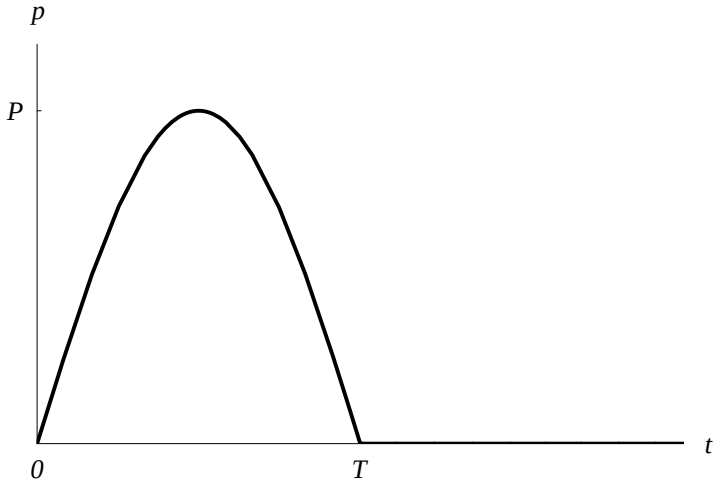

Figure 2.3: Plot of the time-dependent axial traction applied at $x = 0$.

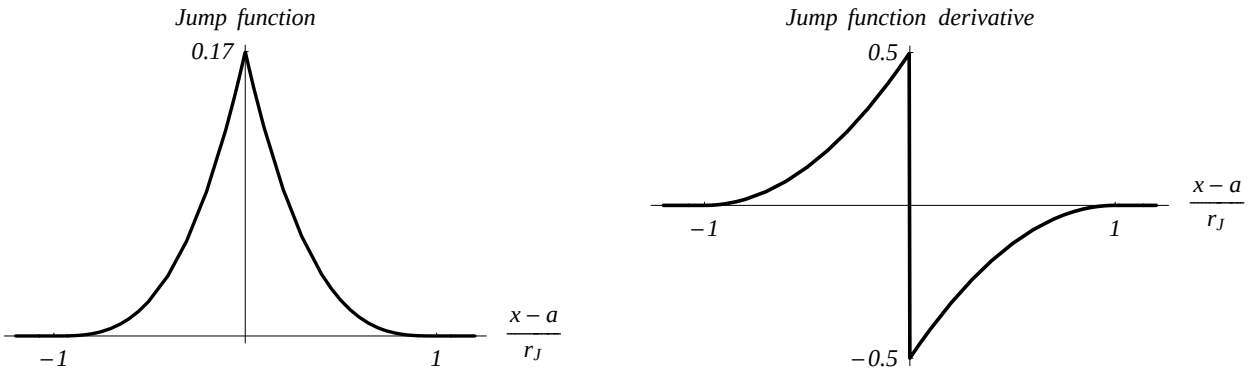

Figure 2.4: Plots of the jump function $\varkappa\left(\frac{x-a}{r_J}\right)$, and its derivative.

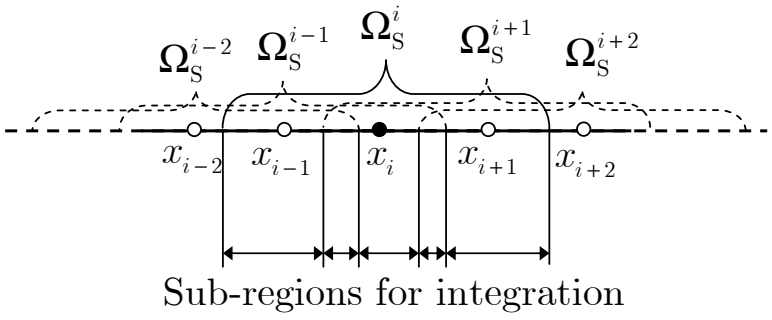

Figure 2.5: Subdomain Ω_S^i of node x_i, and integration subregions obtained by the intersection of Ω_S^i with supports of domains of influence of neighboring nodes.

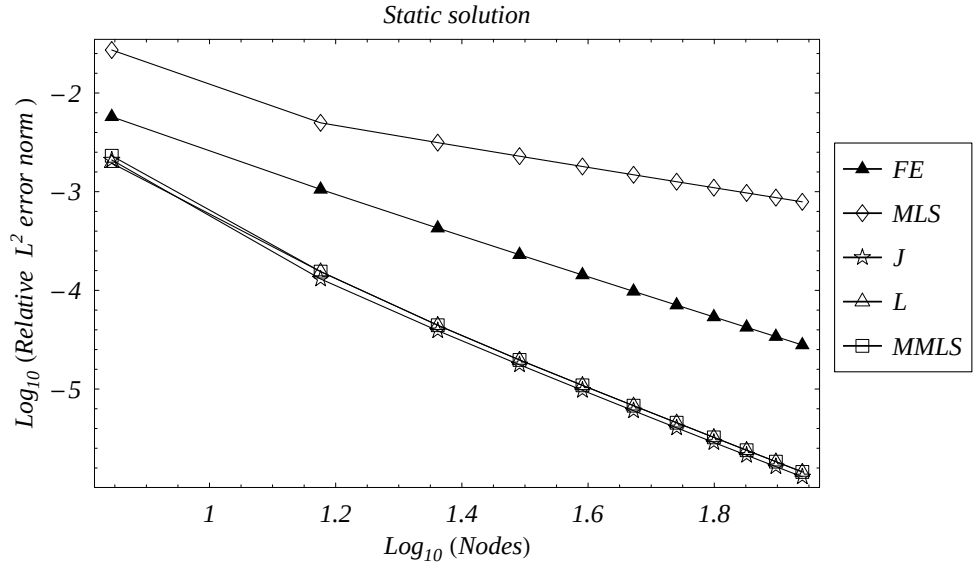

(a)

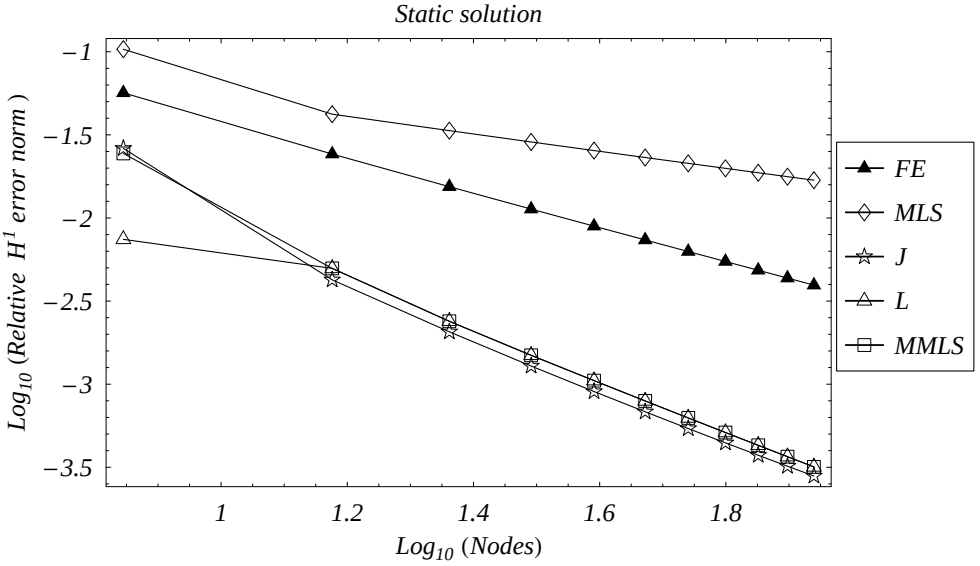

(b)

Figure 2.6: (a) Relative L^2 error norm and, (b) relative H^1 error norm for static deformations under uniformly distributed load along the length of the bar.

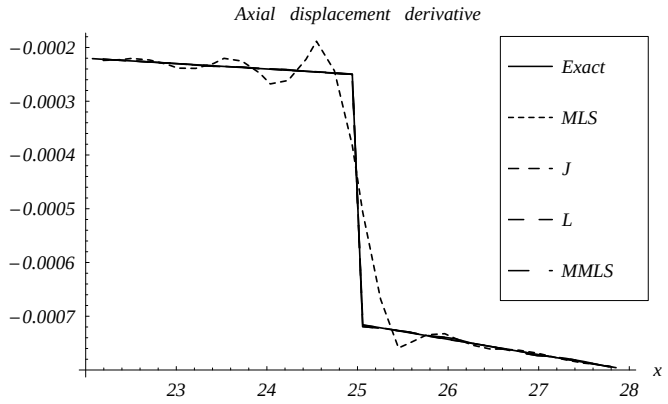

(a)

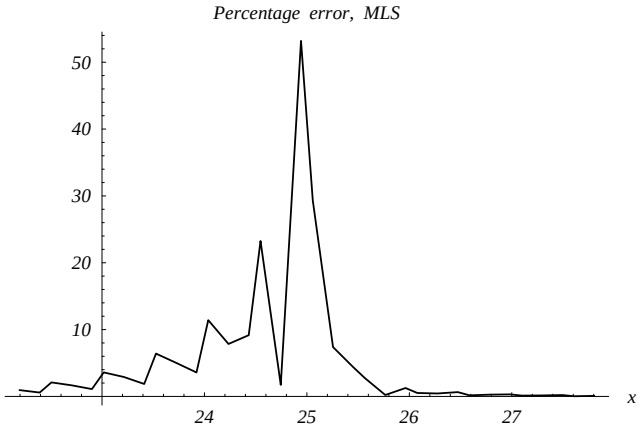

(b)

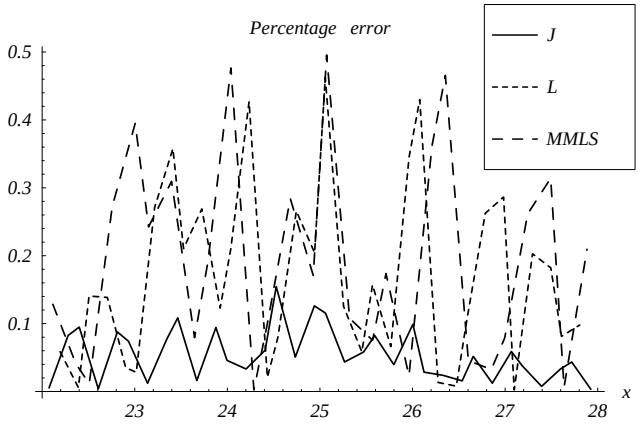

(c)

Figure 2.7: (a) Axial displacement gradient near the material interface for a static deformation, and the percentage error in the derivative of the solution for the uniformly distributed load, P/L, obtained with (b) the MLS basis functions without treatment of the material discontinuity; (c) the MLS basis functions with the three methods of treating the material discontinuity.

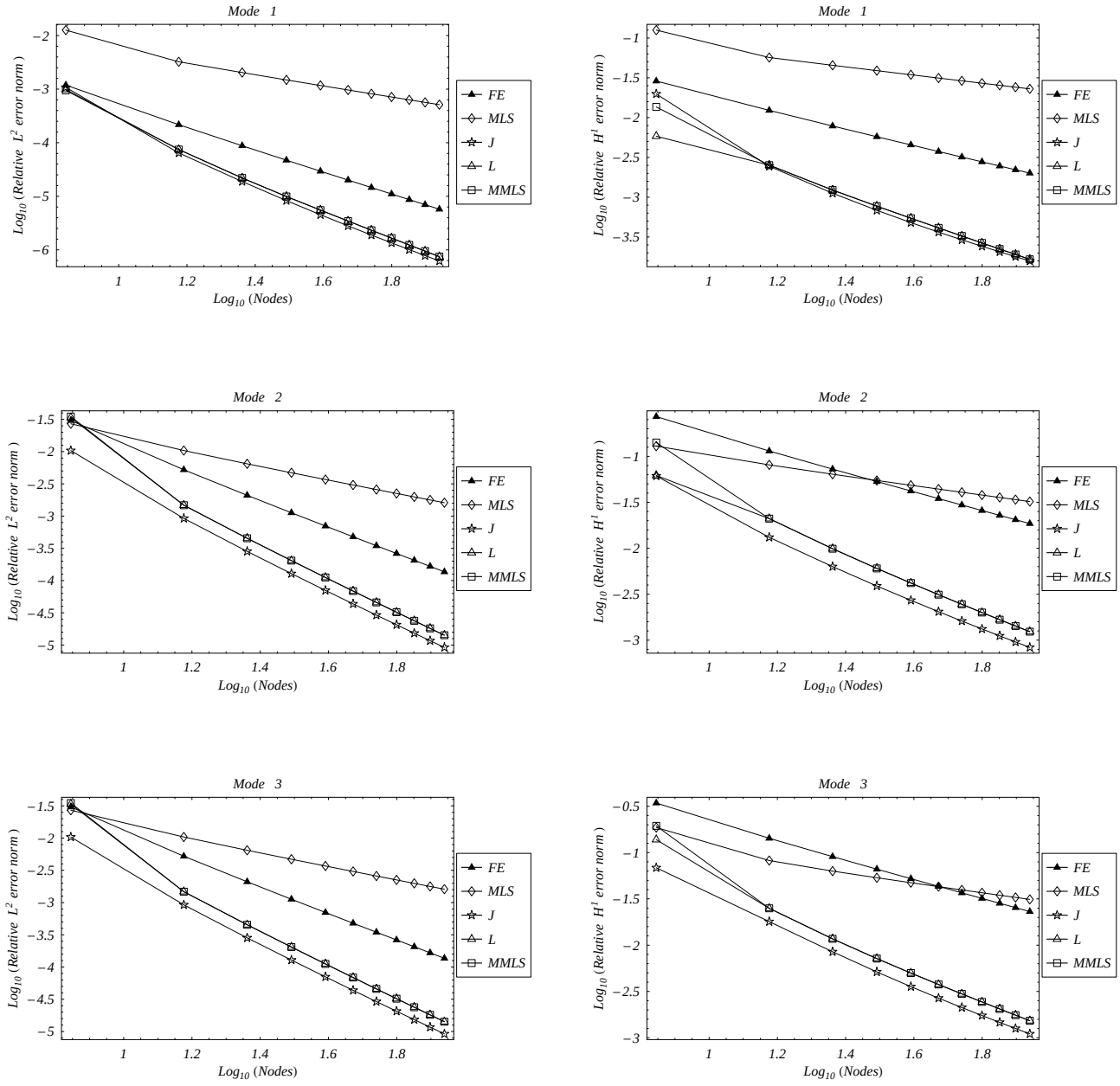

Figure 2.8: Relative L^2 and H^1 error norms for the first three mode shapes.

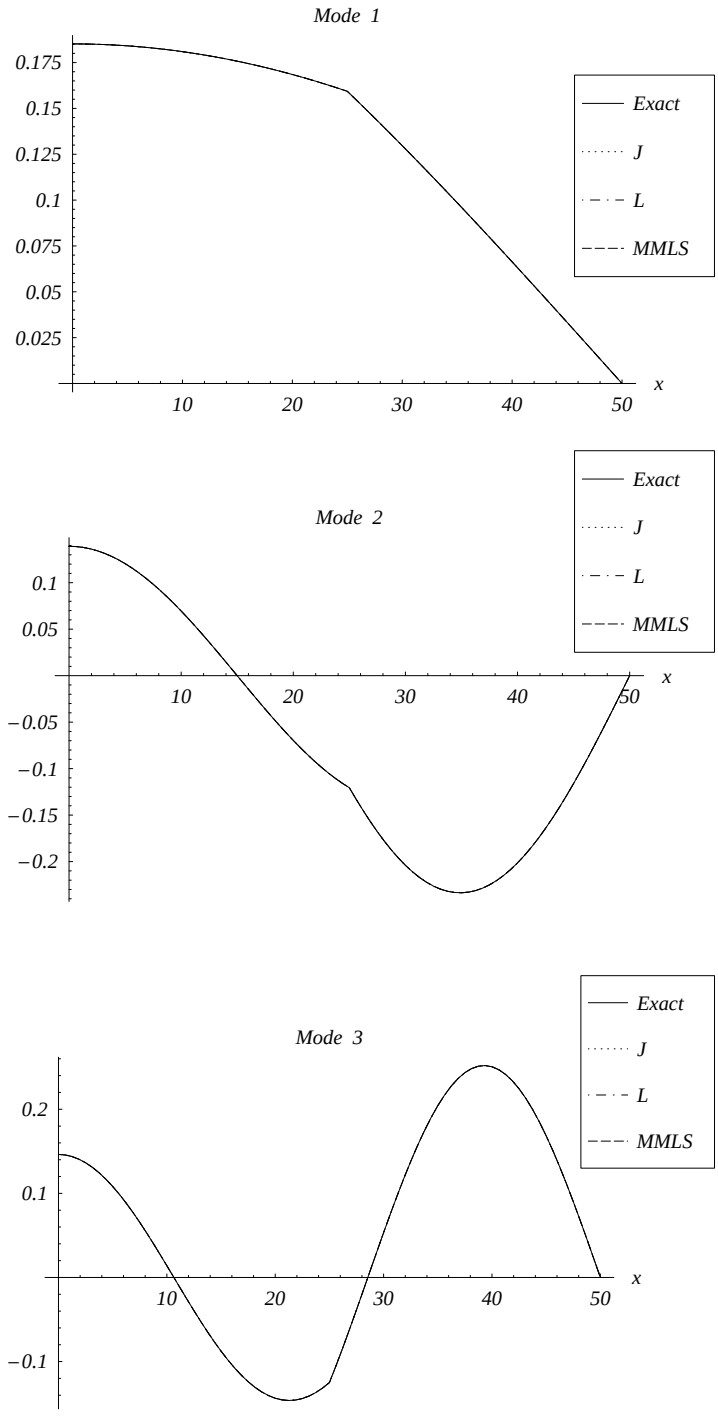

Figure 2.9: First three mode shapes of the segmented bar.

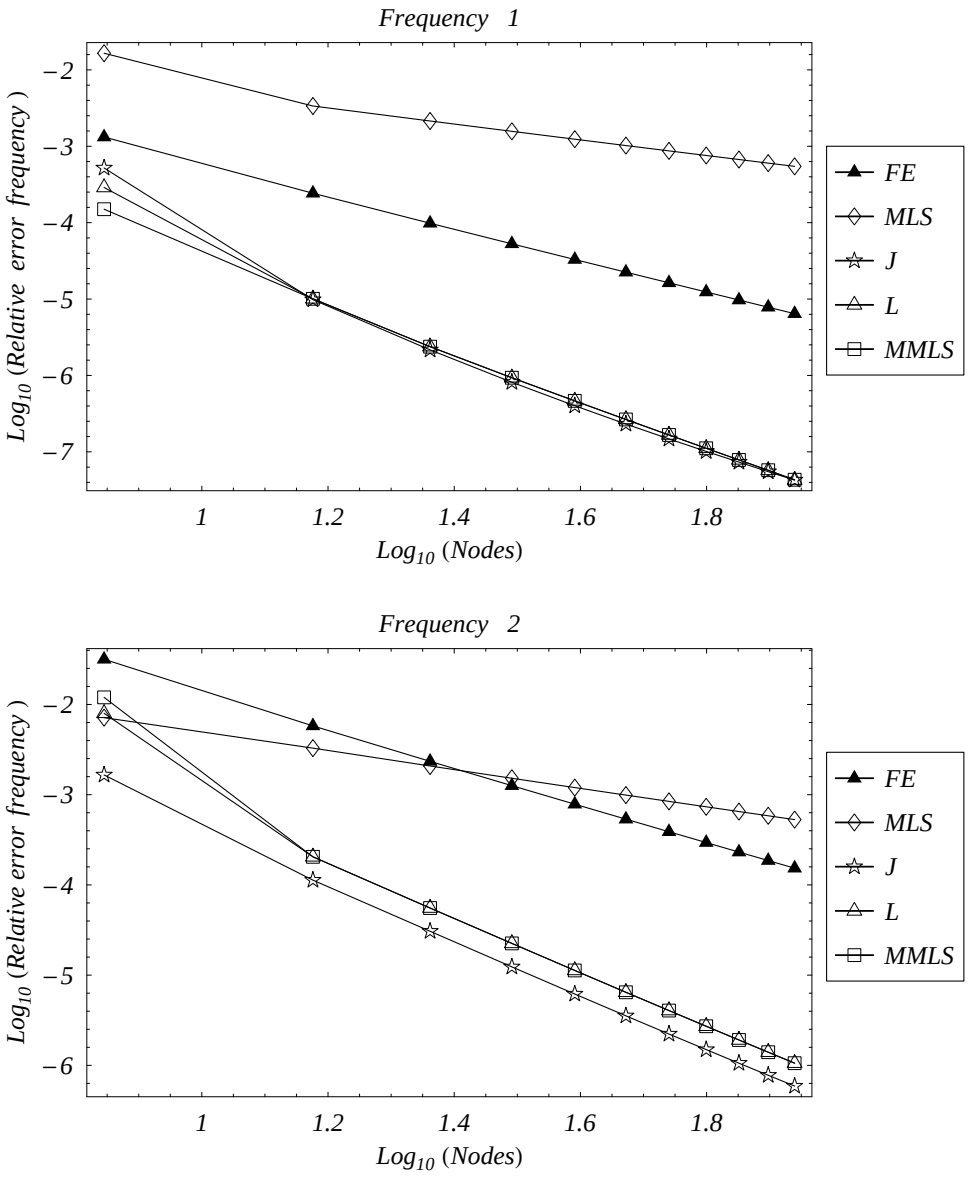

Figure 2.10: Relative error in the estimation of the first two natural frequencies.

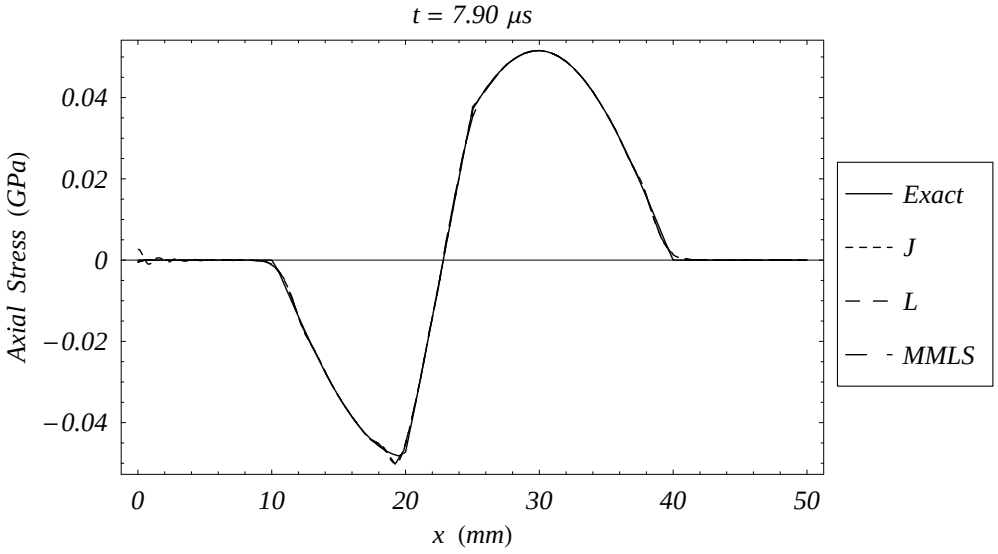

(a)

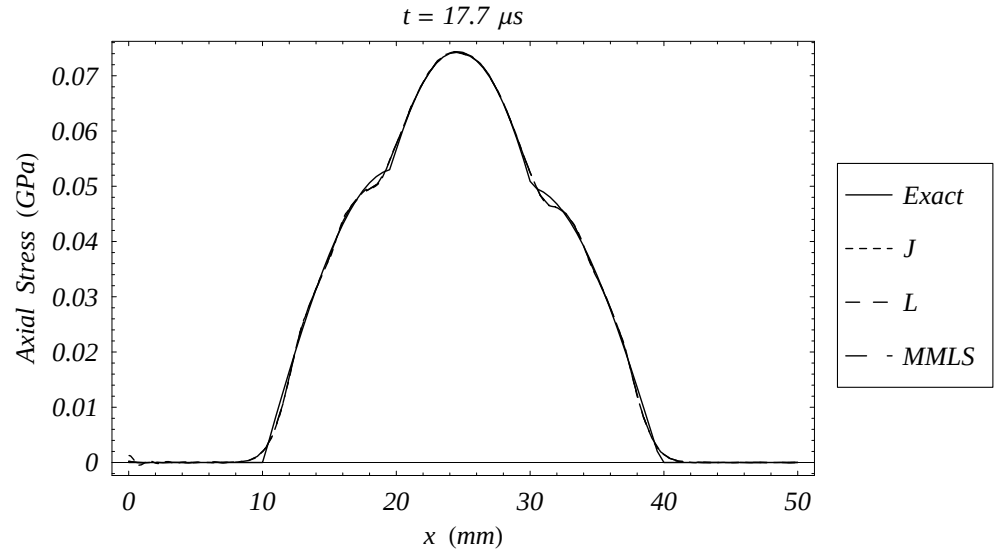

(b)

Figure 2.11: Snapshots of the traveling stress wave at (a) $t = \frac{a}{c_1} + \frac{3T}{4}$, and (b) $t = \tau + 2T$.

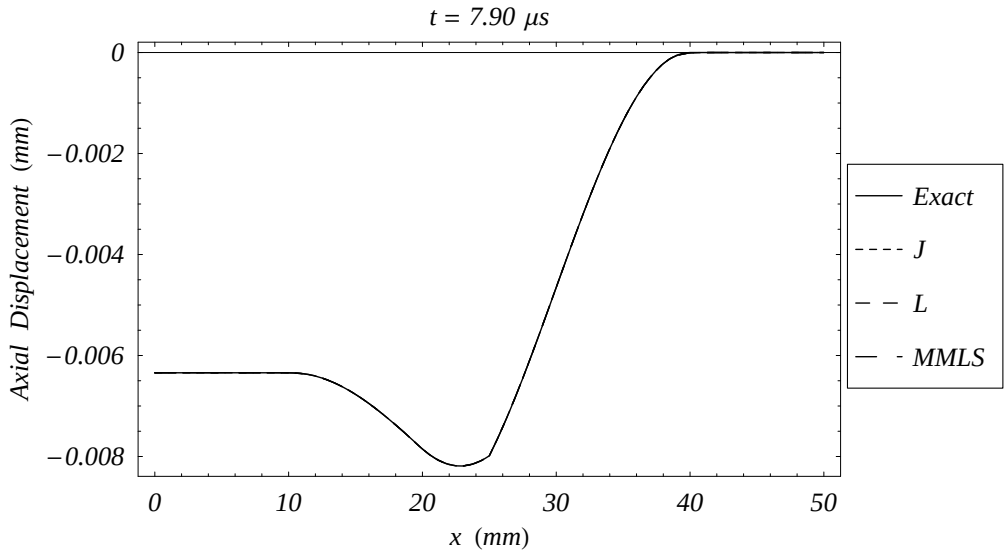

(a)

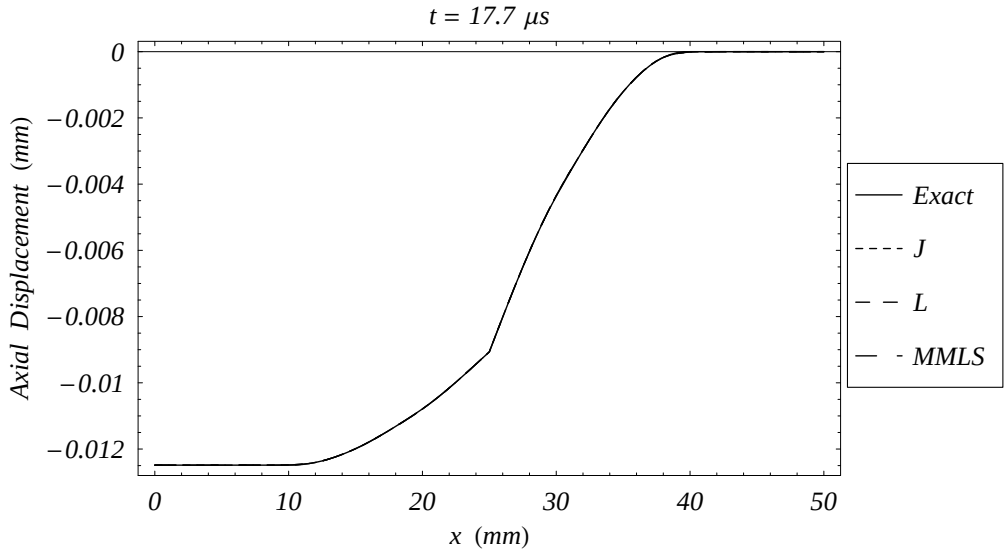

(b)

Figure 2.12: Snapshots of the displacement wave at (a) $t = \frac{a}{c_1} + \frac{3T}{4}$, and (b) $t = \tau + 2T$.

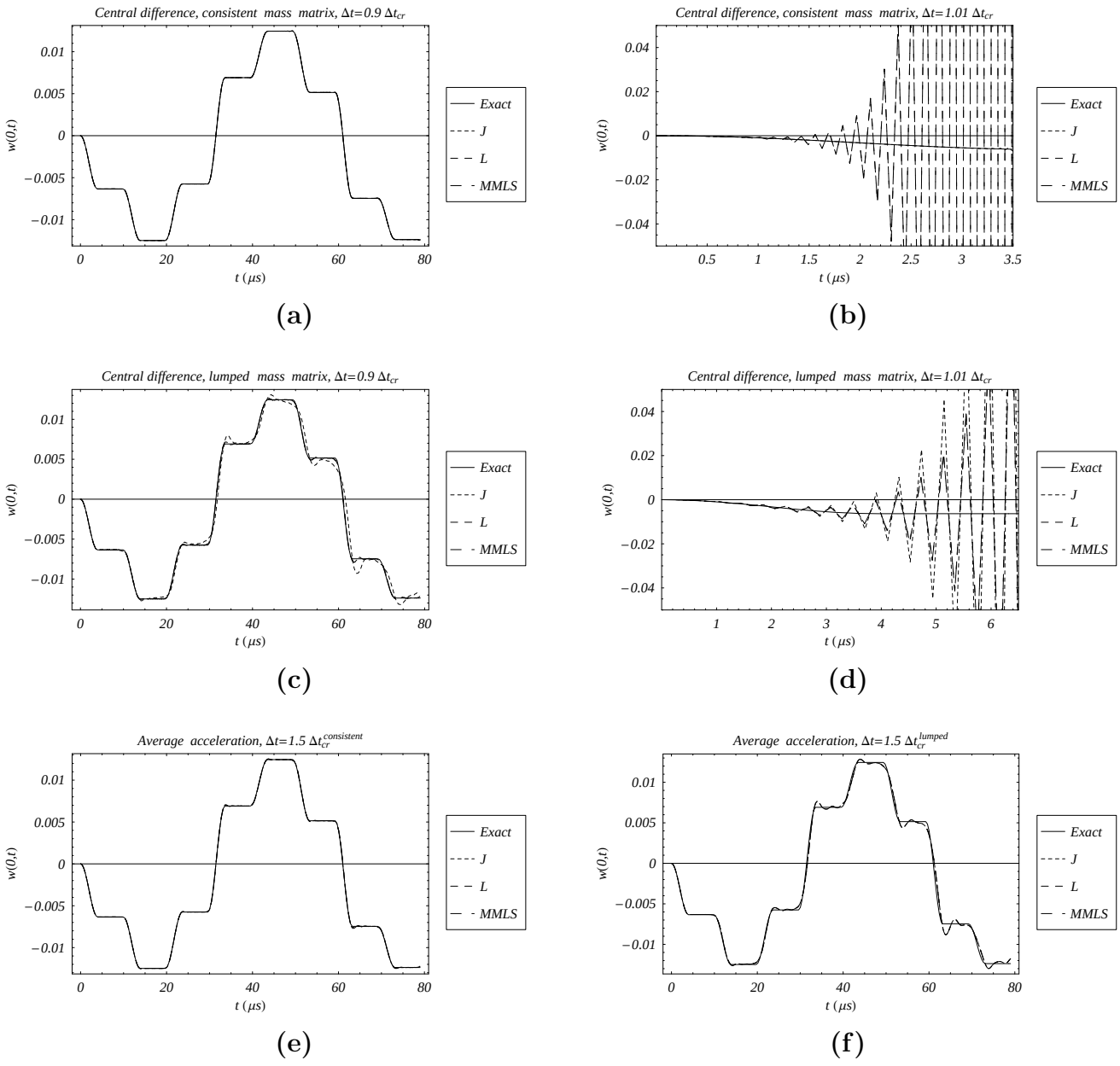

Figure 2.13: Time history of the free end displacement obtained with (a) central difference, consistent mass matrix, and $\Delta t = 0.9\Delta t_{\rm cr}$; (b) central difference, consistent mass matrix, and $\Delta t = 1.01\Delta t_{\rm cr}$; (c) central difference, lumped mass matrix, and $\Delta t = 0.9\Delta t_{\rm cr}$; (d) central difference, lumped mass matrix, and $\Delta t = 1.01\Delta t_{\rm cr}$; (e) average acceleration, consistent mass matrix, and $\Delta t = 1.5\Delta t_{\rm cr}^{\rm consistent}$; (f) average acceleration, consistent mass matrix, and $\Delta t = 1.5\Delta t_{\rm cr}^{\rm lumped}$.

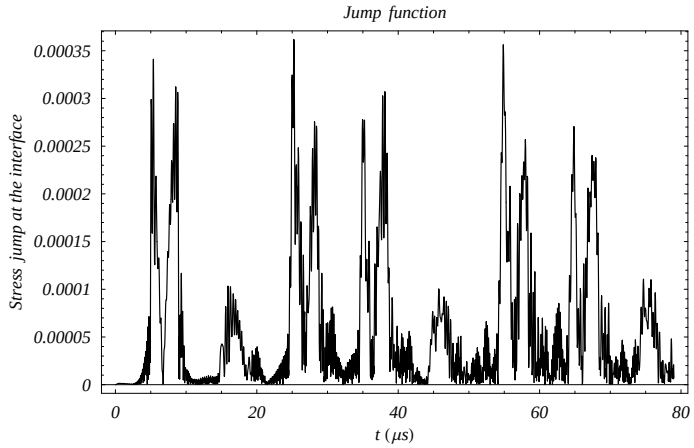

(a)

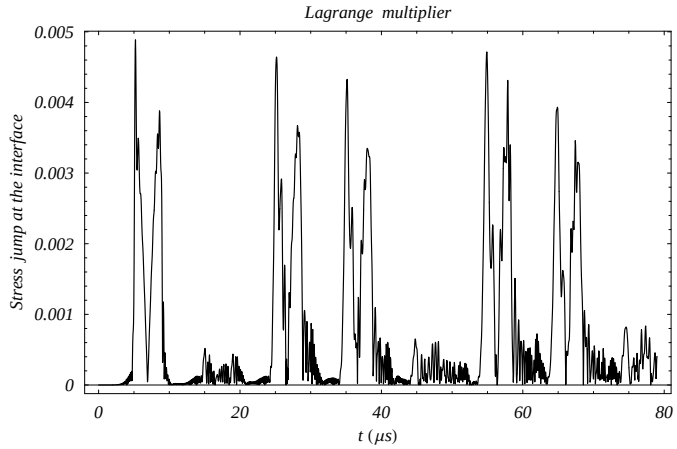

(b)

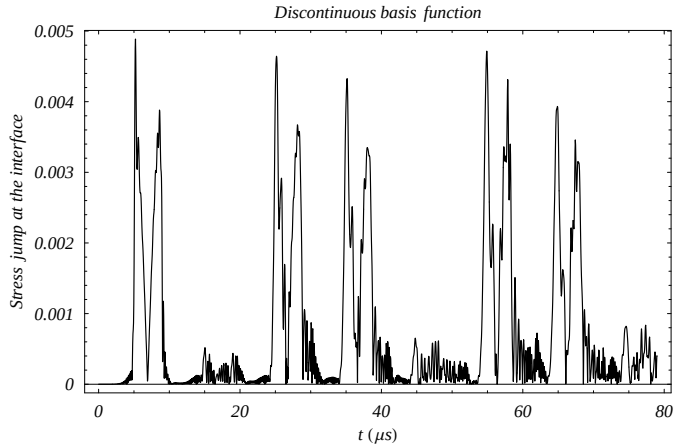

(c)

Figure 2.14: Time history of the jump in the axial stress at the interface using (a) the special jump function, (b) the Lagrange multiplier, and (c) the modified MLS basis functions with discontinuous derivatives.

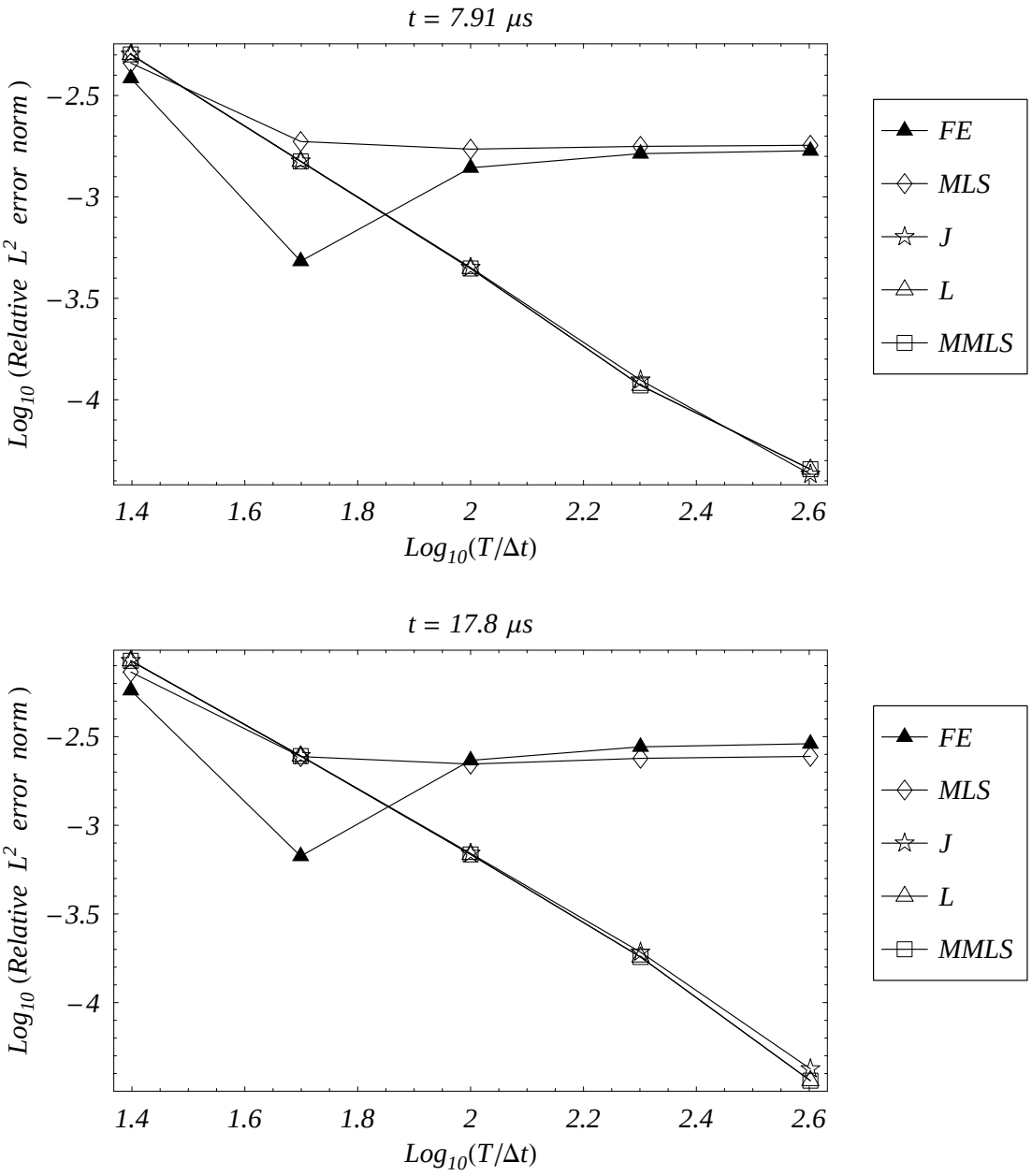

Figure 2.15: At two different times, effect of the time step size on the L^2 relative error norm in the axial displacement.

Chapter 3

Pull-in Instability in Electrically Actuated Narrow Microbeams

3.1 Introduction

The recent technological developments have opened promising research opportunities and engineering priorities in micromechanics. The study of electrostatically actuated MicroElectroMechanical Systems (MEMS) is a branch of micromechanics. These MEMS find wide applications in switches (see, e.g., Nguyen, Katehi and Rebeiz (1998)), micro-mirrors (see, e.g., Hung and Senturia (1999)) and micro-resonators (see, e.g., Tilmans and Legtenberg (1994)). At the microscopic scale high energy densities and large forces are available, and the electrostatic actuation may be more effective than other kinds of actuation.

An electrostatically actuated microbeam is an elastic beam suspended above a stationary rigid plate, both made of conductive materials, and a dielectric medium filling the gap between them. An applied electric voltage between the two electrodes results in the deflection of the elastic beam and a consequent change in the MEMS capacitance. The applied electrostatic force has an upper limit beyond which the electrostatic Coulomb force is not balanced by the elastic restoring force in the deformable beam, the beam spontaneously deflects towards the stationary rigid plate, and the device collapses. This phenomenon, called pull-in instability, was simultaneously observed experimentally by Taylor (1968) and Nathanson, Newell, Wickstrom and Davis (1977). The accurate estimation of the pull-in voltage is crucial in the design of electrostatically actuated MEM devices. In particular, in micro-mirrors (see, e.g., Hung and Senturia (1999)) and micro-resonators (see, e.g., Tilmans and Legtenberg (1994)) the designer avoids this instability in order to achieve stable motions; in switching applications (see, e.g., Nguyen, Katehi and Rebeiz (1998)) the designer exploits this effect

Material in this Chapter is part of the paper "Electromechanical Model of Electrically Actuated Narrow Microbeams," accepted for publication in *Journal of Microelectromechanical Systems*

to optimize the device's performance.

Accurate estimates of the pull-in parameters have been obtained by three-dimensional (3-D) numerical simulations based on either the finite element (FE) or the boundary element analyses (see, e.g., Gabbay, Mehner and Senturia (2000) and Senturia, Harris, Johnson, Kim, Nabors, Shulman and White (1992)); however, these approaches are time-consuming. Therefore, considerable effort has been devoted to developing reliable 1-D distributed models of electrostatically actuated microbeams. In Tilmans and Legtenberg (1994), a wide clamped-clamped microbeam is modelled with the classical linear beam theory, and the electrostatic force is computed by completely discarding fringing field effects. These assumptions are justified for small beam deflections and wide beams. In Osterberg and Senturia (1997), an effective Young's modulus is considered in order to account for plane stress and plane strain deformations appropriate for narrow and wide beams respectively. The effects of fringing field is considered by accounting for the microbeam's finite width but neglecting its finite thickness. In Abdel-Rahman, Younis and Nayfeh (2002), the beam mid-plane stretching is accounted for in order to treat large deflections. Nevertheless, no improvements with respect to Tilmans and Legtenberg (1994) on the electric modeling are considered, rendering this model suitable for a wide microbeam with initial gap size comparable with the beam thickness. In Kuang and Chen (2004), the fringing field correction of Osterberg and Senturia (1997) is combined with the finite deflection approach of Abdel-Rahman, Younis and Nayfeh (2002) resulting in a model that accurately predicts the pull-in parameters of wide beams undergoing moderate displacements. None of these works is applicable to narrow beams where effects of fringing fields due to the finite thickness are not negligible, as observed in Pamidighantam, Puers, Baert and Tilmans (2002).

Furthermore, the consideration of the mid-plane stretching makes the governing equation nonlinear, and the problem of numerically extracting the pull-in parameters more challenging. The shooting method used in Abdel-Rahman, Younis and Nayfeh (2002) to solve nonlinear differential equations relies on good initial estimates of unknown parameters and may diverge. In Younis, Abdel-Rahman and Nayfeh (2003) two variants of the Galerkin method are employed by using the beam mode shapes as basis functions. In the first variant the electrostatic force is expanded in Taylor series around the undeformed configuration and terms up to the fifth order are retained. The second variant accounts exactly for the electrostatic force. The estimate of the pull-in parameter computed with the first method does not agree well with that obtained with the shooting method. The pull-in parameter obtained from the second variant is very sensitive to the number of modes used as basis, and acceptable results are obtained only when an odd number of modes greater than one are included in the basis functions. Both techniques neglect fringing field effects. The use of mode shapes as basis limits the applicability of the method to beam geometries for which

eigenvalues and eigenfunctions can be easily computed. In Kuang and Chen (2004), the differential quadrature method is used and computed results seem very accurate; nevertheless, the global nature of the method seems to forbid its application to more complicated MEMS geometries.

In this Chapter, we present a model for analyzing narrow microbeams undergoing finite deflections. The beam is modelled by using a large deflection theory, see, e.g., Landau and Lifshitz (1986). This model does not account for finite deformations, and is applicable when the MEMS gap size and the microbeam thickness are considerably smaller than the beam span. Indeed, small strains are experienced whenever the microbeam deflection is much smaller than the microbeam length, even if the maximum deflection exceeds the beam thickness. We solve the resulting nonlinear fourth-order differential equation by using two distinct approaches: (i) reducing the distributed system to a one-degree-of-freedom system, and (ii) retaining the distributed system, and using the MLPG and the FE methods in conjunction with the efficient Displacement Iteration Pull-In Extraction (DIPIE) algorithm developed in Degani-Bochobza, Elata and Nemirovsky (2002). In particular, we derive a consistent electromechanical model where finite thickness of the beam is considered in both the mechanical and the electrical models. With the Method of Moments (MoM), see, e.g., Harrington (1993), an expression for the electrostatic load is established which simultaneously accounts for the fringing field capacitance due to finite width and finite thickness of the microbeam. The approach followed here is similar to that used in structural mechanics to study Saint-Venant problems, see, e.g., Iesan (1987). That is, deformations of a slender beam are studied by initially solving a 2-D problem defined on the cross-section of the beam and using these results to build a 1-D model of the beam with distributed forces/loads acting on its length. Whereas in Gabbay, Mehner and Senturia (2000) a reduced order discrete model valid for a specific MEMS is deduced from 3-D numerical simulations, here a 1-D distributed model of a narrow microbeam is proposed with 2-D numerical simulations needed to determine an expression for the electrostatic force. The distributed 1-D model is studied using both the MLPG and the FE methods. Basis functions for representing the test and the trial functions in the MLPG method are constructed using the GMLS approximation. While in the FE work Hermitian basis functions (i.e., beam elements) are exploited. The present reduced order one-degree-of-freedom model differs from the classical mass-spring model of Nathanson, Newell, Wickstrom and Davis (1977) since we account for the axial stress, nonlinear stiffening, charge redistribution, and fringing fields. It also differs from that of Younis, Abdel-Rahman and Nayfeh (2003) since we retain the complete nonlinear behavior of the electrostatic force and consider fringing fields, and it differs from that of Pamidighantam, Puers, Baert and Tilmans (2002) since we simultaneously treat the pull-in voltage and deflections as unknowns, i.e. the pull-in deflection is not empirically chosen as was done in Pamidighantam, Puers, Baert and Tilmans (2002). Two sample problems, namely

a cantilever and a clamped-clamped microbeam are considered. Results from the proposed one-degree-of-freedom and the distributed models are compared with those available in the literature, i.e. Osterberg and Senturia (1997), Abdel-Rahman, Younis and Nayfeh (2002), Kuang and Chen (2004) , and also with those obtained from 3-D FE simulations. Some of the 3-D FE results for a cantilever beam are borrowed from Pamidighantam, Puers, Baert and Tilmans (2002). Other results for the cantilever beam, and results for the clamped-clamped microbeam have been obtained by using the commercial FE code ANSYS.

Three goals of the present work are: (i) propose a consistent 1-D distributed electromechanical model for a narrow microbeam, (ii) establish a reduced order one-degree-of-freedom model that gives a good estimate of the pull-in parameters (deflection and voltage), and (iii) extend the MLPG method employed earlier to analyze linear beam problems to the analysis of those nonlinear beam problems where nonlinearities arise simultaneously due to electrostatic loads and membrane stretching.

The rest of the Chapter is organized as follows. In Section 3.2, we give governing equations of an electrostatically actuated clamped-clamped and a cantilever narrow microbeam; in Section 3.3, we derive an expression for the distributed electrostatic force that simulates well the fringing field effects. In Section 3.4, we describe a one-degree-of-freedom model, and in Section 3.5, we briefly present the MLPG and the FE methods and apply the DIPIE algorithm for extracting the pull-in parameters. In Section 3.6, we compare the proposed fringing fields corrections with some of the classical formulas available in the literature. The proposed one-degree-of-freedom, and the distributed electromechanical models are validated by comparing predictions from them with those from other distributed models, and from ANSYS and COVENTORWARE FE solutions. Section 3.7 summarizes conclusions of this work. The Method of Moments used in Section 3.3 is briefly outlined in Appendix C. The fundamentals of the GMLS approximation are recalled in Appendix A.2.

3.2 Model development

We consider a narrow microbeam of length ℓ, width b, and thickness h either clamped-clamped or clamped-free, as depicted in Figures 3.1 and 3.2. The microbeam is suspended above an infinite ground plane with an initial gap g_0. Both bodies are perfect conductors and are separated by a dielectric medium of permittivity $\epsilon_0\epsilon_{\rm r}$, where ϵ_0 is the vacuum permittivity, and $\epsilon_{\rm r}$ is the relative permittivity. A positive potential difference V between the two conductors causes the microbeam to electrostatically deflect downwards.

3.2.1 Governing equation for mechanical deformations

Within the large deflection beam theory, see, e.g., Abdel-Rahman, Younis and Nayfeh (2002), the deflection w in the z direction is given by, (see Figures 3.3 and 3.4)

$$EI\frac{\mathrm{d}^4 w}{\mathrm{d}x^4} - N(w)\frac{\mathrm{d}^2 w}{\mathrm{d}x^2} = \tilde{F}_{\mathrm{e}}(w), \tag{3.1}$$

where E is Young's modulus, I the moment of inertia of the cross section about the y axis, N the axial force which is constant along the beam axis, $\tilde{F}_{\mathrm{e}}$ the deflection dependent electrostatic force per unit length, and x the axial coordinate. A beam is considered narrow, when its width b is less than five times its thickness h, see, e.g., Osterberg and Senturia (1997). For wide beams the mechanical stiffness, EI, should be modified as given in Osterberg and Senturia (1997).

For a cantilever beam the axial force vanishes, while for a clamped-clamped beam it is given by

$$N(w) = \frac{EA}{2\ell}\int_0^{\ell}\left(\frac{\mathrm{d}w}{\mathrm{d}x}\right)^2 \mathrm{d}x + N_0, \tag{3.2}$$

where A is the area of cross section of the beam, and N_0 is the residual axial load. For a narrow beam, the residual axial load is $N_0 = \tilde{\sigma}A$, where $\tilde{\sigma}$ is the effective residual axial stress. The residual stress is equal to $\sigma_0(1-\nu)$, where σ_0 is the initial uniform biaxial stress in the material, see, e.g., Osterberg and Senturia (1997) and ν is Poisson's ratio for the material of the beam.

For a fixed-fixed beam, the deflection is subjected to the following four kinematic boundary conditions:

$$w(0) = 0, \qquad \frac{\mathrm{d}w}{\mathrm{d}x}(0) = 0, \qquad w(\ell) = 0, \qquad \frac{\mathrm{d}w}{\mathrm{d}x}(\ell) = 0, \tag{3.3}$$

while for a cantilever beam the deflection should satisfy the two kinematic boundary conditions at the clamped end, and the two kinetic boundary conditions at the free end $x = \ell$:

$$w(0) = 0, \qquad \frac{\mathrm{d}w}{\mathrm{d}x}(0) = 0, \qquad \frac{\mathrm{d}^2 w}{\mathrm{d}x^2}(\ell) = 0, \qquad \frac{\mathrm{d}^3 w}{\mathrm{d}x^3}(\ell) = 0. \tag{3.4}$$

3.2.2 Distributed force due to electric field

The distributed force, $\tilde{F}_{\mathrm{e}}(w)$, on the deformable microbeam due to the electric field depends on the potential difference between the two conductors and on their geometries. Since only small deformations of the beam are considered, it is reasonable to assume that at every point x the electrostatic force per unit length, $\tilde{F}_{\mathrm{e}}$, depends only on the local deflection $w(x)$ and equals the force per unit length acting on an infinitely long straight beam separated by a distance $g(x) = g_0 - w(x)$ from a ground plane as shown in Figure 3.5. The force $\tilde{F}_{\mathrm{e}}$ may be

computed by differentiating the energy per unit length stored in the capacitor with respect to the gap g, i.e.,

$$\tilde{F}_{\mathrm{e}} = -\frac{1}{2}V^2\frac{\partial C_{\mathrm{g}}}{\partial g}. \tag{3.5}$$

Here C_{g} is the capacitance per unit length of the 2-D conductors' system, and V is the voltage difference between the two plates. The capacitance C_{g} is comprised of the parallel-plate capacitance, and the fringing field capacitance due to the finite width and the finite thickness of the beam.

3.2.3 Dimensionless governing equations

For convenience we introduce the nondimensional deflection $\hat{w} = w/g_0$, and the nondimensional abscissa $\hat{x} = x/\ell$. In terms of non-dimensional variables (3.1) becomes

$$\frac{\mathrm{d}^4\hat{w}}{\mathrm{d}\hat{x}^4}(\hat{x}) - \left[N_1\int_0^1\left(\frac{\mathrm{d}\hat{w}}{\mathrm{d}\hat{x}}\right)^2\mathrm{d}\hat{x} + \hat{N}_0\right]\frac{\mathrm{d}^2\hat{w}}{\mathrm{d}\hat{x}^2}(\hat{x}) = \hat{F}_{\mathrm{e}}\left(\hat{w}\left(\hat{x}\right)\right), \tag{3.6}$$

where for a clamped-clamped beam

$$N_1 = 6\frac{g_0^2}{h^2}, \qquad \hat{N}_0 = \frac{N_0\ell^2}{EI} = 12\frac{\tilde{\sigma}\ell^2}{Eh^2}, \qquad \hat{F}_{\mathrm{e}}(\hat{w}(\hat{x})) = \frac{12\ell^4}{Eg_0bh^3}\tilde{F}_{\mathrm{e}}(w(x)), \tag{3.7}$$

and for a cantilever beam

$$N_1 = \hat{N}_0 = 0. \tag{3.8}$$

The capacitance per unit length C_{g} may be expressed as

$$C_{\mathrm{g}} = C_{\mathrm{g}}^0\mathcal{F}\left(\beta,\eta\right), \tag{3.9}$$

where $\mathcal{F}$ represents the fringing field function,

$$C_{\mathrm{g}}^0 = \epsilon_0\epsilon_{\mathrm{r}}\frac{b}{g} \tag{3.10}$$

is the capacitance per unit length when all fringing effects are neglected, and

$$\beta = \frac{h}{b}, \qquad \eta = \frac{h}{g}. \tag{3.11}$$

Therefore, the dimensionless electrostatic force is

$$\hat{F}_{\mathrm{e}} = \frac{\mu}{\left(1-\hat{w}\right)^2}\left(\mathcal{F} + \eta\frac{\partial\mathcal{F}}{\partial\eta}\right), \tag{3.12}$$

where the electrostatic load parameter μ is given by

$$\mu = \frac{6\ell^4\epsilon_0\epsilon_{\mathrm{r}}V^2}{Eh^3g_0^3}. \tag{3.13}$$

In Section 3.3 we will derive an expression for $\hat{F}_{\mathrm{e}}$ applicable to a narrow microbeam.

Henceforth we drop the superimposed hat on dimensionless variables and use a prime to indicate derivative with respect to the dimensionless axial coordinate. Therefore the governing equation (3.1) in terms of nondimensional variables is

$$w^{IV}(x) - N(w)\, w''(x) = F_{\mathrm{e}}(w(x)), \tag{3.14}$$

where for a clamped-clamped beam

$$N(w) = N_1 \int_0^1 (w')^2 \,\mathrm{d}x + N_0, \tag{3.15}$$

and for a cantilever beam

$$N(w) = 0. \tag{3.16}$$

3.2.4 Weak formulation

For a clamped-clamped microbeam, we introduce the following weak formulation, see, e.g., Mura and Koya (1992), of the problem described by the governing equation (3.14) and the nondimensional version of the boundary conditions (3.3):

$$\begin{aligned} 0 = &\int_0^1 w''\tilde{w}''\,\mathrm{d}x + N(w)\int_0^1 w'\tilde{w}'\mathrm{d}x - \int_0^1 F_{\mathrm{e}}\tilde{w}\mathrm{d}x \\ &+ (\lambda_1\tilde{w}(0) + \lambda_2\tilde{w}'(0) + \lambda_3\tilde{w}(1) + \lambda_4\tilde{w}'(1)) + \left(\tilde{\lambda}_1 w(0) + \tilde{\lambda}_2 w'(0) + \tilde{\lambda}_3 w(1) + \tilde{\lambda}_4 w'(1)\right). \end{aligned} \tag{3.17}$$

Here, λ_1, λ_2, λ_3 and λ_4 are Lagrange multipliers used to impose the four kinematic boundary conditions (3.3), $\tilde{w}$ is a smooth test function which need not satisfy the kinematic boundary conditions, and $\tilde{\lambda}_1$, $\tilde{\lambda}_2$, $\tilde{\lambda}_3$ and $\tilde{\lambda}_4$ are arbitrary scalar numbers.

For a cantilever microbeam (3.17) becomes

$$\int_0^1 w''\tilde{w}''\,\mathrm{d}x - \int_0^1 F_{\mathrm{e}}\tilde{w}\mathrm{d}x + (\lambda_1\tilde{w}(0) + \lambda_2\tilde{w}'(0)) + \left(\tilde{\lambda}_1 w(0) + \tilde{\lambda}_2 w'(0)\right) = 0, \tag{3.18}$$

where only two Lagrange multipliers are employed since only two kinematic boundary conditions are prescribed.

The consideration of Lagrange multipliers allows for the simultaneous application of the MLPG and the FE methods. Indeed, the GMLS basis functions (see Appendix A.2) used in the MLPG method do not have the Kronecker delta property, see, e.g., Atluri and Zhu (1998), and special techniques, such as Lagrange multipliers, are needed to enforce kinematic boundary conditions.

3.3 Computation of the electric force field

The problem of computing the capacitance per unit length of the present system of conductors has been addressed in the literature on semiconductor-integrated circuits, see, e.g., Barke (1988), and microwave striplines, see, e.g., Collins (1992). Several empirical and analytical expressions have been proposed but none of them seem to be applicable to a narrow microbeam.

We derive here an empirical formula for the capacitance per unit length of the line to ground system, shown in Figure 3, for a narrow microbeam. The empirical formula is based on a least square fitting of numerical values obtained by using the well-known Method of Moments (MoM), see, e.g., Harrington (1993), outlined in Section 3.3 for piecewise constant basis functions and the collocation method.

3.3.1 Empirical formula for the capacitance

The capacitance C_{g} of the line to ground system of Figure 3.5 equals twice the capacitance $\bar{C}_{\mathrm{g}}$ of two identical rectangular conductors depicted in Figure 3.6. Therefore, we consider this auxiliary system involving finite size conductors and exploit symmetry conditions.

By using the MoM, we numerically compute the capacitance per unit length C_{g} for different values of dimensionless parameters β and η defined in (3.11) ranging from 0.2 to 2, and 0.4 to 5 respectively. The resulting data are then least-squares fitted by a function of the following form:

$$C_{\mathrm{g}} = \epsilon_0 \epsilon_{\mathrm{r}} \left(\frac{\eta}{\beta} + c_0 + c_1 \left(\frac{\eta}{\beta} \right)^{c_2} + c_3 \eta^{c_4} \right), \tag{3.19}$$

where c_0, c_1, c_2, c_3 and c_4 are constants. The first term on the right hand side of (3.19) describes the parallel-plate capacitance, the third term accounts for the fringing field capacitance due to the finite width b, and the fourth term models the fringing field capacitance due to the finite thickness. Numerical values of the optimized constants are

$$c_0 = -0.36, \quad c_1 = 0.85, \quad c_2 = 0.24, \quad c_3 = 2.5, \quad c_4 = 0.24. \tag{3.20}$$

In the chosen range of variation for β and η, the maximum deviation in the capacitance between the estimate obtained by substituting from (3.20) into (3.19) and the fully converged numerical solution achieved by using the MoM is less than 2%. Therefore, the fringing field that we propose to use in (3.9) is

$$\mathcal{F}(\beta, \eta) = 1 - 0.36 \frac{\beta}{\eta} + 0.85 \left(\frac{\beta}{\eta} \right)^{0.76} + 2.5 \frac{\beta}{\eta^{0.76}}. \tag{3.21}$$

3.3.2 Validation of the capacitance estimate

In Table 3.1 we compare capacitance values computed from (3.9) by substituting the expression for the fringing field $\mathcal{F}(\beta,\eta)$ from relation (3.21), and from relations available in the literature, i.e. Palmer's formula (see, e.g., Palmer (1927))

$$\mathcal{F}(\beta,\eta) = 1 + \frac{2}{\pi}\frac{\beta}{\eta}\left(1 + \ln\left(\pi\frac{\eta}{\beta}\right)\right), \tag{3.22}$$

the parallel-plate approximation $\mathcal{F}(\beta,\eta) = 1$, and the Meijs-Fokkema relation (Meijs and Fokkema (1984))

$$\mathcal{F}(\beta,\eta) = 1 + 0.77\frac{\beta}{\eta} + 1.06\left(\frac{\beta}{\eta}\right)^{0.75} + 1.06\frac{\beta}{\eta^{0.5}}\,. \tag{3.23}$$

We use a fully converged solution obtained with the MoM for comparing accuracies of different formulas. It is clear that, for narrow microbeams with $0.5 \le b/h \le 5$, $0.2 \le g/h \le 2$, the Palmer formula and the parallel plate approximation give erroneous values of the capacitance per unit line. As stated in Meijs and Fokkema (1984), values from the Meijs-Fokkema formula have a maximum deviation of 2% for $\eta/\beta = b/g \ge 1,\ 0.1 \le \eta = h/g \le 4$, and of 6% for $\eta/\beta \ge 0.3$ and $\eta < 10$. The estimate is worst when the gap size is larger than the beam width, i.e. $g/b > 1$. In this case, the error in the capacitance values from the Meijs-Fokkema formula is $\sim 6\%$ which is usually unacceptable. It is also evident that the proposed empirical formula provides accurate estimates for values of β and η that are outside the range of their values used for least squares fitting.

In Figure 3.7 we have plotted the percentage error in the capacitance versus the gap/thickness for $\beta = h/b = 0.2$ (narrow beam), and $\beta = 2$ (significantly narrow beam) computed with the different formulas, and taking as reference the converged numerical values obtained by applying the MoM. As expected the present interpolation formula (3.21) provides accurate results for both values of β. The Mejis-Fokkema relation (3.23) gives precise results for a narrow beam but has moderate discrepancies for a significantly narrow beam. The Palmer expression (3.22) and the parallel plate approximation which totally neglect finite thickness of the beam provide poor estimates of the electric capacitance for narrow and significantly narrow micro-beams yielding large errors. The electrostatic force estimated from the two methods is acceptable only for small gaps. Since the gap varies as the beam deforms, formulas (3.22) and (3.23) may not give accurate values of the pull-in voltage.

3.4 One-degree-of-freedom model

A closed-form solution of the boundary-value problem defined by (3.14) and the pertinent boundary conditions cannot be found. Here we give an approximate solution based on a

Geometry		MoM	% Deviations			
β	η	$C_{\mathrm{g}}/(\epsilon_0\epsilon_{\mathrm{r}})$	(3.21)	Meijs-Fokkema (3.23)	Palmer (3.22)	Parallel-Plate
0.1	0.5	8.14	-1.6	-0.4	-9.2	-38.6
0.1	1	13.71	-0.7	< 0.1	-6.5	-27.1
0.1	2.5	29.61	< 0.1	0.7	-4.1	-15.7
0.1	5	55.38	0.2	1.0	-3.0	-9.9
0.1	10	106.19	0.3	1.2	2.2	-6.2
0.2	0.5	5.37	-1.1	-0.4	-17.2	-53.5
0.2	1	8.42	-0.4	-0.1	-12.3	-40.7
0.2	2.5	16.80	< 0.1	0.8	-8.0	-25.6
0.2	5	30.06	0.3	1.5	-5.6	-16.9
0.2	10	55.86	0.5	1.9	-4.0	-10.9
0.5	0.5	3.61	< 0.1	-0.8	-34.5	-72.3
0.5	1	5.12	0.4	-0.6	-25.7	-61.0
0.5	2.5	8.97	0.4	-0.7	-17.7	-44.3
0.5	5	14.71	0.6	2.1	-12.9	-32.1
0.5	10	25.50	0.9	3.4	-9.1	-21.9
1	0.5	2.96	0.6	-1.7	-51.9	-83.1
1	1	3.96	0.7	-1.8	-40.3	-74.8
1	2.5	6.29	0.4	-0.1	-29.3	-60.2
1	5	9.52	0.5	2.2	-22.4	-47.5
1	10	15.30	1.1	4.6	-16.4	-34.9
2	0.5	2.59	0.8	-2.9	-71.8	-90.4
2	1	3.34	0.7	-3.5	-57.3	-85.0
2	2.5	4.90	< 0.1	-1.7	-43.8	-74.5
2	5	6.88	< 0.1	1.4	-53.3	-63.7
2	10	10.16	0.7	5.4	-27.4	-50.9
5	0.5	2.34	0.3	-5.2	∞	-95.7
5	1	2.92	-0.1	-6.2	-81.5	-93.2
5	2.5	4.03	-1.4	-4.8	-64.7	-87.6
5	5	5.25	-1.6	-1.0	-55.0	-81.0
5	10	7.04	-0.7	4.9	-45.9	-71.6

Table 3.1: Comparison between the capacitances per unit length computed by the Method of Moments (MoM) with those from (3.9) by substituting in it the expression (3.21) for the fringing field, and from three formulas available in the literature.

one-degree-of-freedom model of the MEMS. The approximate solution is constructed by expressing the dimensionless deflection field as the product of an unknown deflection parameter ζ and a given trial function $\bar{w}(x)$ satisfying the kinematic boundary conditions:

$$w(x) = \zeta \bar{w}(x). \tag{3.24}$$

The governing equation for ζ is derived by multiplying both sides of (3.14) by $\bar{w}$, integrating over the beam span, and substituting into the resulting equation the approximate solution (3.24). After integrating by parts the governing equation for ζ becomes

$$(k_0 + k_1)\zeta + k_2\zeta^3 = \mu f_{\mathrm{e}}(\zeta), \tag{3.25}$$

where

$$k_0 = \int_0^1 (\bar{w}''(x))^2 \mathrm{d}x, \tag{3.26a}$$

$$k_1 = N_0 \int_0^1 (\bar{w}'(x))^2 \mathrm{d}x, \tag{3.26b}$$

$$k_2 = N_1 \left(\int_0^1 (\bar{w}'(x))^2 \mathrm{d}x \right)^2, \tag{3.26c}$$

$$f_{\mathrm{e}}(\zeta) = \frac{1}{\mu} \int_0^1 F_{\mathrm{e}}(\zeta \bar{w}(x)) \bar{w}(x) \mathrm{d}x. \tag{3.26d}$$

Note that F_{e} is linear in μ, therefore f_{e} is independent of μ. The left hand side of (3.25) represents the restoring elastic force, while the right hand side the electrostatic force. Furthermore, the term multiplying ζ represents the stiffness of a linear elastic beam, and that multiplying ζ^3 the strain-stiffening effect. The lumped electrostatic force depends on the adopted fringing field correction, and it cannot in general be expressed analytically. The pull-in parameters are determined by requiring that equilibrium exists, i.e., (3.25) is satisfied. Note that the stiffness of the system vanishes at this equilibrium, and equilibrium configuration is unaffected by small perturbations of the deflection. Therefore, pull-in occurs in an equilibrium state for which the first derivative of the equilibrium equation (3.25) with respect to the deflection parameter ζ vanishes.

This implies that the pull-in deflection and voltage should satisfy simultaneously (3.25), and its derivative with respect to ζ, i.e.,

$$(k_0 + k_1) + 3k_2\zeta^2 = \mu \frac{\mathrm{d}f_{\mathrm{e}}(\zeta)}{\mathrm{d}\zeta}. \tag{3.27}$$

By eliminating μ from (3.25) and (3.27), we obtain

$$f_{\mathrm{e}}(\zeta)((k_0 + k_1) + 3k_2\zeta^2) - \frac{\mathrm{d}f_{\mathrm{e}}(\zeta)}{\mathrm{d}\zeta}((k_0 + k_1)\zeta + k_2\zeta^3) = 0. \tag{3.28}$$

By solving (3.28) for ζ, and by substituting the value of ζ into (3.25) we determine the pull-in instability parameters, i.e. deflection and voltage. We emphasize that once the trial function $\bar{w}(x)$ has been chosen, (3.28) reduces to a nonlinear algebraic equation for ζ, where the derivative $\mathrm{d}f_{\mathrm{e}}(\zeta)/\mathrm{d}\zeta$ can be computed for any ζ by numerical integration. In general, (3.25) cannot be solved analytically and standard root finding techniques such as the bisection algorithm, see, e.g., Press, Flannery, Teukolsky, and Vetterling (1989), may be applied.

When k_2 is different from zero, fringing fields are taken into account, and arbitrary trial functions are used, multiple solutions may be present. We determine the pull-in parameters by considering the lowest root of (3.28). In our numerical simulations, we found that (3.28) has one solution.

We choose as trial function $\bar{w}(x)$ the normalized linear static deflection of the microbeam due to a uniformly distributed applied load. Therefore, for a clamped-clamped microbeam we take

$$\bar{w}(x) = 16x^2(1-x)^2, \tag{3.29}$$

and consequently

$$k_0 = \frac{1024}{5}, \quad k_1 = N_0\frac{512}{105}, \quad k_2 = N_1\left(\frac{512}{105}\right)^2. \tag{3.30}$$

For a cantilever microbeam we choose

$$\bar{w}(x) = \frac{1}{3}x^2(6-4x+x^2), \tag{3.31}$$

thus

$$k_0 = \frac{16}{5}, \quad k_1 = 0, \quad k_2 = 0. \tag{3.32}$$

In beam's undeformed configuration, the electrostatic force acts as a uniformly distributed load, and the nonlinear mechanical stiffness is zero. Therefore the chosen trial function represents the actual microbeam deflection when small voltages are involved. Moreover, from the analysis of the distributed model with the MLPG and the FE methods it appears that the shape of the deformed beam does not change appreciably as the voltage is increased. These ensure the effectiveness of the present choice, which is validated by numerical results presented in Section 3.6.

3.5 Numerical methods

3.5.1 Discrete nonlinear formulation

In order to seek an approximate solution of the nonlinear problem, we find the deflection by using either the MLPG method with the GMLS basis functions described in Atluri, Cho and

Kim (1999) and outlined in Appendix A.2, or the FE method with the Hermite polynomial basis functions, see, e.g., Bathe (1986). In both cases, indicating by N the number of nodes on the beam, the trial solution is expressed as

$$w^h(x) = \psi(x)^{\mathrm{T}}\hat{\mathbf{s}}, \tag{3.33}$$

where $\psi(x)$ is a $2N$ vector comprised of the basis functions, and $\hat{\mathbf{s}}$ is the vector of $2N$ nodal unknowns. For the GMLS approximation, $\hat{\mathbf{s}}$ represents the fictitious nodal values, see, e.g., Atluri, Cho and Kim (1999). The number of unknowns in the problem is $2N + N_L$, where N_L is the number of Lagrange multipliers, which equals 4 for a clamped-clamped beam, see (3.17), and 2 for a cantilever beam, see (3.18). By substituting the approximation (3.33) in either (3.17) or (3.18), considering displacement test functions of the form

$$\tilde{w} = \gamma\,\psi(x) \tag{3.34}$$

where γ is a $2N$ row vector of arbitrary constants, and by introducing a N_L vector $\tilde{\lambda}$ of arbitrary constants, we get the following discrete nonlinear equations

$$\mathbf{K}(\hat{\mathbf{s}})\,\hat{\mathbf{s}} + \mu\mathbf{G}(\hat{\mathbf{s}}) + \mathbf{V}^{\mathrm{T}}\gamma = \mathbf{0}, \tag{3.35a}$$

$$\mathbf{V}\,\hat{\mathbf{s}} = \mathbf{0}, \tag{3.35b}$$

where

$$\mathbf{K}(\hat{\mathbf{s}}) = \int_0^1 \psi''(x)\psi''(x)^{\mathrm{T}}\mathrm{d}x + N(\psi(x)^{\mathrm{T}}\hat{\mathbf{s}})\int_0^1 \psi'(x)\psi'(x)^{\mathrm{T}}\mathrm{d}x, \tag{3.36a}$$

$$\mathbf{G}(\hat{\mathbf{s}}) = -\int_0^1 F_{\mathrm{e}}(\psi(x)^{\mathrm{T}}\hat{\mathbf{s}})\psi(x)\mathrm{d}x, \tag{3.36b}$$

$$\text{clamped-clamped:} \quad V_{1i} = \psi_i(0), \quad V_{2i} = \psi_i'(0), \quad V_{3i} = \psi_i(1), \quad V_{4i} = \psi_i'(1), \tag{3.36c}$$

$$\text{cantilever:} \quad V_{1i} = \psi_i(0), \quad V_{2i} = \psi_i'(0), \tag{3.36d}$$

and $i = 1, ..., 2N$.

Let rows of the $(2N - N_L) \times 2N$ matrix $\mathbf{Y}$ be comprised of $(2N - N_L)$ linearly independent null vectors of the $N_L \times 2N$ matrix $\mathbf{V}$, and set

$$\hat{\mathbf{s}} = \mathbf{Y}^{\mathrm{T}}\mathbf{s}. \tag{3.37}$$

Substitution from (3.37) into (3.35b) gives

$$\mathbf{V}\,\mathbf{Y}^{\mathrm{T}}\mathbf{s} = \mathbf{0}, \tag{3.38}$$

which are identically satisfied for every $(2N - N_L)$-vector $\mathbf{s}$. Premultiplying both sides of (3.35a) by $\mathbf{Y}$, postmultiplying both sides by $\hat{\mathbf{s}}$, and substituting from (3.37) we obtain the following reduced system of $(2N - N_L)$ nonlinear equations for $\mathbf{s}$:

$$\bar{\mathbf{K}}(\mathbf{s})\,\mathbf{s} + \mu\bar{\mathbf{G}}(\mathbf{s}) = \mathbf{0}, \tag{3.39}$$

where

$$\bar{\mathbf{K}}\left(\mathbf{s}\right) = \mathbf{Y}\mathbf{K}\left(\mathbf{Y}^{\mathrm{T}}\mathbf{s}\right)\mathbf{Y}^{\mathrm{T}}, \qquad \bar{\mathbf{G}}\left(\mathbf{s}\right) = \mathbf{Y}\,\mathbf{G}\left(\mathbf{Y}^{\mathrm{T}}\mathbf{s}\right). \tag{3.40}$$

Having found $\mathbf{s}$ from (3.39), $\hat{\mathbf{s}}$ is computed from (3.37).

3.5.2 DIPIE algorithm

We use the Displacement Pull-In Extraction (DIPIE) algorithm (see, e.g., Degani-Bochobza, Elata and Nemirovsky (2002)) to solve the set of equations (3.39) and find the complete bifurcation path. It treats the applied voltage as an additional unknown, using the deflection $\bar{w}$ of a pre-chosen beam point $\bar{x}$ as the driving parameter for the iteration scheme. In this way, the original problem, which has both stable and unstable equilibrium states, is replaced by a sequence of equivalent problems.

If the deflection $\bar{w}_{k-1}$ is known, the solution $(\mathbf{s}_k, \mu_k) = (\mathbf{s}_{k-1} + \Delta\mathbf{s}_k, \mu_{k-1} + \Delta\mu_k)$ at the deflection $\bar{w}_k = \bar{w}_{k-1} + \Delta\bar{w}_k$ is found by solving the system of equations:

$$\bar{\mathbf{K}}(\mathbf{s}_k)\mathbf{s}_k + \mu_k\bar{\mathbf{G}}(\mathbf{s}_k) = \mathbf{0}, \tag{3.41a}$$

$$\psi(\bar{x})^{\mathrm{T}}\mathbf{Y}^{\mathrm{T}}\mathbf{s}_k = \psi(\bar{x})^{\mathrm{T}}\mathbf{Y}^{\mathrm{T}}\mathbf{s}_{k-1} + \Delta\bar{w}_k. \tag{3.41b}$$

The solution of the set of nonlinear equations (3.41), in terms of the unknowns Δs_k and $\Delta\mu_k$, is found by using Newton's iterations. Hence at the generic τ-th iteration

$$\begin{bmatrix} \bar{\mathbf{T}}_k^{(\tau)}\left(\mathbf{s}_k^{(\tau)}\right) & \bar{\mathbf{G}}\left(\mathbf{s}_k^{(\tau)}\right) \\ \psi(\bar{x})^{\mathrm{T}}\mathbf{Y}^{\mathrm{T}} & 0 \end{bmatrix} \begin{bmatrix} \Delta\mathbf{s}_k^{(\tau)} \\ \Delta\mu_k^{(\tau)} \end{bmatrix} = - \begin{bmatrix} \bar{\mathbf{K}}\left(\mathbf{s}_k^{(\tau)}\right)\mathbf{s}_k^{(\tau)} + \mu_k^{(\tau)}\bar{\mathbf{G}}\left(\mathbf{s}_k^{(\tau)}\right) \\ \psi(\bar{x})^{\mathrm{T}}\mathbf{Y}^{\mathrm{T}}\mathbf{s}_k^{(\tau)} - \Delta\bar{w}_k \end{bmatrix}, \tag{3.42}$$

where $\left(\Delta\mathbf{s}_k^{(\tau)}, \Delta\mu_k^{(\tau)}\right)$ indicates the τ-th solution increment; $\left(\mathbf{s}_k^{(\tau)}, \mu_k^{(\tau)}\right)$ is the updated solution at the $(\tau-1)$-th iteration, i.e.,

$$\mathbf{s}_k^{(\tau)} = \mathbf{s}_{k-1} + \sum_{h=1}^{\tau-1}\Delta\mathbf{s}_k^{(h)}, \quad \mu_k^{(\tau)} = \mu_{k-1} + \sum_{h=1}^{\tau-1}\Delta\mu_k^{(h)};$$

$\mathbf{T}_k^{(\tau)}\left(\mathbf{s}_k^{(\tau)}\right)$ is the tangent stiffness at the $(\tau-1)$ -th iteration, i.e.,

$$\mathbf{T}_k^{(\tau)}\left(\mathbf{s}_k^{(\tau)}\right) = 2N_1\int_0^1\left(\psi'(x)^{\mathrm{T}}\mathbf{Y}^{\mathrm{T}}\mathbf{s}_k^{(\tau)}\right)\psi'(x)\mathrm{d}x\int_0^1\psi'(x)^{\mathrm{T}}\left(\psi'(x)^{\mathrm{T}}\mathbf{Y}^{\mathrm{T}}\mathbf{s}_k^{(\tau)}\right)\mathrm{d}x + \bar{\mathbf{K}}\left(\mathbf{s}_k^{(\tau)}\right) + \mu^{(\tau)}\mathbf{Y}\mathbf{D}_k^{(\tau)}\mathbf{Y}^{\mathrm{T}} \tag{3.43}$$

with

$$\mathbf{D}_k^{(\tau)} = -\int_0^1\frac{\partial F_{\mathrm{e}}}{\partial w^h}\left(\psi(x)^{\mathrm{T}}\mathbf{Y}^{\mathrm{T}}\mathbf{s}_k^{(\tau)}\right)\psi(x)\psi(x)^{\mathrm{T}}\mathrm{d}x. \tag{3.44}$$

The iterations are performed until the infinity norm of the incremental solution, i.e., its maximum value over the beam span satisfies

$$\max_{x\in(0,1)} \left[\psi(x)^{\mathrm{T}}\mathbf{Y}^{\mathrm{T}}\Delta\mathbf{s}_k^{(\tau)}\right] \leq \varepsilon_k, \tag{3.45}$$

where

$$\varepsilon_k = \varepsilon^{\mathrm{A}} + \varepsilon^{\mathrm{R}} \max_{x\in(0,1)} \left[\psi(x)^{\mathrm{T}}\mathbf{Y}^{\mathrm{T}}\Delta\mathbf{s}_k^{(1)}\right], \tag{3.46}$$

ε^{A} and ε^{R} are preassigned small numbers. For a clamped-clamped microbeam we choose $\bar{x}$ equal to the mid-span, and for a cantilever microbeam we take $\bar{x}$ equal to the beam length. In order to extract the pull-in parameters we monitor the electrostatic parameter $\Delta\mu_k$, since pull-in occurs when this parameter changes sign. We use a constant step for iterating the deflection and, if necessary, additional iterations are performed for pull-in parameters.

3.6 Results and comparisons

In Osterberg and Senturia (1997) the mid-plane stretching, and the fringing field capacitance due to the finite thickness of the beam are neglected, and the Palmer approximate formula (3.22) is used. Therefore, expressions for the dimensionless force per unit length, and of the dimensionless axial load are:

$$N = \begin{cases} N_0, & \text{clamped-clamped} \\ 0, & \text{cantilever} \end{cases}, \qquad F_{\mathrm{e}} = \frac{\mu}{(1-w)^2}\left(1 + \frac{2}{\pi}\frac{\beta}{\eta}\right). \tag{3.47}$$

In Abdel-Rahman, Younis and Nayfeh (2002) the mid-plane stretching is considered but all fringing field effects are neglected. Consequently, the electric force per unit length is given by

$$F_{\mathrm{e}} = \frac{\mu}{(1-w)^2}. \tag{3.48}$$

In Kuang and Chen (2004) the mid-plane stretching is accounted for, and the fringing field effects are treated as in Osterberg and Senturia (1997).

Here we compare predictions of the models developed by Osterberg and Senturia (1997), Abdel-Rahman, Younis and Nayfeh (2002), and Kuang and Chen (2004) with those of the present model for two sample problems: a cantilever, and a clampled-clamped microbeam. Both geometries have been analyzed in Pamidighantam, Puers, Baert and Tilmans (2002) by using the software COVENTORWARE. Recent findings of Coventor Inc. do not agree with results of Pamidighantam, Puers, Baert and Tilmans (2002) for the clamped-clamped beam. Moreover, for the problem analyzed by Pamidighantam, Puers, Baert and Tilmans (2002) the microbeam deflections are relatively small, the nonlinear stiffening does not seem

	Clamped-Clamped	Cantilever: case (1)	Cantilever: case (2)
ℓ, $[\mu m]$	100	100	300
b, $[\mu m]$	1	1	0.5
h, $[\mu m]$	2	2	1
g_0, $[\mu m]$	4	4	2.5
E, $[GPa]$	169	169	77
ν	0.066	0.066	0.33
ϵ_r	1	1	1

Table 3.2: Geometric and material parameters for the problems studied. For the cantilever beam problem, case (1) refers to the geometry analyzed herein with ANSYS, while case (2) to the problem analyzed in Pamidighantam, Puers, Baert and Tilmans (2002).

significant, and the numerical findings do not include the pull-in deflection which is a crucial design parameter.

Therefore, we performed our own 3-D FE simulations using ANSYS. Details of the performance of simulating MEMS problems with ANSYS are given in Shapoorabadi and Kirk (2004). Following guidelines of Shapoorabadi and Kirk (2004) on the accuracy of different simulation options, we used the tool ROM 144. We adapted the "Sample Miniature Clamped-Clamped Beam Analysis", example 6.6 in the tutorial of ANSYS 8.0, to a narrow microbeam by extending the surrounding dielectric medium in order to accurately model the fringing fields. The region analyzed and its discretization into FEs are reported in Figure 3.8 for the clamped-clamped microbeam; only half of the system is modelled due to symmetry conditions, and a refined mesh is employed in the gap region. In particular, the dielectric medium is considered as a block of length $100\mu m$, semi-width $24\mu m$, and thickness $24\mu m$. For the cantilever microbeam problem, the dielectric domain has been also increased along the beam axis by $24\mu m$ in order to model fringing fields at the free end. The elements SOLID 45 (8-node brick elements) were used to model the microbeam, while SOLID 122 (20-node tetrahedral elements) were used to model the dielectric. Geometric nonlinearities have been included in the simulation. Table 3.2 lists the geometry and the material properties of the problems studied. The used mesh densities and the dielectric region dimensions correspond to the minimum required to obtain a fully converged solution for the pull-in parameters. Indeed, performing numerical experiments by varying both the dielectric region and the mesh density for the beam and the dielectric, we established that the third significant digit of the pull-in voltage and the pull-in deflection does not change by considering either a more refined mesh or a larger dielectric domain.

While using (3.39) a uniform grid of 9 uniformly spaced nodes has been used for both the MLPG and the FE methods, and results were found practically indistinguishable from those obtained by considering more nodes. Numerical integrations have been performed by using 10 Gauss quadrature points located in each element for the FE method, and in each

subinterval partitioning the entire domain as is done in Atluri, Cho and Kim (1999) for the MLPG method. The GMLS basis functions are generated by complete monomials of degree 3 ($m = 4$), see (A.20) in Appendix A.2. The radius R of the weight functions in (A.29) for the GMLS approximation is 5 times the distance between two adjacent nodes. The power α in (A.29) is set equal to 5, see Atluri, Cho and Kim (1999) for a discussion of the effect of α on the trial function's degree of smoothness. The tuning of parameters for the MLPG analysis stems from the results in Andreaus, Batra and Porfiri (2005), where effect of different parameters are analyzed, and general guidelines are given. As a rule of thumb, increasing any of the parameters α, R, and m results in a more accurate solution but with more computational time. In the DIPIE algorithm for the clamped-clamped microbeam, the increment of the driving parameter $\Delta\bar{w}_k$ equals 2.5×10^{-3}, while for the cantilever microbeam the increments of the driving parameter are 4.0×10^{-3} for case (1), and 1.0×10^{-2} for case (2) in Table 3.2. These choices are motivated by the need to estimate the third significant digit in the dimensional pull-in maximum deflection. The tolerances in Newton's iterations for the DIPIE algorithm are $\varepsilon^{\mathrm{A}} = 10^{-6}$ and $\varepsilon^{\mathrm{R}} = 10^{-4}$, see (3.46).

Results of different computations on the clamped-clamped microbeam are given in Table 3.3; results of the ANSYS FE simulations are considered to be most reliable since they do not involve a-priori assumptions on the mechanical and the electrical behavior of the system. Three different values of the initial stress σ_0, representative of pretensioned, stress-free and precompressed beams, have been examined. Results from models of Osterberg and Senturia (1997), Abdel-Rahman, Younis and Nayfeh (2002), and Kuang and Chen (2004) have also been computed with the MLPG and the FE methods, and with the corresponding reduced 1 d.o.f. models. The accuracy of the proposed 1 d.o.f. model explained in Section 3.4 can be ascertained by comparing predictions from it with those from the MLPG and the FE methods. The complete neglect of the fringing field effects leads to significant underestimation of the electrostatic force, consequent overestimation of the pull-in voltage, and underestimation of the pull-in deflection as is evident from the results computed with the model of Abdel-Rahman, Younis and Nayfeh (2002). By introducing into the model of Abdel-Rahman, Younis and Nayfeh (2002) the fringing field (3.22), as is done in Kuang and Chen (2004), the pull-in voltage and the pull-in deflection are significantly improved; nevertheless, the pull-in voltage is still overestimated due to the neglect of the finite thickness of the beam in the computation of the electrostatic force. Instead, the pull-in deflection computed by using the model of Kuang and Chen (2004) is in good agreement with the ANSYS FE solution. The removal of the mid-plane stretching effect done in Osterberg and Senturia (1997) for the clamped-clamped beam significantly decreases the accuracy of the pull-in deflection, since it completely ignores the nonlinear stiffening which for the present geometry ($g_0/h = 2$) is extremely relevant. The model developed in Osterberg and Senturia (1997) is based on assuming small deflections of the microbeam, and therefore it is

(a) $\sigma_0 = 100MPa$

	V_{PI}, $[V]$			$\|w_{\text{PI}}\|_\infty$, $[\mu m]$		
ANSYS	902			2.47		
	1 d.o.f.	MLPG	FE	1 d.o.f	MLPG	FE
Abdel-Rahman, Younis and Nayfeh (2002)	1513	1510	1510	2.13	2.11	2.11
Kuang and Chen (2004)	1003	999	1000	2.55	2.53	2.53
Osterberg and Senturia (1997)	783	783	783	1.96	1.96	1.96
Present Work	945	942	942	2.48	2.46	2.47

(b) $\sigma_0 = 0MPa$

	V_{PI}, $[V]$			$\|w_{\text{PI}}\|_\infty$, $[\mu m]$		
ANSYS	830			2.57		
	1 d.o.f.	MLPG	FE	1 d.o.f	MLPG	FE
Abdel-Rahman, Younis and Nayfeh (2002)	1373	1371	1371	2.24	2.23	2.24
Kuang and Chen (2004)	923	920	920	2.63	2.62	2.62
Osterberg and Senturia (1997)	663	660	660	1.96	1.96	1.96
Present Work	868	865	866	2.57	2.56	2.56

(c) $\sigma_0 = -100MPa$

	V_{PI}, $[V]$			$\|w_{\text{PI}}\|_\infty$, $[\mu m]$		
ANSYS	750			2.64		
	1 d.o.f.	MLPG	FE	1 d.o.f	MLPG	FE
Abdel-Rahman, Younis and Nayfeh (2002)	1225	1223	1224	2.39	2.39	2.39
Kuang and Chen (2004)	838	836	836	2.73	2.73	2.73
Osterberg and Senturia (1997)	516	506	506	1.96	1.97	1.97
Present Work	786	785	785	2.68	2.68	2.68

Table 3.3: Comparison of pull-in voltages, V_{PI} , and pull-in deflections infinity norm, $\|w_{\text{PI}}\|_\infty$, of the clamped-clamped microbeam obtained from different models, different methods, and with different values of the initial stress, σ_0; (a) $\sigma_0 = 100MPa$, (b) $\sigma_0 = 0$, and (c) $\sigma_0 = -100MPa$. The MLPG and the FE refer to solutions of the one-dimensional boundary-value problem with the MLPG and the FE methods respectively.

(a) Beam (1) of Table 3.2

	V_{PI}, $[V]$			$\|w_{\mathrm{PI}}\|_{\infty}$, $[\mu m]$		
ANSYS	93			1.84		
	1 d.o.f.	MLPG	FE	1 d.o.f	MLPG	FE
Abdel-Rahman, Younis and Nayfeh (2002)	166	165	165	1.79	1.79	1.79
Osterberg (1997), Kuang (2004)	102	102	102	2.20	2.19	2.20
Present Work	98	98	98	2.11	2.11	2.11

(b) Beam (2) of Table 3.2

	V_{PI}, $[V]$			$\|w_{\mathrm{PI}}\|_{\infty}$, $[\mu m]$		
COVENTORWARE	1.2			(not available)		
	1 d.o.f.	MLPG	FE	1 d.o.f	MLPG	FE
Abdel-Rahman, Younis and Nayfeh (2002)	2.18	2.17	2.17	1.12	1.12	1.12
Osterberg (1997), Kuang (2004)	1.25	1.25	1.25	1.40	1.40	1.40
Present Work	1.21	1.21	1.21	1.33	1.33	1.33

Table 3.4: Comparison of pull-in voltages and pull-in deflections of the cantilever microbeam obtained from different models and different methods. The MLPG and the FE refer to solutions of the one-dimensional boundary-value problem with the MLPG and the FE methods respectively.

incapable of accurately estimating pull-in parameters for the present geometry. The pull-in voltage is instead underestimated, since by neglecting the membrane stretching, the overall mechanical compliance is overestimated. As is evident from the results listed in Table 3.3, the present work, by properly accounting for the fringing field effects due to the beam finite thickness, provides a consistent electromechanical theory that gives accurate results for narrow clamped-clamped microbeams undergoing severe displacements. Figure 3.9 reports the voltage versus the maximum deflection for the three values of the initial stress obtained using the five models. The curves are computed by using the simple 1 d.o.f. model explained in Section 3.4. For increasing voltages, the maximum deflections predicted by these models differ significantly; the response predicted by the present model is closest to that given by ANSYS.

Results of computations on the two sample cantilever microbeams whose parameters are listed in Table 3.2 are given in Table 3.4. The discrepancy between the pull-in voltage predicted by Abdel-Rahman, Younis and Nayfeh (2002), and the ones resulting from either ANSYS or COVENTORWARE (see Pamidighantam, Puers, Baert and Tilmans (2002)) signifies the importance of fringing fields for a reliable understanding of the pull-in instability in a narrow microbeam. Wherease we computed results with ANSYS, those with COVENTORWARE are from Pamidighantam, Puers, Baert and Tilmans (2002). When compared to the models of Osterberg and Senturia (1997), and Kuang and Chen (2004), the present model

improves both the estimates of the pull-in voltage and the pull-in deflection. Indeed, models of Osterberg and Senturia (1997) and Kuang and Chen (2004) underestimate the electrostatic force by neglecting the fringing field effects due to the beam finite thickness, therefore overestimate the pull-in voltage, and lead to less accurate estimates of the pull-in deflection. For the five different models Figure 3.10 exhibits the voltage versus the maximum deflection for the geometry identified as case (1) in Table 3.2. The curves are computed by using the simple 1 d.o.f. model presented in Section 3.6. As for the clamped-clamped microbeam, the complete neglect of fringing fields yields severely erroneous predictions. Accounting for fringing fields in narrow cantilever microbeams dramatically increases the accuracy, and a detailed model of fringing field effects, as has been done in the present work, gives results with relatively low errors.

For the second cantilever microbeam geometry and for the stress-free clamped-clamped microbeam, Figure 3.11 depicts the deformed shapes of the microbeams just prior to the pull-in voltage. They give an idea of the maximum deflection of the beam just before the pull-in voltage is reached.

The nondimensional pull-in parameter μ for different values of the beam width b, and with values of other parameters listed in Table 3.2, computed with different MEMS models, is given in Figures 3.12 and 3.13 for a cantilever, and a clamped-clamped beam respectively; the corresponding results for the maximum pull-in deflections are exhibited in Figures 3.14 and 3.15. The curves are computed by using the simple 1 d.o.f. model. For each beam the nondimensional pull-in parameter μ increases monotonically with a decrease in the value of β from 2.0 to 0.2. From Figures 3.14 and 3.15, it is clear that the nondimensional pull-in maximum deflection significantly changes with the width of the beam, and consistently differs from the values used in Pamidighantam, Puers, Baert and Tilmans (2002) for deriving empirical estimates of the pull-in voltage (0.45 for cantilever, and 0.40 for clamped-clamped microbeams). Indeed, for the narrow microbeam with $\beta = 2$, the nondimensional pull-in maximum deflections are 0.56 and 0.66 for the cantilever and the clamped-clamped configurations, respectively.

3.7 Conclusions

The main conclusions of the present work can be summarized as follows. The available models in the literature for studying electrically actuated microbeams do not give good estimates of the pull-in voltage for a narrow microbeam with width smaller than five times the thickness. The proper choices of the beam bending stiffness, and the fringing field due to the finite width of the beam are generally not sufficient to accurately model narrow microbeams. The effect of the beam finite thickness should be considered in order to derive

a consistent electromechanical model.

The classical empirical formulas for computing the line to ground capacitance cannot be applied to narrow microbeams, since the aspect ratio of the microbeam cross section may exceed the typical aspect ratios of integrated circuits. Furthermore, when large deflections are considered the gap size along the microbeam span may attain values larger than those encountered in typical electronic circuits. Therefore, empirical formulas are needed to properly describe the electrical capacitance of narrow microbeams. In the present work, an empirical formula suitable for narrow microbeams is derived from least squares fit to values computed by the method of moments. Values obtained from this formula are compared with those from other formulas in the literature, and predictions from its use are shown to be valid for a narrow microbeam.

A one-degree-of-freedom model that gives very good values of the pull-in voltage for narrow clamped-clamped, and cantilever beams is proposed. It differs from the classical spring-mass model since the nonlinear stiffening due to the axial stress, charge redistribution and fringing fields are taken into account. Moreover, the complete nonlinear behavior of the electrostatic force is retained and the pull-in voltage and deflections are treated as unknowns, i.e., the pull-in deflection is not empirically chosen as was done in Pamidighantam, Puers, Baert and Tilmans (2002). It is shown that the pull-in deflections noticeably change with the aspect ratio of the beam cross-section, and can not be a-priori determined.

The one-degree-of-freedom model results have been validated by comparing them with those obtained by solving the nonlinear one-dimensional boundary-value problem with the MLPG, and the FE methods in conjunction with the DIPIE algorithm. Results from the MLPG, and the FE methods are virtually indistinguishable when the same number of nodes are used. The convergence rate of the DIPIE method does not vanish when the pull-in state is approached, and the number of iterations remains reasonable.

The MLPG method represents an efficient alternative to the FE method for studying microbeams and estimating the pull-in parameters. In particular, the MLPG method is applicable to any microbeam geometry, and it does not require the use of a mesh on the MEMS domain. This alleviates mesh entanglement problems and remeshing difficulties that may arise when analyzing finite deformations of MEMS devices, and simplifies the generation of the numerical model since no interconnectivity rules among nodes are required.

The computed pull-in voltage for a clamped-clamped, and a cantilever microbeam is found to match well with that obtained from the solution of the 3-dimensional problem with the commercial computer code ANSYS. The 3-dimensional simulations are considerably more expensive than those for the proposed one-dimensional distributed model.

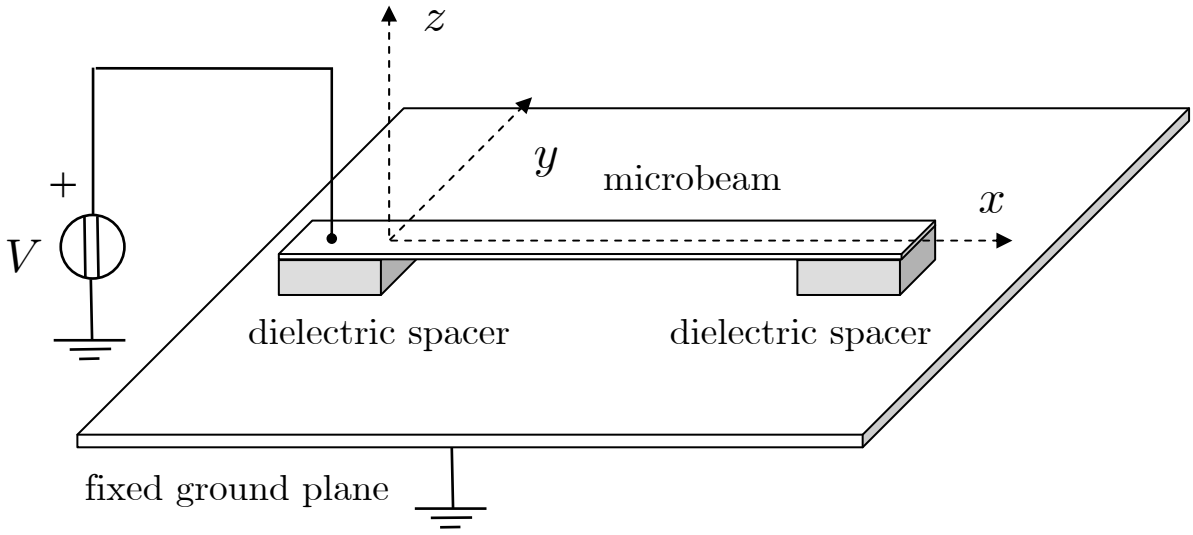

Figure 3.1: Electrostatically actuated clamped-clamped microbeam.

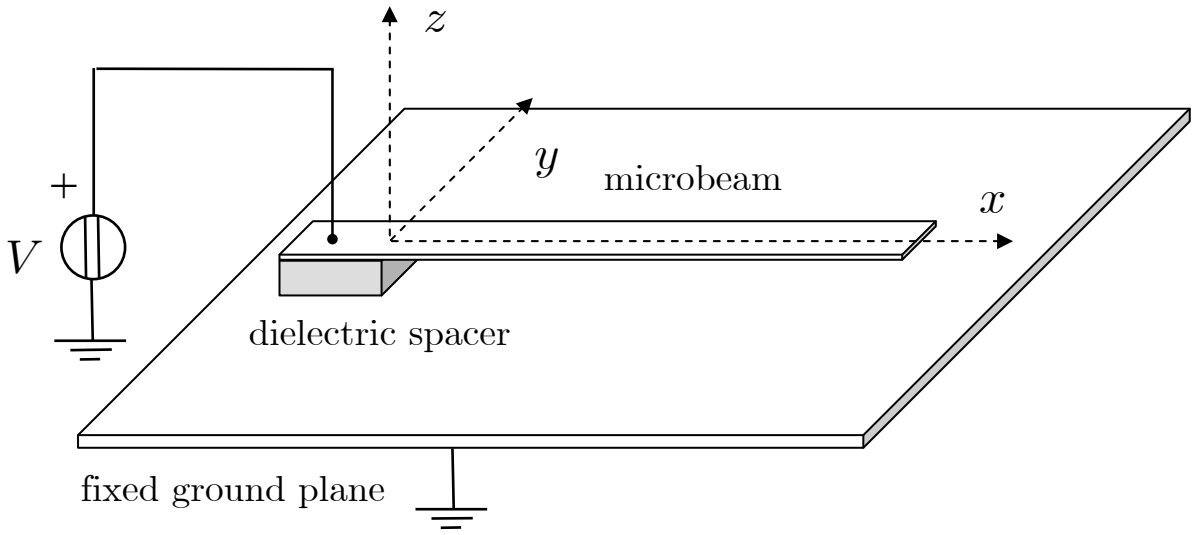

Figure 3.2: Electrostatically actuated cantilever microbeam.

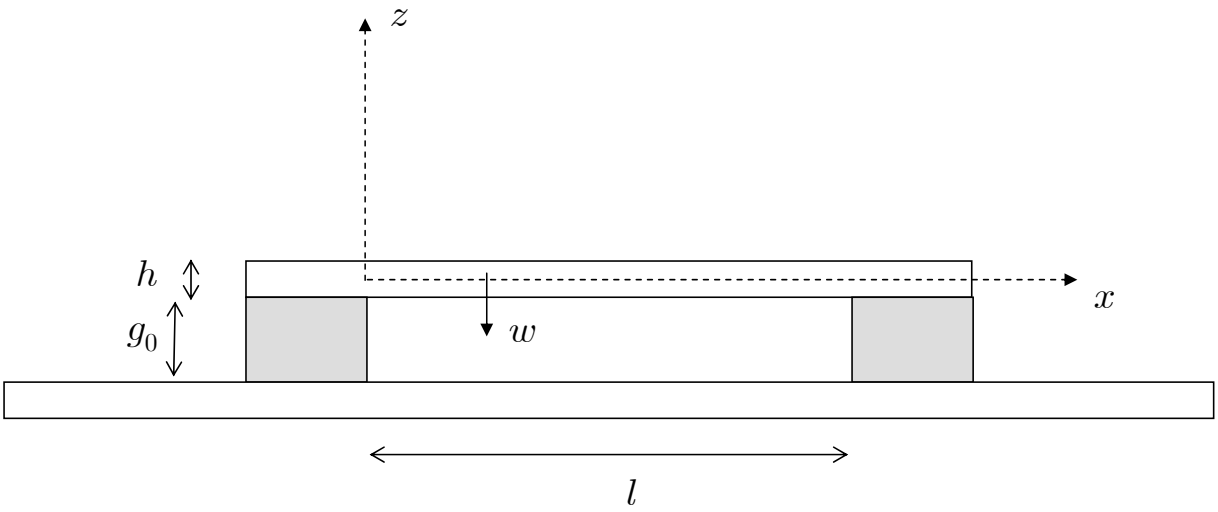

Figure 3.3: Side view of the clamped-clamped microbeam.

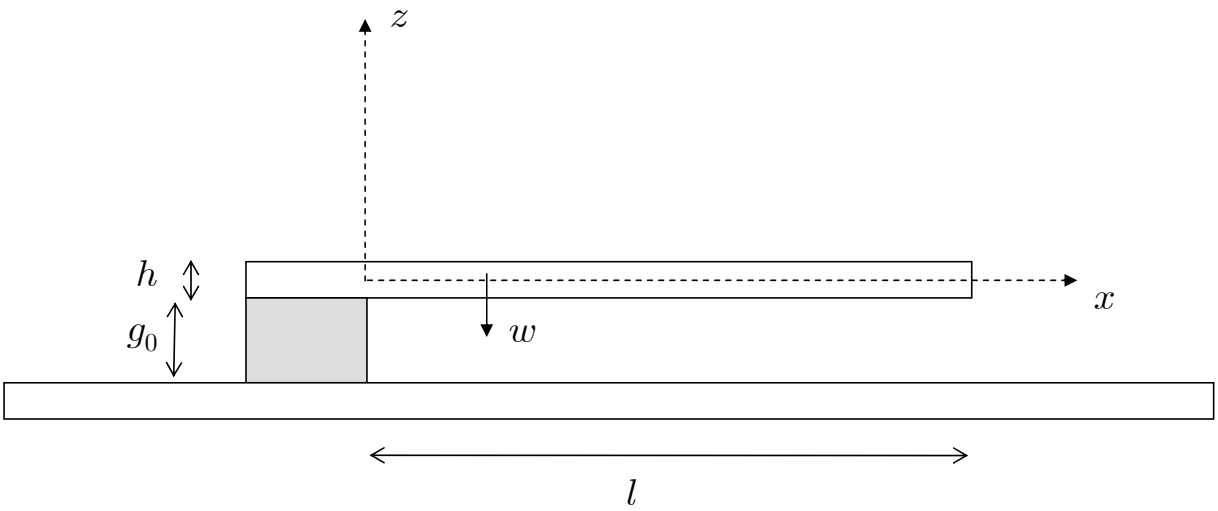

Figure 3.4: Side view of the cantilever microbeam.

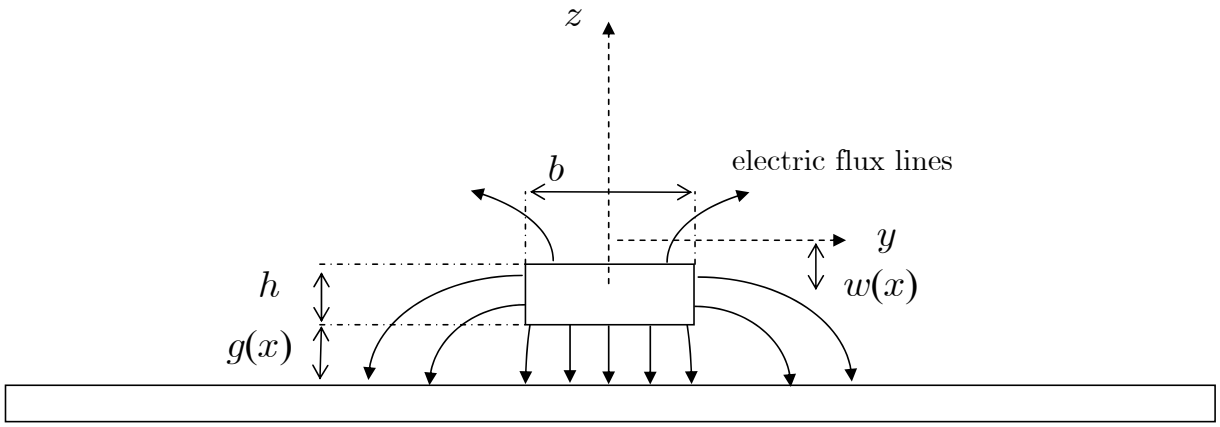

Figure 3.5: Schematic view of the beam cross section with grounded electrode

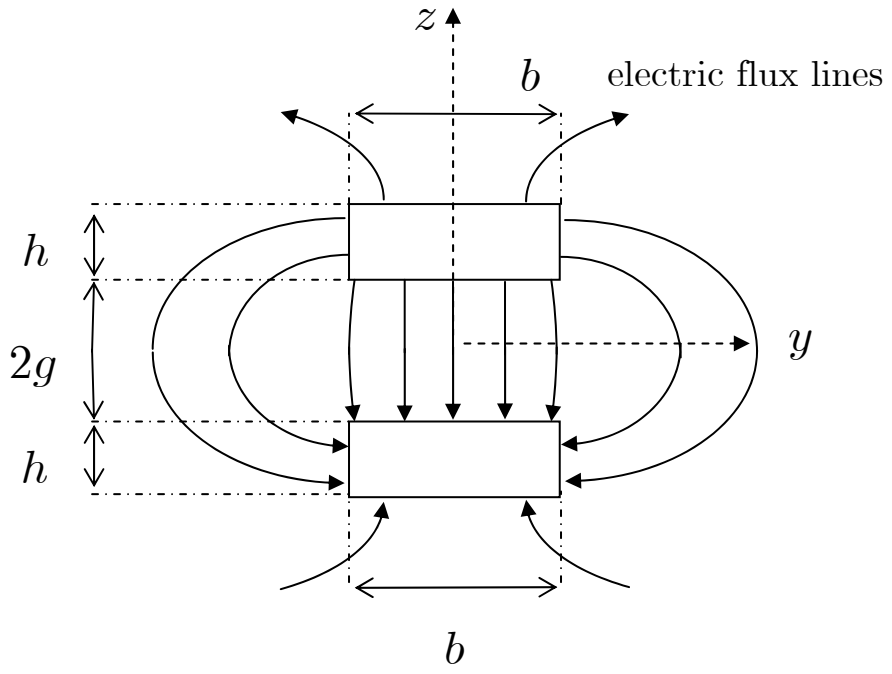

Figure 3.6: A system of auxiliary conductors for computing the electrostatic capacitance.

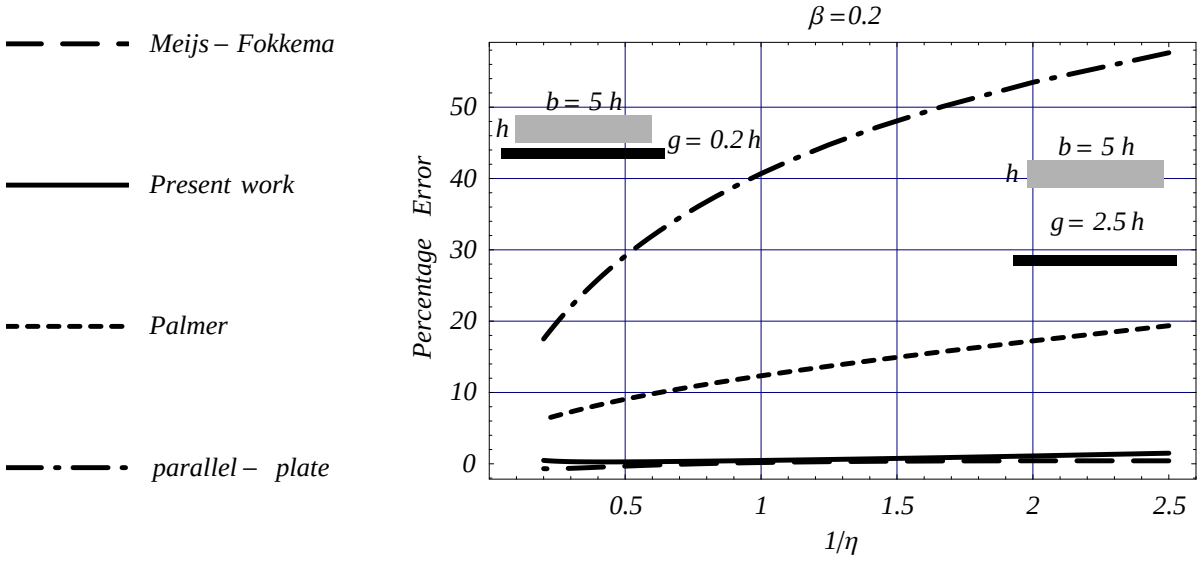

(a)

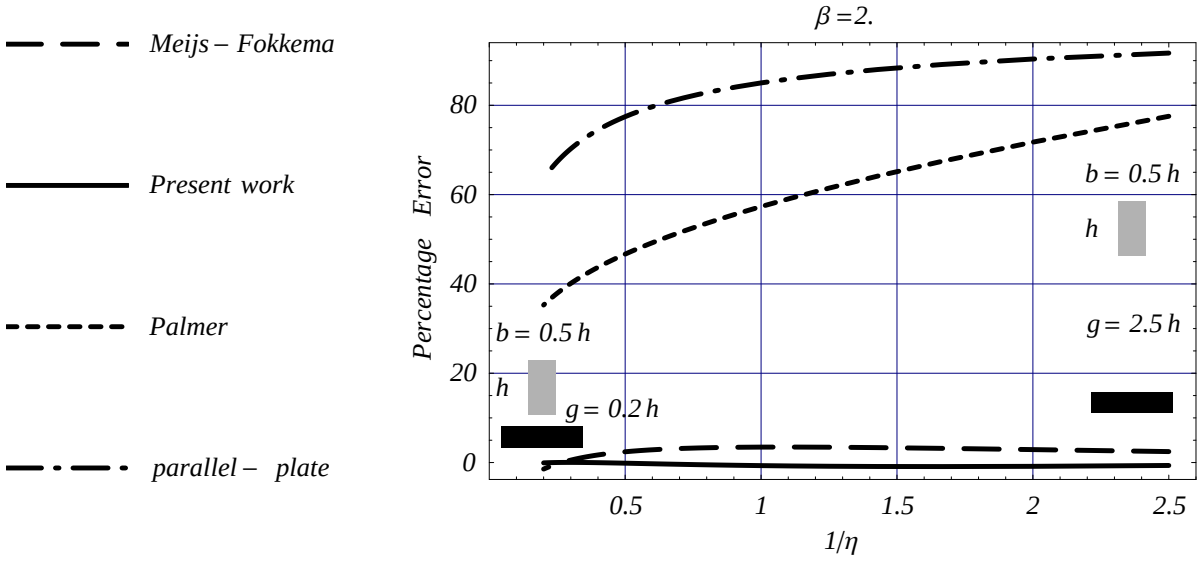

(b)

Figure 3.7: Taking the capacitance computed with the method of moments as reference, comparison of the error in the capacitance per unit length for a narrow microbeam obtained with different methods: (a) $\beta = 0.2$; (b) $\beta = 2$.

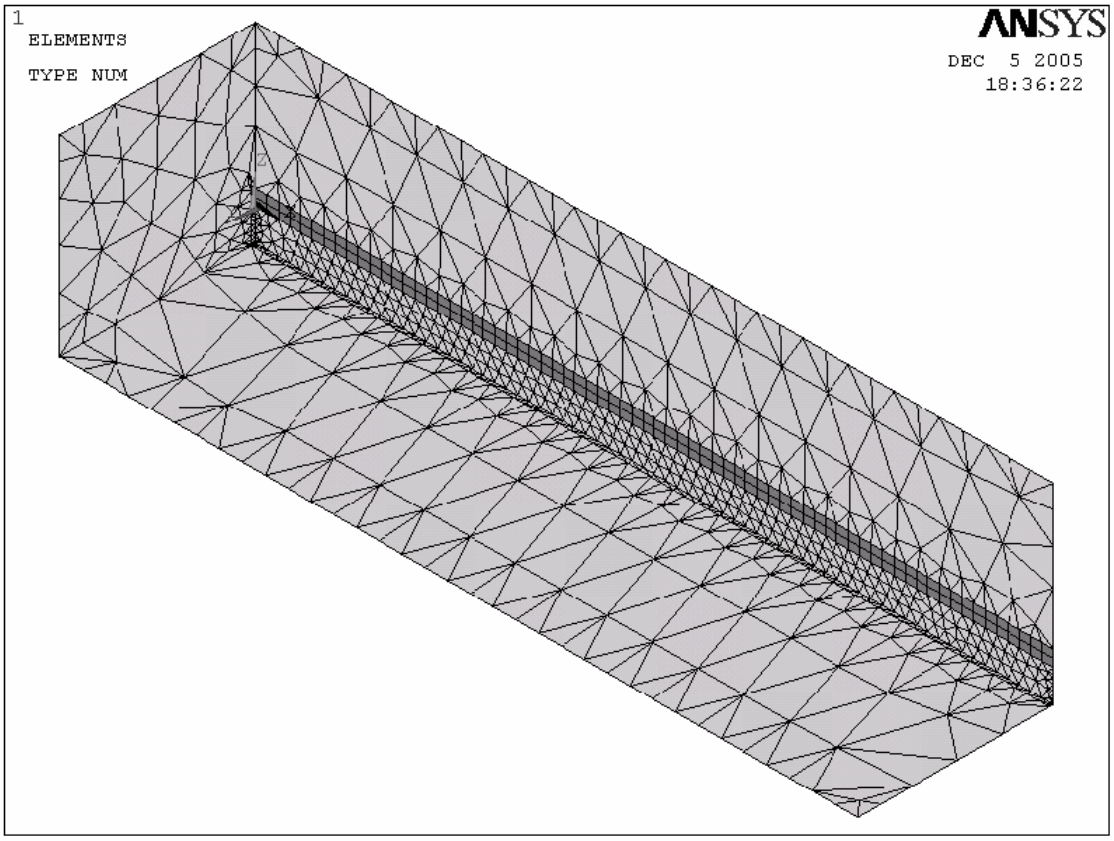

Figure 3.8: Schematics of the 3D FE mesh used for simulations of the clamped-clamped beam by ANSYS. The domain in light grey (discretized with tetrahedral elements) is the dielectric, the one in dark grey (discretized with brick elements) is the microbeam.

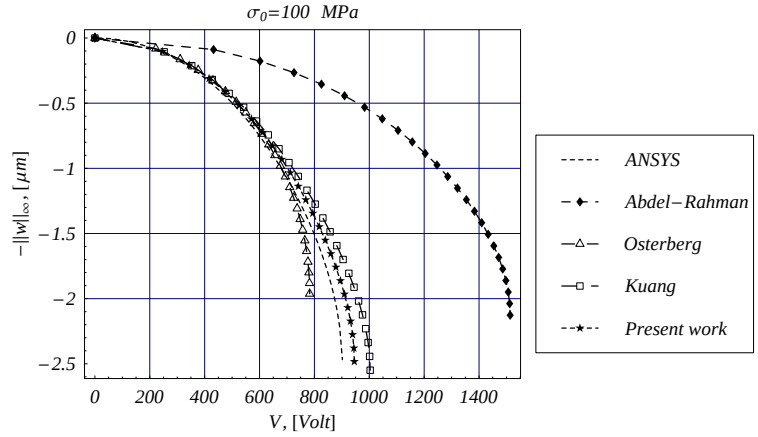

(a)

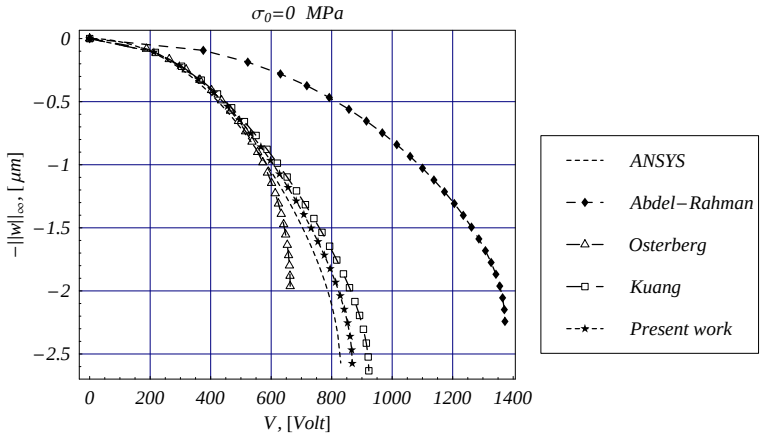

(b)

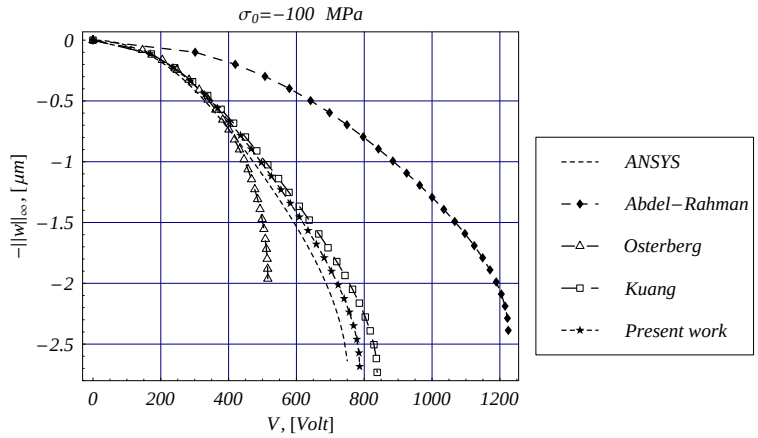

(c)

Figure 3.9: Plots of the maximum displacement versus the applied voltage for the clamped-clamped microbeam problem under different initial states of stress. Results from all models are reported up to their predicted pull-in instability. (a) $\sigma_0 = 100MPa$; (b) $\sigma_0 = 0MPa$; (c) $\sigma_0 = -100MPa$.

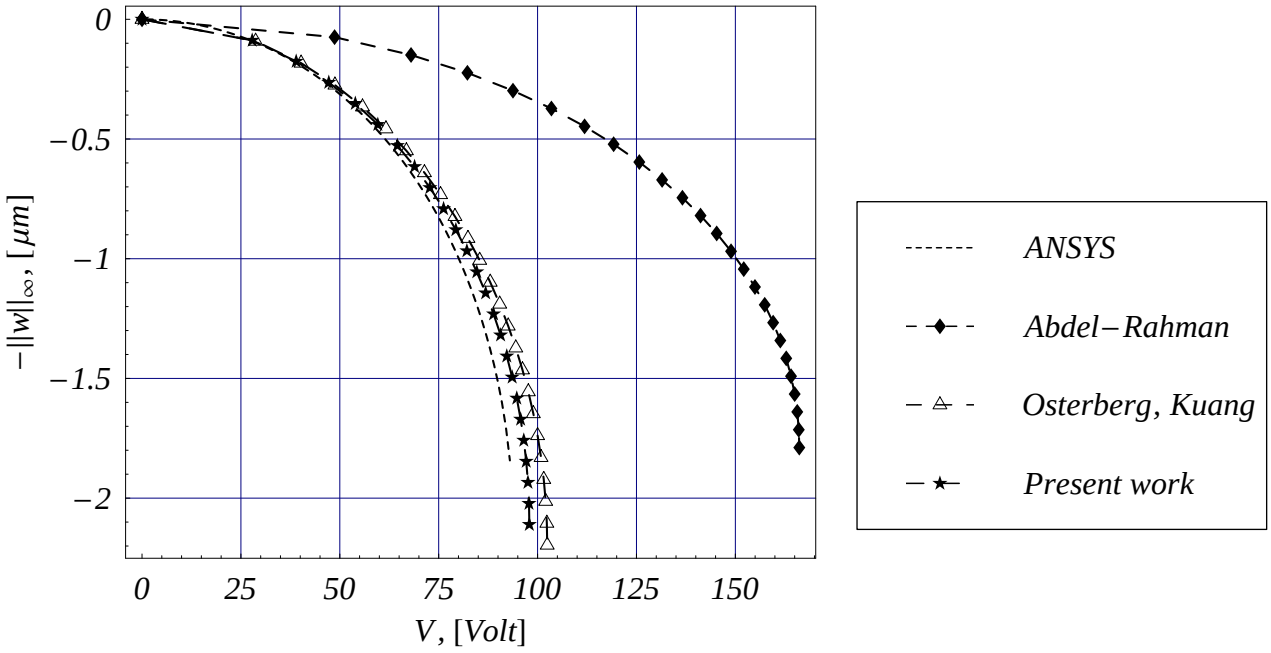

Figure 3.10: Plot of the maximum displacement versus the applied voltage for the cantilever microbeam of case (1), Table 3.2. Results from all models are reported up to their predicted pull-in instability.

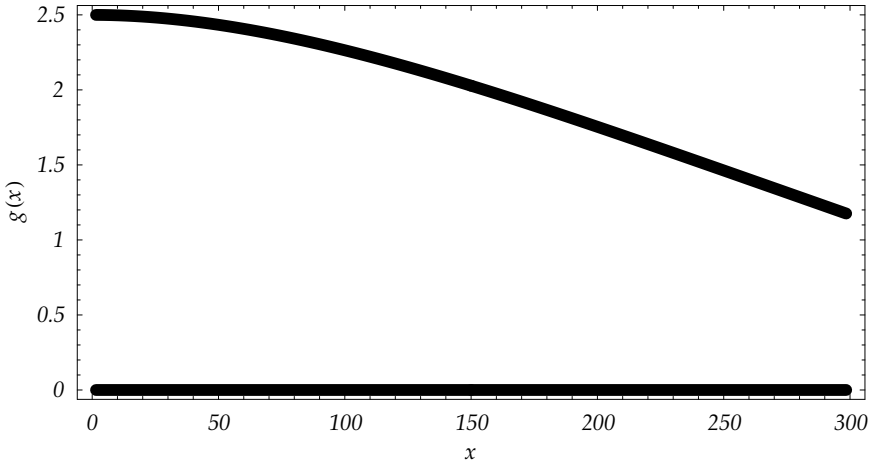

(a)

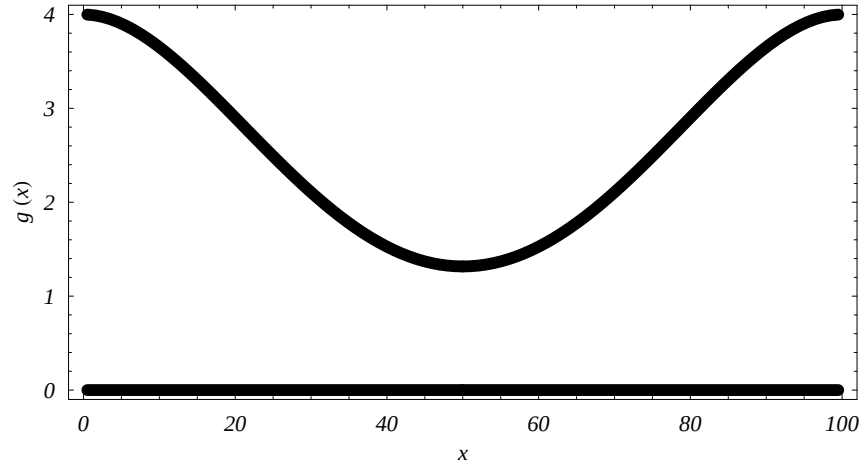

(b)

Figure 3.11: Deformed shapes of microbeams just prior to the pull-in voltage. Dimensions along the x- and the y-axes are in μm; (a) cantilever microbeam of case (2), Table 3.2; (b) clamped-clamped microbeam with $\sigma_0 = 0MPa$.

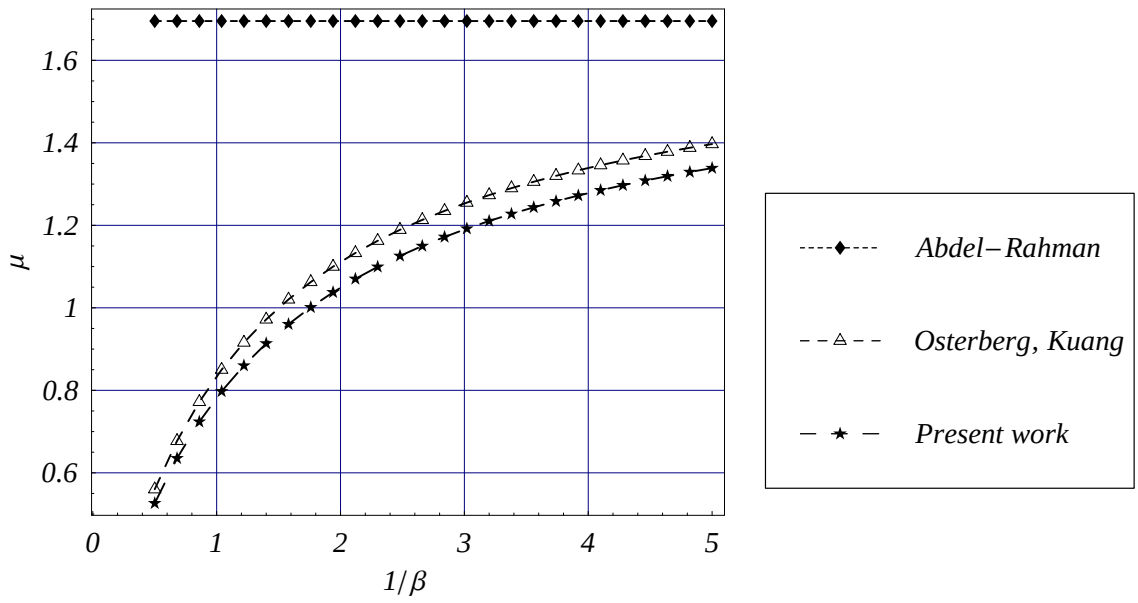

Figure 3.12: For the cantilever beam identified as case (2) in Table 3.2, comparison of the nondimensional pull-in voltage μ vs. $1/\beta$ computed from the present 1 d.o.f. model with those from Osterberg and Senturia (1997), Abdel-Rahman, Younis and Nayfeh (2002), and Kuang and Chen (2004).

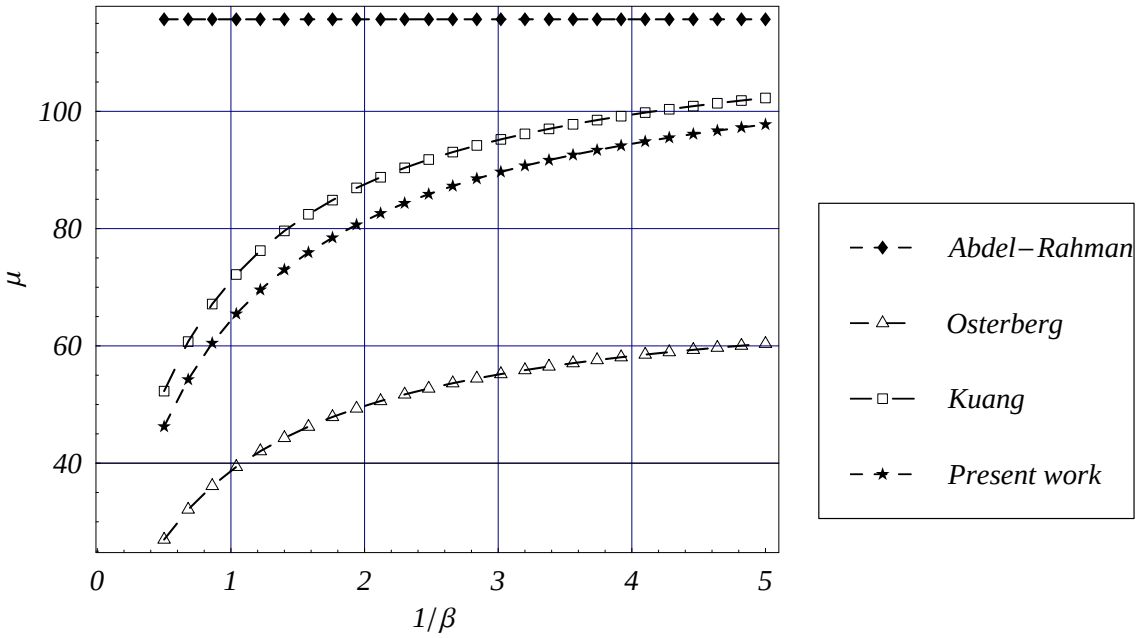

Figure 3.13: For the clamped-clamped microbeam of Table 3.2 with $\sigma_0 = 0MPa$, comparison of the non-dimensional pull-in voltage μ vs. $1/\beta$ computed from the present 1 d.o.f. model with those from Osterberg and Senturia (1997), Abdel-Rahman, Younis and Nayfeh (2002), and Kuang and Chen (2004).

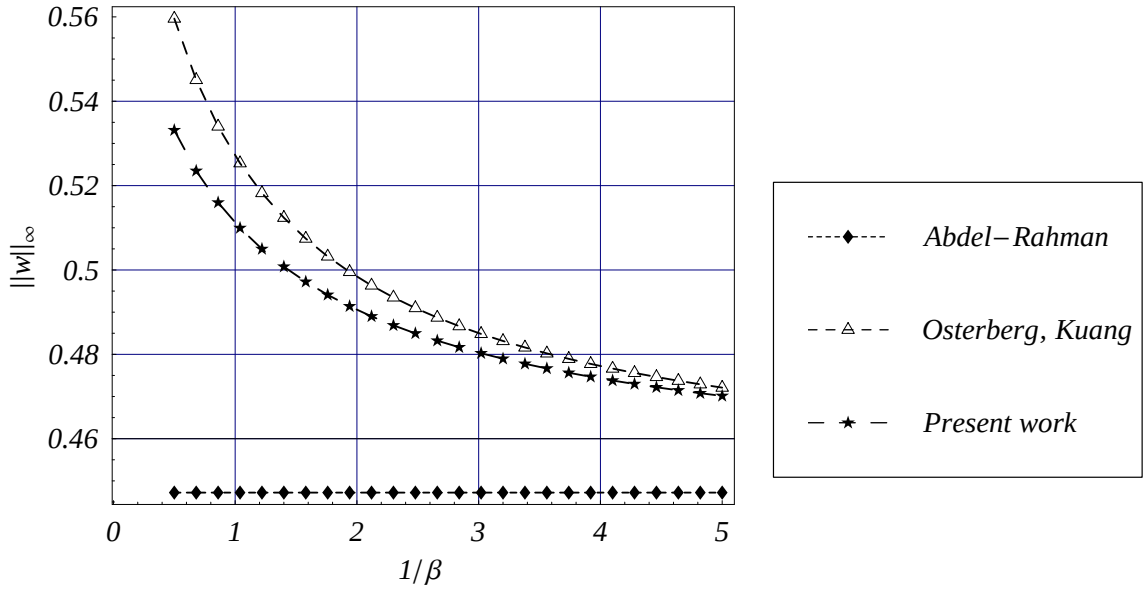

Figure 3.14: For the cantilever beam identified as case (2) in Table 3.2, comparison of the maximum pull-in non-dimensional deflection $\|w\|_\infty$ vs. $1/\beta$ computed from the present 1 d.o.f. model with those from Osterberg and Senturia (1997), Abdel-Rahman, Younis and Nayfeh (2002), and Kuang and Chen (2004).

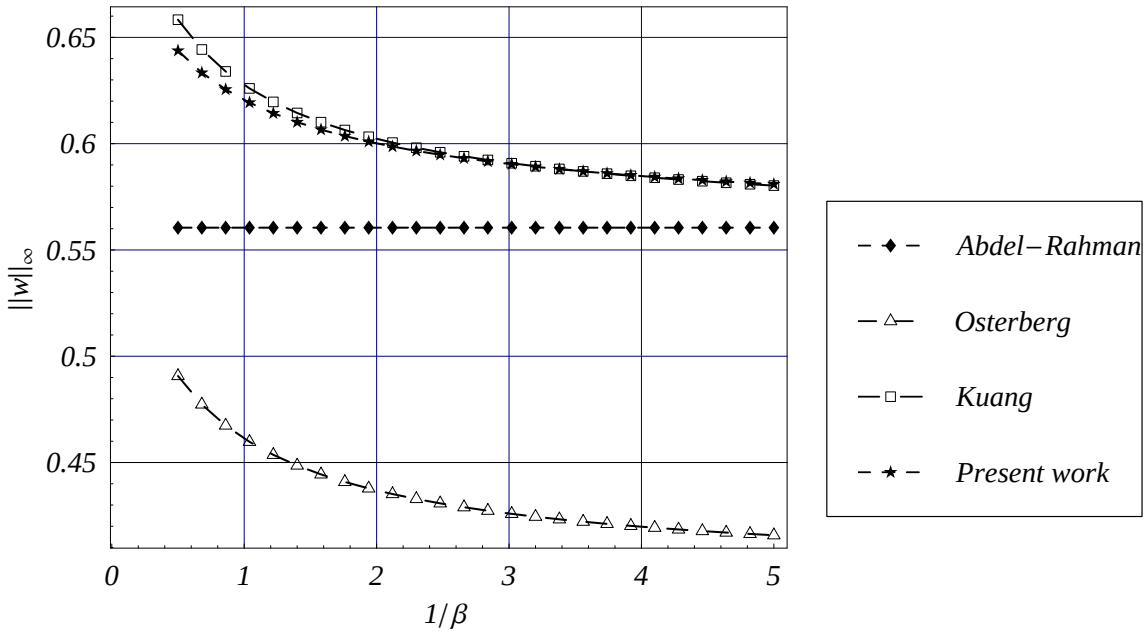

Figure 3.15: For the clamped-clamped microbeam described in Table 3.2 with $\sigma_0 = 0MPa$, comparison of the maximum pull-in non-dimensional deflection $\|w\|_\infty$ vs. $1/\beta$ computed from the present 1 d.o.f. model, with those from Osterberg and Senturia (1997), Abdel-Rahman, Younis and Nayfeh (2002), and Kuang and Chen (2004).

Chapter 4

Vibrations of Cracked Euler-Bernoulli Beams

4.1 Introduction

Most load carrying systems and structures degrade or accumulate cracks during service. For safety reasons, it is desirable that any existing cracks be detected and located before they cause more serious damage and eventual system failure. Visual inspection is costly and tedious and often does not yield a quantifiable result. For some components visual inspection is virtually impossible. Therefore, the development of structural health monitoring techniques has received increasing attention in recent years (see, e.g., Dimarogonas (1996)). Among these techniques, it is believed that the use of vibration data offers the most desirable alternative to actually dismantling the structure. In this method one excites the structure either in free vibration or in forced harmonic oscillations and extracts the natural frequencies and, if possible, the mode shapes. The main idea behind damage detection schemes that rely on modal data is that a damage in the system will manifest itself as changes in the modal characteristics.

The structural health monitoring and diagnostics generally require accurate models for the structures, since the measured modal characteristics generally do not change much with damage; e.g., the changes in natural frequencies due to cracks become significant only when the structure is close to failure. As for the computational costs involved in the identification procedure a good compromise between accuracy and simplicity should be a key feature of a mathematical model intended to be part of the on-line health monitoring procedure. Therefore in the last two decades, several investigators have been working on the development of reliable and robust mathematical models of damaged structural elements, especially slender

Material in this Chapter is part of the paper "Vibrations of Cracked Euler-Bernoulli Beams Using Meshless Local Petrov-Galerkin (MLPG) Method," appeared in *CMES: Computer Modeling in Engineering & Sciences*.

beams. The different theoretical modeling techniques for cracked slender structures can be grouped in two basic categories: i) "lumped flexibility" models; and ii) "continuous" models.

The first category is based on the representation of a crack as a lumped flexibility element (generally a spring), without affecting the modeling of the undamaged regions (see, e.g., Gudmunson (1983), and Chondros and Dimarogonas (1998) for modeling aspects; Ostachowicz and Krawczuk (1991), and Khiem and Lien (2004) for a multiple cracks scenario; and Rizos, Aspragathos and Dimarogonas (1988) for the damage identification). The determination of the equivalent lumped stiffness is usually performed in the framework of classical fracture mechanics, starting from the knowledge of the stress intensity factors. On the other hand, the basic idea behind the second modeling strategy is to obtain a continuous, one-dimensional model of the cracked beam at the level of approximation of classical beam theory (see, e.g., Christides and Barr (1984) for modeling aspects; Shen and Pierre (1990, 1994) for computational insights; Chondros and Dimarogonas (1998), and Chondros (2001) for comparisons between the lumped flexibility and the continuous models; Carneiro and Inman (2002) for the derivation of a continuous model including shear deformations). The governing equations of the one-dimensional cracked beam are derived via a variational principle, e.g. the Hu-Washizu-Barr method. The modification of the stress field induced by the crack is incorporated through a local empirical function which assumes an exponential decay with the distance from the crack. This additional crack function can be determined in several ways, but none of them seems to be satisfactory. The adopted techniques range from crude numerical analysis to experimental investigations passing through qualitative fracture mechanics. For a complicated structure with multiple cracks, the solution of the governing equations of motion requires numerical techniques, e.g. the finite element method (Gounaris and Dimarogonas (1988), and Gounaris, Papadoupolos and Dimarogonas (1996)) or the Myklestad approach of Mahmoud, Zaid and Al Harashani (1999).

In the development of these theoretical models, it is assumed that the crack remains open during the vibration period. However, unless a static preload exists, during vibrations of the beam the state of stress in the cracked section varies from tension to compression, i.e. the crack opens and closes with time. This results in a modification of the crack section stiffness, the extremal values being the stiffness of the open crack and that of the intact beam. Thus, the non-linear behavior of the closing crack introduces characteristics of the non-linear systems. However, for many practical applications, the system can be considered bilinear, and the fatigue crack can be introduced in the form of the so-called "breathing crack" model which opens when the normal strain near the crack tip is positive, otherwise it closes. The vibration of a beam with a closing crack has been studied in several works: in Chondros and Dimarogonas (2001), and Shen and Chu (1992) a continuous cracked beam theory is assumed and Galerkin procedures are applied; in Sundermeyer and Weaver (1995) a

lumped flexibility theory is used and analytical solutions are presented; in Qian, Gu and Jiang (1990), Ruotolo, Surace, Crespo and Storer (1996), and Pugno, Surace and Ruotolo (2000) a finite element model of the cracked beam is used, where reduced stiffness of an element accounts for the crack's presence by "smearing" the crack effect on an entire element; in Luzzato (2003) a "smeared crack" model is compared with a finite element solution of a lumped flexibility model.

In the present Chapter we propose an accurate numerical technique for the analysis of a beam with multiple cracks based on MLPG6 formulation, that is, the trial and test functions are chosen from the same space. Adopting the lumped flexibility approach, each fatigue crack is modelled as a rotational spring and several damage scenarios are addressed. We study the modal characteristics of a beam with multiple open cracks and its transient behavior when the cracks are breathing.

Recent literature (Atluri, Cho and Kim (1999), and Raju and Phillips (2003)) shows increasing interest in the analysis of beams by the use of MLPG methods. In Atluri, Cho and Kim (1999) the static analysis of thin beams is presented using the MLPG6 method. In particular, the conventional Moving Least Squares (MLS) approximation presented in Lancaster and Salkauskas (1981) is generalized to treat 4-th order boundary value problems, and the resulting Generalized Moving Least Squares (GMLS) approximation is used to construct simultaneously the test and trial functions. In Raju and Phillips (2003) the static analysis of thin beams is addressed by the use of a Petrov-Galerkin implementation of the MLPG method, where the trial functions are constructed using the GMLS approximation and the test functions are chosen from a different space. The GMLS basis functions are generally continuously differentiable over the entire domain which results in continuous derivatives of the trial solution. Thus the treatment of cracked beams necessitates the use of special techniques to account for the slope discontinuities at the crack stations (a similar problem has been studied in Batra, Porfiri and Spinello (2004) for heat conduction in a bimaterial body). In the present chapter we use the MLPG6 variant and adopt a substructure approach, by making use of Lagrange multipliers to model the spring effects at the crack locations and relate deformations of the intact beam segments. Warlock, Ching, Kapila and Batra (2002) employed the method of Lagrange multipliers to enforce traction boundary conditions at a contact surface.

The rest of the Chapter is organized as follows. In Section 4.2 we study the dynamics of a multiply cracked beam with the MLPG method. The presence of cracks is accounted for by the introduction of suitable Lagrange multipliers, which guarantee the deflection continuity at the crack locations. The static deformations, the transient behavior, and the modal properties are considered in the analysis. The stability of the mixed formulation is discussed, and the inf-sup condition is proved. In Section 4.3 we consider effects of cracks

opening and closing during the beam vibration period; i.e., we consider the transient analysis of a beam with breathing cracks. In Section 4.4 we report results of numerical experiments, and compare present results with those from other numerical methods, exact solutions and/or experimental findings. Indeed, we compare the finite element and meshless methods in the analysis of static deformations and in the estimation of the modal properties, and we compare the meshless method with the method proposed in Sundermeyer and Weaver (1995) for the analysis of the transient deformations of a beam with breathing cracks. For the sake of brevity, the approach is presented for a simply supported beam, although it has been found suitable also for other boundary conditions. A description of the GMLS approximation is found in Appendix A.2

4.2 Vibrations of a multiply cracked beam

4.2.1 Governing equations

A beam of length l, cross-sectional area $A = h \times b$, moment of inertia $I = bh^3/12$, Young's modulus E, mass density per unit volume ρ_V, and with n cracks located at points c_1,..., c_n is considered. The simplest way to account, with a reasonable accuracy, for effects of cracks on the dynamic properties of a slender beam is to represent cracks as lumped flexibility elements and to model the intact regions as Euler-Bernoulli beams. Therefore, following Gudmunson (1983), and Chondros and Dimarogonas (1998), cracks are modeled as n massless rotational springs whose stiffnesses are denoted by $k_1, \ldots, k_n$ As a consequence, we divide the beam into $n+1$ sub-intervals $\Omega_i = [c_{i-1}, c_i]$ ($c_0 \equiv 0$, and $c_{n+1} \equiv l$) of length l_i, introduce the $n+1$ local abscissas ξ_i, and consider $n+1$ deflection fields $w_i(\xi_i)$. Figure 4.1 exhibits the geometry of the cracked beam.

The vibrations of each undamaged beam segment are governed by

$$K_M w_i^{IV}(\xi_i, t) + \rho\, \ddot{w}_i(\xi_i, t) = p_i(\xi_i, t), \qquad \xi_i \in (0, l_i), \quad t > 0, \tag{4.1}$$

where the rotatory inertia has been neglected, $\rho = \rho_V A$ is the linear mass density, $K_M = EI$ is the bending stiffness, $p_i(\xi_i, t)$ is an applied distributed transverse load, and a superimposed dot means time derivative. The boundary conditions for the generic $i-th$ subinterval are

$$\begin{cases} w_i(l_i, t) = w_{i+1}(0, t), \quad w_i''(l_i, t) = w_{i+1}''(0, t), \\ w_i'''(l_i, t) = w_{i+1}'''(0, t), \quad w_i''(l_i, t) = -\dfrac{k_i}{K_M}\left(w_{i+1}'(0, t) - w_i'(l_i, t)\right) \end{cases}. \tag{4.2}$$

For the two boundary elements Ω_1 and Ω_{n+1} the following additional constraints are imposed:

$$\begin{cases} w_1(0,t) = 0, \quad w_1''(0,t) = 0, \\ w_{n+1}(l_{n+1},t) = 0, \quad w_{n+1}''(l_{n+1},t) = 0 \end{cases}. \tag{4.3}$$

Following Chondros and Dimarogonas (1998), values of the rotational spring constants k_i can be found from the section geometry, the crack depth a_i, and the material properties:

$$k_i = \frac{1}{\alpha_i}, \quad \alpha_i = \frac{6\pi(1-\nu^2)}{EI} I_c\left(\frac{a_i}{h}\right), \tag{4.4}$$

where ν is the Poisson ratio and

$$I_c(z) = 0.6272\,z^2 - 1.04533\,z^3 + 4.5948\,z^4 - 9.9736\,z^5 + 20.2948\,z^6 + \\ - 33.0251\,z^7 + 47.1063\,z^8 - 40.7556\,z^9 + 19.6\,z^{10}, \tag{4.5}$$

with z indicating severity of the i-th crack. This modeling technique provides reasonable results as long as cracks remain open during the vibration period. The crack opening and closing (breathing crack) introduce weak non-linearities in the beam motion, and modify natural frequencies of vibrations. In the following Section we analyze the effect of breathing cracks by a meshless method together with a classical time integration scheme.

4.2.2 Semi-discrete formulation

In order to derive a weak formulation of the aforementioned fourth-order problem suitable for numerical methods, we introduce the augmented Lagrangian that is a function of the deflection fields w_i in the undamaged beam segments, and the Lagrange multipliers λ_i:

$$L(w_1,...,w_{n+1},\lambda_0,...,\lambda_{n+1}) = \\ \frac{1}{2}\sum_{i=1}^{n+1}\int_0^{l_i}\left[\rho\,\ddot{w}_i^2 - K_M\left(w_i''\right)^2 + 2p_i w_i\right]\mathrm{d}\xi_i - \frac{1}{2}\sum_{i=1}^{n} k_i\left(w_{i+1}'(0) - w_i'(l_i)\right)^2 - \\ \sum_{i=1}^{n}\lambda_i\left(w_{i+1}(0) - w_i(l_i)\right) - \lambda_0 w_1(0) - \lambda_{n+1} w_{n+1}(l_{n+1}), \tag{4.6}$$

where we have omitted the dependence on time of the deflection fields, Lagrange multipliers and of the applied load. The Lagrange multipliers λ_0 and λ_{n+1} are used to impose the displacement boundary conditions at the ends, while the other Lagrange multipliers impose

the continuity of deflections at the crack locations. We emphasize that the proposed formulation leads to continuous deflections along the entire beam span. On the other hand, the continuity of the bending moments and of the shear forces at the crack locations are satisfied only approximately. By extremizing the Action on the set of isochronous motions we obtain

$$\sum_{i=1}^{n+1}\int_0^t\int_0^{l_i}\left[\rho\,\ddot{w}_i\,\delta w_i + K_M w_i''\delta w_i'' - p_i w_i\right]\mathrm{d}\xi_i\mathrm{d}t+$$
$$\sum_{i=1}^{n} k_i\left(w_{i+1}'(0) - w_i'(l_i)\right)\left(\delta w_{i+1}'(0) - \delta w_i'(l_i)\right)+$$
$$\int_0^t\left[\lambda_0\delta w_1(0) + \lambda_{n+1}\delta w_{n+1}(l_{n+1}) + \sum_{i=1}^{n}\lambda_i\left(\delta w_{i+1}(0) - \delta w_i(l_i)\right)\right]\mathrm{d}t+$$
$$\int_0^t\left[\delta\lambda_0 w_1(0) + \delta\lambda_{n+1}w_{n+1}(l_{n+1}) + \sum_{i=1}^{n}\delta\lambda_i\left(w_{i+1}(0) - w_i(l_i)\right)\right]\mathrm{d}t = 0. \quad (4.7)$$

Next, we consider $n+1$ distinct sets of scattered points $\mathcal{N}_i = \left\{\xi_{i_1},...,\xi_{i_{N_i}}\right\}$ with $\xi_{i_1} = 0$, $\xi_{i_{N_i}} = l_i = \xi_{(i+1)_1}$, for the subintervals Ω_i, and derive independently $n+1$ distinct set of basis functions $\psi_i(\xi_i)$ of the type (A.28). We denote with N the total number of nodes scattered on the entire beam, and we emphasize that at each crack location two overlapping nodes are placed. For convenience, these trial functions are derived by assuming for each subinterval the same order for the monomial basis functions in the GMLS approximation and the same form of the weight functions (A.29). Furthermore, we denote by R_{i_j} the radius of the support of the *j-th* weight function of the *i-th* subdomain. We consider test functions of the form:

$$\delta w_i = \psi_i^{\mathrm{T}}(\xi_i)\,\mu_i, \quad (4.8)$$

where μ_i is a $2N_i$-vector of arbitrary constants.

By substituting in (4.7) the GMLS approximation together with the considered test functions, and by accounting for the arbitrariness of the real constants μ_i's we obtain the following semi-discrete formulation

$$\begin{cases} \mathbf{M}\ddot{\hat{\mathbf{s}}} + \mathbf{K}\hat{\mathbf{s}} + \mathbf{\Lambda}\lambda = \mathbf{F} \\ \mathbf{\Lambda}^{\mathrm{T}}\hat{\mathbf{s}} = \mathbf{0} \end{cases}. \quad (4.9)$$

The generalized displacement vector is comprised of nodal displacements and rotations in all segments of the beam:

$$\hat{\mathbf{s}} = \left[\begin{array}{cccc} \hat{\mathbf{s}}_1 & \cdots & \hat{\mathbf{s}}_i & \cdots & \hat{\mathbf{s}}_{n+1} \end{array} \right]^{\mathrm{T}}. \tag{4.10}$$

The mass matrix $\mathbf{M}$ is a symmetric nonnegative definite block diagonal matrix

$$\mathbf{M} = \left[\begin{array}{cccc} \mathbf{m}_1 & \mathbf{0} & \cdots & \mathbf{0} \\ \mathbf{0} & \mathbf{m}_2 & \mathbf{0} & \cdots \\ \cdots & \mathbf{0} & \cdots & \cdots \\ \mathbf{0} & \cdots & \cdots & \mathbf{m}_{(n+1)} \end{array} \right], \tag{4.11}$$

with

$$\mathbf{m}_i = \rho \int_{\Omega_i} \psi_i \left(\psi_i\right)^{\mathrm{T}} \mathrm{d}\xi_i. \tag{4.12}$$

Therefore, the beam segments are inertially uncoupled by the lumped flexibilities appearing in the cracked beam model but are elastically coupled.

The symmetric nonnegative definite stiffness matrix can be decomposed as

$$\mathbf{K} = \mathbf{K}^0 + \sum_{i=1}^{n} \mathbf{K}_i^{spr}, \tag{4.13}$$

where the block-diagonal stiffness contribution $\mathbf{K}^0$ is obtained from the segments' stiffness matrices following the same procedure as that used for assembling of $\mathbf{M}$ from the segments' mass matrices:

$$\mathbf{K} = \left[\begin{array}{cccc} \mathbf{k}_1 & \mathbf{0} & \cdots & \mathbf{0} \\ \mathbf{0} & \mathbf{k}_2 & \mathbf{0} & \cdots \\ \cdots & \mathbf{0} & \cdots & \cdots \\ \mathbf{0} & \cdots & \cdots & \mathbf{k}_{(n+1)} \end{array} \right], \tag{4.14}$$

with

$$\mathbf{k}_i = K_M \int_{\Omega_i} \left(\psi_i\right)'' \left(\left(\psi_i\right)''\right)^{\mathrm{T}} \mathrm{d}\xi_i. \tag{4.15}$$

On the other hand, the contribution of the i-th crack to the beam stiffness $\mathbf{K}_i^{spr}$ has non-zero entries only in correspondence with the i-th and $(i+1)$-th beam segments, i.e.:

$$\mathbf{K}_i^{spr}=k_i \begin{bmatrix} \mathbf{0} & \cdots & \cdots & \cdots & \cdots & \mathbf{0} \\ \cdots & \cdots & \cdots & \cdots & \ldots & \cdots \\ \cdots & \cdots & \mathbf{A}_i & \mathbf{B}_i & \cdots & \cdots \\ \cdots & \cdots & \mathbf{B}_i^{\mathrm{T}} & \mathbf{C}_i & \cdots & \cdots \\ \cdots & \cdots & \cdots & \cdots & \cdots & \cdots \\ \mathbf{0} & \cdots & \cdots & \cdots & \cdots & \mathbf{0} \end{bmatrix}, \tag{4.16}$$

where matrices $\mathbf{A}_i$, $\mathbf{B}_i$ and $\mathbf{C}_i$ are given by

$$\begin{aligned} \mathbf{A}_i &= (\psi_i)'(l_i)\left((\psi_i)'(l_i)\right)^{\mathrm{T}}, \\ \mathbf{B}_i &= -(\psi_i)'(l_i)\left((\psi_{i+1})'(0)\right)^{\mathrm{T}}, \\ \mathbf{C}_i &= (\psi_{i+1})'(0)\left((\psi_{i+1})'(0)\right)^{\mathrm{T}}. \end{aligned} \tag{4.17}$$

The constraint matrix $\mathbf{\Lambda}$ is assembled by appending the column vectors

$$\mathbf{\Lambda} = \begin{bmatrix} \mathbf{\Lambda}_0 & \mathbf{\Lambda}_1 & \cdots & \mathbf{\Lambda}_i & \cdots & \mathbf{\Lambda}_n & \mathbf{\Lambda}_{n+1} \end{bmatrix}, \tag{4.18}$$

where

$$\mathbf{\Lambda}_0 = \begin{bmatrix} \mathbf{a}_0 \\ \mathbf{0} \\ \cdots \\ \mathbf{0} \end{bmatrix}, \quad \mathbf{\Lambda}_i = \begin{bmatrix} \mathbf{0} \\ \cdots \\ \mathbf{a}_i \\ \mathbf{b}_i \\ \mathbf{0} \\ \cdots \\ \mathbf{0} \end{bmatrix}, \quad \mathbf{\Lambda}_{n+1} = \begin{bmatrix} \mathbf{0} \\ \mathbf{0} \\ \cdots \\ \mathbf{b}_{n+1} \end{bmatrix}. \tag{4.19}$$

The column vectors with subscripts 0 and $n+1$ arise from the need to satisfy displacement boundary conditions, while the one with subscript i is due to the i-th crack. The subvectors are related to the test and the trial functions as

$$\mathbf{a}_0 = \psi_1(0), \qquad \mathbf{a}_i = -\psi_i(l_i), \qquad \mathbf{b}_i = \psi_{i+1}(0), \qquad \mathbf{b}_{n+1} = \psi_{n+1}(l_{n+1}). \tag{4.20}$$

Finally, the force vector $\mathbf{F}$ is given by

$$\mathbf{F} = \begin{bmatrix} \mathbf{f}_1 & \cdots & \mathbf{f}_i & \cdots & \mathbf{f}_{n+1} \end{bmatrix}^{\mathrm{T}}, \tag{4.21}$$

with

$$\mathbf{f}_i = \int_{\Omega_i} p_i \psi_i \mathrm{d}\xi_i. \tag{4.22}$$

4.2.3 Inf-sup test

In order to achieve a stable and optimal procedure for the MLPG method employing a set of Lagrange multipliers, the considered mixed formulation for static problems should satisfy the ellipticity condition (on the space of displacements fields satisfying the kinematic boundary conditions) and the inf-sup condition (see, e.g., Bathe (1996)). For this linear problem the ellipticity condition is readily satisfied, while additional effort is needed to provide criteria for satisfying the inf-sup condition, which reads:

$$\inf_{\lambda \in \mathbb{R}^{n+2}/0} \sup_{w^h \in W^h/0} \frac{\lambda_0 w_1^h(0) + \sum_{i=1}^{n} \lambda_i \left(w_{i+1}^h(0) - w_i^h(l_i) \right) + \lambda_{n+1} w_{n+1}^h(l_{n+1})}{\|\lambda\| \, \|w^h\|} \geq \beta > 0, \tag{4.23}$$

where β is a constant independent of the nodal locations, and $W^h \subset H^2(0, l_1) \times ... \times H^2(0, l_n)$ is the GMLS solution space. The norm of the approximate deflection field is defined by

$$\left\| w^h \right\|^2 = \sum_{i=1}^{n+1} \int_0^{l_i} \left[\left(w_i^h \right)^2 + l^2 \left(\left(w_i^h \right)' \right)^2 + l^4 \left(\left(w_i^h \right)'' \right)^2 \right] \mathrm{d}\xi_i, \tag{4.24}$$

while the norm of the vector of scalars λ is given by

$$\|\lambda\|^2 = \lambda^{\mathrm{T}} \lambda. \tag{4.25}$$

When these two conditions are satisfied, the stability of the MLPG formulation is guaranteed, and optimal error bounds are obtained for the chosen GMLS solution.

We show below that the inf-sup condition is satisfied when m, the order of the monomial basis in (A.20), is greater than 1. Indeed, in this case the GMLS approximation is able to exactly reproduce affine functions (see (A.21) when $\mathbf{a}(\bar{x})$ is a constant). Therefore, for a typical λ, we choose deflection fields of the form

$$\begin{cases} \bar{w}_i^h(\xi_i) = \lambda_{i-1} \left(1 - \dfrac{\xi_i}{l_i} \right), & i = 1, ..., n \\ \bar{w}_{n+1}^h(\xi_i) = \lambda_n + \dfrac{\lambda_{n+1} - \lambda_n}{l_{n+1}} \xi_{n+1} \end{cases}. \tag{4.26}$$

The norm of this deflection is easily computed as:

$$\left\|\bar{w}^h\right\|^2 = \sum_{i=1}^{n+1} \lambda_{i-1}^2 \left(\frac{l_i}{3} + \frac{l^2}{l_i}\right) + \lambda_{n+1}^2 \left(\frac{l_{n+1}}{3} + \frac{l^2}{l_{n+1}}\right) + \lambda_{n+1}\lambda_n \left(\frac{l_{n+1}}{3} - 2\frac{l^2}{l_{n+1}}\right). \tag{4.27}$$

Equation (4.27) may be alternatively rewritten in matrix notation as:

$$\left\|\bar{w}^h\right\|^2 = \lambda^{\mathrm{T}} \mathbf{S} \lambda, \tag{4.28}$$

where the $(n+2, n+2)$ matrix $\mathbf{S}$ defined by

$$\mathbf{S} = \begin{bmatrix} \left(\frac{l_1}{3} + \frac{l^2}{l_1}\right) & 0 & \cdots & \cdots & 0 \\ 0 & \left(\frac{l_2}{3} + \frac{l^2}{l_2}\right) & 0 & \cdots & 0 \\ \cdots & 0 & \cdots & \cdots & \cdots \\ 0 & 0 & 0 & \left(\frac{l_{n+1}}{3} + \frac{l^2}{l_{n+1}}\right) & \frac{1}{2}\left(\frac{l_{n+1}}{3} - 2\frac{l^2}{l_{n+1}}\right) \\ 0 & \cdots & \cdots & \frac{1}{2}\left(\frac{l_{n+1}}{3} - 2\frac{l^2}{l_{n+1}}\right) & \left(\frac{l_{n+1}}{3} + \frac{l^2}{l_{n+1}}\right) \end{bmatrix}, \tag{4.29}$$

appears. The eigenvalues $\sigma_1, ..., \sigma_{n+2}$ of $\mathbf{S}$ are:

$$\sigma_i = \left(\frac{l_i}{3} + \frac{l^2}{l_i}\right), \qquad i = 1, ..., n, \tag{4.30}$$

$$\sigma_{n+1} = \frac{l_{n+1}}{2}, \qquad \sigma_{n+2} = \frac{l_{n+1}}{6} + 2\frac{l^2}{l_{n+1}}. \tag{4.31}$$

Hence $\mathbf{S}$ is a positive definite matrix, and

$$\max \sigma_i \left\|\lambda\right\|^2 \geq \left\|\bar{w}^h\right\|^2 \geq \min \sigma_i \left\|\lambda\right\|^2. \tag{4.32}$$

By substituting (4.26) in the argument of the inf-sup we obtain

$$\frac{\lambda_0 \bar{w}_1^h(0) + \sum_{i=1}^{n} \lambda_i \left(\bar{w}_{i+1}^h(0) - \bar{w}_i^h(l_i)\right) + \lambda_{n+1} \bar{w}_{n+1}^h(l_{n+1})}{\left\|\lambda\right\| \left\|\bar{w}^h\right\|} = \frac{\left\|\lambda\right\|}{\sqrt{\lambda^{\mathrm{T}} \mathbf{S} \lambda}}. \tag{4.33}$$

Hence, we have

$$\sup_{w^h \in W^h/0} \frac{\lambda_0 w_1^h(0) + \sum_{i=1}^{n} \lambda_i \left(w_{i+1}^h(0) - w_i^h(l_i) \right) + \lambda_{n+1} w_{n+1}^h(l_{n+1})}{\|\lambda\| \, \|w^h\|} \geq \frac{\|\lambda\|}{\sqrt{\lambda^{\mathrm{T}} \mathbf{S} \lambda}} \tag{4.34}$$

with λ still a variable. Therefore, for the mixed GMLS approximation with $m > 1$ we have

$$\inf_{\lambda \in \mathbb{R}^{n+2}/0} \sup_{w^h \in W^h/0} \frac{\lambda_0 w_1^h(0) + \sum_{i=1}^{n} \lambda_i \left(w_{i+1}^h(0) - w_i^h(l_i) \right) + \lambda_{n+1} w_{n+1}^h(l_{n+1})}{\|\lambda\| \, \|w^h\|} \geq \inf_{\lambda \in \mathbb{R}^{n+2}/0} \frac{\|\lambda\|}{\sqrt{\lambda^{\mathrm{T}} \mathbf{S} \lambda}} = \frac{1}{\sqrt{\max \sigma_i}}, \tag{4.35}$$

and the inf-sup condition is satisfied.

4.2.4 Modal analysis

The natural frequencies and mode shapes of the undamaged beam are obtained by searching for solutions of the type

$$\hat{\mathbf{s}}(t) = \breve{\mathbf{s}} \exp(i\omega t), \quad \lambda(t) = \breve{\lambda} \exp(i\omega t), \tag{4.36}$$

of (4.9) and by discarding the applied loads. Therefore, the following eigenvalue problem arises:

$$\begin{cases} -\omega^2 \mathbf{M} \breve{\mathbf{s}} + \mathbf{K} \breve{\mathbf{s}} + \mathbf{\Lambda} \breve{\lambda} = \mathbf{0} \\ \mathbf{\Lambda}^{\mathrm{T}} \breve{\mathbf{s}} = \mathbf{0} \end{cases}. \tag{4.37}$$

The second equation in (4.37) provides $2 + n$ constraints on the mode shapes $\breve{\mathbf{s}}$.We modify the eigenvalue problem (4.37) so that the imposed constraints are automatically satisfied.

Let us consider the *null space* of $\mathbf{\Lambda}^{\mathrm{T}}$, denoted by $\ker \mathbf{\Lambda}^{\mathrm{T}}$. When the inf-sup condition is satisfied the dimension of the kernel of $\mathbf{\Lambda}^{\mathrm{T}}$ is

$$\dim \ker \mathbf{\Lambda}^{\mathrm{T}} = (2N - 2 - n), \tag{4.38}$$

since $2 + n$ Lagrange multipliers appear in this formulation and the system is solvable (see, e.g., Bathe (1996) for a discussion of the relations between solvability and stability conditions). Next, we introduce the matrix $\mathbf{Y}$ whose columns constitute a basis for $\ker \mathbf{\Lambda}^{\mathrm{T}}$,

the dimensions of $\mathbf{Y}$ are $(2N \times (2N-2-n))$. By using the rectangular matrix $\mathbf{Y}$ we can express the generic modal shape $\breve{\mathbf{s}}$ in terms of the reduced $(2N-2)$-dimensional vector $\mathbf{x}$ by

$$\breve{\mathbf{s}} = \mathbf{Y}\mathbf{x}, \tag{4.39}$$

and automatically satisfy the second equation in (4.37).

Premultiplying the first equation in (4.37) by $\mathbf{Y}^{\mathrm{T}}$ and by taking into account (4.39) we obtain the reduced system

$$-\omega^2 \mathbf{M}^* \mathbf{x} + \mathbf{K}^* \mathbf{x} = \mathbf{0}, \tag{4.40}$$

where

$$\mathbf{M}^* = \mathbf{Y}^{\mathrm{T}}\mathbf{M}\mathbf{Y}, \ \mathbf{K}^* = \mathbf{Y}^{\mathrm{T}}\mathbf{K}\mathbf{Y}. \tag{4.41}$$

Next, we solve for $\mathbf{x}$, and obtain the complete vector of unknowns using (4.39). We note that the kinematical boundary conditions are satisfied by the introduction of Lagrange multipliers, while the natural boundary conditions are satisfied only in the weak sense. Furthermore we can always assume that

$$\mathbf{Y}^{\mathrm{T}}\mathbf{Y} = \mathbf{1}, \tag{4.42}$$

by choosing orthonormal basis for the null space of $\mathbf{\Lambda}^{\mathrm{T}}$. We note that the mass and the stiffness matrices of the reduced system are symmetric and positive definite.

4.2.5 Free motion

We integrate the differential equations of motion (4.9) with initial conditions

$$\begin{cases} \hat{\mathbf{s}}\,(0) = \hat{\mathbf{s}}_0 \\ \dot{\hat{\mathbf{s}}}\,(0) = \dot{\hat{\mathbf{s}}}_0 \end{cases} \tag{4.43}$$

satisfying the boundary conditions

$$\mathbf{\Lambda}^{\mathrm{T}}\hat{\mathbf{s}}_0 = \mathbf{0}, \quad \mathbf{\Lambda}^{\mathrm{T}}\dot{\hat{\mathbf{s}}}_0 = \mathbf{0}, \tag{4.44}$$

and vanishing external load, by applying the Newmark family of methods (see, e.g., Hughes (2001)) to the reduced system

$$\mathbf{M}^* \ddot{\mathbf{x}} + \mathbf{K}^* \mathbf{x} = \mathbf{0}, \tag{4.45}$$

with initial conditions:

$$\begin{cases} \mathbf{x}(0) = \mathbf{Y}^{\mathrm{T}} \hat{\mathbf{s}}_0 \\ \dot{\mathbf{x}}(0) = \mathbf{Y}^{\mathrm{T}} \dot{\hat{\mathbf{s}}}_0 \end{cases}. \tag{4.46}$$

This family of algorithms consists of the following recursive relations:

$$\begin{cases} \mathbf{M}^* \mathbf{a}_{n+1} + \mathbf{K}^* \mathbf{x}_{n+1} = \mathbf{0}, \\ \mathbf{x}_{n+1} = \mathbf{x}_n + \Delta t \mathbf{v}_n + \dfrac{\Delta t^2}{2} \left[(1 - 2\beta) \mathbf{a}_n + 2\beta \mathbf{a}_{n+1} \right], \\ \mathbf{v}_{n+1} = \mathbf{v}_n + \Delta t \left[(1 - \gamma) \mathbf{a}_n + \gamma \mathbf{a}_{n+1} \right], \end{cases} \tag{4.47}$$

where $\mathbf{a}_n$, $\mathbf{v}_n$ and $\mathbf{x}_n$ are approximations of $\ddot{\mathbf{x}}(t_n)$, $\dot{\mathbf{x}}(t_n)$ and $\mathbf{x}(t_n)$ respectively, Δt is the time step, and β and γ are parameters.

4.3 Effects of crack opening and closing

During the vibration period of a cracked beam, the n cracks will open and close in time depending on the vibration amplitude. In order to model the effects of the cracks opening and closing, we consider a bilinear behavior of each crack. When the i-th crack is open, the i-th and $(i+1)$-th beam segments are elastically coupled by the rotational spring k_i (see the continuity conditions (4.2). On the other hand, when the i-th crack is closed, the i-th and $(i+1)$-th beam segments are rigidly connected, and the boundary conditions become

$$\begin{array}{ll} w_i(l_i, t) = w_{i+1}(0, t), & w_i''(l_i, t) = w_{i+1}''(0, t), \\ w_i'''(l_i, t) = w_{i+1}'''(0, t), & w_i'(l_i, t) = w_{i+1}'(0, t). \end{array} \tag{4.48}$$

The i-th single edge crack is assumed to be open or closed depending on the sign of the curvature $w_{i+1}''(0, t)$:

- if the crack is on the upper beam surface, the crack is open when the curvature is negative and vice-versa,
- if the crack is on the bottom beam surface, the crack is open when the curvature is positive and vice-versa.

When the i-th crack is closed the augmented Lagrangian (4.6) needs to be modified by removing the strain energy contribution from the spring k_i, and by introducing an additional Lagrange multiplier ζ_i to enforce the continuity of rotations at the crack location. Therefore, the equations of motion of the cracked beam are

$$\begin{aligned} &\mathbf{M}\ddot{\hat{\mathbf{s}}} + \mathbf{K}^0\hat{\mathbf{s}} + \sum_{i=1}^{n} \delta_i \mathbf{K}_i^{spr}\hat{\mathbf{s}} + \mathbf{\Lambda}\lambda + \sum_{i=1}^{n} (1-\delta_i)\,\mathbf{\Upsilon}_i\zeta_i = \mathbf{0}, \\ &\mathbf{\Lambda}^{\mathrm{T}}\hat{\mathbf{s}} = \mathbf{0}, \\ &(1-\delta_i)\,\mathbf{\Upsilon}_i^{\mathrm{T}}\hat{\mathbf{s}} = \mathbf{0}, \qquad i = 1, \ldots n, \end{aligned} \tag{4.49}$$

where δ_i is equal to 1 or 0 if the i-th crack is open or closed. The new vector $\mathbf{\Upsilon}_i$ is given by

$$\mathbf{\Upsilon}_i = \left[\begin{array}{ccccccc} \mathbf{0} & \cdots & \mathbf{c}_i & \mathbf{d}_i & \mathbf{0} & \cdots & \mathbf{0} \end{array} \right]^{\mathrm{T}}, \tag{4.50}$$

where the subvectors are decomposed by:

$$\mathbf{c}_i = -\left(\psi_i\right)'(l_i)\,, \qquad \mathbf{d}_i = \left(\psi_i\right)'(0)\,. \tag{4.51}$$

If q cracks are closed, the number of Lagrange multipliers is $2+n+q$, and the third set of equations in (4.49) consists of q equations.

The instantaneous values of the δ's depend on the sign of curvature at the crack locations. The aforestated weak formulation does not guarantee continuity of the curvature along the beam span. Therefore, the generic δ_i can be estimated either from the average curvature at the i-th crack location, or from the curvature of any of the two segments.

Vibration cycle is referred to as the time interval between two consecutive sign changes in the curvature at any crack location; the so-called transition time separates two consecutive vibration cycles. During each vibration cycle, labelled by the index τ, the time integration of the non-linear equations of motion can be performed by applying the Newmark family of methods to the reduced equations during the τ-th cycle:

$$\mathbf{M}_\tau^* \ddot{\mathbf{x}}_\tau(t) + \mathbf{K}_\tau^* \mathbf{x}_\tau(t) = \mathbf{0}. \tag{4.52}$$

The set (4.52) of linear ordinary differential equations with constant coefficients has been obtained with the same procedure as that used for open cracks, provided that the actual constraints are accounted for during the current vibration cycle τ. Numerical integration gives estimates of transition times only within the accuracy of the time step Δt. If a transition occurs in between the J and $J+1$ integration steps, which separate the vibration cycles τ

and $\tau+1$, then the the initial conditions for the $\tau+1$ vibration cycle can be derived as follows:

$$\begin{cases} \mathbf{x}_{\tau+1}\left(t_{J+1}\right) = {\mathbf{Y}_{\tau+1}}^{\mathrm{T}}\mathbf{Y}_{\tau}\mathbf{x}_{\tau}\left(t_{J+1}\right) \\ \mathbf{v}_{\tau+1}\left(t_{J+1}\right) = {\mathbf{Y}_{\tau+1}}^{\mathrm{T}}\mathbf{Y}_{\tau}\mathbf{v}_{\tau}\left(t_{J+1}\right) \end{cases}, \tag{4.53}$$

where columns of the matrix $\mathbf{Y}_{\tau}$ constitute an orthonormal basis for $\ker \mathbf{\Lambda}_{\tau}^{\mathrm{T}}$. The left-hand side of (4.53) are the projection of the solution $\mathbf{x}_{\tau}$ and $\mathbf{v}_{\tau}$ on the basis of the solution at the subsequent cycle $\mathbf{x}_{\tau+1}$ and $\mathbf{v}_{\tau+1}$.

4.4 Computation and discussion of results

For investigating the characteristics of the proposed method, several tests are performed on the sample problem of a simply supported beam with a single crack located at the mid-span.

When the beam is subjected to a constant distributed load p, the static deflection is

$$\begin{cases} w_1\left(\xi_1\right) = \dfrac{pl^2\left(2k_1 l + 3K_M\right)}{48K_M k_1}\xi_1 - \dfrac{pl}{12K_M}\xi_1^3 + \dfrac{p}{24K_M}\xi_1^4 \\ w_2\left(\xi_2\right) = \dfrac{pl^3\left(5k_1 l + 12K_M\right)}{384K_M k_1} - \dfrac{pl^2}{16k_1}\xi_2 - \dfrac{pl^2}{16K_M}\xi_2^2 + \dfrac{p}{24K_M}\xi_2^4 \end{cases}. \tag{4.54}$$

The exact modal properties of a beam with one open crack are given in Sundermeyer and Weaver (1995). The odd natural frequencies are roots of the trascendental characteristic equation:

$$\frac{-4k_1}{K_M}\cos\left(\frac{l\beta}{2}\right) + \beta\left(\sin\left(\frac{l\beta}{2}\right) - \cos\left(\frac{l\beta}{2}\right)\tanh\left(\frac{l\beta}{2}\right)\right) = 0, \tag{4.55}$$

while the even ones are

$$\beta = \frac{r\pi}{l}, \quad r = 2, 4, 6, ... \tag{4.56}$$

The odd mode shapes are

$$\begin{aligned} &w_1\left(\xi_1\right) = A\left[\sin\left(\beta\xi_1\right) + \alpha\sinh\left(\beta\xi_1\right)\right], \\ &w_2\left(\xi_2\right) = A\left[\sin\left(\beta\left(\frac{l}{2} - \xi_2\right)\right) + \alpha\sinh\left(\beta\left(\frac{l}{2} - \xi_2\right)\right)\right], \qquad \alpha = \frac{\cos\left(\dfrac{l\beta}{2}\right)}{\cosh\left(\dfrac{l\beta}{2}\right)}, \end{aligned} \tag{4.57}$$

while the even ones are

$$\begin{cases} w_1(\xi_1) = A\sin(\beta\xi_1) \\ w_2(\xi_2) = A\sin(\beta(\xi_2 - l/2)) \end{cases}. \tag{4.58}$$

The constant A is chosen by ensuring that

$$\int_0^{l/2} (w_1(\xi_1))^2 \, \mathrm{d}\xi_1 + \int_0^{l/2} (w_2(\xi_2))^2 \, \mathrm{d}\xi_2 = 1. \tag{4.59}$$

The GMLS basis functions are generated by complete monomials of degree 2 ($m = 3$). This choice is motivated by the need of satisfying the inf-sup condition, guaranteeing an accurate GMLS reconstruction, and of reducing the computational time. For $m = 3$ the GMLS trial functions require the inversion of a 3×3 matrix, which can be done analytically once for all. Every beam segment is discretized with the same number of nodes $N_1 = N_2$, and the nodal spacing is uniform. The radius of support of each weight function is the same and equals $sl_1/(N_1 - 1) = sl_2/(N_2 - 1)$, where s is the ratio between the weight function radius and the distance between two adjacent nodes. In order to achieve smooth approximate solutions, the power α in (A.29) is set equal to 5. Increasing the order of differentiability of the weight functions does not lead to additional computational effort, therefore it is generally advisable to exploit high values of α. The numerical integrations needed for computing the stiffness matrix, the mass matrix, and the load vector are performed using the non-element local technique described in Atluri, Cho and Kim (1999) with 10 quadrature points in each subregion of intersection of sub-domains.

We compare the MLPG results with those obtained from the traditional Finite Element method (FEM), which may be directly derived upon replacing the GMLS approximation with the Hermitian interpolation function (see, e.g., Hughes (2001)) in the stiffness matrix, in the mass matrix, and in the force vector. We emphasize that within the FEM there is no need to use a mixed formulation based on the introduction of Lagrange multipliers for prescribing the boundary and the interface conditions. The trial functions of the FEM possess the Kronecker Delta property and the constraints are simply imposed by eliminating from the stiffness matrix, the mass matrix, and the force vector the entries corresponding to constrained nodes.

We analyze deformations of an aluminum beam with following values of material and geometric parameters:

$$\begin{aligned} E = 72\,Gpa, \quad \rho_V = 2800\,kg/m^3, \quad \nu = 0.35, \quad l = 235\,mm, \\ h = 23\,mm, \quad b = 7\,mm, \quad a_1 = 0.4h. \end{aligned} \tag{4.60}$$

Experiments on this beam, with different crack severities are reported in Chondros and Dimarogonas (1998), Chondros and Dimarogonas (2001), and Chondros (2001).

4.4.1 Convergence analysis

Convergence tests are performed for both the analysis of static deformations, and modal properties with $s = 4.7$. To observe the convergence, three relative error norms are used. They are defined below, where the superscript h indicates the numerical solution (MLPG or FE) and the superscript *exact* refers to the analytical solution.

- Relative L_2 error norm:

$$\frac{\sqrt{\sum_{i=1}^{2}\int_0^{l_i}\left(w_i^h - w_i^{exact}\right)^2 \mathrm{d}\xi_i}}{\sqrt{\sum_{i=1}^{2}\int_0^{l_i}\left(w_i^{exact}\right)^2 \mathrm{d}\xi_i}}, \tag{4.61}$$

- Relative H_1 error norm:

$$\frac{\sqrt{\sum_{i=1}^{2}\int_0^{l_i}\left[\left(w_i^h - w_i^{exact}\right)^2 + l^2\left(\left(w_i^h\right)' - \left(w_i^{exact}\right)'\right)^2\right]\mathrm{d}\xi_i}}{\sqrt{\sum_{i=1}^{2}\int_0^{l_i}\left[(w_i^{exact})^2 + l^2\left((w_i^{exact})'\right)^2\right]\mathrm{d}\xi_i}}, \tag{4.62}$$

- Relative H_2 error norm:

$$\frac{\sqrt{\sum_{i=1}^{2}\int_0^{l_i}\left[\left(w_i^h - w_i^{exact}\right)^2 + l^2\left(\left(w_i^h\right)' - \left(w_i^{exact}\right)'\right)^2 + l^4\left(\left(w_i^h\right)'' - \left(w_i^{exact}\right)''\right)^2\right]\mathrm{d}\xi_i}}{\sqrt{\sum_{i=1}^{2}\int_0^{l_i}\left[(w_i^{exact})^2 + l^2\left((w_i^{exact})'\right)^2 + l^4\left((w_i^{exact})''\right)^2\right]\mathrm{d}\xi_i}}, \tag{4.63}$$

In Figure 4.2, we report for static deformations of a beam loaded by a uniformly distributed load on the top surface the error norms for solutions computed with the FE and the meshless methods. The results show that the convergence rates of L_2, H_1 and H_2 error norms for

the two methods are almost the same and approximately equal 4, 3 and 2 respectively. In general, the error of the MLPG solution is lower than that of the FE solution.

Figure 4.3 shows the relative errors in the resonance frequencies of the three lowest vibration modes. Also in this case, the convergence rates for the two methods are almost the same and approximately equal 4. Nevertheless, it may be seen that the magnitude of the error obtained with the meshless approach is less than that with the FEM.

Figures 4.4, 4.5 and 4.6 show, respectively, the convergence rates of L_2, H_1 and H_2 error norms for the three lowest modes computed with the two numerical methods. The results show that, also in this case, the convergence rates of L_2, H_1 and H_2 error norms for the two methods are almost the same and approximately equal 4, 3 and 2 respectively. The magnitude of the error in the highest modes achieved with the MLPG method is still lower than that obtained with the FEM.

4.4.2 Variations of weight functions radii

From the above analysis, it is evident that when increasing the number of nodes the MLPG method tends to reach a stable convergence rate similar to the FEM. On the other hand when only a few nodes are employed non monotonic behaviors are exhibited and the MLPG solution is more accurate than the FE solution (see, e.g., Figure 4.3). This is due to the fact that for coarse grids the local feature of the MLPG method is lost and each node is affecting almost all nodes, increasing the computational time for evaluating every matrix entry but also considerably improving the accuracy of the GMLS reconstruction capability.

Here we investigate the behavior of the MLPG solution when the number of nodes in each segment is kept constant (4 nodes per segment) while the radius of the weight functions is increased until each node is affecting all the other ones ($1.5 \leq s \leq 4$).

Figure 4.7 shows the error in the static deflection computed with the MLPG and the FE methods. It is clear that increasing the radius of the weight functions leads to a significant improvement of the MLPG solution. Indeed, for $s \leq 3$ the FE solution is more accurate than the MLPG one, but when $s > 3$ the situation is completely reversed and the MLPG method gives significantly less errors than the FEM.

Figure 4.8 shows the four lowest natural frequencies computed with the MLPG and the FE methods. Also in this case, an increase in the weight functions radii leads to a great improvement. Whereas, the error in the first natural frequency monotonically decreases with an increase in the parameter s, the errors in other frequencies do not decrease monotonically; however, they are always much lower (about 100 times) than those for the FE solution.

In Figure 4.9 we report the exact ratio of the first natural frequency of the intact beam to that

of the cracked beam for different values of the crack depth a (solid line) and its approximation by using the $4+4$ nodes configuration with $s=3$. The open circles indicate experimental values from either Chondros and Dimarogonas (1998) or Chondros (2001). It is clear that the computed values agree very well with the analytical ones; however, the two differ somewhat from the experimental values. This may be due to an inaccurate mathematical model or to unrefined experimental measurements. Nevertheless, the experimental program aimed at validating the lumped flexibility conducted first in Gudmunson (1983) on cracked cantilever beams validates the mathematical model and suggests that the discrepancies are due to experimental errors. A possible source of errors is the realization of the hinges for the vibration testing of the simply supported beam. Indeed, from the experimental viewpoint, the realization of hinges represents a much more challenging problem than fixing the edges. Furthermore, while the quoted experimental tests of Gudmunson (1983) were conducted on beams cracked by saw-cuts, those of Chondros and Dimarogonas (1998), and of Chondros (2001) refer to fatigue cracks. It is well known that the controlled introduction of fatigue cracks involves several experimental difficulties not encountered in the saw cut method.

4.4.3 Transient analysis for a breathing crack

Here, we analyze free vibrations of the cracked beam when the crack is assumed to breath. We assume that the crack is located on the lower surface of the beam, the beam is initially undeformed and is excited according to the first mechanical mode shape of the intact beam. The nonlinearity introduced by the bilinear behavior of the breathing crack does not allow for a simple analytical solution of the transient problem.

Accordingly, we compare our results with those obtained by the algorithm of Sundermeyer and Weaver (1995). The technique in Sundermeyer and Weaver (1995) relies on the *a priori* knowledge of the mode shapes of the intact beam and of the beam with the open crack, and consists of consecutive calculations of the beam mode amplitudes. At each vibration cycle the deflection is expressed in terms of a finite number of mode shapes: if the crack is closed the modal shapes of the intact beam are used, otherwise the mode shapes of the cracked beam in (4.57) and (4.58) are used. The transition times between the two crack states are determined by continuously monitoring the sign of the curvature at the crack location. The initial conditions for free oscillations at each vibration cycle are determined by simply converting the sets of natural coordinates at the transition times. We note that at the instants of crack opening and closing, several concomitant mode shapes may arise since the mode shapes of the intact and the cracked beam are in general not orthogonal.

The numerical integration of governing equations (4.52) is performed by using the $4+4$ nodes configurations described in the previous subsection with $s=3$ and the damped un-

conditionally stable Newmark integration scheme (see, e.g., Hughes (2001)) with

$$\beta = 0.3025, \quad \gamma = 0.6, \quad \Delta t = 1.04\,\mu s. \tag{4.64}$$

This choice of parameters introduces a small numerical damping, which rapidly damps out undesired oscillations at the transition instants. The transition times are computed by continuously monitoring the average curvature at the crack location: i.e., the average of the curvatures of the two beam segments at the crack location.

In Figure 4.10 we compare the time evolution of the deflections at the crack station computed with the proposed technique and that presented in Sundermeyer and Weaver (1995) with 25 mode shapes. Figure 4.11 compares the time history of the relative rotation at the crack station computed with the two methods. It is evident that the solution with the MLPG method agrees very well with that given in Sundermeyer and Weaver (1995).

4.4.4 Remarks

As is rather well known, Euler's beam theory simulates well deformations of a thin beam. For a thick beam one should employ either the Timoshenko beam theory or a higher-order shear and normal deformable beam theory such as that proposed by Batra and Vidoli (2002). Qian, Batra and Chen (2003a,b; 2004a,b), and Qian and Batra (2004, 2005) have studied by the MLPG method static and dynamic deformations of both homogeneous and functionally graded isotropic thick plates, and have compared the performance of the MLPG1 and the MLPG6 formulations. For a thick beam one will very likely need to modify the expression for the rotational spring constants k_i in (4.2).

We have considered cracks aligned along the depth of the beam which is appropriate for a thin beam. For cracks either parallel or inclined to the longitudinal centroidal axis of the beam, one will need to modify the problem formulation. Ching and Batra (2001), and Batra and Ching (2002) have applied the MLPG method to determine crack-tip fields in a pre-cracked plate deformed either statically or dynamically.

Even though the CPU time required to compute an element of the stiffness matrix in the MLPG6 formulation adopted here has been rather large as compared to that in the FEM, Atluri, Han and Rajendran (2004) have shown that it is not so in their mixed MLPG formulation in which both displacements and strains are interpolated with the MLS basis functions.

4.5 Conclusions

We have used the MLPG method to study vibrations of a cracked beam. When studying dynamic problems for cracked beams the penalty method does not seem to be adequate since it leads to ill-conditioned problems. Therefore, the treatment of vibrations of cracked beams necessitates the use of Lagrange multipliers to account for the relative rotation at the crack locations and satisfy the kinematic boundary. The accurate estimation of the relative rotation at the crack locations is crucial for the identification process based on mode shapes (see, e.g., Rizos, Aspragathos and Dimarogonas (1988)) and for the transient analysis of a breathing crack (see, e.g., Sundermeyer and Weaver (1995)).

The stability of the method is assessed by analytically proving the inf-sup condition. The MLPG method is initially applied to compute the modal characteristics (both frequencies and mode shapes), and to analyze the transient and static deformations of beams with multiple open cracks. The derivation of reduced systems, where the imposed constraints are automatically satisfied, has been presented. It is also extended to treat the effects of breathing cracks on the dynamics of a cracked beam. Each crack is modeled as a bilinear spring with spring constant changing according to the value of the beam curvature at the crack location. Computational details for the derivation of the initial conditions at each vibration cycle have been provided. The numerical time integration is performed by the use of the Newmark family of methods, and the spatial integration in the MLPG formulation employs Gaussian quadrature.

Numerical results for a simply supported beam are presented and compared with those obtained from analytical, FE and semi-analytical methods. In particular, results of the MLPG method are compared with those of the FEM for both the static and the beam modal analysis. The convergence rates of the MLPG formulation are similar to those of the FEM, but for a fixed number of degrees of freedom the MLPG results are generally more accurate than the FE ones. Furthermore, the accuracy of the MLPG method may be controlled by modifying the supports of the weight function used in the GMLS approximation. It is shown that with few nodes and very large supports extremely accurate estimates of both the static deformations and the modal properties may be achieved. This represents a very favorable feature of the MLPG method with respect to the FEM. When comparing the computational time of the MLPG method with the computational time of the FEM for a fixed number of nodes the FEM clearly wins but, when the accuracy is also considered the comparison is not so bad. Indeed, very few nodes in the MLPG method may be satisfactory for highly accurate numerical solutions valid over wide frequency ranges. The possibility of using a reduced number of degrees of freedom is desirable when analyzing transient deformations with breathing cracks. Indeed, the use of small stiffness and mass matrices greatly alleviates

the computational time when solving these non-linear transient problems. The MLPG predictions are in very good agreement with those of the method of Sundermeyer and Weaver (1995), which is based on the exact knowledge of the cracked beam mode shapes and is difficult to extend to more complicated structures, such as cracked frames. Furthermore, the possibility of retaining reduced order numerical models may be crucial in identification or optimization processes when algorithms should be built based on the number of degrees of freedom.

The present implementation of MLPG method represents an interesting alternative to the classical FEM for the analysis of cracked beams (see Table 4.1 for a summary of comparison between the two methods).

	MLPG	**FEM**
Weak formulation	Local	Global
Information needed about the nodes	Locations only	Locations and connectivity
Subdomains	Not necessarily disjoint	Disjoint
Trial functions	Relatively complex and difficult to express (GMLS) but easy to generate as closed-form expressions	Hermite polynomials
Integration rule	Higher order	Lower order
Mass matrix	Symmetric, banded, positive definite	Symmetric, banded, positive definite
Stiffness matrix	Symmetric, banded, positive definite	Symmetric, banded, positive definite
Assembly of equations	Required only for connecting different intact segments	Required
Stresses and strains	Smooth everywhere in the intact segments	Good at integration points
Addition of nodes	Easy	Difficult
Determination of time step size for stability in transient analysis	Relatively easy	Relatively easy
Imposition of essential boundary conditions	Lagrange multipliers are needed (reduced effort)	Simple rows, columns deletions are needed
CPU time for computing a single matrix entry	Considerable	Little
Number of nodes required for high accuracy	Few	High
CPU time for a prescribed accuracy on the modal properties or on the static deformations	Moderate	Moderate

Table 4.1: Comparison of the MLPG method and the FEM for vibrations of a cracked beam.

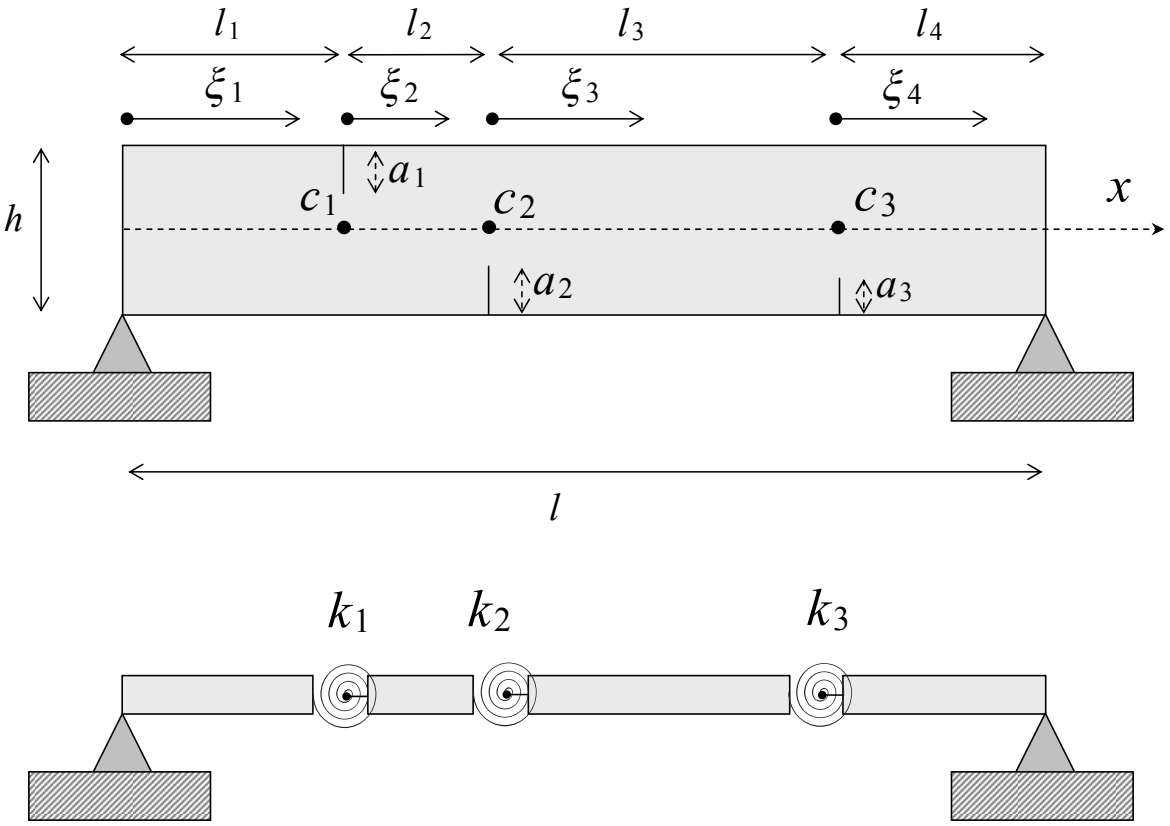

Figure 4.1: Sketch of a cracked beam and of its lumped flexibility model.

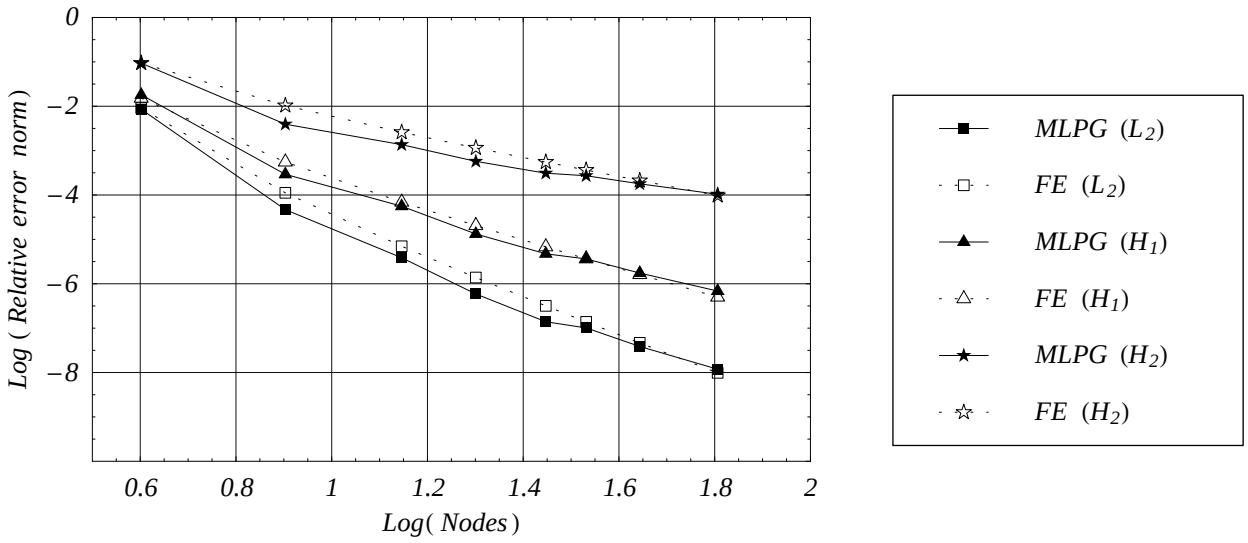

Figure 4.2: For a uniformly loaded beam, convergence of the error norms with a decrease in the nodal spacing or an increase in the number of uniformly distributed nodes.

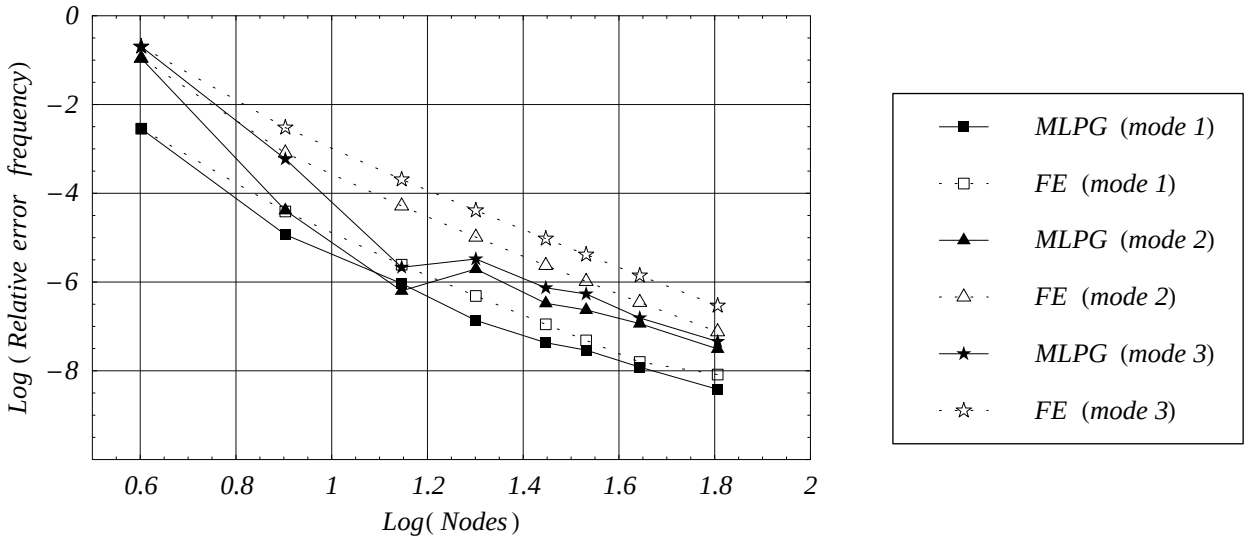

Figure 4.3: Convergence rates of the first three natural frequencies.

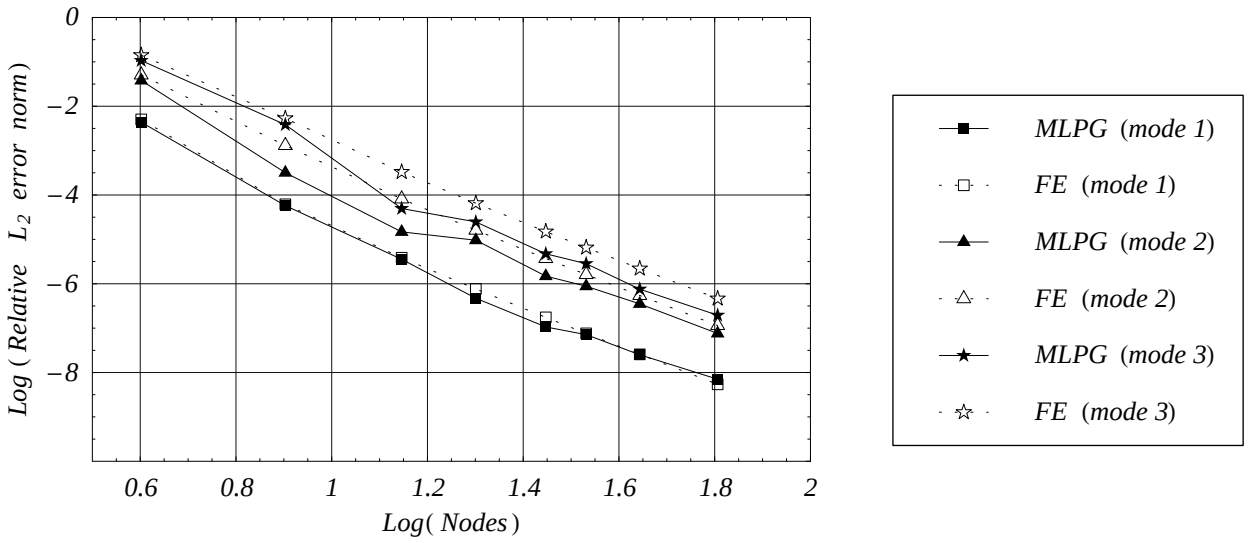

Figure 4.4: Convergence rates of the three lowest modes in L_2 norm.

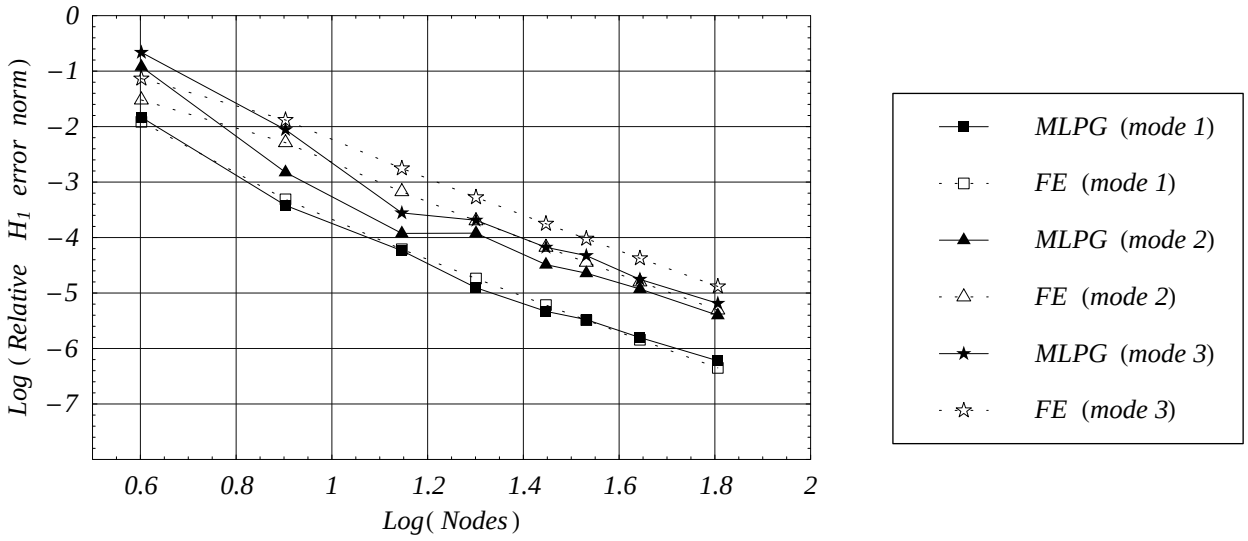

Figure 4.5: Convergence rates of the three lowest modes in H_1 norm.

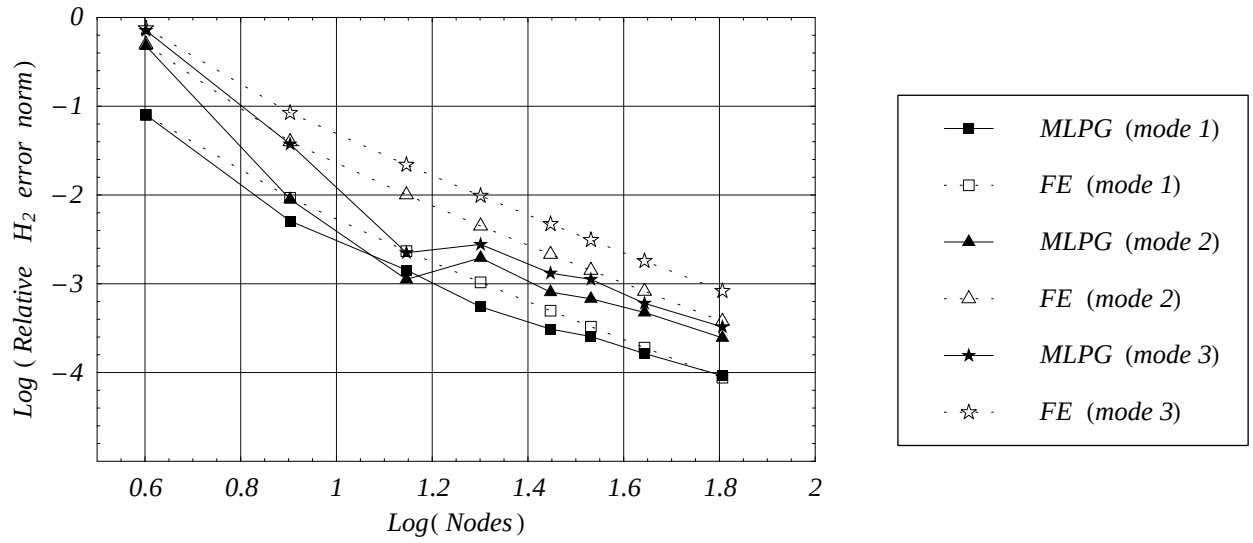

Figure 4.6: Convergence rates of the three lowest modes in H_2 norm.

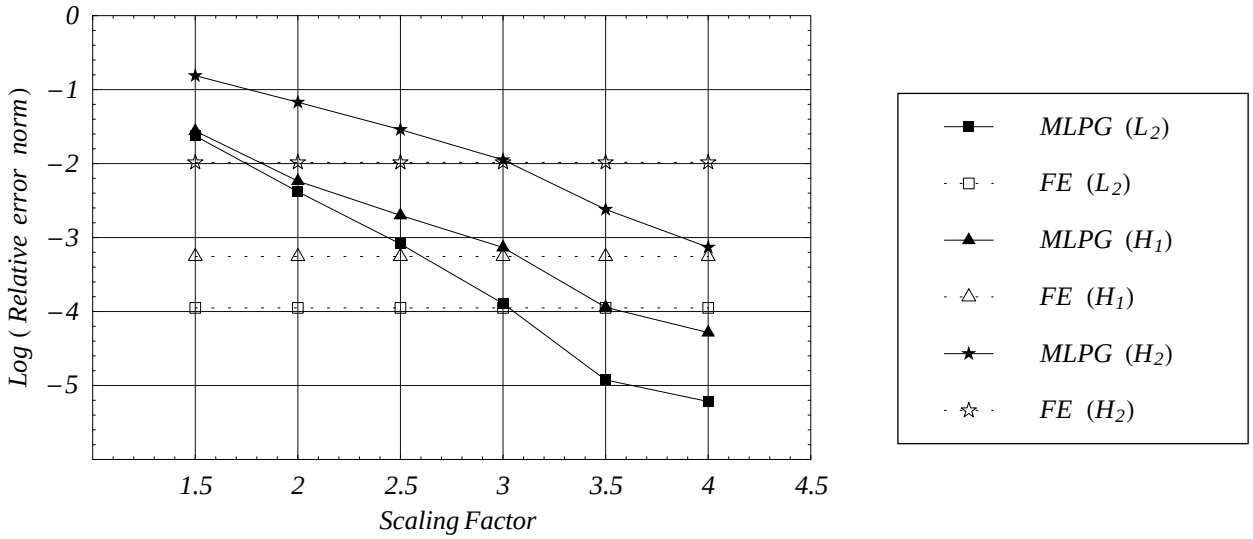

Figure 4.7: For uniform loading and for $4 + 4$ nodes, convergence with the weight functions radii.

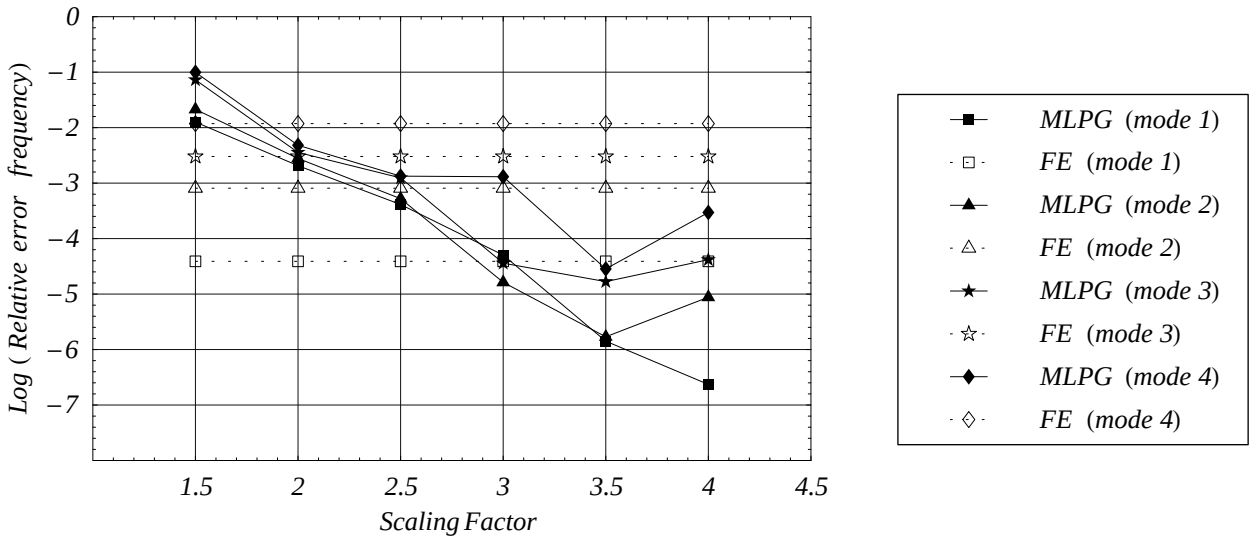

Figure 4.8: Dependence of the relative error of the four lowest resonance frequencies for $4+4$ nodes upon the weight functions radii.

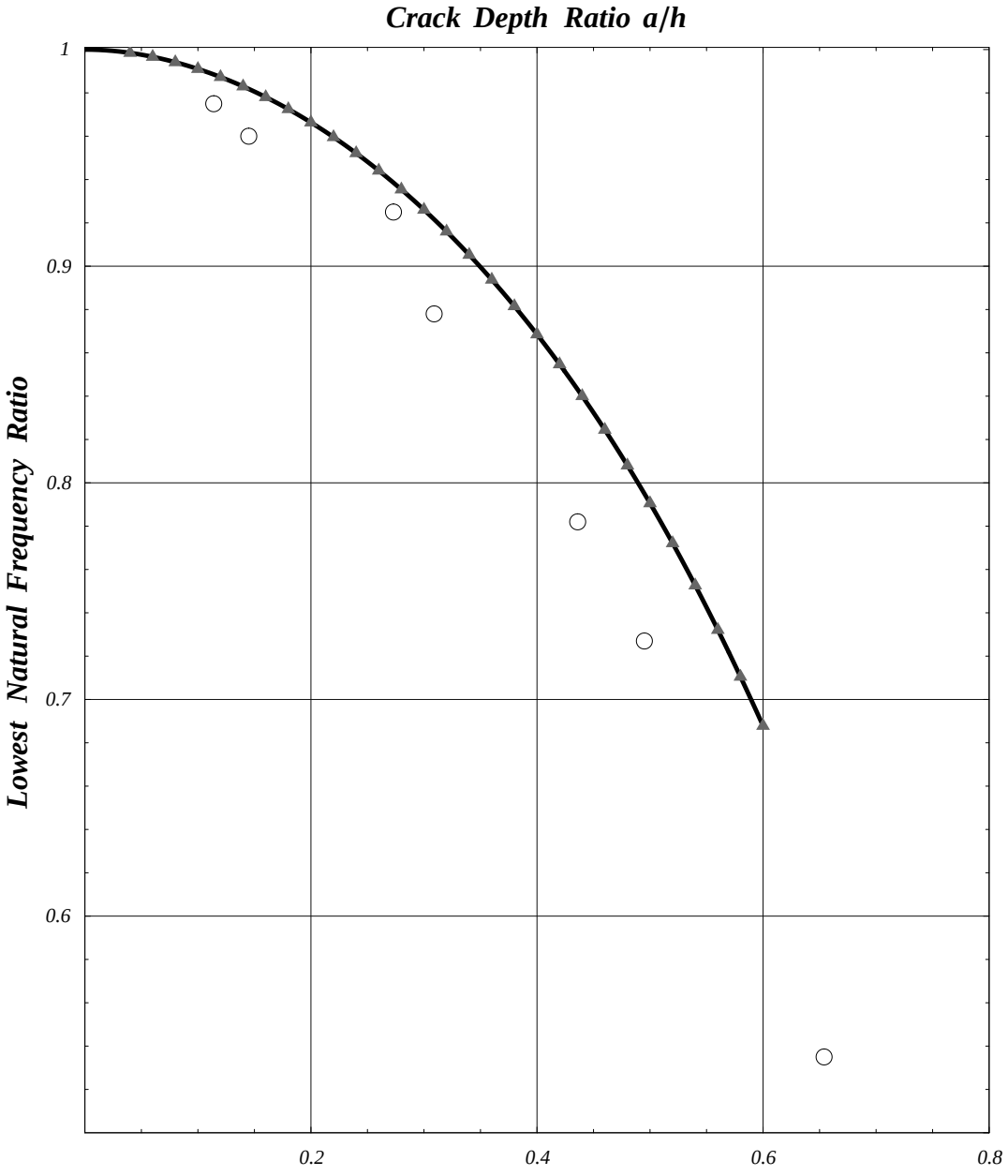

Figure 4.9: Exact (solid), approximate (triangles) and experimental (circles) lowest frequency ratio with different crack severities.

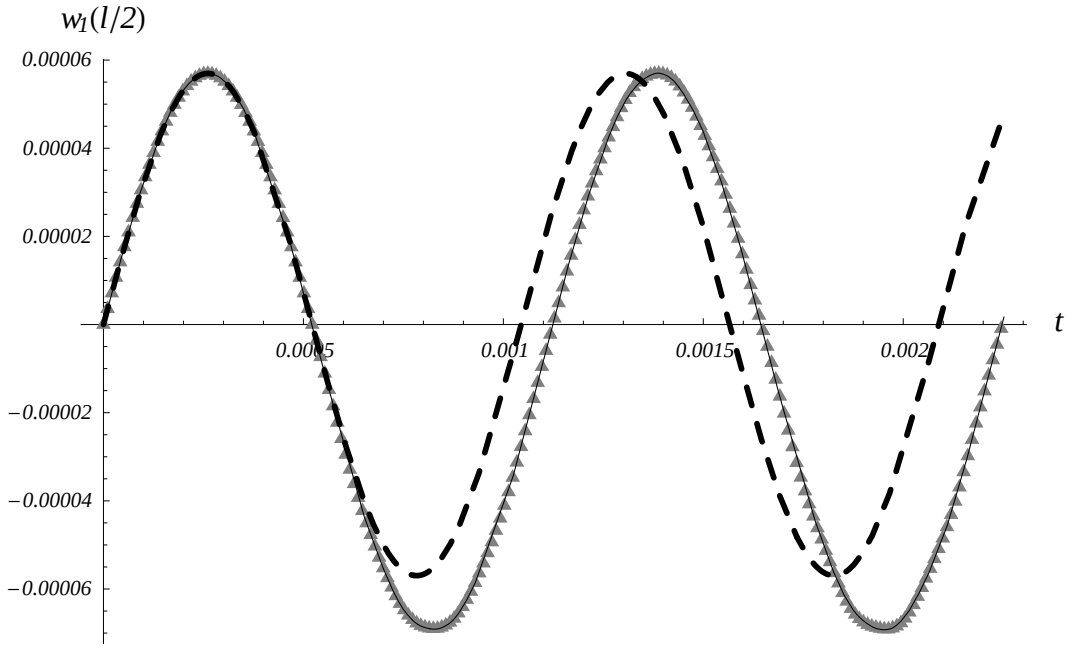

Figure 4.10: Time evolution of the deflection field at the crack station: breathing crack with 25 mode shapes (solid), breathing crack with the MLPG method (triangles), and exact solution for the intact beam (dashed).

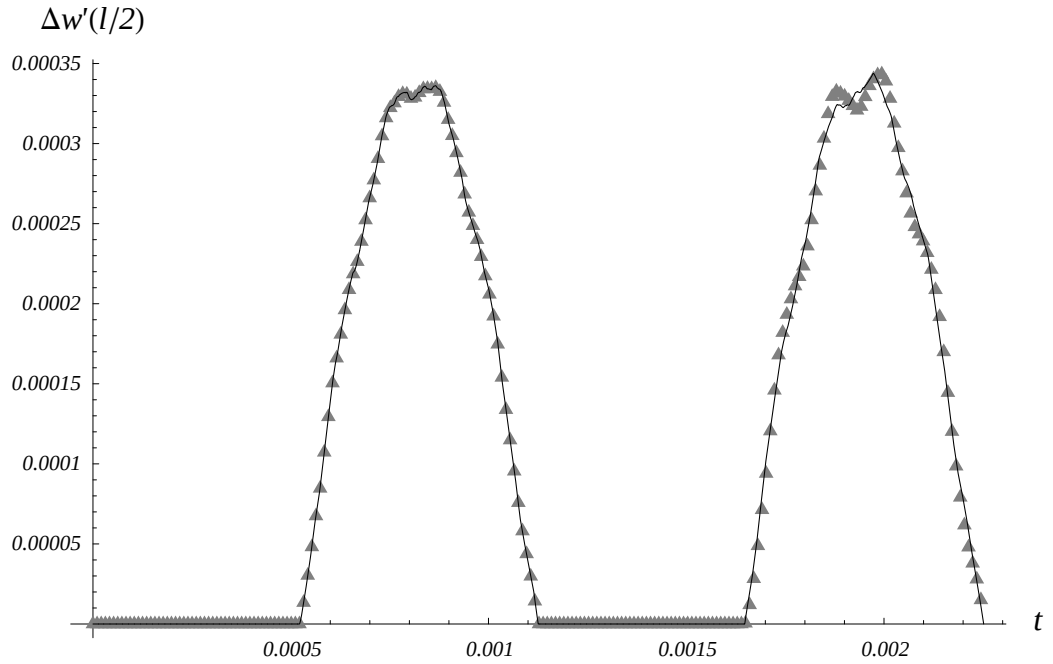

Figure 4.11: Time evolution of the change of rotations at the crack station: breathing crack with 25 mode shapes (solid), and breathing crack with the proposed method (triangles).

Chapter 5

Analysis of Rubber-like Materials

5.1 Introduction

Rubber-like materials are frequently used in the automotive industry, mechanical, civil, electrical and electronic engineering (see, e.g., Nagdi (1993)), and as biological tissues. For example, arterial walls (see, e.g., Ogden (2004)) are modeled as rubber-like materials.

In Continuum Mechanics rubber-like solids are generally modeled as isotropic, incompressible and hyperelastic. From a theoretical point of view, the incompressibility constraint facilitates finding analytical solutions for isotropic hyperelastic problems; see, e.g., Ogden (2004). Besides homogeneous deformations, there are five families of inhomogeneous deformations (Saccomandi (2001)) that can be produced in every incompressible hyperelastic solid. Some works have investigated the possibility of treating rubber as a nearly incompressible material by separating the strain energy for distortional deformations from that for the dilatational ones by using Penn's invariants (Penn (1970)), and the multiplicative decomposition of the deformation gradient into a volume preserving deformation and a pure dilatation, see, e.g., Crisfield (1998). In Charrier, Dacorogna, Hanouzet and Laborde (1988) it is proved that the behavior of slightly compressible materials may approximate well that of incompressible materials.

The analysis of problems for rubber-like materials is a challenging task in computational mechanics due to extremely large deformations and the nearly incompressible or genuinely incompressible material response. For a complete review and bibliography of works on numerical modeling of rubber-like materials we refer the reader to Gadala (1986), and Mackerle (2004). Many finite element methods (FEMs) have been developed to avoid the volumetric locking resulting from the incompressibility constraint. Among them are: the mixed formu-

Material in this Chapter is part of the paper "Analysis of Rubber-like Materials using Meshless Local Petrov-Galerkin (MLPG) Method," submitted for possible publication in a refereed journal.

lation (Hermann (1965), Batra (1980), and Peng and Chang (1997)), the hybrid methods (Scharnost and Pian (1978)), the selective reduced integration (Hughes (2001)), the perturbed Lagrange formulation (Chen, Han, Tu and Duan (1997)), and the rank-one filtering method (Chen, Pan and Chang (1995)). In addition to difficulties in dealing with incompressibility, FEMs frequently break down when applied to elastomers in which excessive deformations lead to mesh entanglement.

Here we analyze finite deformations of rubber-like materials with the MLPG method. We derive a local mixed formulation in which both the pressure and the displacement fields are regarded as unknowns. By splitting the strain energy density into purely deviatoric and dilatational parts, we treat simultaneously nearly incompressible and fully incompressible materials. The essential boundary conditions are imposed through a set of Lagrange multipliers defined on the boundary. The concept of secondary nodes developed in Kim and Atluri (2000) for enriching the set of trial functions without increasing noticeably the computational cost is adopted. The method is applied to the solution of different sample problems, and it is shown that their accurate solution can be computed with very few nodes. Moreover, it is shown that when a purely displacement formulation is adopted in the MLPG method a locking phenomenon similar to that encountered in the FEM occurs, suggesting thereby the need for a mixed formulation. The main contributions of this Chapter are: the derivation of a mixed nonlinear local weak formulation of the problem where the displacement, the pressure and constraint reactions are treated as unknowns applicable to completely incompressible or nearly incompressible materials; showing that pure displacement meshless formulations are not suitable for avoiding locking phenomenon; adapting the secondary nodes to nonlinear problems, and demonstrating that accurate approximate solutions can be obtained with a few nodes.

The rest of the Chapter is organized as follows. In Section 5.2 we derive a local symmetric weak formulation valid for hyperelastic materials, and specialize it to the analysis of rubber-like materials under plane strain deformations. Section 5.2 also presents the MLPG discrete nonlinear equations for determining an approximate solution. In Section 5.3, we apply the proposed method to the solution of linear and nonlinear problems. Section 5.4 summarizes conclusions of this work. The MLS approximation using primary and secondary nodes is described in Appendix A.1, the elasticity tensor for a nearly incompressible hyperelastic material is presented in Appendix D along with general concepts in nonlinear hyperelasticity.

5.2 Application of the MLPG method to non-linear elastic problems

5.2.1 Local weak formulation

Following Bathe (1996), we consider three distinct configurations of a body in the Euclidean space: the reference configuration Ω, an intermediate one Ω^0, and the present one Ω^t. Material points in Ω are indicated by $\mathbf{x}$, those in Ω^0 by $\mathbf{x}^0$, and those in Ω^t by $\mathbf{x}^t$. A field (scalar or tensor) $\mathbf{q}$ in the reference configuration is indicated by $\mathbf{q}^0$ or $\mathbf{q}^t$ when pushed-forward in the intermediate or in the actual configuration, respectively; while its increment from the intermediate to the actual configuration is denoted by $\Delta\mathbf{q}(\mathbf{x})$. Furthermore, $\mathbf{w}$ indicates the displacement vector, $\mathbf{F}$ the deformation gradient, $\mathbf{C}$ the right Cauchy-Green strain tensor, $\mathbf{E}$ the Green-St.Venant strain tensor, $\mathbf{S}$ the second Piola-Kirchhoff stress tensor, and $\mathbf{P}$ the first Piola-Kirchhoff stress tensor. A mixed pressure/displacement formulation is used here; the stress tensor depends on both the Green-St.Venant strain tensor $\mathbf{E}$ and the pressure field p. The boundary of the domain Ω is partitioned into two disjoint parts:

$$\partial\Omega = \Gamma_{\mathbf{w}} \cup \Gamma_{\mathbf{t}}. \tag{5.1}$$

On the boundary $\Gamma_{\mathbf{w}}$ displacements are prescribed as

$$\mathbf{w}^t(\mathbf{x}) = \bar{\mathbf{w}}(\mathbf{x}), \qquad \mathbf{x} \in \Gamma_{\mathbf{w}}, \tag{5.2}$$

while on the boundary $\Gamma_{\mathbf{t}}$ dead loads are prescribed by

$$\mathbf{P}^t(\mathbf{x})\,\mathbf{n}(\mathbf{x}) = \bar{\mathbf{t}}(\mathbf{x}), \qquad \mathbf{x} \in \Gamma_{\mathbf{t}}. \tag{5.3}$$

For a generic subdomain Ω_s of domain Ω the principle of virtual work (see, e.g., Simo and Hughes (1998)) gives

$$\int_{\Omega_s} \mathbf{S}^t(\mathbf{x}) \cdot \mathrm{Sym}\left[\left(\mathbf{F}^t\right)^{\mathrm{T}}(\mathbf{x})\,\nabla\varphi(\mathbf{x})\right] \mathrm{d}\Omega = \int_{\Omega_s} \mathbf{b}(\mathbf{x}) \cdot \varphi(\mathbf{x})\,\mathrm{d}\Omega + \int_{\partial\Omega_s} \mathbf{P}^t(\mathbf{x})\,\mathbf{n}(\mathbf{x}) \cdot \varphi(\mathbf{x})\ \mathrm{d}\Gamma, \tag{5.4}$$

where φ is a virtual displacement or a test function, ∇ is the gradient with respect to reference coordinates, Sym indicates the symmetric part, and superscript T indicates transposition.

For a two-dimensional domain, the boundary term can be divided into three parts: the line integral inside the domain L_s, the line integral on the boundary $\Gamma_{\mathbf{t}s}$ of the body where natural boundary conditions are prescribed, and the line integral on the boundary $\Gamma_{\mathbf{w}s}$ of the body

where essential boundary conditions are prescribed. Hence, by substituting for the traction boundary condition we obtain

$$\int_{\partial\Omega_s} \mathbf{P}^t(\mathbf{x})\,\mathbf{n}(\mathbf{x})\cdot\varphi(\mathbf{x})\;\mathrm{d}\Gamma = \int_{L_s} \mathbf{P}^t(\mathbf{x})\,\mathbf{n}(\mathbf{x})\cdot\varphi(\mathbf{x})\;\mathrm{d}\Gamma + \int_{\Gamma_{\mathbf{t}s}} \bar{\mathbf{t}}(\mathbf{x})\cdot\varphi(\mathbf{x})\;\mathrm{d}\Gamma + \int_{\Gamma_{\mathbf{w}s}} \mathbf{r}^t(\mathbf{x})\cdot\varphi(\mathbf{x})\;\mathrm{d}\Gamma, \quad (5.5)$$

where

$$\mathbf{r}^t(\mathbf{x}) = \mathbf{P}^t(\mathbf{x})\,\mathbf{n}(\mathbf{x}), \quad (5.6)$$

represents the unknown constraint reaction field in the reference configuration acting at boundary points with prescribed displacements. By choosing test functions that vanish on the interior contour L_s the weak formulation of the non-linear problem in the reference configuration is

$$\int_{\Omega_s} \mathbf{S}^t(\mathbf{x})\cdot\mathrm{Sym}\left[\left(\mathbf{F}^t\right)^{\mathrm{T}}(\mathbf{x})\,\nabla\varphi(\mathbf{x})\right]\;\mathrm{d}\Omega = \int_{\Omega_s} \mathbf{b}(\mathbf{x})\cdot\varphi(\mathbf{x})\;\mathrm{d}\Omega + \int_{\Gamma_{\mathbf{t}s}} \bar{\mathbf{t}}(\mathbf{x})\cdot\varphi(\mathbf{x})\;\mathrm{d}\Gamma + \int_{\Gamma_{\mathbf{w}s}} \mathbf{r}^t(\mathbf{x})\cdot\varphi(\mathbf{x})\;\mathrm{d}\Gamma. \quad (5.7)$$

In order to impose essential boundary conditions on $\Gamma_{\mathbf{w}}$ in a weak sense we consider the additional integral equation

$$\int_{\gamma_s} \mathbf{w}^t(\mathbf{x})\cdot\;\lambda(\mathbf{x})\;\mathrm{d}\Gamma = \int_{\gamma_s} \bar{\mathbf{w}}(\mathbf{x})\cdot\lambda(\mathbf{x})\;\mathrm{d}\Gamma, \quad (5.8)$$

where λ is a smooth test field defined on the portion γ_s of $\Gamma_{\mathbf{w}}$.

The nearly incompressibility condition is accommodated by requiring that

$$p^t(\mathbf{x}) = \bar{p}^t\left(\mathbf{E}^t(\mathbf{x})\right), \quad (5.9)$$

where $\bar{p}^t$ is the pressure computed from the deformation gradient. This leads to the local weak formulation

$$\int_{\Omega_s} p^t(\mathbf{x})\,\xi(\mathbf{x})\;\mathrm{d}\Omega = \int_{\Omega_s} \bar{p}^t(\mathbf{x})\,\xi(\mathbf{x})\;\mathrm{d}\Omega, \quad (5.10)$$

where ξ is a smooth test field defined on Ω.

5.2.2 Total Lagrangian mixed formulation

In order to derive a total Lagrangian formulation (see, e.g., Bathe (1996)) of the problem suitable for numerical implementation we regard the present configuration as a neighboring

configuration of the intermediate configuration, and linearize the weak formulation in the neighborhood of the intermediate configuration.

Therefore, we adopt the following incremental form of the stress tensor

$$\mathbf{S}^t(\mathbf{x}) \simeq \mathbf{S}^0(\mathbf{x}) + \mathbb{C}(\mathbf{x})\left(\mathbf{E}^t(\mathbf{x}) - \mathbf{E}^0(\mathbf{x})\right) + \mathbf{H}(\mathbf{x})\left(p^t(\mathbf{x}) - p^0(\mathbf{x})\right), \tag{5.11}$$

where

$$\mathbb{C} = \left.\frac{\partial \mathbf{S}}{\partial \mathbf{E}}\right|_0, \qquad \mathbf{H} = \left.\frac{\partial \mathbf{S}}{\partial p}\right|_0. \tag{5.12}$$

and $\cdot|_0$ implies that the quantity is evaluated in the intermediate configuration. The constitutive relation (5.11) is still non-linear in the displacement increment $\Delta\mathbf{w}$ from Ω^0 to Ω^t, since the difference of the two strains is not linear in the gradient of the incremental displacement. However, since

$$\mathbf{E}^t - \mathbf{E}^0 \simeq \mathrm{Sym}\left[\left(\mathbf{F}^0\right)^{\mathrm{T}} \nabla \Delta\mathbf{w}\right], \qquad \Delta\mathbf{w} = \mathbf{w}^t - \mathbf{w}^0, \tag{5.13}$$

we obtain the following linearized constitutive equation

$$\mathbf{S}^t \simeq \mathbf{S}^0 + \mathbb{C}\mathrm{Sym}\left[\left(\mathbf{F}^0\right)^{\mathrm{T}} \nabla \Delta\mathbf{w}\right] + \mathbf{H}\Delta p. \tag{5.14}$$

Substituting for $\mathbf{S}^t$ from (5.14) into (5.7), and decomposing the external virtual work in the RHS of (5.7) into the virtual work done by loads that keep the body in equilibrium in the intermediate configuration and the virtual work done by the incremental loads, the incremental form of the symmetric weak formulation (5.7) becomes

$$\begin{aligned}
&\int_{\Omega_s} \nabla\Delta w\, S^0 \cdot \nabla\varphi \,\mathrm{d}\Omega + \int_{\Omega_s} \mathbb{C}\mathrm{Sym}\left[\left(\mathbf{F}^0\right)^{\mathrm{T}} \nabla\Delta\mathbf{w}\right] \cdot \mathrm{Sym}\left[\left(\mathbf{F}^0\right)^{\mathrm{T}} \nabla\varphi\right] \mathrm{d}\Omega + \\
&\int_{\Omega_s} \Delta p \mathbf{H} \cdot \mathrm{Sym}\left[\left(\mathbf{F}^0\right)^{\mathrm{T}} \nabla\varphi\right] - \int_{\Gamma_{\mathbf{w}s}} \Delta\mathbf{r}(\mathbf{x}) \cdot \varphi(\mathbf{x}) \,\mathrm{d}\Gamma = \int_{\Omega_s} \mathbf{b}^0(\mathbf{x}) \cdot \varphi(\mathbf{x}) \,\mathrm{d}\Omega + \\
&\int_{\Gamma_{\mathbf{t}s}} \bar{\mathbf{t}}^0(\mathbf{x}) \cdot \varphi(\mathbf{x}) \,\mathrm{d}\Gamma + \int_{\Gamma_{\mathbf{w}s}} \mathbf{r}^0(\mathbf{x}) \cdot \varphi(\mathbf{x}) \,\mathrm{d}\Gamma - \\
&\int_{\Omega_s} \mathbf{S}^0 \cdot \mathrm{Sym}\left[\left(\mathbf{F}^0\right)^{\mathrm{T}} \nabla\varphi\right] \mathrm{d}\Omega + \int_{\Omega_s} \Delta\mathbf{b}(\mathbf{x}) \cdot \varphi(\mathbf{x}) \,\mathrm{d}\Omega + \int_{\Gamma_{\mathbf{t}s}} \Delta\bar{\mathbf{t}}(\mathbf{x}) \cdot \varphi(\mathbf{x}) \,\mathrm{d}\Gamma.
\end{aligned} \tag{5.15}$$

In order to determine the incremental displacement field, the incremental pressure field, and the constraint reactions we consider also the incremental forms of (5.8) and (5.10). That is

$$\int_{\gamma_s} \Delta\mathbf{w}(\mathbf{x}) \cdot \lambda(\mathbf{x}) \,\mathrm{d}\Gamma = \int_{\gamma_s} \Delta\bar{\mathbf{w}}(\mathbf{x}) \cdot \lambda(\mathbf{x}) \,\mathrm{d}\Gamma, \tag{5.16}$$

and

$$\begin{aligned}
&\int_{\Omega_s} \Delta p(\mathbf{x})\, \xi(\mathbf{x}) \,\mathrm{d}\Omega - \int_{\Omega_s} \left(\mathbf{Q} \cdot \mathrm{Sym}\left[\left(\mathbf{F}^0\right)^{\mathrm{T}} \nabla\Delta\mathbf{w}\right]\right) \xi(\mathbf{x}) \,\mathrm{d}\Omega = \\
&\qquad - \int_{\Omega_s} p^0(\mathbf{x})\, \xi(\mathbf{x}) \,\mathrm{d}\Omega + \int_{\Omega_s} \bar{p}^0(\mathbf{x})\, \xi(\mathbf{x}) \,\mathrm{d}\Omega,
\end{aligned} \tag{5.17}$$

where

$$\mathbf{Q} = \frac{\partial \bar{p}}{\partial \mathbf{E}}|_0. \tag{5.18}$$

Henceforth we consider only plane strain problems with deformations in the x_1x_2-plane, and adopt the Voigt vector notation. We thus introduce the quantities

$$\mathbf{S}^0 = \begin{bmatrix} S^0_{11} & S^0_{12} & 0 & 0 \\ S^0_{12} & S^0_{22} & 0 & 0 \\ 0 & 0 & S^0_{11} & S^0_{12} \\ 0 & 0 & S^0_{12} & S^0_{22} \end{bmatrix}, \quad \mathbf{B} = \begin{bmatrix} 1+\dfrac{\partial w^0_1}{\partial x_1} & 0 & \dfrac{\partial w^0_2}{\partial x_1} & 0 \\ 0 & \dfrac{\partial w^0_1}{\partial x_2} & 0 & 1+\dfrac{\partial w^0_2}{\partial x_2} \\ \dfrac{\partial w^0_1}{\partial x_2} & 1+\dfrac{\partial w^0_1}{\partial x_1} & 1+\dfrac{\partial w^0_2}{\partial x_2} & \dfrac{\partial w^0_2}{\partial x_1} \end{bmatrix}. \tag{5.19}$$

$$\mathbf{H} = \begin{Bmatrix} H_{11} \\ H_{22} \\ H_{12} \end{Bmatrix}, \quad \mathbf{Q} = \begin{Bmatrix} Q_{11} \\ Q_{22} \\ Q_{12} \end{Bmatrix}, \tag{5.20}$$

$$\mathbf{s}^0 = \begin{Bmatrix} S^0_{11} \\ S^0_{22} \\ S^0_{12} \end{Bmatrix}, \ \Delta\mathbf{w} = \begin{Bmatrix} \Delta w_1 \\ \Delta w_2 \end{Bmatrix}, \ \mathbf{w}^0 = \begin{Bmatrix} w^0_1 \\ w^0_2 \end{Bmatrix}, \ \varphi = \begin{Bmatrix} \varphi_1 \\ \varphi_2 \end{Bmatrix}, \ \Delta\mathbf{d} = \begin{Bmatrix} \dfrac{\partial \Delta w_1}{\partial x_1} \\ \dfrac{\partial \Delta w_1}{\partial x_2} \\ \dfrac{\partial \Delta w_2}{\partial x_1} \\ \dfrac{\partial \Delta w_2}{\partial x_2} \end{Bmatrix}, \tag{5.21}$$

$$\mathbf{r}^0 = \begin{Bmatrix} r^0_1 \\ r^0_2 \end{Bmatrix}, \ \Delta\mathbf{r} = \begin{Bmatrix} \Delta r_1 \\ \Delta r_2 \end{Bmatrix}, \ \mathbf{r}^0 = \begin{Bmatrix} r^0_1 \\ r^0_2 \end{Bmatrix}, \ \Delta\lambda = \begin{Bmatrix} \Delta\lambda_1 \\ \Delta\lambda_2 \end{Bmatrix}, \quad \delta = \begin{Bmatrix} \dfrac{\partial \varphi_1}{\partial x_1} \\ \dfrac{\partial \varphi_1}{\partial x_2} \\ \dfrac{\partial \varphi_2}{\partial x_1} \\ \dfrac{\partial \varphi_2}{\partial x_2} \end{Bmatrix}, \tag{5.22}$$

$$\mathbf{b}^0 = \begin{Bmatrix} b^0_1 \\ b^0_2 \end{Bmatrix}, \quad \bar{\mathbf{t}}^0 = \begin{Bmatrix} \bar{t}^0_1 \\ \bar{t}^0_2 \end{Bmatrix}, \quad \Delta\mathbf{b} = \begin{Bmatrix} \Delta b_1 \\ \Delta b_2 \end{Bmatrix}, \quad \Delta\bar{\mathbf{t}} = \begin{Bmatrix} \Delta\bar{t}_1 \\ \Delta\bar{t}_2 \end{Bmatrix}. \tag{5.23}$$

In this notation (5.15), (5.16) and (5.17) can be written as

$$\int_{\Omega_s} \delta^{\mathrm{T}} \left(\mathbb{B}+\mathbf{S}^0\right) \Delta\mathbf{d}\, \mathrm{d}\Omega + \int_{\Omega_s} \delta^{\mathrm{T}} \mathbb{H} \Delta p\, \mathrm{d}\Omega - \int_{\Gamma_{\mathbf{w}s}} \lambda^{\mathrm{T}} \Delta\mathbf{r}\, \mathrm{d}\Gamma = -\int_{\Omega_s} \delta^{\mathrm{T}} \mathbb{S}\, \mathrm{d}\Omega + \int_{\Omega_s} \varphi^{\mathrm{T}} \mathbf{b}^0\, \mathrm{d}\Omega + \int_{\Gamma_{\mathbf{t}s}} \varphi^{\mathrm{T}} \bar{\mathbf{t}}^0\, \mathrm{d}\Gamma + \int_{\Gamma_{\mathbf{w}s}} \lambda^{\mathrm{T}} \mathbf{r}^0\, \mathrm{d}\Gamma + \int_{\Omega_s} \varphi^{\mathrm{T}} \Delta\mathbf{b}\, \mathrm{d}\Omega + \int_{\Gamma_{\mathbf{t}s}} \varphi^{\mathrm{T}} \Delta\bar{\mathbf{t}}\, \mathrm{d}\Gamma, \quad (5.24)$$

$$\int_{\gamma_s} \lambda^{\mathrm{T}} \Delta\mathbf{w}\, \mathrm{d}\Gamma = \int_{\gamma_s} \lambda^{\mathrm{T}} \Delta\bar{\mathbf{w}}\, \mathrm{d}\Gamma, \quad (5.25)$$

$$\int_{\Omega_s} \xi \Delta p\, \mathrm{d}\Omega - \int_{\Omega_s} \xi \mathbb{Q}^{\mathrm{T}} \Delta\mathbf{d}\, \mathrm{d}\Omega = \int_{\Omega_s} \xi \left(\bar{p}^0 - p^0\right)\, \mathrm{d}\Omega, \quad (5.26)$$

where

$$\mathbb{B} = \mathbf{B}^{\mathrm{T}}\mathbf{L}\mathbf{B}, \qquad \mathbb{S} = \mathbf{B}^{\mathrm{T}}\mathbf{s}^0, \qquad \mathbb{H} = \mathbf{B}^{\mathrm{T}}\mathbf{H}, \qquad \mathbb{Q} = \mathbf{B}^{\mathrm{T}}\mathbf{Q}, \quad (5.27)$$

and $\mathbf{L}$ is the elasticity matrix. We note that matrices $\mathbf{S}^0$, $\mathbf{B}$, $\mathbf{L}$, $\mathbf{H}$ and $\mathbf{Q}$ depend on the state of deformation and on the pressure in the intermediate configuration.

5.2.3 Discrete formulation

In order to find an approximate solution of the linearized elastic problem, we approximate components of the displacement and pressure fields by using N 2-D MLS basis functions given by (A.12) in the Appendix :

$$w_1(\mathbf{x}) = \psi^{\mathrm{T}}(\mathbf{x})\, \hat{\mathbf{w}}_1, \qquad w_2(\mathbf{x}) = \psi^{\mathrm{T}}(\mathbf{x})\, \hat{\mathbf{w}}_2, \qquad p(\mathbf{x}) = \psi^{\mathrm{T}}(\mathbf{x})\, \hat{\mathbf{p}}. \quad (5.28)$$

The constraint reactions field is instead approximated by using $2N_B$ 1-D MLS basis functions obtained from (A.12) by approximating the boundary of the domain by piecewise linear segments, and by placing a set of nodes on each straight line, i.e.:

$$\lambda_1(\mathbf{x}) = \chi(\mathbf{x})^{\mathrm{T}}\, \hat{\lambda}_1, \qquad \lambda_2(\mathbf{x}) = \chi(\mathbf{x})^{\mathrm{T}}\, \hat{\lambda}_2. \quad (5.29)$$

For convenience we group nodal displacements and nodal reactions into two vectors $\hat{\mathbf{w}}$ and $\hat{\lambda}$. In order to obtain a set of linearly independent algebraic equations for the $3N + 2N_B$ nodal unknowns, we use N local 2-D sub-domains Ω_{si}, and N_B local 1-D subdomains γ_{si}, N independent scalar test fields φ_i defined on each Ω_{si} and vanishing on L_{si}, and N_B independent scalar test fields ϕ_i defined on γ_{si}. Therefore, the following algebraic problem arises:

$$\begin{bmatrix} \mathbf{K}_{\mathbf{ww}} & \mathbf{K}_{\mathbf{wp}} & \mathbf{K}_{\mathbf{w}\lambda} \\ \mathbf{K}_{\mathbf{pw}} & \mathbf{K}_{\mathbf{pp}} & \mathbf{0} \\ \mathbf{K}_{\lambda\mathbf{w}} & \mathbf{0} & \mathbf{0} \end{bmatrix} \begin{Bmatrix} \hat{\mathbf{w}} \\ \hat{\mathbf{p}} \\ \hat{\lambda} \end{Bmatrix} = \begin{Bmatrix} \Delta\mathbf{f}_w \\ \mathbf{0} \\ \Delta\mathbf{f}_\lambda \end{Bmatrix} + \begin{Bmatrix} \mathbf{f}_w \\ \mathbf{0} \\ \mathbf{f}_\lambda \end{Bmatrix} + \begin{Bmatrix} \mathbf{R}_w \\ \mathbf{R}_p \\ \mathbf{R}_\lambda \end{Bmatrix}, \quad (5.30)$$

where the explicit form of the tangent stiffness matrix and of the load vector can be deduced from (5.24), (5.25), and (5.26). For problems involving dead loads, the incremental load is a given constant vector, and the tangent stiffness matrix and the residual loads depend on the deformation and pressure fields in the intermediate configuration.

5.3 Computation and discussion of results

In order to validate the problem formulation and the developed computer code we consider a square plate of side $b = 1$, and we numerically analyze several problems whose analytical solution is found by using fictitious loads; see, e.g., remarks after (30) of Batra and Liang (1997). We consider a Bubnov-Galerkin formulation in which the test functions are chosen from the same space as the trial solutions. We consider a regular grid of 49 primary nodes as shown in Figure 5.1 Linear monomial basis, $m = 3$, is used, and the origin of the coordinate axes is located at the bottom left corner. The size r_i of the support of each weight function is chosen to be $1/2$ in order to guarantee the non-singularity of matrices in the MLS approximation. Values assigned to other constants defining weight functions in (A.17) are $k = 1$, $c_i = r_i/4$. To numerically evaluate integrals appearing in the linearized weak formulation of the problem, we use 6×6 quadrature points in each intersection of supports of weight functions associated with different primary nodes. The following L^2 logarithmic error norm is used to compare computed results with the exact solution:

$$\text{ERR} = \log_{10} \frac{\sqrt{\int_\Omega \left[\left(w_1^{EX} - w_1^{MLPG}\right)^2 + \left(w_2^{EX} - w_2^{MLPG}\right)^2 \right] \mathrm{d}\Omega}}{\sqrt{\int_\Omega \left(w_1^{EX}\right)^2 + \left(w_2^{EX}\right)^2 \mathrm{d}\Omega}}, \tag{5.31}$$

where superscripts EX and $MLPG$ stand for the exact and the numerical solutions respectively.

We first solve a linear elastic problem for a homogeneous and isotropic body to show advantages of the mixed formulation with respect to the pure displacement formulation. We show that as Poisson's ratio ν approaches $1/2$ the pure displacement formulation locks. In this case, the numerical solution is obtained by solving the system of equations (5.30) with zero initial stresses, and

$$\mathbb{B} = \frac{E}{2\,(1+\nu)} \begin{bmatrix} 4/3 & 0 & 0 & -2/3 \\ 0 & 1 & 1 & 0 \\ 0 & 1 & 1 & 0 \\ -2/3 & 0 & 0 & 4/3 \end{bmatrix}, \qquad \mathbb{H} = \begin{Bmatrix} 1 \\ 0 \\ 0 \\ 1 \end{Bmatrix}, \qquad \mathbb{Q} = -\frac{E}{2\,(1+\nu)\,(1-2\nu)} \mathbb{P}, \tag{5.32}$$

E being Young's modulus.

Problems 2, 3, 4, and 5 focus on finite deformations of Mooney-Rivlin rubber-like materials under different loadings and boundary conditions; they represent, respectively, the uniform extension, uniform shear, nonuniform extension, and nonuniform shear. Problem 6 analyzes the stress intensity factor in a body made of a Mooney-Rivlin material undergoing either small or large mode-I deformations. In this case we use secondary nodes presented in Appendix A to improve the solution accuracy. The size of the support of the weight function

of a secondary node in (A.18) equals the maximum distance between a secondary node and its associated primary node. In all these cases parameters for the Mooney-Rivlin material, defined in Appendix D, are:

$$A_{10} = 1, \qquad A_{20} = 0.05, \qquad k = 10^3. \tag{5.33}$$

The nonlinear problems are solved by the Newton-Raphson method (see, e.g., Crisfield (1998)) with the total load divided into small increments, and the load step changed according to the number of steps needed for the solution to converge. The norm of the incremental solution in Newton's iterations is computed by using the norm of the interpolated fields rather than of the fictitious nodal values.

Problems 2, 3, 4, and 5 are solved using the method of fictitious loads. In particular, we choose an isochoric deformation and we determine the corresponding applied loads from the Mooney-Rivlin constitutive equation in Appendix D, and the balance of linear momentum. The pressure field corresponding to an isochoric deformation, see (5.9), is zero since the bulk modulus k is finite.

5.3.1 Linear elastic problem for a cantilever

We consider the "cantilever" beam problem studied in Timoshenko and Goodier (1970) for which the exact solution is

$$w_1 = -\frac{2P}{Eb^3}\left(x_2 - \frac{b}{2}\right)\left[3x_1\left(2b - x_1\right) + \left(2 + \frac{\nu}{1-\nu}\right)x_2\left(x_2 - b\right)\right], \tag{5.34}$$

$$w_2 = \frac{2P}{Eb^3}\left[\left(x_1\right)^2\left(3b - x_1\right) + 3\frac{\nu}{1-\nu}\left(b - x_1\right)\left(x_2 - \frac{b}{2}\right)^2 + \left(4 + \frac{5\nu}{1-\nu}\right)b^2 x_1\right], \tag{5.35}$$

where the right edge is clamped, a distributed load with resultant P is applied on the left edge, b is the height of the beam, and its width is one. In a consistent set of units the problem is analyzed for $P = -0.1$, $E = 1$, and $\nu = 0.4$, $\nu = 0.499$, and $\nu = 0.49999999$. In Table 5.1 we report results of the mixed and the pure displacement formulations in terms of the tip deflection for the three chosen values of Poisson's ratio. The pure displacement formulation locks when the incompressibility constraint is severe, while the mixed formulation is insensitive to variations of Poisson's ratio in the neighborhood of 1/2. Thus the pure displacement formulation may not give accurate results as $\nu \to 1/2$.

5.3.2 Uniform extension

We consider simple tensile deformations of the plate, and assume that the left and the bottom edges are on rollers, while traction acts on the other two edge as determined by substituting

	Pure Displacement	Mixed
$\nu = 0.4$	0.60	1.20
$\nu = 0.499$	6.59	0.79
$\nu = 0.49999999$	10.9	0.80

Table 5.1: For a cantilever beam, percentage error in the tip deflection computed with mixed and pure displacement MLPG formulations.

the following isochoric displacement field in the Mooney-Rivlin constitutive relation:

$$f_1(x_1, x_2) = 2x_2, \qquad f_2(x_1, x_2) = \frac{1}{2}x_1. \tag{5.36}$$

The logarithmic norm (5.31) of the error in displacements is -4.51. In Figure 5.2 we show the initial shape of the plate, and the final locations of nodes resulting from the exact solution (empty circle) and the MLPG solution (dots). For this problem no body forces are present and the high accuracy of the computed solution depends strongly on the linearity of the exact displacement field which can be reproduced exactly by the MLS basis functions.

5.3.3 Uniform shear

We study uniform shear deformations by clamping the left edge of the square plate, and by loading other edges as determined by substituting the following isochoric deformation field into the Mooney-Rivlin constitutive relation:

$$f_1(x_1, x_2) = x_1, \qquad f_2(x_1, x_2) = x_2 - \frac{3}{4}x_1, \tag{5.37}$$

The logarithmic norm (5.31) of the error in displacements is -3.84. In Figure 5.3 we exhibit the initial shape of the plate, and the final locations of nodes resulting from the exact solution (empty circle) and the MLPG solution (dots). For this case the same comments as those for the homogeneous extension apply.

5.3.4 Nonuniform extension

We now analyze inhomogeneous finite deformations of the plate. We assume that the plate is supported on rollers on the left and the bottom edges, and body forces and surface tractions are applied according to the stress field determined by the Mooney-Rivlin constitutive relation with the isochoric deformation field:

$$f_1(x_1, x_2) = x_1 + \log[x_1 + 1]\frac{1}{\log 2}, \tag{5.38}$$

$$f_2(x_1, x_2) = x_2\frac{(x_1 + 1)\log 2}{(x_1 + 1)\log 2 + 1} + \log[x_1 + 1]\frac{1}{\log 2}. \tag{5.39}$$

The logarithmic norm (5.31) of the error in computed displacements is -2.78. In Figure 5.4 we evince the initial shape of the plate and the final locations of the nodes resulting from the exact solution (empty circle) and the MLPG solution (dots).

5.3.5 Nonuniform shear

We assume that the plate is clamped at the left edge, and body forces and surface tractions are applied according to the stress field determined by the Mooney-Rivlin constitutive relation with deformation field:

$$f_1(x_1, x_2) = x_1, \qquad f_2(x_1, x_2) = x_2 - \frac{1}{2}(x_1)^2, \tag{5.40}$$

The logarithmic norm (5.31) of the error in displacements computed by the MLPG method is -2.48. In Figure 5.5 we evince the initial shape of the plate, and the final locations of nodes resulting from the exact solution (empty circle) and the MLPG solution (dots).

5.3.6 Crack problem

We consider a cracked plate whose geometry is reported in Figure 5.6. By exploiting the symmetry of the problem, we numerically analyze deformations of the quarter of the domain depicted in Figure 5.6. In order to accurately analyze effects of the crack, we use secondary nodes in the neighborhood of the crack tip, all over the domain, and on the boundaries as shown in Figure 5.7. The secondary nodes located in the neighborhood of the crack tip are needed for accurately estimating the stress concentration there. The secondary nodes on the boundaries and in the domain are needed for satisfying well the boundary conditions and improving the solution inside the domain. From numerical experiments we have observed that locating only secondary nodes in the neighborhood of the crack tip leads to poor solutions with spurious pressure modes. The total number of nodes used in the simulation is 168.

The plate is loaded with a uniformly distributed dead load of value $\sigma_0 = 0.65$, and the crack length equals half of the plate width. In Figure 5.8 we exhibit the deformed shape of the plate. Recalling that nominal tractions are prescribed on the top surface of the plate, it does not need to stay horizontal during the deformation process. Also, the total axial force stays constant even though the width of the plate decreases.

The J-integral in finite elasticity is given by (see, e.g., Legrain, Moes and Verron (2005))

$$J = \int_\Gamma \left(W n_1 - \mathbf{n} \cdot \mathbf{P}^t \frac{\partial \mathbf{w}^t}{\partial x_1} \right) \mathrm{d}\Gamma, \tag{5.41}$$

where Γ is the integration contour surrounding the crack tip in the reference configuration, W is the strain energy density defined by (D.6) in Appendix D, $\mathbf{n}$ is the unit outward normal, and n_1 is its component in the crack direction. In order to evaluate J, we use a circular contour of radius 0.125 centered at the crack tip.

For the linear elastic problem the exact value J_L of the J-integral is given by (see, e.g., Kim and Atluri (2000)):

$$J_L = c\pi(1.325)^2 \frac{1-\nu^2}{E}\sigma_0^2 \tag{5.42}$$

where $2c$ is the crack length, being 1 in the present case. In Figure 5.9, we exhibit the J-integrals computed for the linear and the nonlinear elastic problems. A similar problem has been studied in Legrain, Moes and Verron (2005) under plane stress conditions, and similar variations of the J-integral for the linear and the nonlinear problems have been found.

As an additional test of the MLPG mixed formulation, we compute the J-integral for the linear elastic problem with the pure displacement formulation, and the proposed mixed pressure-displacement formulation. With the pure displacement formulation the error in the computed values of J is 71.3%, while when using the mixed formulation the error is only 1.14%.

Figure 5.10 exhibits the crack opening displacements computed using the present MLPG mixed formulation, and the commercial FE code ANSYS using the 8-node element PLANE183 and 1057 nodes with high concentration at the crack tip. The good agreement between the two numerical solutions further validates the present mixed formulation. We note that the proposed MLPG mixed formulation requires only 168 nodes as compared to the 1057 nodes with the FE method.

Figure 5.11 reports the concentration of the first Piola-Kirchhoff stress, defined as P_{22}/σ_0 for different values of the dead tractions. It shows how the mixed formulation enhanced by secondary nodes is able to capture the stress concentration without leading to spurious oscillatory behaviors. From Figure 5.11 it can be concluded that increasing the tension in the plate decreases the order of singularity of the first Piola-Kirchhoff stress at the crack tip. Figure 5.12 reports instead the concentration of the Cauchy stress, defined as σ_{22}/σ_0 for different values of the dead tractions. From Figure 5.12 it can be seen that increasing the tension in the plate increases the order of singularity of the Cauchy stress at the crack tip. By comparing plots in Figures 5.11 and 5.12 one evinces that for a nonlinear elastic problem the orders of singularity in the Cauchy stress and in the first Piola-Kirchhoff stress are different. Indeed for finite deformation these two tensors are different and they are related by the deformation gradient.

5.3.7 Remarks

When solving numerically boundary-value problems for incompressible materials by the FEM, one uses elements (equivalently basis functions for the trial solution and the test function) that satisfy the Babuska-Brezzi condition as explained in Bathe (1996). In general, one needs to employ sophisticated analysis techniques to verify whether or not an element satisfies this condition. Hughes (2001) has listed various FEs that do not satisfy this condition but still perform very well in the numerical solution of boundary-value problems for linear elastic incompressible materials. For nonlinear boundary-value problems, the analysis becomes more involved, and the complexity increases further for the MLPG formulation. Even though we have not proved analytically that our choice of basis functions for the pressure and the displacement fields satisfies the Babuska-Brezzi condition, numerical experiments performed thus far and reported herein have indicated that these basis functions perform very well, and do not exhibit locking phenomenon for incompressible materials. It was proved in Batra, Porfiri and Spinello (2006a) that the MLPG formulation for 1-D transient linear elastic problems with Lagrange multipliers used to enforce essential boundary conditions satisfies the Babuska-Brezzi condition.

Secondary nodes may be useful in those problems where stress concentrations or critical behavior are expected in certain regions. Indeed, by adding secondary nodes the number of quadrature points needed for the numerical integration of the stiffness matrix and the load vector is not increased. Therefore, by adding secondary nodes one is able to increase the number of nodal degrees of freedom without noticeably increasing the computational time in assembling of the numerical formulation. Nevertheless, massive use of secondary nodes may lead to ill-conditioned problems, since the basis functions of secondary nodes are not significantly different from those of primary nodes especially when the density of secondary nodes is high.

5.4 Conclusions

We have studied finite plane strain deformations of a rubber-like material with the MLPG method, and a local weak formulation where both the pressure and the displacement fields are treated as unknowns. Differing from the finite element work, all variables are interpolated with the same set of MLS basis functions. By using Penn's invariants the deformation is decomposed into a dilatation and a distortion, and consequently the strain energy is split into two parts: one depending only on dilatational strains and the other on distortional strains. In order to impose the essential boundary conditions, we consider an augmented formulation, where a set of Lagrange multipliers is defined on the relevant boundaries. A

total Lagrangian formulation is derived and the resulting set of nonlinear algebraic equations governing finite deformations are solved by Newton-Raphson's iterations.

A computer code has been developed and used to solve different problems. Computed results for a body made of a Mooney-Rivlin material under various loading conditions are shown to compare very well with either analytical solutions or numerical solutions obtained with a finite element commercial code.

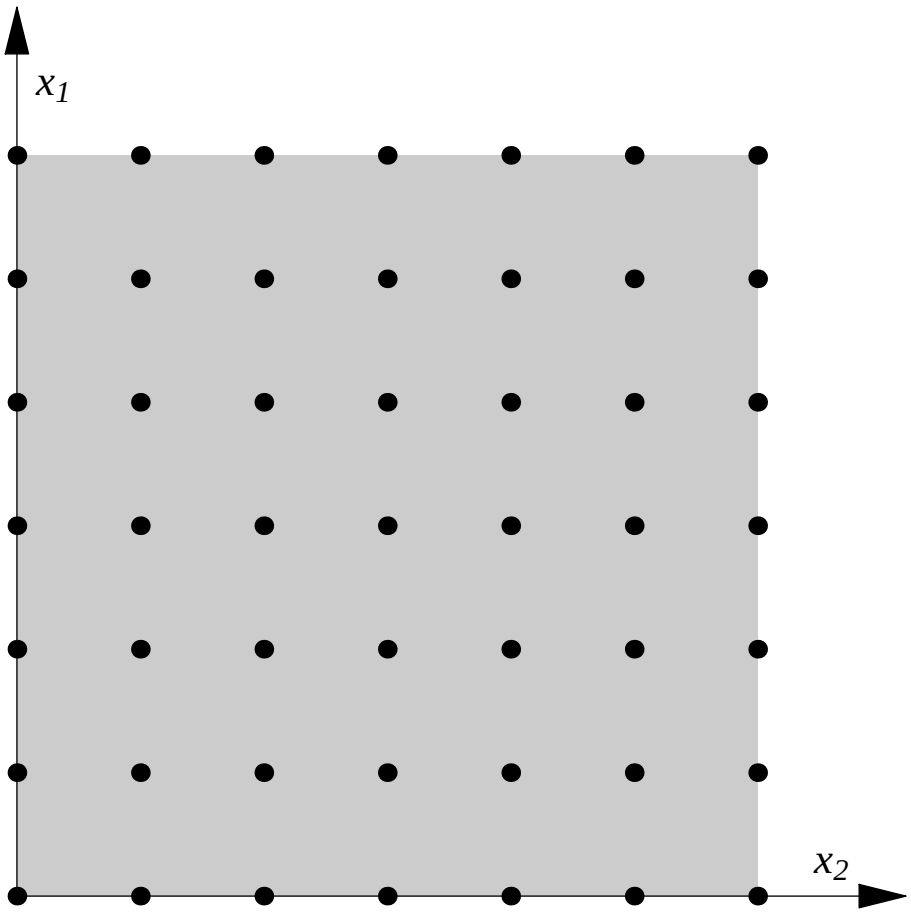

Figure 5.1: Geometry and locations of primary nodes for the sample problem studied.

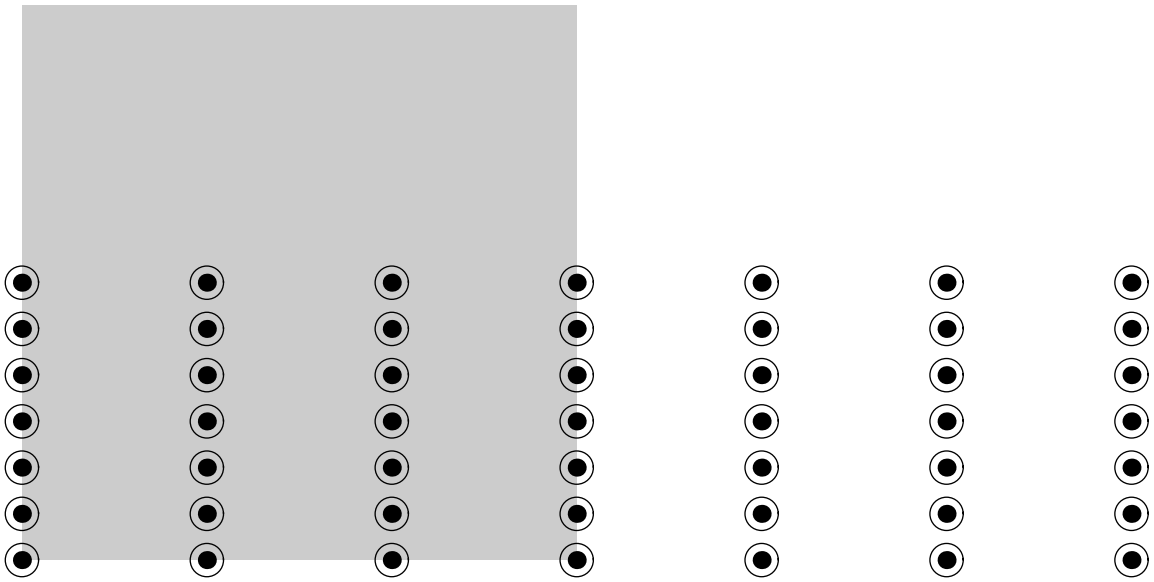

Figure 5.2: Uniform extension of a plate: undeformed configuration (shaded), exact solution (empty circles), MLPG solution (dots).

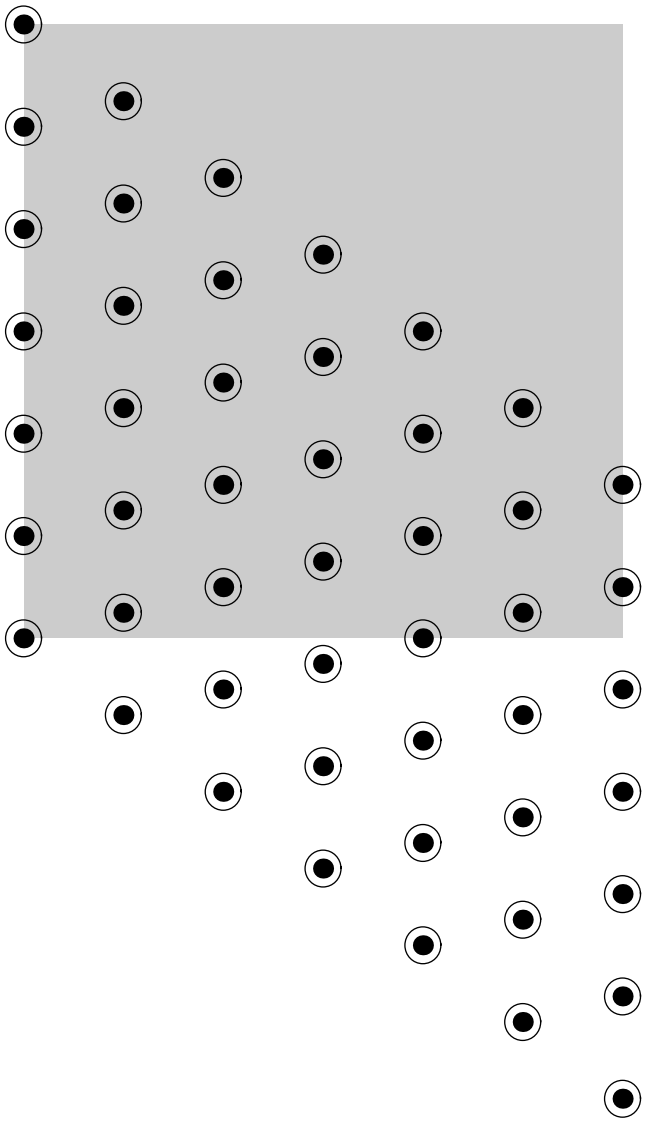

Figure 5.3: Uniform shear of a plate: undeformed configuration (shaded), exact solution (empty circles), MLPG solution (dots).

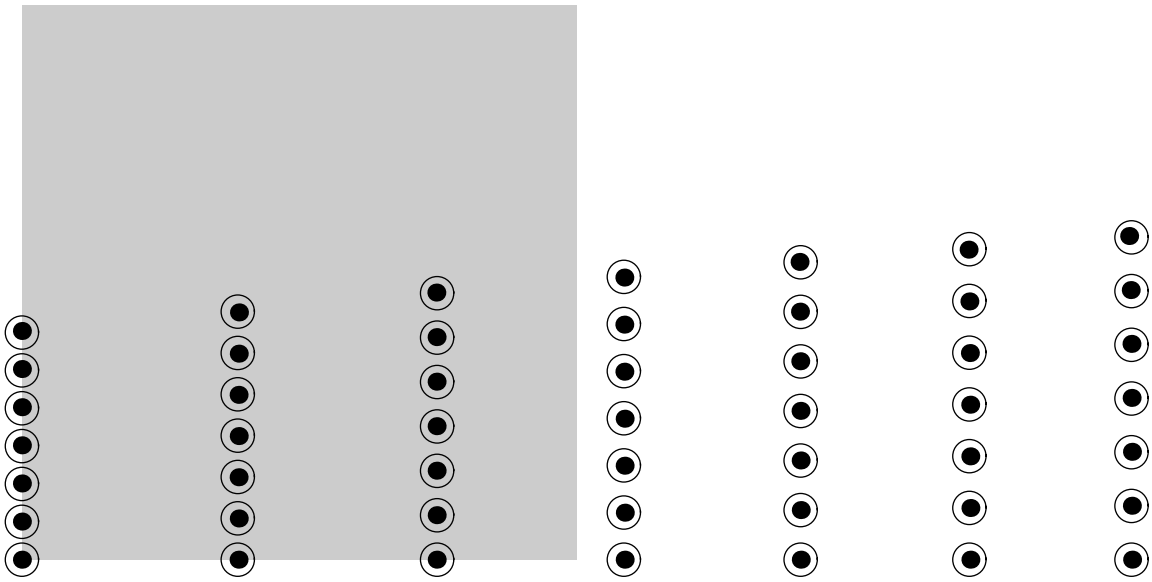

Figure 5.4: Nonuniform extension of a plate: undeformed configuration (shaded), exact solution (empty circles), MLPG solution (dots).

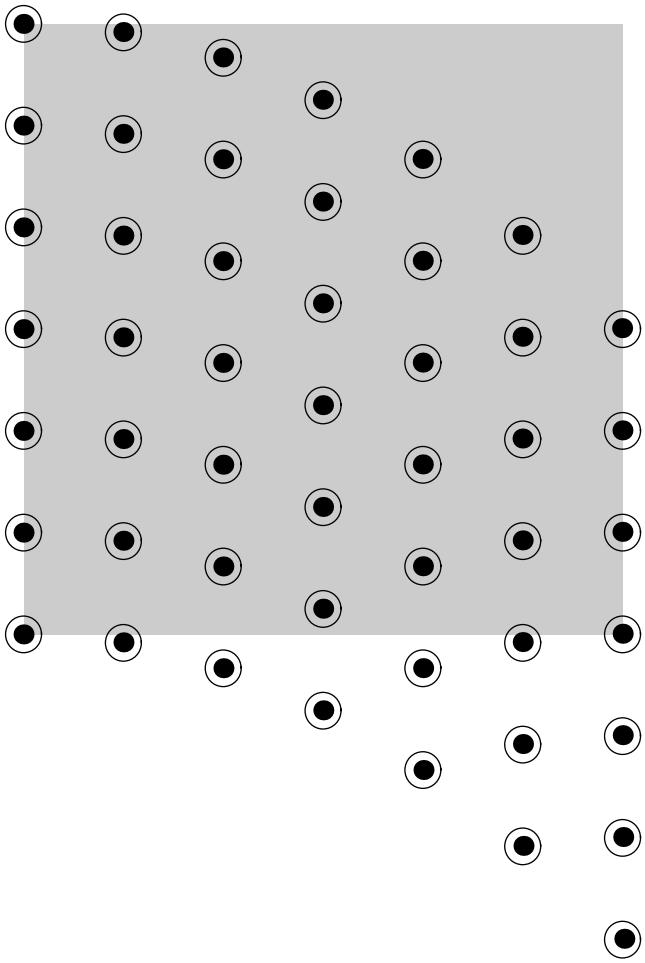

Figure 5.5: Nonuniform shear of a plate: undeformed configuration (shaded), exact solution (empty circles), MLPG solution (dots).

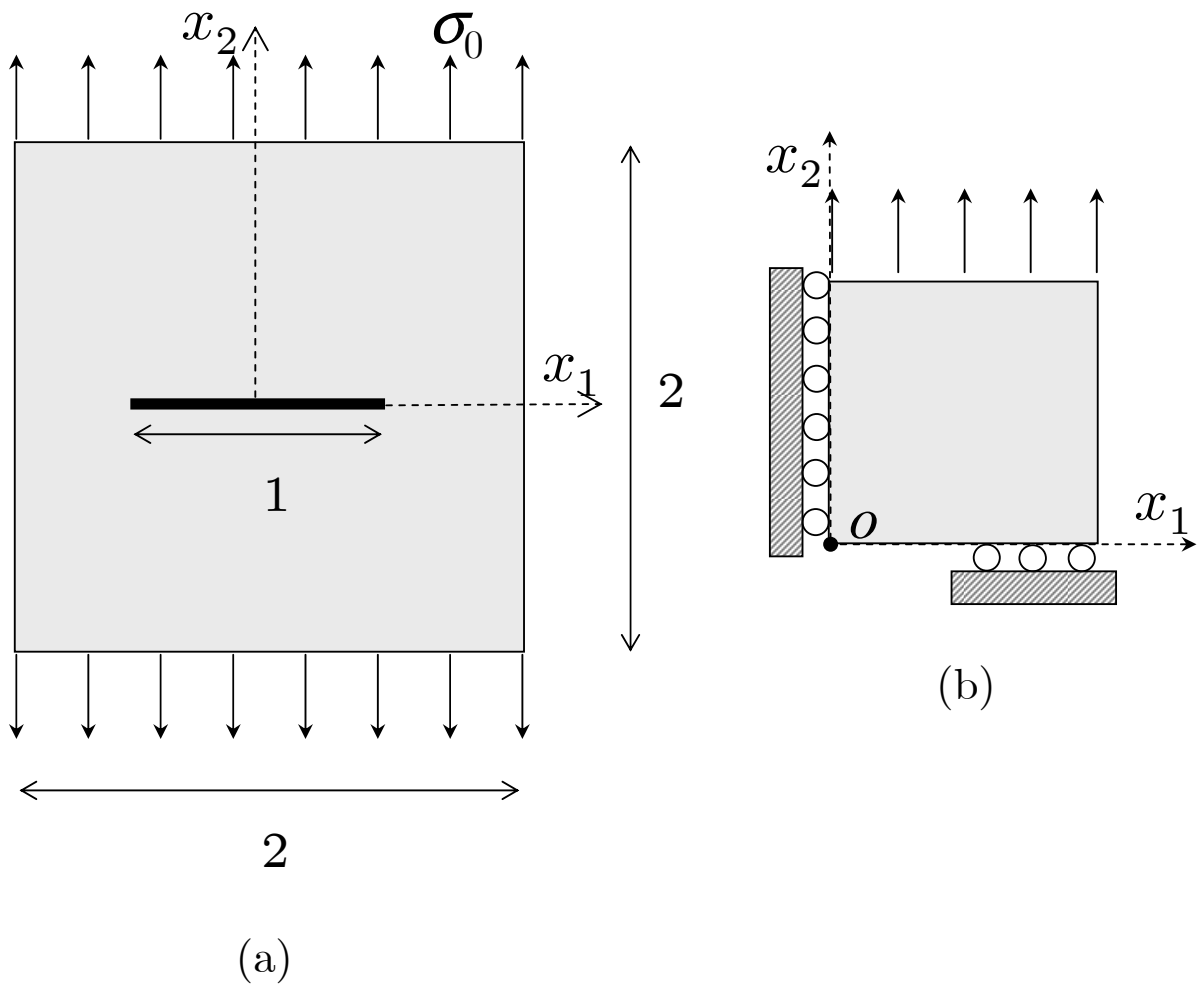

Figure 5.6: Geometry of a cracked plate loaded in mode-I.

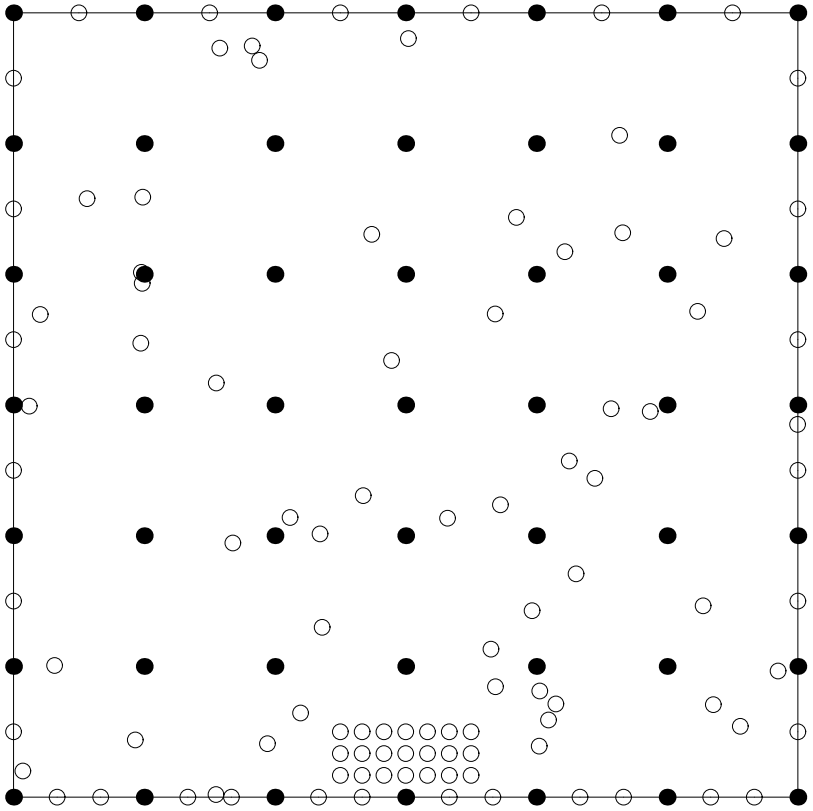

Figure 5.7: Locations of primary (filled circles) and secondary (empty circles) nodes in the quarter of a cracked plate.

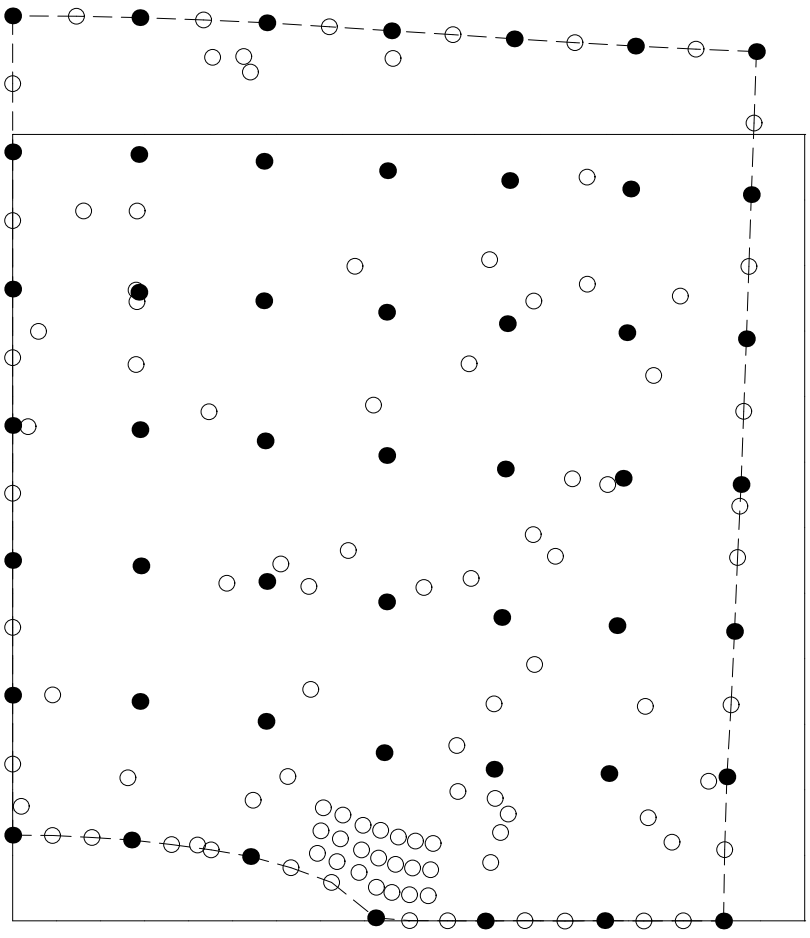

Figure 5.8: Undeformed (solid line), deformed (dotted) shape of the cracked plate, and final locations of primary (filled circles) and secondary (empty circles) nodes.

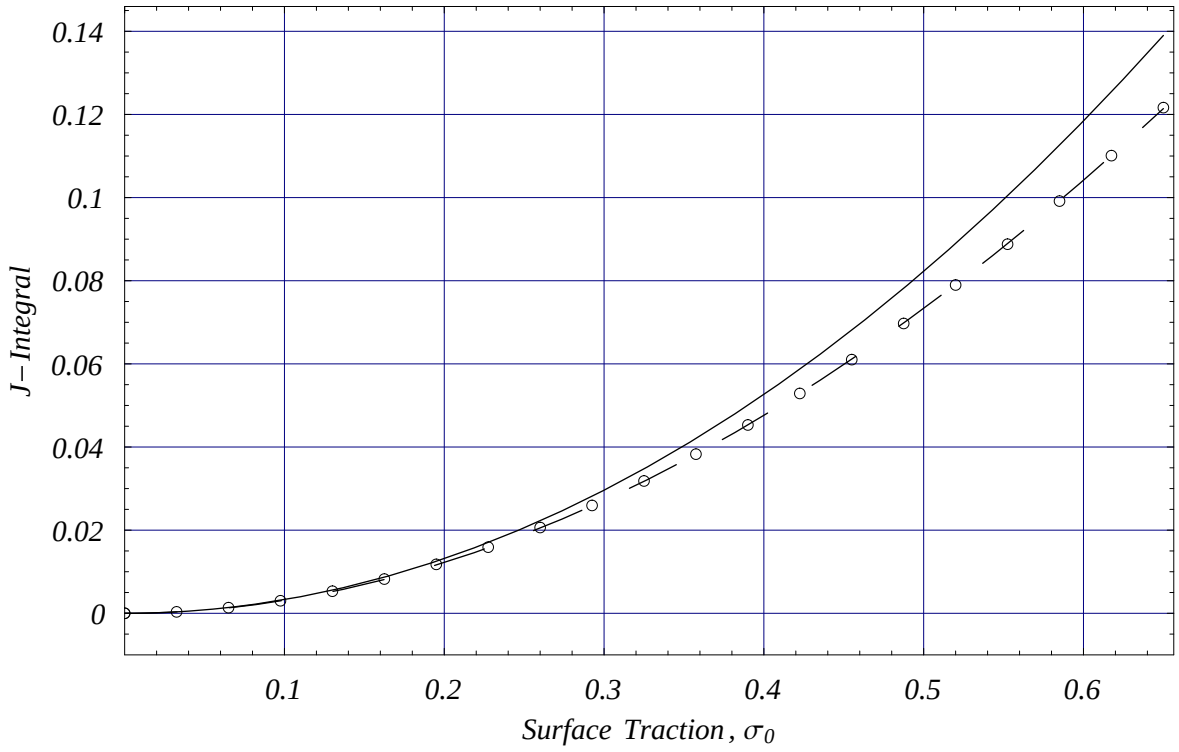

Figure 5.9: J-integral from the linear analysis (solid line), and J-integral from the nonlinear analysis (empty circles and dashed fitting curve) versus applied nominal surface traction.

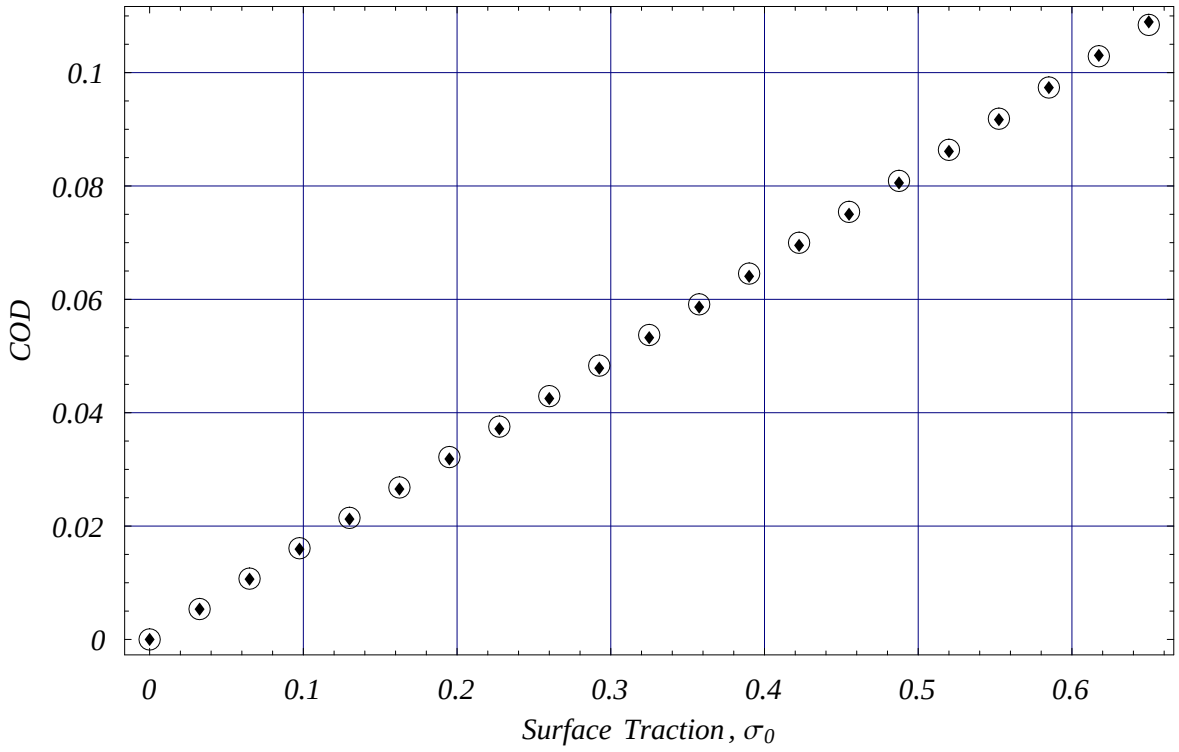

Figure 5.10: Crack opening displacement computed using the MLPG formulation (diamond), and ANSYS FE code (empty circles) versus applied nominal surface traction.

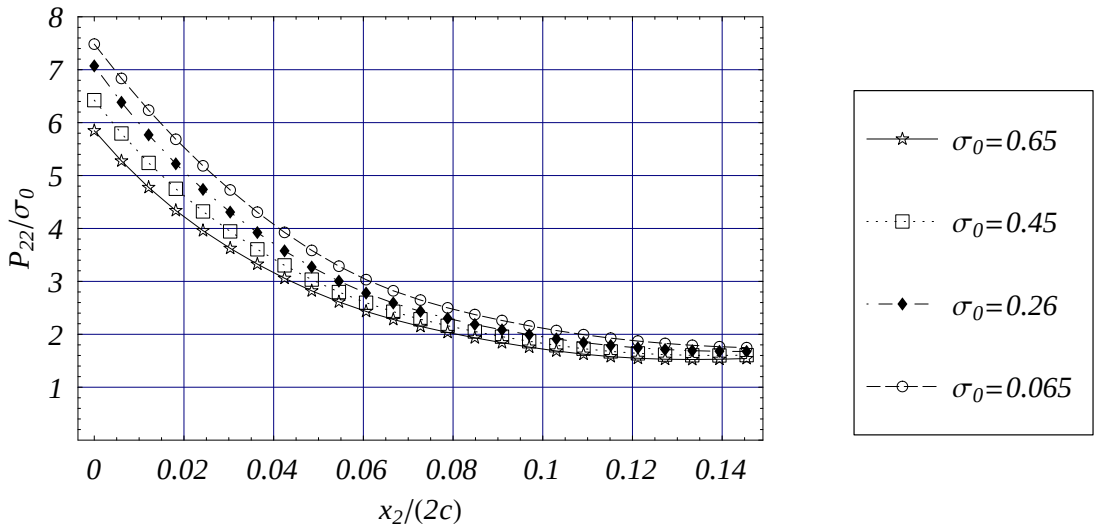

Figure 5.11: Normalized first Piola Kirchhoff stress in the neighborhood of the crack tip for different values of the applied nominal surface traction σ_0.

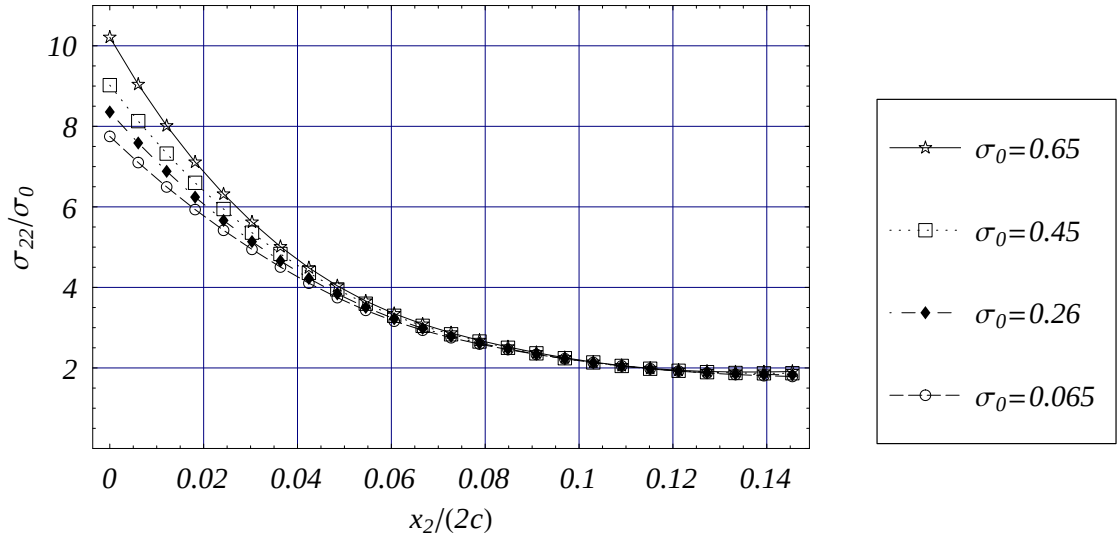

Figure 5.12: Normalized Cauchy stress in the neighborhood of the crack tip for different values of the applied nominal surface traction σ_0.

Chapter 6

Contributions

We have used the meshless local Bubnov-Galerkin (MLPG6) formulation to analyze free and forced vibrations of a segmented bar. Three different techniques have been employed to satisfy the continuity of the axial stress at the interface between two materials: Lagrange multipliers, jump functions, and modified moving least square basis functions with discontinuous derivatives. The essential boundary conditions are satisfied in all cases by the method of Lagrange multipliers. The related mixed semidiscrete formulations have been shown to be stable, and optimal in the sense that the ellipticity and the inf-sup (Babuška-Brezzi) conditions are satisfied. Numerical results obtained for a bimaterial bar have been compared with those from the analytical, and the finite element methods. The monotonic convergence of first two natural frequencies, first three mode shapes, and a static solution in the L^2, and H^1 norms has been demonstrated. The relative error in the numerical solution for a transient problem is also very small.

A consistent one-dimensional distributed electromechanical model of an electrically actuated narrow microbeam with width/height between 0.5 and 2.0 has been derived, and the pull-in parameters have been extracted with different methods. The model accounts for the position-dependent electrostatic loading, the fringing field effects due to both the finite width and the finite thickness of a microbeam, the mid-plane stretching, the mechanical distributed stiffness, and the residual axial load. Both clamped-clamped, and clamped-free (cantilever) microbeams are considered. The method of moments has been used to estimate the electrostatic load. The resulting nonlinear fourth-order differential equation under appropriate boundary conditions has been solved by two methods. Initially, a one-degree-of-freedom model was proposed to find an approximate solution of the problem. Subsequently, the meshless local Petrov-Galerkin and the Finite Element methods were used, and results from the three methods were compared. For the MLPG method the kinematic boundary conditions were enforced by introducing a set of Lagrange multipliers, and the trial and the test functions are constructed using the generalized moving least squares approximation. The nonlinear system of algebraic equations arising from the MLPG and the FE methods were

solved by using the Displacement Iteration Pull-In Extraction algorithm. Three dimensional FE simulations of narrow cantilever and clamped-clamped microbeams were also performed with the commercial code ANSYS. Furthermore, computed results were compared with those obtained from other distributed models available in the literature, and it was shown that improper fringing fields give over-estimation of the pull-in voltages and inaccurate estimations of the pull-in deflections.

We have also used the meshless local Bubnov-Galerkin (MLPG6) formulation to analyze vibrations and transient deformations of a beam with multiple cracks. The trial and the test functions were constructed using the Generalized Moving Least Squares approximation. The smoothness of the GMLS basis functions required the use of special techniques to account for the slope discontinuities at the crack locations. Therefore, a set of Lagrange multipliers was introduced to model the spring effects at the crack locations and relate motions of the intact beam segments. The method was applied to study static and transient deformations of a cracked beam, and to determine its modal properties (frequencies and mode shapes). Numerical results obtained for a simply supported beam were compared with experimental findings, analytical predictions, and finite element solutions.

Large deformations of rubber-like materials have also been analyzed by the MLPG method. A local mixed total Lagrangian weak formulation of non-linear elastic problems was presented. The deformation gradient was split into deviatoric and dilatational parts. The strain energy density was written as the sum of two functions: one a function of deviatoric strain, and the other a function of dilatational strain. The incompressibility or near incompressibility constraint was accounted for by introducing the pressure field, and penalizing the part of the strain energy density depending upon the dilatational strains. Unlike in the mixed FE formulation, it was shown that in the MLPG method there is no need for different sets of basis functions for displacement and pressure fields. Basis functions for approximating the trial solution and the test functions are generated by the Moving Least Squares method using the concept of primary and secondary nodes. The formulation does not require shadow elements or a background mesh, and therefore avoids mesh distortion difficulties in large deformation problems. Results computed with the MLPG method for a few sample problems are found to compare very well with either the corresponding analytical solutions or solutions obtained with a commercial FE code.

Bibliography

Abdel-Rahman, E. M., Younis, M. I. and Nayfeh, A. H., "Characterization of the mechanical behavior of an electrically actuated microbeam," *Journal of Micromechanics and Microengeering,* Vol. 12, 2002, pp. 759-766.

Andreaus, U., Batra, R. C. and Porfiri, M., "Vibrations of Cracked Euler-Bernoulli Beams Using Meshless Local Petrov-Galerkin (MLPG) Method," *CMES: Computer Modeling in Engineering & Sciences*, Vol. 9, 2005, pp. 111-132.

Ansys Inc., *ANSYS Release 8.0 documentation.*

Atluri, S. N. and Zhu, T., "A new Meshless Local Petrov-Galerkin (MLPG) approach in computational mechanics," *Computational Mechanics,* Vol. 22, 1998, pp. 117-127.

Atluri, S. N., Cho, J. Y. and Kim, H.-G., "Analysis of Thin Beams, Using the Meshless Local Petrov-Galerkin Method, with Generalized Moving Least Squares Interpolations," *Computational Mechanics*, Vol. 24, 1999, pp. 334-347.

Atluri, S. N. and Shen, S. P., *The Meshless Local Petrov-Galerkin (MPLG) Method,* Tech. Science Press, California, 2002.

Atluri, S. N. and Shen, S., "The Meshless Local Petrov-Galrkin (MLPG) Method: A Simple & Less-costly Alternative to Finite Element and Boundary Element Methods," *CMES: Computer Modeling in Engineering & Sciences*, Vol. 3, 2004, pp. 11-51.

Atluri, S. N., Han, Z. D. and Rajendran, A. M., "A new implementation of the meshless finite volume method, through the MLPG "Mixed" approach," *CMES: Computer Modeling in Engineering & Sciences,* Vol. 6, 2004, pp. 491-513.

Barke, E., "Line-to-Ground Capacitance Calculation for VLSI: A Comparison," *IEEE Transactions on Computer-Aided Design,* Vol. 7, 1988, pp. 295-298.

Bathe, K. J., *Finite Element Procedures,* Prentice-Hall, Englewood Cliffs, New Jersey, 1996.

Batra, R. C., "Finite plane strain deformation of rubberlike materials,". *International Journal for Numerical Methods in Engineering,* Vol. 15, 1980, pp. 145-160.

Batra, R. C. and Ching H.-K., "Analysis of Elastodynamic Deformations near a Crack/Notch Tip by the Meshless Local Petrov-Galerkin (MLPG) Method," *CMES: Computer Modeling in Engineering & Sciences*, Vol. 3, 2002, pp. 717-730.

Batra, R. C. and Liang, X.-Q., "Finite Dynamic Deformations of Smart Structures," *Computational Mechanicas,* Vol. 20, 1997, pp. 427-438.

Batra, R., Porfiri, M. and Spinello, D., "Treatment of Material Discontinuity in Two Meshless Local Petrov-Galerkin (MLPG) Formulations of Axisymmetric Transient Heat Conduction," *International Journal for Numerical Methods in Engineering*, Vol. 61, 2004, pp. 2461-2479.

Batra, R. C., Porfiri, M. and Spinello, D., "Free and Forced Vibrations of a Segmented Bar by a Meshless Local Petrov-Galerkin (MLPG) Formulation," *Computational Mechanics,* DOI 10.1007/s00466-006-0049-6, 2006a, (available online).

Batra, R. C., Porfiri,M. and Spinello, D., "Electromechanical Model of Electrically Actuated Narrow Microbeams," *Journal of MicroElectroMechanical Systems,* 2006b, (accepted).

Batra, R. C., Porfiri,M. and Spinello, D., "Analysis of Electrostatic MEMS using Meshless Local Petrov-Galerkin (MLPG) method," *Journal of Engineering Analysis with Boundary Elements,* 2006c, (accepted).

Batra, R. C. and Vidoli, S., "Higher Order Piezoelectric Plate Theory Derived from a Three-Dimensional Variational Principle," *AIAA Journal*, Vol. 40, 2002, pp. 91-104.

Batra, R. C. and Wright, T. W., "Steady State Penetration of Rigid Perfectly Plastic Targets," *International Journal of Engineering Science*, Vol. 24, 1986, pp. 41-54.

Belytschko, T., Lu, Y. Y. and Gu, L., "Element-free Galerkin Methods," *International Journal for Numerical Methods in Engineering*, Vol. 37, 1994, pp. 229-256.

Charrier, P., Dacorogna, B., Hanouzet, B. and Laborde, P., "An existence theorem for sligthly incompressible materials in non linear elasticity," *SIAM Journal on Mathematical Analysis* Vol. 19, 1988, pp. 70-85.

Chen, J. S., Pan, C. and Chang, T. Y. P., "On the control of pressure oscillations in bilinear-displacements costant-pressure elements," *Computer Methods in Applied Mechanics and Engineering,* Vol. 128, 1995, pp. 137-152.

Chen, J. S., Pan, C. and Wu, C. T., "Large deformation of rubber based on a reproducing kernel particle method," *Computational Mechanics,* Vol. 19, 1997, pp. 211-227.

Chen, J. S., Han, W., Tu, C. T. and Duan, W., "On the perturbed Lagrangian for nearly incompressible and incompressible hyperelasticity," *Computer Methods in Applied Mechanics and Engineering,* Vol. 142, 1997, pp. 335-351.

Ching H.-K. and Batra, R. C., "Determination of Crack Tip Fields in Linear Elastostatics by the Meshless Local Petrov-Galerkin (MLPG) Method," *CMES: Computer Modeling in Engineering & Sciences*, Vol. 2, 2001, pp. 273-289.

Chondros, T. G., "The continuous crack flexibility model for crack identification," *Fatigue & Fracture of Engineering Materials & Structures*, Vol. 24, 2001, pp. 643-650.

Chondros, T. G., Dimarogonas, A. D. and Yao, J., "A continuous cracked beam vibration theory," *Journal of Sound and Vibration*, Vol. 215, 1998, pp. 17-34.

Chondros, T. G. and Dimarogonas, A. D., "Vibration of a beam with a breathing crack," *Journal of Sound and Vibration*, Vol. 239, 2001, pp. 57-67.

Christides, S. and Barr, A. D. S., "One-dimensional theory of cracked Bernoulli-Euler beams," *International Journal of Mechanical Sciences,* Vol. 26, 1984, pp. 639-648.

Crisfield, M. A., *Non-linear Finite Element Analysis of Solids and Structures Vol 2, Advanced Topics,* Wiley, Chichester, 1998.

Collins, E. R., *Foundations for Microwave Engineering 2nd Edition,* McGraw-Hill, New York, 1992, pp. 130-153.

Cordes, L. W. and Moran, B., "Treatment of Material Discontinuity in the Element-Free Galerkin Method," *Computer Methods in Applied Mechanics and Engineering*, Vol. 139, 1996, pp. 75-89.

Carneiro, S. H. S. and Inman, D. J., "Continuous model for the transverse vibration of cracked Timoshenko beams," *Transactions of the ASME,* Vol. 124, 2002, pp. 310-320.

Coventor Inc., "Pull-in Voltage Analysis of Electrostatically-Actuated Beams Verifying Accuracy of Coventor Behavioral Models", available online at *www.coventor.com.*

Degani-Bochobza, O., Elata, D. and Nemirovsky, Y., "An Efficient DIPIE Algorithm for CAD of Electrostatically Actuated MEMS devices," *Journal of Microelectromechanical Systems,* Vol. 11, 2002, pp. 612-620.

Dimarogonas, A. D., "Vibration of cracked structures: A state of the art review," *Engineering Fracture Mechanics*, Vol. 55, 1996, pp. 831-857.

Duarte, C. A. M. and Oden, J. T., "Hp clouds—an hp Meshless Method," *Numerical Methods for Partial Differential Equations,* Vol. 12, 1996, pp. 673-705.

Ferreira, A. J. M., Batra, R. C., Roque, C. M. C., Qian L. F. and Martins, P. A. L. S., "Static Analysis of Functionally Graded Plates Using Third-order Shear Deformation Theory and a Meshless Method," *Composite Structures,* Vol. 69, 2005, pp. 449-457.

Gabbay, L. D., Mehner, J. E. and Senturia, S. D., "Computer-aided generation of nonlinear reduced-order dynamic macromodels I: Non-stress-stiffened case," *Journal of Microelectromechanical Systems,* Vol. 9, 2000, pp. 262-269.

Gadala, M. S., "Numerical solution of non-linear problems of continua-I, Survey of incompressibility constraints and software aspects," *Computers and Structures,* Vol. 22, 1986, pp. 841-855.

Gounaris, G. and Dimarogonas, A., "A finite element of a cracked prismatic beam for structural analysis," *Computers & Structures,* Vol. 28, 1988, pp. 309-313.

Gounaris, G., Papadoupolos C. A. and Dimarogonas, A., "Crack Identification in beams by coupled response measurements. *Computers & Structures,* Vol. 58, 1996, pp. 299-305.

Gudmunson, P., "The dynamic behaviour of slender structures with cross-sectional cracks," *Journal of the Mechanics and Physics of Solids*, Vol. 31, 1983, pp. 329-345.

Gu, Y. T. and Liu, G. R., "A Meshless Local Petrov-Galerkin (MLPG) Method for Free and Forced Vibration Analyses for Solids," *Computational Mechanics,* Vol. 27, 2001a, pp. 188-198.

Gu, Y. T. and Liu, G. R., "A meshless local Petrov–Galerkin (MLPG) formulation for static and free vibration analysis of thin plates," *Computer Modeling in Engineering & Sciences,* Vol. 2, 2001b, pp. 463-476.

Harrington, R. F., *Field Computation by Moment Methods.* Piscataway, NJ: IEEE Press, 1993, pp. 229.

Hermann, L. R., "Elasticity equations for incompressible and nearly incompressible materials by variational theorem," *AIAA Journal,* Vol. 3, 1965, pp. 1896-1900.

Hughes, T. J. R., *The Finite Element Method. Linear Static and Dynamic Finite Element Analysis,* Prentice-Hall, New Jersey, 2001.

Hung, E. S. and Senturia, S. D., "Extending the Travel Range of Analog-Tuned Electrostatic actuators," *Journal of Microelectromechanical Systems,* Vol. 8, 1999, pp. 497-505.

Iesan, D., *Saint-Venant's problem,* Springer-Verlag, New York, 1987.

Kansa, E. J., "Multiquadrics-A Scattered Data Approximation Scheme with Applications to Computational Fluid Dynamics, ii: Solutions to Parabolic, Hyperbolic and Elliptic Partial Differential Equations," *Computer & Mathematics with Applications*, Vol. 19, 1990, pp. 147-161.

Khiem, N. T., Lien, T. V., "Multi-crack detection for beam by the natural frequencies," *Journal of Sound and Vibration*, Vol. 1-2, 2004, pp. 175-184.

Kim, H.-G. and Atluri, S. N., "Arbitrary Placement of Secondary Nodes, and Error Control, in the Meshless Local Petrov-Galerkin (MLPG) Method," *CMES: Computer Modeling in Engineering & Sciences*, Vol. 1, 2000, pp. 11-32.

Krongauz, Y. and Belytschko, T., "EFG Approximation with Discontinuous Derivatives," *International Journal for Numerical Methods in Engineering*, Vol. 41, 1998, pp. 1215-1233.

Kuang, J.-H. and Chen, C.-J., "Dynamic characteristics of shaped micro-actuators solved using the differential quadrature method," *Journal of Micromechanics and Microengeering,* Vol. 14, 2004, pp. 647-655.

Lancaster, P. and Salkauskas, K., "Surfaces Generated by Moving Least Squares Methods," *Mathematics of Computation*, Vol. 37, 1981, pp. 141-158.

Landau, L. D. and Lifshitz, E. M., *Theory of elasticity,* New York, Pergamon Press, 1986.

Legrain, G., Moes, N. and Verron, E., "Stress analysis around crack tips in finite strain problems using the eXtended finite element method," *International Journal for Numerical Methods in Engineering,* Vol. 63, 2005, pp. 290-314.

Liu, G. R., *Mesh Free Methods,* CRC Press, Boca Raton, Florida, 2003.

Liu, W. K., Jun, S., Adee, J. and Belytschko, T., "Reproducing Kernel Particle Methods for Structural Dynamics," *International Journal for Numerical Methods in Engineering*, Vol. 38, 1995, pp. 1655-1679.

Liu, W., Jun, S. and Zhang, Y., "Reproducing kernel particle method," *International Journal for Numerical Methods in Fluids*, Vol. 20, 1995, pp. 1081-1106.

Lucy, L. B., "A Numerical Approach to the Testing of the Fission Hypothesis," *The Astronomical Journal*, Vol. 82, 1977, pp. 1013-1024.

Luzzato, E., "Approximate computation of non-linear effects in a vibrating cracked beam," *Journal of Sound and Vibration*, Vol. 265, 2003, pp. 745-763.

Mahmoud, M. A., Zaid, M. A. and Al Harashani, S., "Numerical frequency analysis on uniform beams with a transverse crack," *Communications in Numerical Methods in Engineering*, Vol. 15, 1999, pp. 709-715.

Mackerle, L., "Rubber and rubber-like materials, finite-element analyses and simulations, an addendum: a bibliography (1997-2003)," *Modelling and Simulation in Materials Science and Engineering,* Vol. 12, 2004, pp. 1031-1053.

Meijs, N. V. D. and Fokkema, J. T., "VLSI circuit reconstruction from mask topology," *Integration,* Vol. 2, 1984, pp. 85-119.

Meirovitch, L., *Fundamentals of Vibrations,* McGraw Hill, New York, 2001.

Melenk, J. M. and Babuska, I., "The Partition of Unity Finite Element Method: Basic Theory and Applications," *Computer Methods in Applied Mechanics and Engineering*, Vol. 139, 1996, pp. 289-314.

Mura, T. and Koya, T., *Variational methods in mechanics,* Oxford University Press, New York, 1992.

Nagdi, K., *Rubber as an Engineering Material: Guidelines for Users,* Hanser, New York, 1993.

Nathanson, H. C., Newell, W. E., Wickstrom, R. A. and Davis, J. R, "The Resonant Gate Transistor," *IEEE transactions on Electron Devices* Vol. 14, 1977, pp. 117-133.

Nayroles, B., Touzot, G. and Villon, P., "Generalizing the Finite Element Method: Diffuse Approximation and Diffuse Elements," *Computational Mechanics*, Vol. 10, 1992, pp. 307-318.

Nguyen, C. T. C., Katehi, L. P. B. and Rebeiz, G. M., "Micromachined devices for wireles communications," *Proceedings IEEE,* Vol. 86, 1998, pp. 1756-1768.

Noguchi, H. and Sachiko, M., "Analysis of Structure with Material Interface by Meshfree Method," *CMES: Computer Modeling in Engineering & Sciences*, 2006, (to appear).

Ogden, R. W., *Nonlinear Elasticity with Application to Material Modeling. Lecture notes 6 in IPPTPAN,* Warsaw, 2004.

Osterberg, P. M. and Senturia, S. D., "M-TEST: A test chip for MEMS material property measurement using electrostatically actuated test structures," *Journal of Microelectromechanical Systems,* Vol. 6, 1997, pp. 107-118.

Ostachowicz, W. M. and Krawczuk, M., "Analysis of the effect of cracks on the natural frequencies of a cantilever beam," *Journal of Sound and Vibration*, Vol. 150, 1991, pp. 191-201.

Palmer, H. B., "Capacitance of a parallel-plate capacitor by the Schwartz-Christoffel transformation," *Transactions AIEE,* Vol. 56, 1927, p. 363.

Pamidighantam, S., Puers, R., Baert, K. and Tilmans, H. A. C., "Pull-in voltage analysis of electrostatically actuated beam structures with fixed-fixed and fixed-free end conditions," *Journal of Micromechanics and Microengeering,* Vol. 12, 2002, pp. 458-464.

Peng, S. H. and Chang, W., "A compressible approach in finite element analysis of rubber-elastic materials," *Computers and Structures,* Vol. 62, 1997, pp. 573-593.

Penn, R.-W., "Volume changes accompanying the extension of rubber," *Journal of Rheology,* Vol. 4, 1970, pp. 509-517.

Press, W. H., Flannery, B. P., Teukolsky, S. H. and Vetterling, W. T., *Numerical Recipes,* Cambridge University Press, New York, 1989.

Pugno, N., Surace, C. and Ruotolo, R., "Evaluation of the non-linear dynamic response to harmonic excitation of a beam with several breathing cracks," *Journal of Sound and Vibration*, Vol. 235, 2000, pp. 749-762.

Qian, L. F. and Batra, R. C., "Transient Thermoelastic Deformations of a Thick Functionally Graded Plate," *Journal of Thermal Stresses*, Vol. 27, 2004, pp. 705-740.

Qian, L. F. and Batra, R. C., "Design of Bidirectional Functionally Graded Plate for Optimal Natural Frequencies," *Journal of Sound and Vibration*, Vol. 280, 2005, pp. 415-424.

Qian, L. F., Batra, R. C. and Chen, L. M., "Elastostatic Deformations of a Thick Plate by Using Higher-order Shear and Normal Deformable Plate Theory and Two Meshless Local Petrov-Galerkin (MLPG) Methods," *CMES: Computer Modeling in Engineering & Sciences*, Vol. 4, 2003a, pp. 161-176.

Qian, L. F., Batra, R. C. and Chen, L. M., "Free and Forced Vibrations of Thick Rectangular Plates by Using Higher-order Shear and Normal Deformable Plate Theory and Meshless Local Petrov-Galerkin (MLPG) Method," *CMES: Computer Modeling in Engineering & Sciences*, Vol. 4, 2003b, pp. 519-534.

Qian, L. F., Batra, R. C. and Chen, L. M., "Analysis of Cylindrical Bending Thermoelastic Deformations of Functionally Graded Plates by a Meshless Local Petrov-Galerkin Method," *Computational Mechanics*, Vol. 33, 2004a, pp. 263-273.

Qian, L. F., Batra, R. C. and Chen, L. M., "Static and Dynamic Deformations of a Thick Functionally Graded Elastic Plate by Using a Higher-Order Shear and Normal Deformable Plate Theory and Meshless Local Petrov-Galerkin (MLPG) Method," *Composites: Part B*, Vol. 35, 2004b, pp. 685-697.

Qian, G. L., Gu, S.-N. and Jiang, J.-S., "The dynamic behaviour and crack detection of a beam with a crack," *Journal of Sound and Vibration,* Vol. 138, 1990, pp. 233-243.

Raju, I. S. and Phillips, D. R., "Further developments in the MLPG Method for Beam Problems," *CMES: Computer Modeling in Engineering & Sciences,* Vol. 4, 2003, pp. 141-159.

Rivlin, R. S., "Large Elastic deformations of isotropic materials IV, furher developments of general theory," *Philosophical Transactions of the Royal Society of London A,* 1948, pp.

379-397.

Rizos, P. F., Aspragathos, N. and Dimarogonas, A. D., "Identification of crack location and magnitude in a cantilever beam from the vibration mode," *Journal of Sound and Vibration*, Vol. 138, 1988, pp. 381-388.

Ruotolo, R., Surace, C., Crespo, P. and Storer, D., "Harmonic analysis of the vibrations of a cantilevered beam with a closing crack," *Computers & Structures*, Vol. 61, 1996, pp. 1057-1074.

Scharnost, T. and Pian, T. H. H., "Finite element analysis of rubber-like materials by a mixed model," *International Journal for Numerical Methods in Engineering,* Vol. 12, 1978, pp. 665-676.

Saccomandi, G., *Universal results in finite elasticity. Non-Linear Elasticity,* (edited by Y. Fu and R. Ogden) Cambridge University Press, Cambridge, 2001.

Senturia, S. D., Harris, R. M., Johnson, B. P., Kim, S., Nabors, K., Shulman, M. A. and White, J. K., "A computer-aided design system for microelectromechanical systems (MEMCAD)," *Journal of Microelectromechanical Systems,* Vol. 1, 1992, pp. 3-13.

Shapoorabadi, R. J. and Kirk, A. G., "Comparison of three finite element models for analysis of MEMS micromirrors," *Proceedings SPIE, International Conference on Applications of Photonic Technology, Photonics North,* Vol. 5577, 2004, pp.849-859.

Shen, M.-H. H. and Chu, Y. C., "Vibrations of a beam with a fatigue crack," *Computers & Structures*, Vol. 45, 1992, pp. 79-93.

Shen, M.-H. H. and Pierre C., "Natural modes of Bernoulli-Euler beams with symmetric cracks," *Journal of Sound and Vibration*, Vol. 138, 1990, pp. 115-134.

Shen, M.-H. H. and Pierre, C., "Free vibrations of beams with single-edge crack," *Journal of Sound and Vibration*, Vol. 170, 1994, pp. 237-259.

Simo, J. C. and Hughes, J. R. T., *Computational Inelasticity,* Springer, NewYork, 1998.

Sukumar, N., Moran, B. and Belytschko, T., "The Natural Element Method in Solid Mechanics," *International Journal for Numerical Methods in Engineering*, Vol. 43, 1998, pp. 839-887.

Sundermeyer, J. M. and Weaver, R. L., "On crack identification and characterization in a beam by non-linear vibration analysis," *Journal of Sound and Vibration*, Vol. 183, 1995, pp. 857-871.

Taylor, G. I., "The Coalescence of Closely Spaced drops when they are at different electric potentials," *Proceedings of the Royal Society A,* Vol. 306, 1968, pp. 423-434.

Tilmans, H. A. and Legtenberg, R., "Electrostically driven vacuum-encapsulated polysilicon resonators: Part II. Theory and Performance," *Sensors and Actuators A,* Vol. 45, 1994, pp. 67-84.

Timoshenko, S. P. and Goodier, J. N., *Theory of Elasticity, 3rd edition.* Mc Graw Hill, New York, 1970.

Vidoli, S. and Batra, R. C., "Derivation of Plate and Rod Equations for a Piezoelectric Body from a Three-Dimensional Variational Principle," *Journal of Elasticity*, Vol. 59, 2000, pp. 23-50.

Warlock, A., Ching, H.-K., Kapila, A. K. and Batra, R. C. "Plane Strain Deformations of an Elastic Material Compressed in a Rough Rectangular Cavity," *International Journal of Engineering Science*, Vol. 40, 2002, pp. 991-1010.

Wendland, H., "Piecewise Polynomial, Positive Definite and Compactly Supported Radial Basis Functions of Minimal Degree," *Advances in Computational Mathematics*, Vol. 4, 1995, pp. 389-396.

Younis, M. .I, Abdel-Rahman, E. M. and Nayfeh, A. H., "A Reduced-Order Model for Electrically Actuated Microbeam-Based MEMS," *Journal of Microelectromechanical Systems,* Vol. 12, 2003, 6pp. 72-680.

Zhang, G. M. and Batra, R. C., "Modified Smoothed Particle Hydrodynamics Method and its Application to Transient Problems," *Computational Mechanics*, Vol. 34, 2004, pp. 137-146.

Appendix A

MLS and GMLS approximations

A.1 Moving Least Squares (MLS) basis functions

The MLS approximation, proposed by Lancaster and Salkauskas (1981), allows for an accurate reconstruction of a given trial function on the entire domain, from the knowledge of its values at some, suitably chosen, scattered points.

Consider a continuous scalar function q defined on the d-dimensional connected domain Ω. The generic point in Ω is indicated by $\mathbf{x}$ and its coordinates in a rectangular Cartesian coordinate system are $x_1, x_2, \ldots, x_d$. The (fictitious) nodal values at N scattered points $\mathcal{N} = \{\mathbf{x}_1, \mathbf{x}_2, ..., \mathbf{x}_N\}$ in $\bar{\Omega}$ are collected into the N-vector $\hat{\mathbf{q}} = [\hat{q}_1, ..., \hat{q}_N]^{\mathrm{T}}$. The global approximation q^h of q in Ω is defined as

$$q(\mathbf{x}) \simeq q^h(\mathbf{x}) = \mathbf{p}^{\mathrm{T}}(\mathbf{x})\,\mathbf{a}(\mathbf{x}), \quad \mathbf{x} \in \Omega, \tag{A.1}$$

where

$$\mathbf{p}^{\mathrm{T}}(\mathbf{x}) = [p_1(\mathbf{x}), p_2(\mathbf{x}), ..., p_m(\mathbf{x})], \tag{A.2}$$

is a monomial basis. For example in the two-dimensional problem a complete monomial basis of order 2 is

$$\mathbf{p}^{\mathrm{T}}(\mathbf{x}) = [1, x_1, x_2], \quad \text{linear basis}, \quad m = 3. \tag{A.3}$$

The m-vector $\mathbf{a}(\mathbf{x}) = [a_1(\mathbf{x}), \cdots, a_m(\mathbf{x})]^{\mathrm{T}}$ is composed of indeterminate coefficients, which vary with the point $\mathbf{x}$ in the domain Ω. At each location $\bar{\mathbf{x}}$ in Ω these coefficients are determined by a local least square approximation of $q(\mathbf{x})$ on a small neighborhood $\Omega_{\bar{\mathbf{x}}}$ of $\bar{\mathbf{x}}$. The local approximation $q_{\bar{\mathbf{x}}}(\mathbf{x})$ is defined by

$$q(\mathbf{x}) \simeq q_{\bar{\mathbf{x}}}(\mathbf{x}) = \mathbf{p}^{\mathrm{T}}(\mathbf{x})\,\mathbf{a}(\bar{\mathbf{x}}), \quad \mathbf{x} \in \Omega_{\bar{\mathbf{x}}} \subset \Omega. \tag{A.4}$$

Therefore, in a small neighborhood of a generic point $\bar{\mathbf{x}}$ the coefficients a_i are treated as the unknown constants of the classical polynomial least square approximation, and they are

determined by minimizing the following functional $J_{\bar{\mathbf{x}}}$ representing the weighted discrete L^2 error norm

$$J_{\bar{\mathbf{x}}}(\mathbf{a}) = \sum_{i=1}^{N} W_i(\bar{\mathbf{x}}) \left[q_{\bar{\mathbf{x}}}(\mathbf{x}_i) - \hat{q}_i \right]^2 . \tag{A.5}$$

The function W_i is the weight function of node i.

At a given location $\bar{\mathbf{x}}$ only few terms in the summation (A.5) are not zero since the supports of the weight functions W_i are much smaller than the domain Ω. This reduces the memory allocations when implementing the algorithm in a computer code, and strengthens the local character of the MLS approximation.

The functional $J_{\bar{\mathbf{x}}}$ may be rewritten in matrix notation as

$$J_{\bar{\mathbf{x}}}(\mathbf{a}) = (\mathbf{P}\mathbf{a} - \hat{\mathbf{q}})^{\mathrm{T}} \mathbf{W}(\bar{\mathbf{x}}) (\mathbf{P}\mathbf{a} - \hat{\mathbf{q}}), \tag{A.6}$$

where $\mathbf{P}$ is a (N, m) matrix of real numbers:

$$\mathbf{P}^{\mathrm{T}} = \left[\mathbf{p}^{\mathrm{T}}(\mathbf{x}_1) \quad \ldots \quad \mathbf{p}^{\mathrm{T}}(\mathbf{x}_N) \right], \tag{A.7}$$

and $\mathbf{W}$ is the following (N, N) diagonal matrix

$$\mathbf{W}(\bar{\mathbf{x}}) = \textsc{Diag} \left[W_1(\bar{\mathbf{x}}) \quad \ldots \quad W_N(\bar{\mathbf{x}}) \right]. \tag{A.8}$$

The stationarity of $J_{\bar{\mathbf{x}}}$ with respect to $\mathbf{a}$ yields:

$$\mathbf{A}(\bar{\mathbf{x}}) \mathbf{a}(\bar{\mathbf{x}}) = \mathbf{B}(\bar{\mathbf{x}}) \hat{\mathbf{q}}, \tag{A.9}$$

where the (m, m) and the (m, N) matrices $\mathbf{A}$ and $\mathbf{B}$ are defined by

$$\mathbf{A}(\bar{\mathbf{x}}) = \mathbf{P}^{\mathrm{T}} \mathbf{W}(\bar{\mathbf{x}}) \mathbf{P}, \quad \mathbf{B}(\bar{\mathbf{x}}) = \mathbf{P}^{\mathrm{T}} \mathbf{W}(\bar{\mathbf{x}}). \tag{A.10}$$

We note that the matrices $\mathbf{A}$ and $\mathbf{B}$ depend on the spatial coordinate $\bar{\mathbf{x}}$ only through the weight functions, since $\mathbf{P}$ is a matrix of real numbers. Solving for $\mathbf{a}$ in (A.9) and substituting the result in the global approximation (A.4) we get the MLS approximation

$$q^h(\mathbf{x}) = \mathbf{p}^{\mathrm{T}}(\mathbf{x}) \mathbf{A}^{-1}(\mathbf{x}) \mathbf{B}(\mathbf{x}) \hat{\mathbf{q}}, \tag{A.11}$$

which, upon introducing the basis functions $\psi(\mathbf{x})$, can be expressed as

$$q^h(\mathbf{x}) = \psi^{\mathrm{T}}(\mathbf{x}) \hat{\mathbf{q}}, \quad \psi = \left[\psi_1 \quad \ldots \quad \psi_N \right]^{\mathrm{T}}, \quad \psi^{\mathrm{T}}(\mathbf{x}) = \mathbf{p}^{\mathrm{T}}(\mathbf{x}) \mathbf{A}^{-1}(\mathbf{x}) \mathbf{B}(\mathbf{x}). \tag{A.12}$$

For node $\mathbf{x}_i$,

$$q^h(\mathbf{x}_i) \neq \hat{q}_i. \tag{A.13}$$

That is, the value of the approximating function at a node does not equal, in general, the value at that node of the function. Said differently, $\psi_j(\mathbf{x}_i) \neq \delta_{ij}$, where δ_{ij} is the Kronecker delta.

The MLS expansion (A.12) is well defined only if the matrix $\mathbf{A}$ in (A.10) is non-singular. It can be seen that this is the case if and only if the rank of the $n \times m$ matrix $\mathbf{P}_{\overline{\mathbf{x}}}$, obtained from $\mathbf{P}$ by deleting rows corresponding to those nodes whose weight function vanishes at $\overline{\mathbf{x}}$, equals m. Obviously, a necessary condition for a well-defined MLS approximation is that at least m nodal weight functions do not vanish at $\bar{\mathbf{x}}$. However, this condition is not sufficient (see, e.g., Atluri, Cho and Kim (1999)).

The smoothness of the MLS trial functions is completely determined by the smoothness of the weight functions, since the polynomial basis is infinitely differentiable. If α indicates the minimum order of differentiability of all weight functions, then from (A.10) it is evident that the trial functions are at least α times differentiable.

In the analysis, the computation of the derivative of the MLS basis functions in (A.12) is needed. To save computational effort, it is advisable to compute explicitly the first derivative of the inverse of the matrix $\mathbf{A}$ with respect to the coordinate x_j from the identity:

$$\mathbf{A}\mathbf{A}^{-1} = \mathbf{1}; \tag{A.14}$$

hence

$$\frac{\partial(\mathbf{A}^{-1})}{\partial x_j} = -\mathbf{A}^{-1}\frac{\partial \mathbf{A}}{\partial x_j}\mathbf{A}^{-1}, \tag{A.15}$$

where $j = 1, \ldots, d$. Therefore, only the knowledge of the weight functions, and their derivative is needed to compute the derivative of $\mathbf{A}^{-1}$.

In the literature (see, e.g., Atluri and Shen (2002)), fourth-order spline and Gauss weight functions are widely used. For one dimensional problems as those analyzed in Chapter 2, we employ the fourth-order spline weight function:

$$W_i(x) = \begin{cases} 1 - 6\left(\dfrac{d_i}{r_i}\right)^2 + 8\left(\dfrac{d_i}{r_i}\right)^3 - 3\left(\dfrac{d_i}{r_i}\right)^4, & d_i \leq r_i \\ 0, & d_i > r_i \end{cases}, \tag{A.16}$$

where $d_i = |x - x_i|$ is the distance from node x_i to point x on the one dimensional domain, and r_i is the radius of support of the weight function W_i. For two dimensional domains we use Gaussian weight functions with square supports:

$$W_i(\mathbf{x}) = \begin{cases} \dfrac{\exp\left[-\left(\frac{x_1 - x_{i1}}{c_i}\right)^{2k}\right] - \exp\left[-\left(\frac{r_i}{c_i}\right)^{2k}\right]}{1 - \exp\left[-\left(\frac{r_i}{c_i}\right)^{2k}\right]} \dfrac{\exp\left[-\left(\frac{x_2 - x_{i2}}{c_i}\right)^{2k}\right] - \exp\left[-\left(\frac{r_i}{c_i}\right)^{2k}\right]}{1 - \exp\left[-\left(\frac{r_i}{c_i}\right)^{2k}\right]}, & \\ & 0 \leq |x_1 - x_{i1}|, |x_2 - x_{i2}| \leq r_i \\ 0, & |x_1 - x_{i1}|, |x_2 - x_{i2}| > r_i \end{cases} \tag{A.17}$$

where c_i and k are constants controlling the shape of the weight function, and r_i is the length of the side of the square support.

The numerical integration of the MLS basis functions for two or three-dimensional problems may be computationally time-consuming due to the large number of quadrature points required. Therefore, when a large number of nodes is needed in the formulation, it is advisable to make use of the so-called secondary nodes. These nodes provide additional degrees of freedom without significantly increasing the number of required quadrature points. The approach that we suggest for adding secondary nodes in the formulation is similar to that presented in Kim and Atluri (2000) with the main difference being that we do not require a background mesh. We use the traditional MLS approximation for the generation of the entire set of trial functions, whereas in Kim and Atluri (2000) the finite element basis functions are used as weight functions for the primary nodes. We partition the set of nodes into two subsets: the set of primary nodes $\mathcal{N}_P$ and the set of secondary nodes $\mathcal{N}_S$.

Each secondary node $\mathbf{x}_i \in \mathcal{N}_S$ is associated to its closest primary node $\bar{\imath}$, $\mathbf{x}_{\bar{\imath}} \in \mathcal{N}_P$, and its weight function is the product of the weight function of the primary one, $W_{\bar{\imath}}(x)$, and an auxiliary weight function $\tilde{W}_{\bar{\imath}}(x)$. In this way, the support of the weight function of a secondary node is included in the support of the weight function of the corresponding primary node. The number of quadrature points used in the numerical evaluation of matrices and vectors in the discrete formulation (5.30) is only dictated by the number of primary nodes and by supports of their weight functions. Hence integrals in (5.30) can be computed by adding integrals on the partitions of the domain generated by intersecting supports of weight functions of the primary nodes.

For two-dimensional problems we use

$$\tilde{W}_i(\mathbf{x}) = \begin{cases} \left(1 - 6\left(\frac{x_1 - x_{i1}}{\tilde{r}_i}\right)^2 + 8\left(\frac{x_1 - x_{i1}}{\tilde{r}_i}\right)^3 - 3\left(\frac{x_1 - x_{i1}}{\tilde{r}_i}\right)^4\right) \times \\ \qquad \left(1 - 6\left(\frac{x_2 - x_{i2}}{\tilde{r}_i}\right)^2 + 8\left(\frac{x_2 - x_{i2}}{\tilde{r}_i}\right)^3 - 3\left(\frac{x_2 - x_{i2}}{\tilde{r}_i}\right)^4\right), \\ \qquad\qquad 0 \le |x_1 - x_{i1}|, |x_2 - x_{i2}| \le \tilde{r}_i \\ 0, \qquad |x_1 - x_{i1}|, |x_2 - x_{i2}| > \tilde{r}_i \end{cases} \tag{A.18}$$

where $\tilde{r}_i$ is a constant controlling the support of the weight function.

A.2 Generalized Moving Least Squares (GMLS) basis functions

The generalized moving least squares approximation (GMLS) proposed by Atluri, Cho and Kim (1999) generalizes that proposed in Lancaster and Salkauskas (1981) by allowing for the accurate reconstruction of a given trial function on the entire domain, from the knowledge

of its values and of its first derivatives at some, suitably chosen, scattered points.

Consider the function w having continuous first derivative on the domain Ω. The (fictitious) nodal values and (fictitious) derivatives at the scattered points $\mathcal{N} = \{x_1, x_2, ..., x_N\}$ in Ω are collected into the two N-vectors $\hat{\mathbf{w}} = [\hat{w}_1, ..., \hat{w}_N]^{\mathrm{T}}$ and $\hat{\vartheta} = \left[\hat{\vartheta}_1, ..., \hat{\vartheta}_N\right]^{\mathrm{T}}$ respectively, where the superscript T indicates transposition. The global approximation w^h on Ω is defined as

$$w(x) \simeq w^h(x) = \mathbf{p}^{\mathrm{T}}(x)\,\mathbf{a}(x), \quad x \in \Omega, \tag{A.19}$$

where

$$\mathbf{p}^{\mathrm{T}}(x) = \left[1, x, x^2, ..., x^{m-1}\right] \tag{A.20}$$

is a complete monomial basis of degree $m-1$.

The m-vector $\mathbf{a}(x) = [a_1(x), ..., a_m(x)]^{\mathrm{T}}$ is composed of indeterminate coefficients, which vary with the abscissa x on the domain Ω. At each location $\bar{x}$ on Ω these coefficients are determined by a local least square approximation of $w(x)$ on a small neighborhood $\Omega_{\bar{x}}$ of $\bar{x}$. The local approximation $w_{\bar{x}}(x)$ is defined by

$$w(x) \simeq w_{\bar{x}}(x) = \mathbf{p}^{\mathrm{T}}(x)\,\mathbf{a}(\bar{x}), \quad x \in \Omega_{\bar{x}} \subset \Omega. \tag{A.21}$$

In a small neighborhood of a generic point $\bar{x}$ the coefficients a_i are treated as the unknown constants of a classical polynomial least square approximation. Therefore, they are determined by minimizing the functional $J_{\bar{x}}$ representing the weighted discrete H^1 error norm (see, e.g., Atluri, Cho and Kim (1999); Figure A.1 shows the GMLS approximation), and defined by

$$J_{\bar{x}}(\mathbf{a}) = \sum_{i=1}^{N} W_i^{(w)}(\bar{x})\left[w_{\bar{x}}(x_i) - \hat{w}_i\right]^2 + \sum_{i=1}^{N} W_i^{(\vartheta)}(\bar{x})\left[w'_{\bar{x}}(x_i) - \hat{\vartheta}_i\right]^2, \tag{A.22}$$

where the superimposed prime indicates derivative with respect to the x coordinate. Functions $W_i^{(w)}$ and $W_i^{(\vartheta)}$ are weight functions of node i and are characterized by the following properties: (i) they are continuous, (ii) they equal one at $x = x_i$, (iii) they vanish when $x \notin \left(x_i - R_i^{(w)}, x_i + R_i^{(w)}\right)$ and $x \notin \left(x_i - R_i^{(\vartheta)}, x_i + R_i^{(\vartheta)}\right)$, respectively, and are positive elsewhere. The parameters $R_i^{(w)}$ and $R_i^{(\vartheta)}$ measure semi-supports of the weight functions $W_i^{(w)}$ and $W_i^{(\vartheta)}$ respectively.

At a given location $\bar{x}$ only a few terms in summation (A.22) do not vanish since the supports $R_i^{(w)}$ and $R_i^{(\vartheta)}$ of the weight functions $W_i^{(w)}$ and $W_i^{(\vartheta)}$ are much smaller than the size of Ω. This is used to reduce the memory allocations when implementing the algorithm in a computer code. Lower bounds of $R_i^{(w)}$ and $R_i^{(\vartheta)}$ are stated in Atluri, Cho and Kim (1999) for assuring the regularity of the GMLS basis functions.

The stationarity of $J_{\bar{x}}$ with respect of $\mathbf{a}$ yields

$$\mathbf{A}\left(\bar{x}\right)\mathbf{a}\left(\bar{x}\right)=\mathbf{B}\left(\bar{x}\right)\left[\begin{array}{c}\hat{\mathbf{w}}\\ \hat{\vartheta}\end{array}\right], \tag{A.23}$$

where the (m,m) and the (m,N) matrices $\mathbf{A}$ and $\mathbf{B}$ are defined by

$$\mathbf{A}\left(\bar{x}\right)=\mathbf{P}^{\mathrm{T}}\mathbf{W}^{(w)}\left(\bar{x}\right)\mathbf{P}+\left(\mathbf{P}'\right)^{\mathrm{T}}\mathbf{W}^{(\vartheta)}\left(\bar{x}\right)\mathbf{P}',\quad \mathbf{B}\left(\bar{x}\right)=\left[\begin{array}{cc}\mathbf{P}^{\mathrm{T}}\mathbf{W}^{(w)}\left(\bar{x}\right) & \left(\mathbf{P}'\right)^{\mathrm{T}}\mathbf{W}^{(\vartheta)}\left(\bar{x}\right)\end{array}\right]. \tag{A.24}$$

Here $\mathbf{W}^{(w)}$ and $\mathbf{W}^{(\vartheta)}$ are (N,N) diagonal matrices defined by

$$\mathbf{W}^{(w)}\left(\bar{x}\right)=\textsc{Diag}\left[\begin{array}{ccc}W_1^{(w)}\left(\bar{x}\right) & \ldots & W_N^{(w)}\left(\bar{x}\right)\end{array}\right],\quad \mathbf{W}^{(\vartheta)}\left(\bar{x}\right)=\textsc{Diag}\left[\begin{array}{ccc}W_1^{(\vartheta)}\left(\bar{x}\right) & \ldots & W_N^{(\vartheta)}\left(\bar{x}\right)\end{array}\right], \tag{A.25}$$

and $\mathbf{P}$, $\mathbf{P}'$ are (N,m) matrices of real numbers defined by

$$\mathbf{P}^{\mathrm{T}}=\left[\begin{array}{ccc}\mathbf{p}\left(x_1\right) & \ldots & \mathbf{p}\left(x_N\right)\end{array}\right],\quad \left(\mathbf{P}'\right)^{\mathrm{T}}=\left[\begin{array}{ccc}\mathbf{p}'\left(x_1\right) & \ldots & \mathbf{p}'\left(x_N\right)\end{array}\right]. \tag{A.26}$$

Solving (A.23) for $\mathbf{a}\left(\bar{x}\right)$ and substituting for $\mathbf{a}\left(\bar{x}\right)$ in the global approximation (A.21) we obtain the GMLS approximation

$$w^h\left(x,t\right)=\psi^{(w)}\left(x\right)^{\mathrm{T}}\hat{\mathbf{w}}+\psi^{(\vartheta)}\left(x\right)^{\mathrm{T}}\hat{\vartheta}, \tag{A.27}$$

where the vectors of basis functions $\psi^{(w)}\left(x\right)$ and $\psi^{(\vartheta)}\left(x\right)$ are given by

$$\psi^{(w)}=\mathbf{p}\left(x\right)^{\mathrm{T}}\mathbf{A}^{-1}\left(x\right)\mathbf{P}^{\mathrm{T}}\mathbf{W}^{(w)}\left(x\right),\quad \psi^{(\vartheta)}=\mathbf{p}^{\mathrm{T}}\left(x\right)\mathbf{A}^{-1}\left(x\right)\left(\mathbf{P}'\right)^{\mathrm{T}}\mathbf{W}^{(\vartheta)}\left(x\right). \tag{A.28}$$

It is convenient to group the nodal variables and the GMLS basis functions in the $2N$-vectors $\hat{\mathbf{s}}$ and ψ, respectively.

The smoothness of the GMLS trial functions is completely determined by the smoothness of the weight functions, since the monomial basis is infinitely differentiable. If $\alpha-1$ indicates

the minimum order of differentiability of all weight functions, then from (A.24) and (A.28) it is evident that the trial functions will be at least $\alpha - 1$ times differentiable.

In the present work, following Atluri, Cho and Kim (1999), and Raju and Phillips (2003), we assume the same $C^{\alpha-1}(\Omega)$ structure for all weight functions and no distinction is made between the deflection and the rotation weight functions, namely

$$W_i^{(w)}(x) = W_i^{(\vartheta)}(x) = \begin{cases} \left(1 - \left(\frac{x-x_i}{R_i}\right)^2\right)^{\alpha} & \text{if } x \in (x_i - R_i, x_i + R_i) \\ 0 & \text{if } x \notin (x_i - R_i, x_i + R_i) \end{cases} . \tag{A.29}$$

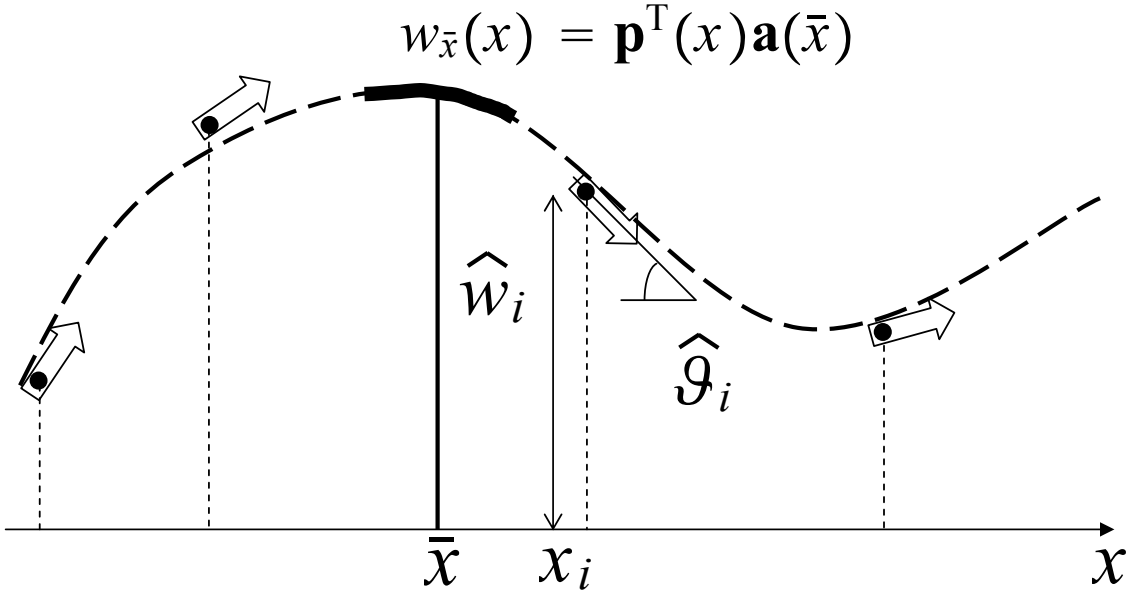

Figure A.1: Sketch of the GMLS approximation.

Appendix B

Closed-form expressions for free and forced vibrations of the segmented bar in Chapter 2

B.1 Free vibrations

We consider in eqs. (2.10) and (2.11) displacement fields of the form

$$w_1(x,t) = \mathtt{W}_1(x)\exp(i\omega t), \quad w_2(x,t) = \mathtt{W}_2(x)\exp(i\omega t). \tag{B.1}$$

Imposing homogeneous form of boundary conditions (2.12), (2.13), (2.14), and (2.15) in (2.10), (2.11), we obtain the following trascendental characteristic equation for the frequency ω:

$$\tan\left(\frac{a}{c_1}\omega\right)\tan\left(\frac{L-a}{c_2}\omega\right) = \frac{c_1 E_2}{c_2 E_1}. \tag{B.2}$$

The corresponding mode shapes are given by

$$\mathtt{W}_1(\omega,x) = \gamma(\omega)\cos\left(\frac{\omega}{c_1}x\right),$$

$$\mathtt{W}_2(\omega,x) = \gamma(\omega)\frac{\cos\left(\frac{a}{c_1}\omega\right)}{\cos\left(\frac{a}{c_2}\omega\right)}\frac{1}{\tan\left(\frac{a}{c_2}\omega\right)-\tan\left(\frac{L}{c_2}\omega\right)}\left[\sin\left(\frac{\omega x}{c_2}\right)-\tan\left(\frac{\omega L}{c_2}\right)\cos\left(\frac{\omega x}{c_2}\right)\right], \tag{B.3}$$

where $\mathtt{W}_1$ is defined on $(0,a)$, and $\mathtt{W}_2$ on (a,L). Adopting the normalization

$$\int_0^a \mathtt{W}_1^2(\omega,x)\,\mathrm{d}x + \int_a^L \mathtt{W}_2^2(\omega,x)\,\mathrm{d}x = 1, \tag{B.4}$$

we get

$$\gamma(\omega) = \frac{\omega}{c_1\sin\left(\frac{L}{c_1}\omega\right) - c_2\cos\left(\frac{a}{c_2}\omega\right)\tan\left(\frac{L-a}{c_2}\omega\right)}. \tag{B.5}$$

B.2 Forced vibrations

Let

$$\mathsf{W}_i(x,s) = \int_0^\infty \exp(-st)\, w_i(x,t)\,\mathrm{d}t, \quad \mathsf{P}(s) = \int_0^\infty \exp(-st)\, p(t)\,\mathrm{d}t, \qquad i=1,2, \tag{B.6}$$

be the one-sided Laplace transforms of w_i and p. Therefore, the system of partial differential equations (2.10) and (2.11) in the Laplace domain becomes

$$\frac{\partial^2 \mathsf{W}_i(x,s)}{\partial x^2} - \frac{s^2}{c_i^2}\mathsf{W}_i(x,s) = 0, \qquad i=1,2, \tag{B.7}$$

whose general solution is

$$\mathsf{W}_i(x,s) = A_i(s)\exp\left(-\frac{s}{c_i}x\right) + B_i(s)\exp\left(\frac{s}{c_i}x\right), \qquad i=1,2, \tag{B.8}$$

where two waves propagating in opposite directions are recognized. The four coefficients are determined by imposing the following boundary conditions in the Laplace domain:

$$\begin{aligned} E_1\frac{\partial \mathsf{W}_1}{\partial x}(0,s) &= \mathsf{P}(s), \\ \mathsf{W}_1(a,s) &= \mathsf{W}_2(a,s), \\ E_1\frac{\partial \mathsf{W}_1}{\partial x}(a,s) &= E_2\frac{\partial \mathsf{W}_2}{\partial x}(a,s), \\ \mathsf{W}_2(L,s) &= 0. \end{aligned} \tag{B.9}$$

Hence we obtain

$$\begin{aligned} A_1(s) &= -\frac{c_1}{E_1}\frac{\alpha\exp\left(-2\dfrac{L-a}{c_2}s\right)+1}{1+\Xi(s)}\frac{\mathsf{P}(s)}{s}, \\ B_1(s) &= \frac{c_1}{E_1}\frac{\alpha\exp\left(-2\dfrac{a}{c_1}s\right)+\exp\left(-2\left(\dfrac{a}{c_1}+\dfrac{L-a}{c_2}\right)s\right)}{1+\Xi(s)}\frac{\mathsf{P}(s)}{s}, \\ A_2(s) &= -2\frac{c_1c_2}{c_1E_2+c_2E_1}\frac{\exp\left(\left(\dfrac{a}{c_2}-\dfrac{a}{c_1}\right)s\right)}{1+\Xi(s)}\frac{\mathsf{P}(s)}{s}, \\ B_2(s) &= 2\frac{c_1c_2}{c_1E_2+c_2E_1}\frac{\exp\left(-\left(\dfrac{a}{c_1}+\dfrac{2L-a}{c_2}\right)s\right)}{1+\Xi(s)}\frac{\mathsf{P}(s)}{s}, \end{aligned} \tag{B.10}$$

where the constant $\alpha = \dfrac{c_1E_2-c_2E_1}{c_1E_2+c_2E_1}$, and the function

$$\Xi(s) = \exp\left(-2\left(\frac{a}{c_1}+\frac{L-a}{c_2}\right)s\right) + \alpha\exp\left(-2\frac{L-a}{c_2}s\right) + \alpha\exp\left(-2\frac{a}{c_1}s\right), \tag{B.11}$$

have been introduced. Identifying the term $\dfrac{1}{1+\Xi(s)}$ as the sum of the corresponding geometric series, we write

$$\begin{aligned}\frac{1}{1+\Xi(s)} &= \sum_{j=0}^{\infty}\left[-\Xi(s)\right]^{j} \\ &= \sum_{j=0}^{\infty}\sum_{k=0}^{j}\sum_{h=0}^{k}\binom{j}{k}\binom{k}{h}(-1)^{j}\,\alpha^{k}\exp\left(-2\left(\frac{(j-k+h)a}{c_1}+\frac{(j-h)(L-a)}{c_2}\right)s\right).\end{aligned} \tag{B.12}$$

Therefore, solutions are given by

$$\mathsf{W}_i(x,s) = G_i(x,s)\,\mathsf{P}(s), \tag{B.13}$$

where

$$\begin{aligned}G_1(x,s) = \frac{c_1}{sE_1}\sum_{j=0}^{\infty}\sum_{k=0}^{j}\sum_{h=0}^{k}\binom{j}{k}\binom{k}{h} \\ \left\{(-1)^{j+1}\left[\alpha^{k+1}\exp\left(-2\left(\frac{(j-k+h)a}{c_1}+\frac{(j-h+1)(L-a)}{c_2}+\frac{x}{2c_1}\right)s\right)+\right.\right. \\ \left.\alpha^{k}\exp\left(-2\left(\frac{(j-k+h)a}{c_1}+\frac{(j-h)(L-a)}{c_2}+\frac{x}{2c_1}\right)s\right)\right]+ \\ (-1)^{j}\left[\alpha^{k+1}\exp\left(-2\left(\frac{(j-k+h+1)a}{c_1}+\frac{(j-h)(L-a)}{c_2}-\frac{x}{2c_1}\right)s\right)+\right. \\ \left.\left.\alpha^{k}\exp\left(-2\left(\frac{(j-k+h+1)a}{c_1}+\frac{(j-h+1)(L-a)}{c_2}-\frac{x}{2c_1}\right)s\right)\right]\right\},\end{aligned} \tag{B.14}$$

and

$$\begin{aligned}G_2(x,s) = \frac{2c_1c_2}{s(c_1E_2+c_2E_1)}\sum_{j=0}^{\infty}\sum_{k=0}^{j}\sum_{h=0}^{k}\binom{j}{k}\binom{k}{h}\alpha^{k} \\ \left\{(-1)^{j+1}\exp\left(-2\left(\frac{(j-k+h)a}{c_1}+\frac{(j-h)(L-a)}{c_2}+\frac{x-a}{2c_2}+\frac{a}{2c_1}\right)s\right)+\right. \\ \left.(-1)^{j}\exp\left(-2\left(\frac{(j-k+h)a}{c_1}+\frac{(j-h)(L-a)}{c_2}+\frac{a}{2c_1}+\frac{2L-a-x}{2c_2}\right)s\right)\right\},\end{aligned} \tag{B.15}$$

are the transfer functions. From the shifting theorem in the real domain (see, e.g., Meirovitch (2001)) the inverse Laplace transforms $g_1(x,t)$ and $g_2(x,t)$ of the transfer functions are easily found. Using the convolution theorem (see, e.g., Meirovitch (2001)), the axial deflections in the time domain are given by

$$w_i(x,t) = \int_0^t g_i(x,t-\vartheta)\,p(\vartheta)\,\mathrm{d}\vartheta, \quad i=1,2.$$

Recalling the expression (2.18) for $p(t)$ we obtain

$$w_1(x,t) = \frac{c_1 PT}{\pi E_1} \sum_{j=0}^{\infty} \sum_{k=0}^{j} \sum_{h=0}^{k} \binom{j}{k} \binom{k}{h} \tag{B.16}$$
$$\left\{ (-1)^{j+1} \left[\alpha^{k+1} \zeta \left(t - 2 \left(\frac{(j-k+h)a}{c_1} + \frac{(j-h+1)(L-a)}{c_2} + \frac{x}{2c_1} \right) \right) + \right.\right.$$
$$\left. \alpha^k \zeta \left(t - 2 \left(\frac{(j-k+h)a}{c_1} + \frac{(j-h)(L-a)}{c_2} + \frac{x}{2c_1} \right) \right) \right] +$$
$$(-1)^j \left[\alpha^{k+1} \zeta \left(t - 2 \left(\frac{(j-k+h+1)a}{c_1} + \frac{(j-h)(L-a)}{c_2} - \frac{x}{2c_1} \right) \right) + \right.$$
$$\left.\left. \alpha^k \zeta \left(t - 2 \left(\frac{(j-k+h+1)a}{c_1} + \frac{(j-h+1)(L-a)}{c_2} - \frac{x}{2c_1} \right) \right) \right] \right\},$$

$$w_2(x,t) = \frac{2c_1 c_2 PT}{\pi (c_1 E_2 + c_2 E_1)} \sum_{j=0}^{\infty} \sum_{k=0}^{j} \sum_{h=0}^{k} \binom{j}{k} \binom{k}{h} \alpha^k \tag{B.17}$$
$$\left\{ (-1)^{j+1} \zeta \left(t - 2 \left(\frac{(j-k+h)a}{c_1} + \frac{(j-h)(L-a)}{c_2} + \frac{x-a}{2c_2} + \frac{a}{2c_1} \right) \right) + \right.$$
$$\left. (-1)^j \zeta \left(t - 2 \left(\frac{(j-k+h)a}{c_1} + \frac{(j-h)(L-a)}{c_2} + \frac{a}{2c_1} + \frac{2L-a-x}{2c_2} \right) \right) \right\},$$

where

$$\zeta(\beta) := \left\{ \begin{array}{c} \left(1 - \cos\frac{\pi\beta}{T}\right) \mathcal{H}(\beta), \quad \beta < T \\ 2\mathcal{H}(\beta), \quad \beta \geq T \end{array} \right. , \qquad \beta \in \mathbb{R}. \tag{B.18}$$

Obviously, $w_1(x,t)$ is defined for $x \in (0,a)$, and $w_2(x,t)$ for $x \in (a,L)$.

Appendix C

Method of moments

The potential ϕ for an arbitrary charge distribution per unit surface, ρ_{S}, is given by

$$\phi\left(y,z\right)=-\frac{1}{2\pi\epsilon_0\epsilon_{\mathrm{r}}}\int_{\Gamma}\rho_{\mathrm{S}}\left(\theta,\zeta\right)\ln\left\|\left(y,z\right)-\left(\theta,\zeta\right)\right\|\,\mathrm{d}\Gamma+C_{\mathrm{T}},\tag{C.1}$$

where $\left\|\left(y,z\right)-\left(\theta,\zeta\right)\right\|=\sqrt{\left(y-\theta\right)^2+\left(z-\zeta\right)^2}$ is the distance from the source point (θ,ζ) to the observation point (y,z), Γ is the overall boundary of the conductors, and C_{T} is a constant that may be neglected since it does not affect the charge distribution. Boundary conditions on the top and the bottom rectangle, say Γ_{t} and Γ_{b}, are $\phi=\bar{V}$ and $\phi=0$ respectively. The boundary of each plate is subdivided into small elements and the charge density, $\rho_{\mathrm{S}i}$, is assumed to be constant in element i (piecewise constant basis functions). For convenience we use the same mesh of N_{e} elements for the two identical rectangles. By substituting the charge density approximation into (C.1), and by imposing the boundary conditions at the geometric centers P_i of the $2N_{\mathrm{e}}$ elements (collocation method), we obtain the following linear system of $2N_{\mathrm{e}}$ equations in $2N_{\mathrm{e}}$ unknowns collected in the vector ρ_{S}:

$$\mathbf{L}\,\rho_{\mathrm{S}}=\mathbf{g}.\tag{C.2}$$

The generic entry of the coefficient matrix $\mathbf{L}$ is given by:

$$i=j:\qquad L_{ii}=\Delta\Gamma_i\left(\ln\left(\Delta\Gamma_i/2\right)-1\right),\tag{C.3}$$

$$i\neq j:\qquad L_{ij}=-\Delta\Gamma_j\left(1-\ln\left\|P_j^{(2)}-P_i\right\|\right)-\left\|P_j^{(1)}-P_i\right\|\cos\beta_{ij}\ln\frac{\left\|P_j^{(2)}-P_i\right\|}{\left\|P_j^{(1)}-P_i\right\|}\tag{C.4}$$

$$+\,\alpha_{ij}\left\|P_j^{(1)}-P_i\right\|\sin\beta_{ij},\tag{C.5}$$

where $\Delta\Gamma_i$ is the length of the i-th element, $P_j^{(1)}$ and $P_j^{(2)}$ are the extrema of the j-th element, β_{ij} is the angle between the segments $P_j^{(1)}P_j^{(2)}$ and $P_j^{(1)}P_i$, and α_{ij} is the angle between the segments $P_iP_j^{(2)}$ and $P_iP_j^{(1)}$. We note that these angles can be computed by using Carnot's

theorem. The element of the vector $\mathbf{g}$ equals $\bar{V}$ if it refers to an element of Γ_{t}, and 0 if it refers to an element of Γ_{b}. From the knowledge of the distributed charge per unit surface area, the charge stored per unit line in each plate may be directly computed, and the capacitance per unit line estimated.

Appendix D

Constitutive relations for hyperelastic and Mooney-Rivlin materials

For an isotropic hyperelastic material the strain energy density (per unit volume in the reference configuration) function can be written as

$$W(\mathbf{F}) = W(I_1, I_2, I_3), \tag{D.1}$$

where I_1, I_2, I_3 are principal invariants of the right Cauchy-Green strain tensor $\mathbf{C}$, and $\mathbf{F}$ is the deformation gradient. From the strain energy function, one obtains the following expression for the second Piola-Kirchhoff stress tensor.

$$\mathbf{S} = 2\frac{\partial W}{\partial I_1}\mathbf{1} + 2\frac{\partial W}{\partial I_2}(I_1\mathbf{1} - \mathbf{C}) + 2\frac{\partial W}{\partial I_3}I_3\mathbf{C}^{-1}. \tag{D.2}$$

For incompressible materials the deformation gradient must satisfy the constraint

$$\det \mathbf{F} = J = 1, \tag{D.3}$$

at each point of the body. Because of the constraint (D.3) derivatives of the strain energy density with respect to the three principal invariants are not independent and the strain energy density is modified as follows to accommodate the constraint:

$$W(\mathbf{F}) = W(I_1, I_2) + p(J - 1), \tag{D.4}$$

where p is called the pressure that can not be determined from the deformation of the body. Hence for the stress tensor we have

$$\mathbf{S} = 2\left(\frac{\partial W}{\partial I_1}\frac{\partial I_1}{\partial \mathbf{C}} + \frac{\partial W}{\partial I_2}\frac{\partial I_2}{\partial \mathbf{C}}\right) + p\mathbf{C}^{-1}. \tag{D.5}$$

For nearly incompressible isotropic hyperelastic materials the stored energy function may be written as (see, e.g., Bathe (1996)):

$$W(\mathbf{C},p) = \bar{W}(\mathbf{C}) + Q(\mathbf{C},p), \tag{D.6}$$

where

$$J_1 = I_1 \left(I_3\right)^{-1/3}, \qquad J_2 = I_2 \left(I_3\right)^{-2/3}, \tag{D.7}$$

and

$$\bar{W}\left(\mathbf{C}\right) = W_1\left(J_1, J_2\right) + W_2\left(J\right), \quad W_2\left(J\right) = kG\left(J\right), \tag{D.8}$$

$$Q\left(\mathbf{C},p\right) = -\frac{1}{2k}\left(\bar{p}\left(J\right) - p\right)^2, \quad \bar{p} = -\frac{\mathrm{d}W_2}{\mathrm{d}J} = -k\frac{\mathrm{d}G}{\mathrm{d}J}. \tag{D.9}$$

Here W_1 and W_2 are the strain energy densities depending on the distortional and the dilatational deformations respectively, k describes the degree of compressibility, the function G vanishes only for isochoric deformations, and $\bar{p}$ is the pressure computed from the deformation gradient. Formally, when $k \to \infty$ the material becomes incompressible. The parameters J_1, J_2 are the reduced invariants proposed by Penn (1970) to separate the deformation into distortional and dilatational parts. Following this decomposition, the second Piola-Kirchhoff stress tensor is written as

$$\mathbf{S} = 2\frac{\partial W}{\partial \mathbf{C}} = 2\left(\frac{\partial \bar{W}}{\partial \mathbf{C}} + \frac{\partial Q}{\partial \mathbf{C}}\right) = \bar{\mathbf{S}} - \frac{2}{k}\left(\bar{p} - p\right)\frac{\partial \bar{p}}{\partial \mathbf{C}}, \qquad \bar{\mathbf{S}} = 2\frac{\partial \bar{W}}{\partial \mathbf{C}}. \tag{D.10}$$

The contribution to the stress field from displacements only may be rewritten as:

$$\bar{\mathbf{S}} = 2\left(\frac{\partial W_1}{\partial J_1}\frac{\partial J_1}{\partial \mathbf{C}} + \frac{\partial W_2}{\partial J_2}\frac{\partial J_2}{\partial \mathbf{C}} - \bar{p}\frac{\partial J}{\partial \mathbf{C}}\right). \tag{D.11}$$

By computing the derivatives of the reduced invariants with respect to the strain tensor, and by introducing the quantities

$$K_1 = \frac{\partial W_1}{\partial J_1}, \qquad K_2 = \frac{\partial W_1}{\partial J_2}, \tag{D.12}$$

the tensor $\bar{\mathbf{S}}$ becomes

$$\bar{\mathbf{S}} = 2\left(K_1 I_3^{-1/3}\left(\mathbf{I} - \frac{1}{3}I_1\mathbf{C}^{-1}\right) + K_2 I_3^{-2/3}\left(I_1\mathbf{I} - \mathbf{C} - \frac{2}{3}I_2\mathbf{C}^{-1}\right)\right) - J\bar{p}\mathbf{C}^{-1}, \tag{D.13}$$

where we used the relations

$$\frac{\partial I_1}{\partial \mathbf{C}} = \mathbf{I}, \qquad \frac{\partial I_2}{\partial \mathbf{C}} = I_1\mathbf{I} - \mathbf{C}, \qquad \frac{\partial I_3}{\partial \mathbf{C}} = I_3\mathbf{C}^{-1}. \tag{D.14}$$

For nearly incompressible materials several forms of the strain energy function are available in the literature, see, e.g., Peng and Chang (1997). Following Chen, Pan and Wu (1997) we use

$$W_1 = \sum_{m+n=1}^{\infty} A_{mn}\left(J_1 - 3\right)^m\left(J_2 - 3\right)^n, \tag{D.15a}$$

$$G = \frac{1}{2}\left(J - 1\right)^2. \tag{D.15b}$$

The expression (D.15b) for the dilatation energy was proposed by Rivlin (1948). We note that the resulting pressure field is given by

$$\bar{p} = -\frac{\mathrm{d}W_2}{\mathrm{d}J} = -k\,(J-1)\,. \tag{D.16}$$

For Mooney-Rivlin materials

$$W_1 = A_{10}\,(J_1 - 3) + A_{01}\,(J_2 - 3)\,. \tag{D.17}$$

Henceforth, we set

$$K_1 = A_{10},\ K_2 = A_{01}. \tag{D.18}$$

The choice of the dilatational strain energy is somewhat non-unique, since it has not been proved so far that it allows for the convergence of the solution for a nearly incompressible body to the solution of the corresponding compressible one, but numerical experiments (see, e.g., Chen, Pan and Wu (1997)) have shown its efficacy.

For the dilatation energy function (D.15b), the stress tensor is given by

$$\mathbf{S} = 2\left(K_1 I_3^{-1/3}\left(\mathbf{I} - \frac{1}{3}I_1\mathbf{C}^{-1}\right) + K_2 I_3^{-2/3}\left(I_1\mathbf{I} - \mathbf{C} - \frac{2}{3}I_2\mathbf{C}^{-1}\right)\right) - pJ\mathbf{C}^{-1}. \tag{D.19}$$

We note that in this formulation the incompressibility constraint is imposed by increasing the value of the parameter k. The approach is equivalent to the one followed in the linear elastic case when the Poisson ratio was chosen close to 1/2.

The elasticity tensor $\mathbb{C}$ has the following expression:

$$\begin{aligned}
\mathbb{C} = 2\frac{\partial \mathbf{S}}{\partial \mathbf{C}} &= \frac{4}{3}K_1 I_3^{-1/3}\left[-2\,\mathbf{C}^{-1}\boxtimes\mathbf{I} + \frac{1}{3}I_1\left[\mathbf{C}^{-1}\otimes\mathbf{C}^{-1} + 3\,\mathbf{C}^{-1}\,\odot\mathbf{C}^{-1}\right]\right] + \\
&\frac{4}{3}K_2 I_3^{-2/3}\left[-4I_1\mathbf{C}^{-1}\boxtimes\mathbf{I} + 4\mathbf{C}^{-1}\boxtimes\mathbf{C}^{-1} + 2I_2\left(\frac{2}{3}\mathbf{C}\otimes\mathbf{C}^{-1} + \mathbf{C}^{-1}\odot\mathbf{C}^{-1}\right) + 3\,(\mathbf{I}\otimes\mathbf{I} - \mathbf{I}\odot\mathbf{I})\right] + \\
&4\,H_{11}I_3^{-2/3}\left(\mathbf{I} - \frac{1}{3}I_1\mathbf{C}^{-1}\right)\otimes\left(\mathbf{I} - \frac{1}{3}I_1\mathbf{C}^{-1}\right) + 4\,H_{12}\left[\left(\mathbf{I} - \frac{1}{3}I_1\mathbf{C}^{-1}\right)\otimes\left(I_1\mathbf{I} - \mathbf{C} - \frac{2}{3}I_2\mathbf{C}^{-1}\right)\right] + \\
&4\,H_{22}I_3^{-4/3}\left(I_1\mathbf{I} - \mathbf{C} - \frac{2}{3}I_2\mathbf{C}^{-1}\right)\otimes\left(I_1\mathbf{I} - \mathbf{C} - \frac{2}{3}I_2\mathbf{C}^{-1}\right) - pJ\left(\mathbf{C}^{-1}\otimes\mathbf{C}^{-1} - 2\,\mathbf{C}^{-1}\,\odot\mathbf{C}^{-1}\right).
\end{aligned} \tag{D.20}$$

with (in rectangular Cartesian coordinates)

$$H_{ij} = \frac{\partial W_1}{\partial J_i \partial J_j}, \qquad \mathbf{A}\boxtimes\mathbf{B} = \frac{1}{2}\left(\mathbf{A}\otimes\mathbf{B} + \mathbf{B}\otimes\mathbf{A}\right), \qquad (\mathbf{A}\odot\mathbf{A})_{ijkl} = \frac{1}{2}\left(A_{ik}A_{jl} + A_{il}A_{jk}\right), \tag{D.21}$$

and

$$\frac{\partial \mathbf{C}^{-1}}{\partial \mathbf{C}} = -\mathbf{C}^{-1}\odot\mathbf{C}^{-1}. \tag{D.22}$$

Similarly the tensor $\mathbf{H}$ relating the incremental stress to the incremental pressure, and the tensor $\mathbf{Q}$ are given by

$$\mathbf{H} = \frac{\partial \mathbf{S}}{\partial p} = -J\mathbf{C}^{-1}, \qquad \mathbf{Q} = 2\frac{\partial \bar{p}}{\partial \mathbf{C}} = -kJ\mathbf{C}^{-1} \equiv k\mathbf{H}. \tag{D.23}$$

Expressions for tensors $\mathbb{C}$, $\mathbf{H}$ and $\mathbf{Q}$ for a natural reference configuration are

$$\mathbb{C} = \frac{4}{3}\left(K_1 + K_2\right)\left(3\mathbf{I} \odot \mathbf{I} - \mathbf{I} \otimes \mathbf{I}\right), \qquad \mathbf{H} = -\,\mathbf{I}, \qquad \mathbf{Q} = -k\mathbf{I}. \tag{D.24}$$

Therefore, for infinitesimal deformations the material behaves as an isotropic linear elastic with constitutive parameters

$$\nu = \frac{1}{2}\left(1 - 2\frac{K_1 + K_2}{k}\right), \qquad E = \left(6 - 4\frac{K_1 + K_2}{k}\right)\left(K_1 + K_2\right). \tag{D.25}$$

Vita

Maurizio Porfiri was born on November 19, 1976 in Rome, Italy. In 2000, he received the Master of Science degree in Engineering Mechanics from the Virginia Polytechnic Institute and State University, Blacksburg, USA; in 2001 he earned the "Laurea" degree in Electrical Engineering with honours from the University of Rome "La Sapienza", Rome, Italy; in 2005 he was awarded with the Ph.D. degree in Theoretical and Applied Mechanics from the University of Rome "La Sapienza" and with the Ph.D. in Mechanics from the University of Toulon et du Var, Toulon, France. In addition, from July 2005 to June 2006, he was a postdoctoral associate in the Bradley Department of Electrical and Computer Engineering at the Virginia Polytechnic Institute and State University.